CORROSION OF AUSTENITIC STAINLESS STEELS AND NI-BASED ALLOYS IN MOLTEN SALTS FOR CONDITIONS IN CONCENTRATED SOLAR POWER PLANTS

by

Qingyang Liu

Submitted in accordance with the requirements for the degree of

Doctor of Philosophy

The University of Leeds

Institute of Functional Surfaces

School of Mechanical Engineering

Sep 2022

The candidate confirms that the work submitted is his own and that appropriate credit has been given where reference has been made to the work of others.

Publication Statement

The candidate confirms that the work submitted is his own, except where work which has formed part of jointly authored publications has been included. The candidate confirms that appropriate credit has been given within the thesis where reference has been made to the work of others.

1. Q. Liu, J. Qian, R. Barker, C. Wang, A. Neville, F. Pessu, Application of double loop electrochemical potentio-kinetic reactivation for characterizing the intergranular corrosion susceptibility of stainless steels and Ni-based alloys in solar nitrate salts used in CSP systems, Engineering Failure Analysis, Vol. 129, 2021, 105717, https://doi.org/10.1016/j.engfailanal.2021.105717.
2. Q. Liu. R. Barker, C. Wang, J. Qian, A. Neville, F. Pessu. The corrosion behaviour of stainless steels and Ni-based alloys in nitrate salts under thermal cycling conditions in concentrated solar power plants, Solar Energy, Vol. 232, 2022, pp. 169-185, https://doi.org/10.1016/j.solener.2021.12.072
3. Q. Liu. J. Qian, R. Barker, C. Wang, A. Neville, F. Pessu. Effect of thermal cycling on the corrosion behaviour of stainless steels and Ni-based alloys in molten salts under air and argon. Solar Energy, vol. 238, 2022, pp. 248-257, https://doi.org/10.1016/j.solener.2022.04.041.
4. Q. Liu. C. Wang, A. Neville, R. Barker, J. Qian, F. Pessu. "Corrosion Characteristics of Iron-Nickel-Chromium Alloys in Molten Nitrate Salts Under Isothermal and Thermal Cycling Conditions." AMPP Annual Conference + Expo, San Antonio, Texas, USA, March 2022. https://onepetro.org/amppcorr/proceedings/AMPP22/5-AMPP22/D051S049R002/488636
5. Q. Liu. J. Qian, A. Neville, F. Pessu. “Solar thermal irradiation cycles and their influence on the corrosion behaviour of stainless steels with molten salt used in Concentrated Solar Power plants”. Solar Energy Material and Solar Cells. Vol. 251, 2023, 112141, https://doi.org/10.1016/j.solmat.2022.112141
6. Q. Liu. J. Qian, A. Neville, F. Pessu. ‘Investigation of the Relationship between Thermo-Mechanical Stress and Early-Stage Corrosion Characteristics of Molten Salt – Oxide – Metal Interfaces In Solar Salts’. Under review by Corrosion Science.

Conferences presented:

- Q. Liu, C. Wang, A. Neville, R. Barker, F. Pessu. Molten salt corrosion characteristic of stainless steel in solar power generation systems. Electrochem 2022, The Royal Society of Chemistry, Edinburgh, UK.
- Q. Liu, C. Wang, A. Neville, R. Barker, F. Pessu. The Evaluation Of Corrosion Behaviour Of Austenitic Stainless Steels And Ni-Based Alloys In Molten Salts Under Isothermal And Thermal Cycling For Condition Concentrated Solar Power Plants. NACE/AMPP, USA. 2022
- Q. Liu, C. Wang, A. Neville, R. Barker, F. Pessu. Effect of Thermal Cycling on the Corrosion behaviour of austenitic stainless steels and Ni-based alloys in molten salts under different molten salt cover gas atmospheres in CSP plants. The European Corrosion Congress EUROCORR, 2021
- Q. Liu, C. Wang, A. Neville, R. Barker, F. Pessu. Molten salt corrosion in solar power plants. Young I_{corr} Competition, Winner, Institute of Corrosion, 2021
- Q. Liu, C. Wang, A. Neville, R. Barker, F. Pessu. Corrosion on the solar tower power plant, CSP Focus China, Beijing 2020
- Q. Liu, C. Wang, A. Neville, R. Barker, F. Pessu. Investigation of corrosion mechanism of austenitic stainless steels and Ni-based alloys in molten salts under thermal cycling condition for CSP plants. Third-class prize, Chinese Renewable Energy Society International Forum, Kunming 2020

In all the papers listed, Qingyang Liu completed all the experimental works, evaluation of data and preparing the publication. All authors contributed to proof reading of the articles prior to publication. The contributions of Dr. Zabeada Aslam is use of Focused Ion Beam sample preparation and Transmission Electron Microscopy. The contributions of Dr. Stuart Micklethwaite to the work are: use the SEM during the Covid-19 pandemic.

Acknowledgements

I would like to express my gratitude to Dr. Frederick Pessu for all the supervision and encouragement he has provided throughout the course of this work. Without his kind support, insight and passion for engineering, none of this would have been possible.

I am extremely grateful to late Prof. Anne Neville for her emotional and financial support. Also I wish to thanks to the co-supervisors: Dr. Richard Barker and Dr. Chun Wang for their help and support during my whole PhD career. Great thanks to Dr. Liuquan Yang and Prof. Dirk Engelberg (University of Manchester) for their great comments and advice as my thesis examiners to enhance the quality of this thesis.

I wish to express my gratitude to the Jiuli-Hitech Metals, Zhejiang, China and University of Leeds, United Kingdom for funding this research.

I wish to thank technicians in the School of Mechanical Engineering and School of Chemical and Processing Engineering, including Jordan, Paul, Tom, Fiona, Stuart and Faye. I would like to thank all the friends in IFS during the PhD candidate career, they are Zezhou & Dongze, Alex, Wenlong, Jonas, Rob, Jialin, Leo, Yasmin, Mike, Harry, Eni.

I would dedicate this work to my Mum, Dad, sister and Chuchu Feng for believing in me and helping me cope with the stress of writing up. Their unreserved love and support are the most reason to keep me moving forward.

Abstract

The material degradation in molten salt is of great interest to renewable energy production industry, especially the wide application of molten salts as thermal energy transfer fluid and storage media in concentrated solar power (CSP) plants at extremely high temperature.

This study presents the investigation of stainless steels (AISI 321, 347) and Ni-based alloys (Alloy 625 and Alloy 825) interaction and degradation in molten salts in the different temperatures and thermal irradiation cycles encountered CSP systems. This includes characterisation and quantification of intergrannular corrosion through the Double loop electrochemical potentiokinetic reactivation (DL-EPR) technique in terms of degree of sensitisation (DOS). The corrosion behaviour of stainless steels and Ni-based alloys were investigated in Solar (nitrate) salts under different solar thermal irradiation profiles, isothermal, thermal cycling and thermal shock conditions in both air and argon.

The results showed that in comparison with isothermal condition, thermal cycling reduces the corrosion rate of test materials, the severity of corrosion attack and the thickness of corrosion product layers. The result also shows that corrosion oxide layer breakdown is due to spallation, and this was supressed by the lower time at maximum temperature and the cooling effect from the extended period at lower temperature during thermal cycling when compared with isothermal conditions, especially in stainless steels.

Further results from this study show that thermal shock induces high material degradation rate than isothermal and thermal cycling. Severe spallation of interfacial corrosion oxide layers was observed under thermal shock conditions than in isothermal and thermal cycling conditions and correlated to the observed overall performance after 28 days. The level of spallation of interfacial oxides across the three temperature profiles investigated in this study is linked to the induced stresses from mismatch in the thermal expansion properties between the corrosion oxide layers and the substrates. The combination of molten salt, high temperatures and argon atmospheres, acts in synergy to increase the kinetics of formation of Na/Fe–rich outer oxide layer with enhanced tendency to degrade by spallation due to tensile stress.

Table of Contents

List of Figures

List of Tables

List of Abbreviations

CE	Counter Electrode
Cp	Specific Heat Capacity
CPDP	Cyclic Potentio-Dynamic Polarization
CR	Corrosion Rate
CRA	Corrosion Resistance Alloys
CSP	Concentrated Solar Power
DGA	Dynamic Gravimetric Analysis
DL-EPR	Double Loop Electrochemical Potentiokinetic Reactivation
DNI	Direct Normal Irradiation
EDX	Energy-Dispersive X-Ray Spectroscopy
EIS	Electrochemical Impedance Spectroscopy
EJ	Exajoule
EP	Electrochemical Polarization
FIB	Focused Ion Beam
GBs	Grain Boundaries
HTF	Heat Transfer Fluids
IN 625	Alloy 625
IN 825	Alloy 825
ISO	Isothermal
IEA	International Energy Association
LCOE	Levelized Cost of Electricity
LFR	Linear Fresnel Reflector
PTC	Parabolic Trough Collector
PDC	Parabolic Dish Collector
PCM	Phase Change Materials

RE	Reference Electrode
SEM	Scanning Electron Microscopy
SPT	Solar Power Tower
TC	Thermal Cycling
TEM	Transmission Electron Microscope
TES	Thermal Energy Storage
WE	Working Electrode
WL	Weight Loss
WG	Weight Gain
XRD	X-Ray Diffraction

Chapter 1. Introduction

1.1 Background

There is a strong motivation to explore alternative and renewable sources of energy (Walczak et al., 2018) due to the rapid growth of world's population, increased industrialisation of emerging economies, and limited sources of conventional energy (fossil fuels) on the global warming. In comparison with other renewable resources (e.g. wind, geothermal and ocean), solar energy is showing encouraging promises due to the great quantities of solar irradiation flux arriving on the earth (Pelay et al., 2017). According to some estimates, annual potential of solar energy is approximately between 1575 and 49837 Exajoule (EJ, 1 EJ=10^{18} J). This is much higher than the world's annual total energy supply for the year 2014 reported by International Energy Association (IEA) as 573 EJ (13699 million tonnes of oil equivalent) (Alva et al., 2018). Therefore, if fully harnessed, solar energy alone can satisfy the world's total energy demand (Alva et al., 2018). Some areas of high insolation identified by the high values of direct normal irradiation (DNI) shown in Figure 1-1, are naturally privileged and the technology of producing solar-based electricity is already under deployment in USA, Africa, Australia and Chile (Walczak et al., 2018).

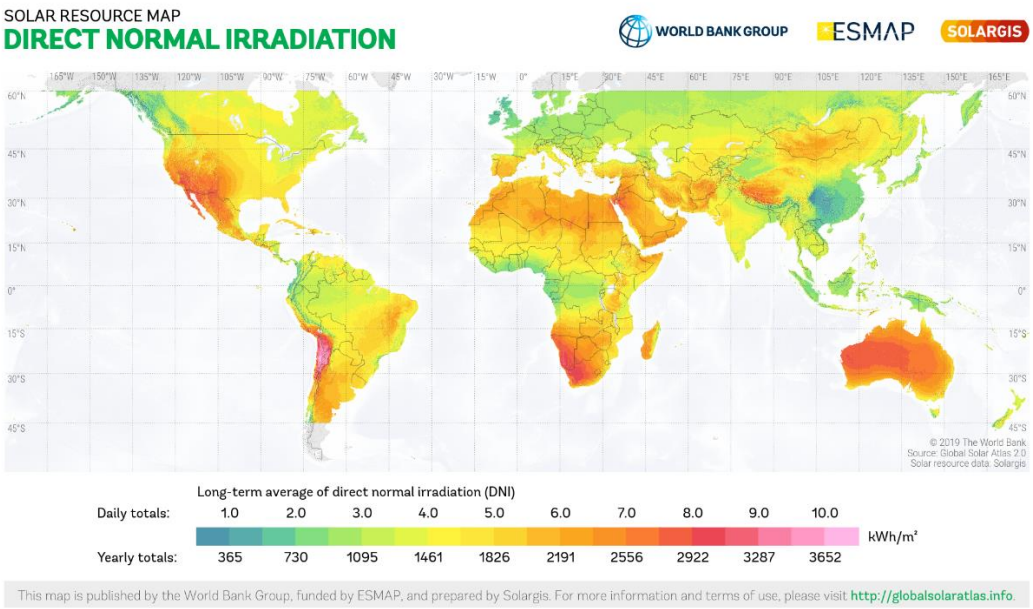

Figure 1-1. Annual distribution of direct normal irradiation (DNI) in the world (2017) (from http://globalsolaratlas.info)

1.1.1 Basic theory and working principles of CSP project

Electricity generation from solar irradiation is achieved by photovoltaic (PV) cells or concentrating solar power (CSP) plants. Compared with photovoltaic (PV) technologies,

concentrating solar power (CSP) has gained particular interest for large scale applications due to its advantage in terms of potential efficiency, low operation cost and low environmental impact, as well as the possibility of integrating thermal energy storage (TES) systems (Alva et al., 2018). The CSP is one of the promising solutions to solve the problem of continuous power generation without sunshine. The CSP technology is based on basic principles. The solar radiation is concentrated by mirrors (heliostats) to a receiver. The solar heat is stored and transported by the heat transfer fluids (HTF) in the receiver and is further transported to the hot storage tank in thermal energy storage system (TES). The thermal energy is used to generate steam in turbine generator. After exchanging the thermal energy, the cold HTF returns to the receiver to repeat the cycle (Vignarooban et al., 2015a).

Molten salts are currently widely used as heat storage material and HTF in CSP plants. This also poses significant threat to all the metallic components used in the CSP plants that interact with these molten salts at extremely high temperatures. These materials are exposed to the severe condition of high operation temperatures and temperature gradients. The metal is susceptible to degrade by a combination of molten salt induced corrosion at metal-salt interface and high temperature oxidation and/or high temperature induced creep at high CSP operating temperature (typically ranging from 500 -1000°C). Corrosion will likely affect the thermal performance of the thermal energy storage (TES) media as materials and/or corrosion products dissolved into the molten salt (TES) will change its thermodynamic properties. Scale on heat exchanger architecture will also affect the systems heat transfer capabilities. Therefore, salt selection and material compatibility is critical for the optimum operation of CSP systems (Bell et al., 2019).

At September 2021, the capacity of the operational CSP technology has increased to 6.2 GW (Figure 1-2) all over the world, with Spain and USA ranking top 2 (Dahash et al., 2019). IEA estimate that the CSP will contribute up to 11% of the global electricity production in 2050 (Ai et al., 2019). A typical CSP plants are composed of four main elements: a concentrator, a high temperature receiver, a fluid transport system and a power generation bloc (e.g., Rankine cycle, String cycle) (Pelay et al., 2017).

The most common CSP plans types includes (a) Parabolic Trough Collector (PTC), (b) Solar Power Tower (SPT), (c) Linear Fresnel Reflector (LFR) and (d) Parabolic Dish Collector (PDC), shown in Figure 1-3 (Vignarooban et al., 2015a). And the comparison between various CSP technologies is summarised in Table 1-1 (Pelay et al., 2017). Among these, the parabolic trough collector is currently the most amateur and utilised technology with more than 90% of CSP installations. Solar power tower (SPT) uses heliostat field collectors

to focus sunlight to central tower receiver. SPT, as well as PDC, is showing the greater potential due to its high thermodynamic efficiency. More than 40% CSP projects under construction and development are operating with SPT. The detailed discussion is shown later in 1.1.2.

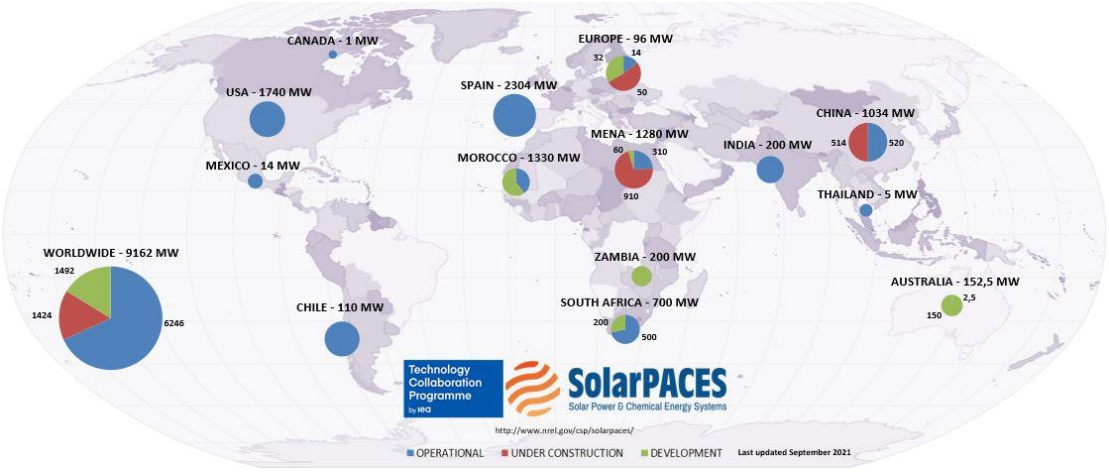

Figure 1-2. The distribution of CSP Projects with capacity around the World (Dahash et al., 2019) (last updated September 2022)

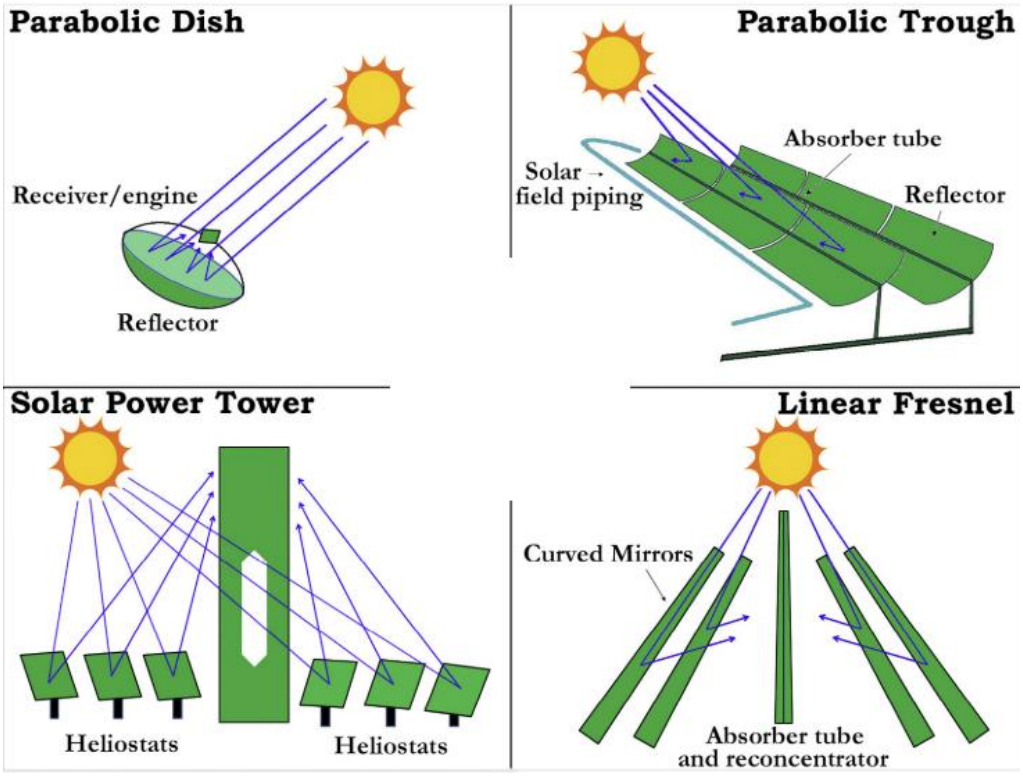

Figure 1-3. Four types of CSP technologies (Vignarooban et al., 2015a)

Table 1-1. Comparison between different CSP technologies (Pelay et al., 2017) (Ai et al., 2019) (Zhang et al., 2013)

CSP technology	Operating temperature (°C)	Advantages	Disadvantages
PTC	20–400	– Relatively low installation cost – Large experimental feedback.	– Relatively large area occupied. – Low thermodynamic efficiency due to low operating temperature.
LFR	50–300	– Relatively low installation cost.	– Low thermodynamic efficiency due to low operating temperature.
SPT	300–1000	– High thermodynamic efficiency due to high operating temperature.	– Large space area occupied. – Relatively high installation cost. – High heat losses.
PDC	120–1500	– Relatively small area occupied. – High thermodynamic efficiency due to high operating temperature.	– Relatively high installation cost. – Little experimental feedback.

1.1.2 Overview of CSP projects around the world

As shown in Figure 1-2 and Figure 1-3, the CSP projects are located in some region with abundant solar irradiation, such as Spain, USA, South Africa, Morocco and China. Among these projects, some plants have already in operational while some plants are still under construction or under development (Dahash et al., 2019). The detailed data for these CSP projects in operational and under construction/development can be found from database online https://www.solarpaces.org/, including the name, country, technology, TES integration method, HTF, heat storage medium and capacity of these plants.

According to the database, over 75% operational CSP plants use parabolic trough to harness solar energy and 50% of these plants are integrated with two-tank indirect TES system using thermal oil or Biphenyl/Diphenyl oxide and solar salt as HTF and heat storage materials. Very few power tower plants operate with two-tank direct TES system. Database also shows that solar power tower (SPT) is increasing its proportion in future CSP plants, integrated with 2-tank direct TES using molten salts as both HTF and heat storage materials.

It can be seen that parabolic troughs are still the mainstream technology because of its maturity; however, solar towers technology is the future because it can achieve much higher thermodynamic efficiencies than parabolic troughs due to having much higher concentration ratios (Tian and Zhao, 2013).

1.2 Significance of corrosion in the concentrated solar power plants

However, the operation of CSPs at temperatures of ~ 600˚C inevitably poses significant corrosion threat to all the metallic components in contact with molten salt. In addition, the recent push towards higher temperature of up to 720˚C to reduce the levelized cost of electricity (LCOE) (Bell et al., 2019) with more aggressive salt types such as chloride and carbonate salt (Mohan et al., 2019) will likely increase the risk of corrosion further. The electro-chemical aggressiveness of molten salts, high temperature conditions within CSP plants and the continuous interaction of molten salts with material surfaces increases the risk of corrosion, catastrophic failure of metallic components and reduce CSP plant efficiencies. In this case, the optimal combination of salt type and metallic materials is of vital importance for safe and stable operation of CSP to avoid any potential failure caused by potential occurrence of corrosion. Many investigations on the corrosion performance of carbon/low-alloys steel, stainless steels and Ni-based alloys with different salts at different temperatures are summarised by Magdalena Walczak into Table 6, Table 8 and Table 10 Ref.(Walczak et al., 2018), respectively. Despite different test methods employed in these tables, almost all the results are conducted under isothermal condition and only provided quick selection for the combination of salt and metals. They concluded that Ni-based alloys with higher alloy content show the best corrosion resistance in nitrate salt at relatively moderate temperature (no more than 600°C). In addition, they agreed that corrosion and corrosion mechanisms is complex and dependent on many variables in molten salts for CSP applications. The salt anion and cation species, temperature, temperature gradient and thermal cycling rate, impurity concentration, atmosphere gas and pressure, alloying element, composition and microstructure all greatly influence corrosion mechanism and rate (Bell et al., 2019).

In the CSP plants, the corrosion may take place at any location where the molten salt is likely to make contact with the metal. This will either result in severe corrosion failure and/or shuts down of the whole CSP system for inspection maintenance. Any outcome will lead to serious economic losses. According to SunShot (Gomez-Vidal, 2017, Gomez-Vidal and Tirawat, 2016), the corrosion rates of molten-salt containment alloys should be lower than 20 μm/year to deliver a 30-year lifetime service.

1.3 Statement of the significance of this research

To keep in pace with the state-of-the-art development of the CSP plants, some critical corrosion issues need to be appropriately addressed. The aim of this research is to establish

a better understanding of the corrosion behaviour and mechanism that occurs in materials such as pipes, valves, and storage tanks; hot and cold which are exposed to molten salts for CSP applications. This includes investigation the appropriate adaptation of metallic material for the pipes, valves, and storage tanks in a various simulated molten salt conditions such as gas atmospheres and temperature cycles encountered in CSPs.

There are only a handful of literatures that have reported on the sensitization, thermal fatigue and creep behaviour of material used as heat transfer pipe and hot tank used in Concentrated Solar Power plants where the material is exposed to high temperature and high temperature gradient and molten salt at the same time. There are also limited literatures available that have investigated the change of nano-mechanical properties of corrosion product and substrate metal exposed to molten salts, in the context of overall material integrity in CSPs. Thermal cycling and thermal fatigue are probable temperature scenarios in CSPs that can significantly influenced material degradation in these systems.

In this study, materials of interests will be investigated at initially at room temperature to evaluate the general conductivity and aggressiveness of the salt chemistries, and at high temperature for deployment with molten salt. The focus of this investigation includes characterisation of corrosion mechanisms, mechanical properties, microstructural observation, thermal fatigue, sensitization, and creep. The research will focus on how thermal cycling affect the molten salt properties and corrosion performance of two austenitic steels and two Ni-based alloys when fully or partially immersed in molten salts or hung above the molten salts. This helps to elucidate the synergy of the complex mix of material degradation mechanism; thermal fatigue, creep deformation, de-alloying, salt vapour corrosion, etc occurring at the thermally active metal-molten salt interface in real CSP scenarios. The corrosion product layer characterization (including the nano-mechanical properties of corrosion product and substrate metal), corrosion rate and rate-controlling step will be compared by immersion test under thermal cycling and isothermal condition.

1.4 Project objectives

The main objective of this research are as follows:

1. To evaluate the corrosiveness of molten salt and corrosion behaviour of focussed materials by potentio-dynamic polarization test.
2. Compare mechanical properties, microstructure and corrosion performances of the stainless steel and Ni-based alloy at room temperature and after exposure to high temperature.

3. To develop a protocol for characterizing thermal cycling/thermal shock and sensitization behaviours of focused alloys with and without molten salt.
4. To investigate the effect of salt vapour and the liquid salt on the material degradation mechanism.
5. To compare the corrosion rate, corrosion product and corrosion mechanism between isothermal, thermal cycling and thermal shock condition through immersion test and probable electrochemical test.
6. To compare the corrosion performance of the focused alloy in molten salt as a function of the atmospherically change from air to argon.
7. To find some additions to salts to design the formation of corrosion products after characterizing the mismatch between corrosion product and metal matrix.
8. To output material selection “maps” for molten salt.

1.5 Thesis structure

Chapter 1 includes the topic of this study is introduced and the motivation of that is discussed. Some basic theories and project objectives are also presented in this chapter.

Chapter 2 includes Fundamentals of corrosion and degradation of metallic material, including the common corrosion and aqueous corrosion mechanism are presented. Also an extensive literature review of material degradation at high temperature with/without molten salt, major corrosion mechanisms in molten salt, material selection, corrosion influencing factors and the innovations of this study are presented. A summary of various techniques and novel methods on characterizing the corrosion products are presented.

Chapter 3 includes the experimental methods and characterization methodology: Materials, preparation procedure, experimental techniques and equipment applied.

Chapter 4 will introduce in detail the setup of cyclic potentiodynamic polarization test in different salt brines. The effect of temperature and salt concentration on the corrosion performance are investigated in this chapter.

Chapter 5 introduce the first published paper, titled ‘Application of double loop electrochemical potentio-kinetic reactivation for characterizing the intergranular corrosion susceptibility of stainless steels and Ni-based alloys in solar nitrate salts used in CSP systems’ published in *ENGINEERING FAILURE ANALYSIS online* *https://doi.org/10.1016/j.engfailanal.2021.105717*.

Chapter 6 introduce the second published paper and one conference paper, titled ‘The corrosion behaviour of stainless steels and Ni-based alloys in nitrate salts under thermal cycling conditions in concentrated solar power plants’ published in *SOLAR ENERGY* online https://doi.org/10.1016/j.solener.2021.12.072 and titled ‘Corrosion Characteristics of Iron-Nickel-Chromium Alloys in Molten Nitrate Salts Under Isothermal and Thermal Cycling Conditions’ published in *AMPP Annual Conference + Expo* online https://onepetro.org/amppcorr/proceedings/AMPP22/5-AMPP22/D051S049R002/488636

Chapter 7 introduce the third published paper, titled ‘Effect of thermal cycling on the corrosion behaviour of stainless steels and Ni-based alloys in molten salts under air and argon’ published in *SOLAR ENERGY* online https://doi.org/10.1016/j.solener.2022.04.041

Chapter 8 introduce the fourth paper, titled ‘Investigation of the Relationship between Thermo-Mechanical Stress and Early-Stage Corrosion Characteristics of Molten Salt – Oxide – Metal Interfaces In Solar Salts’ submitted to *CORROSION SCIENCE*.

Chapter 9 introduces the fifth paper, titled ‘Solar thermal irradiation cycles and their influence on the corrosion behaviour of stainless steels with molten salt used in Concentrated Solar Power plants’ published in *SOLAR ENERGY MATERIALS AND SOLAR CELLS* online https://doi.org/10.1016/j.solmat.2022.112141

Chapter 2. Literature review - Corrosion of alloys at high temperature in molten salt systems

2.1 Introduction

In this chapter, we will introduce the common type of corrosion and material degradation mechanism encountered with molten salt, as well as its influencing factors. Discussion will be presented on thermal energy storage system and Heat transfer fluids, the four main types of material corrosion are introduced in section 2.2, while fundamental theories are discussed in the following section. A summary of the common techniques for inspecting material degradation will be provided and followed by an in-depth discussion on the corrosion performance of different corrosion resistant alloy and the corrosiveness of the different molten salts. Finally, the factors influencing corrosion process are separately discussed to introduce our main scope and focus in this study.

2.2 Thermal energy storage system and Heat transfer fluids

The temporal intermittency and non-availability during peak consumption hours are the main drawback of solar thermal electricity. To address this problem, one solution is to use a backup system (energy hybridization) that burns fossil fuel or biomass (Pelay et al., 2017). Thermal energy storage (TES) system is another solution to store solar thermal energy during the daytime and to release it for electricity production during periods of weak solar irradiation. See Figure 2-1 for schematic of this option (Pelay et al., 2017). About half of the CSP plants currently operating in the world are integrating with TES system (Alva et al., 2018). Figure 2-2 shows the various configurations of TES systems that can be implemented in CSP plants (Pelay et al., 2017). In a two-tank direct system (Figure 2-2a), the heat storage materials also serve as heat transfer fluids (HTF). The HTF is stored in a hot tank after heating in solar field during charge process. The hot HTF in hot tank is pumped through the power cycle and then stored in a cold tank at the entrance of solar field for the next cycle (Herrmann et al., 2004). This concept needs no heat exchanger between heat storage materials and HTF, but suitable materials (molten salts or steam) are required to meet the requirements to be a good HTF and heat storage material (Pelay et al., 2017). The HTF and storage medium can be different in a two-tank indirect system, shown in Figure 2-2b. The storage medium is pumped from cold tank through heat exchanger and is heated by HTF, and then stored in hot tank during the charge process. As for discharge process, the flow direction of heat storage material is reversed to release the heat to HTF. Except for 2 tanks concept, a single tank (Figure 2-2c) store hot and cold materials on the top and bottom

respectively. The zone between hot and cold fluid is called thermocline. The concrete block systems (Figure 2-2d) are rarely used (Pelay et al., 2017).

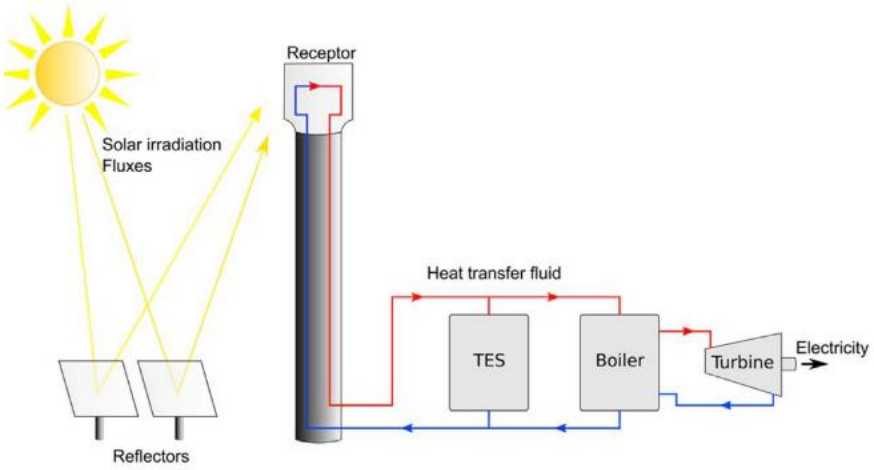

Figure 2-1. CSP plant with a TES system (Pelay et al., 2017)

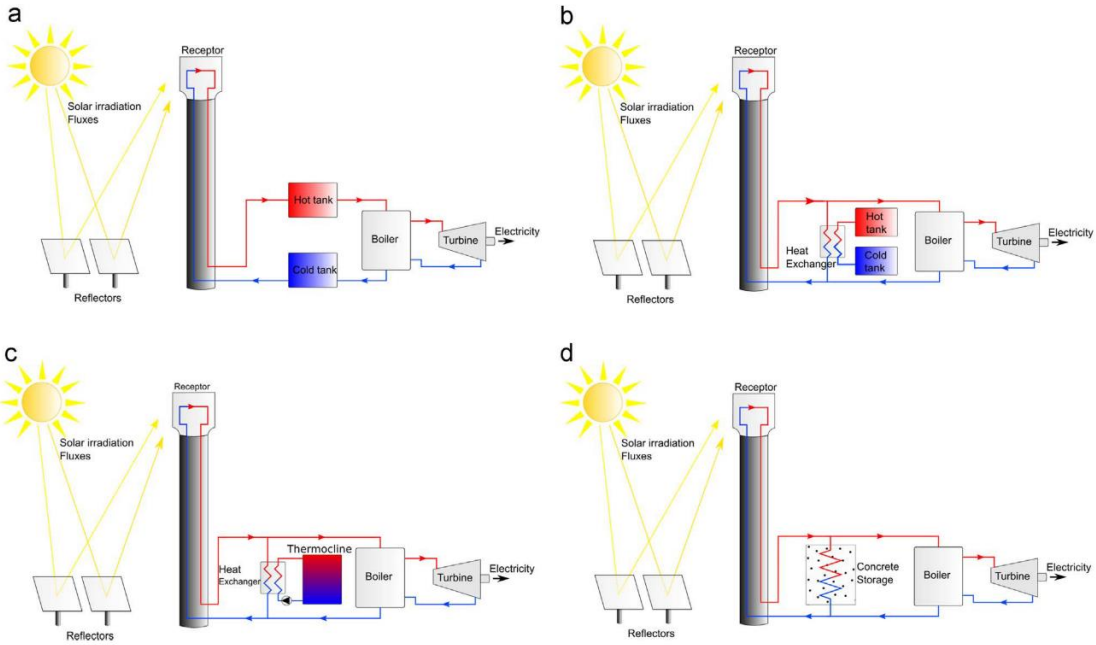

Figure 2-2. TES system in CSP plants (a) two tank direct, (b) two tank indirect, (c) thermocline system and (d) concrete block system (Pelay et al., 2017)

Different types of TES systems correspond to different heat storage materials, which can be classified into sensible, latent and thermochemical categories (with their storage capacity in ascending order).

Sensible heat storage technology is the most used in currently operational CSP plants due to its high reliability, low-cost materials, easy implementation and large available experimental feedback. Sensible heat storage materials store heat energy in their specific heat capacity (C_p). It is a pure physical process without any phase change during charge or

discharge (Pelay et al., 2017). The thermal energy stored can be expressed in following equation (Alva et al., 2018)

$$\boldsymbol{Q = m \times C_p \times \Delta T} \qquad \text{Equation 1}$$

Where m is the mass (kg), C_p is the specific heat capacity ($kJ \cdot kg^{-1} \cdot K^{-1}$) and ΔT is the rise in temperature during charging process.

Sensible heat storage materials include water, liquid metal, thermal oils, earth materials, molten salts, and concrete blocks. Molten salt is the most used as the sensible heat storage media, more than 70% in current CSP plants. The major drawback of sensible heat storages is their low energy density (Alva et al., 2018).

In latent heat storage system, thermal energy is stored or released by changing materials' phase at a constant temperature. Phase change materials (PCM) are typical latent heat storage material that could change phase in a narrow temperature range during charge/discharge process, due to its higher energy density than sensible heat storage materials. However, the drawback of low thermal conductivity and the problem of enormous change in the volume of the storage materials limit its use and development (Alva et al., 2018).

The heat storage materials for chemical heat storage system are involved in a reversible reaction, which react with absorption and release of heat for the purpose of thermal energy storage. Special chemicals can absorb/release a large amount of thermal energy when they break/form certain chemical bonds during endothermal/exothermal reactions. The summary of three heat storage technology is listed in Figure 2-1 (Pelay et al., 2017).

From discussion above, heat transfer fluids (HTF) play an important role in transporting heat from solar receiver to steam generator turbine or serving as heat storage materials in hot tank for power generation when sunlight is not available (Vignarooban et al., 2015a). The fluids considered for practical implementation as HTF in CSP plants include water/steam, synthetic oils, organic solvent and molten salts (Walczak et al., 2018). The optimal HTFs often meet the requirement of combining several properties at the same time: high conductivity and high heat capacity at operational temperature to maximum heat exchange and energy storage, low melting point and high boiling point to improve efficiency of power generation, as well as low vapour pressure, low reactivity, thermal stability, low viscosity, low cost and low risk of corrosion to the metal alloys (Vignarooban et al., 2015b, Federsel et al., 2015) (Liu et al., 2006). Figure 2-3 provides a list of working temperature for various HTFs (Vignarooban et al., 2015a). As shown in Figure 2-3, molten salts have been

commercially proved to be the successful HTF due to their high operating temperature, heat capacity, low vapour pressure and corrosive property, and good thermal and physical properties at elevated temperatures (Peng et al., 2010).

Table 2-1. Summary of heat storage technology (Pelay et al., 2017)

Technology	Cost	Energy density	Heat transfer	Advantages	Disadvantages
Sensible	Low-cost materials	Low	Quite good	-large experimental commercial feedback -easy implementation	-heat loss during storage -low energy density -high freezing point for liquid material
Latent	Low-cost material	Medium	Slow; low thermal conductivity	-constant charge / discharge temperature -medium energy density	-low thermal conductivity -solid deposit on the PCM
Thermochemical	Low-cost material	High	Slow; Low thermal conductivity	-possibility to storage energy during long period without heat loss -high energy density	-incomplete reversibility -storage of gaseous products -necessity of heat transfer enhancement

Thermal and physical properties of some selected molten salts used as HTF was summarised in Table 2-2 (Walczak et al., 2018). Some molten salts mixtures, based on nitrates and nitrites, have been commercially implemented. The Solar salt is widely used for its high thermal stability, consisting of 60% $NaNO_3$ and 40% KNO_3. And Hitec is a ternary mixture of 53% KNO_3, 40% $NaNO_2$ and 7% $NaNO_3$, characterised by lower melting point and lower thermal stability than the Solar Salt (Walczak et al., 2018). While Hitec XL is another ternary nitrate mixture of 48% $Ca(NO_3)_2$, 45% KNO_3 and 7% $NaNO_3$ with even lower melting point and thermal stability than Hitec.

Other molten salts mixture based on nitrate, carbonates and chlorides have also been given consideration and their compatibility is still under study due to technical and economic implications such as corrosion issues of involved materials (e.g., carbon and low-alloy steels, stainless steels and Ni-based alloys) (Walczak et al., 2018). The corrosion issues are discussed in 2.7.

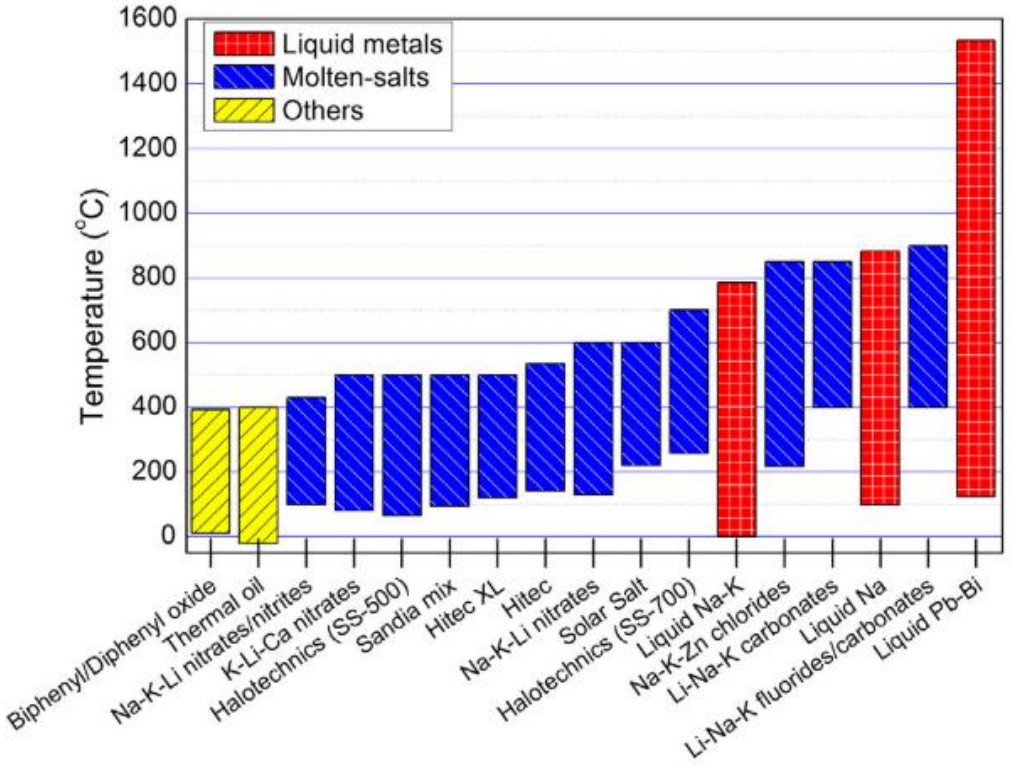

Figure 2-3. Working temperature range for various HTFs (Vignarooban et al., 2015a)

2.3Common types of corrosion and material degradation encountered in CSP plants

Molten salts are widely used as HTF and heat storage material in TES system from the previous discussion. Table 2-2 summarises molten salt mixtures, along with their thermal and physical properties, that have been commercially implemented or considered for implementation in TES of CSP (Walczak et al., 2018). All the metallic components involved in CSP are exposed to severe conditions of high temperature and temperature gradients, the selection and reliable prediction of materials performance is important at the long term (Liu et al., 2016). Corrosion of materials exposed to molten salt of the TES system might become a critical aspect because of risk of developing catastrophic failure of an entire CSP plants.

Corrosion understood as thermodynamically driven degradation of materials may appear in many forms (Walczak et al., 2018). The forms most relevant to TES tanks used in CSP are high temperature corrosion, localised corrosion and/or mechanically assisted corrosion, showing in Figure 2-4 and further described.

Table 2-2. Thermal and physical properties of typical molten salts used as HTF (Walczak et al., 2018)

Composition (wt% proportion or otherwise)	Melting point (°C)	Stability limit (°C)
$NaNO_3$-KNO_3 (60/40)	220	600
$NaNO_3$-KNO_3-$NaNO_2$ (7/53/40)	142	535
$NaNO_3$-KNO_3-$Ca(NO_3)_2$ (7/45/48)	120	500
$NaNO_3$-KNO_3-$NaNO_2$ (28/52/20)	130	600
KNO_3-$NaNO_2$-$Ca(NO_3)_2$ (50–80/0–25/10–45)	< 80	500
$NaNO_3$-KNO_3-$NaNO_2$-$Ca(NO_3)_2$ (9–18/40–52/13–21/20–27)	< 95	500
$NaNO_3$-KNO_3-$LiNO_3$-$NaNO_2$ (14.2/50.5/17.5/17.8)	99	430
$NaNO_3$–KNO_3–$NaNO_2$–$Ca(NO_3)_2$–$CsNO_3$ (6/23/8/19/8)	65	500
$LiNO_3$–KNO_3–$NaNO_3$ (30/57/13)	120	533
$LiNO_3$–KNO_3–$NaNO_3$ (20/52/28)	130	554
$LiNO_3$–KNO_3–$NaNO_3$–$Ca(NO_3)_2$ (10/60/10/20)	132	580
KNO_3–$Ca(NO_3)_2$–$LiNO_3$ (60/10/30)	132	567
K_2CO_3–Na_2CO_3 (44/56)	710	– – –
Li_2CO_3–K_2CO_3 (62/38)	498	– – –
Na_2CO_3-K_2CO_3-Li_2CO_3 (33/35/32)	398	– – –
LiCl–KCl (44/56)	355	– – –
KCl–$ZnCl_2$ (70/30)	428	– – –
NaCl–LiCl (34.42/66.58)	554	– – –
NaCl–KCl–$ZnCl_2$ (13.4/33.7/52.9 mol%) [24,52]	250	800
NaCl–KCl–$ZnCl_2$ (18.6/21.9/59.5 mol%) [52]	~ 250	~ 800
NaCl–KCl–$ZnCl_2$ (13.8/41.9/44.3 mol%) [52]	~ 250	~ 800
LiCl–KCl–CsCl (50.6/22.5/26.9)	263	– – –

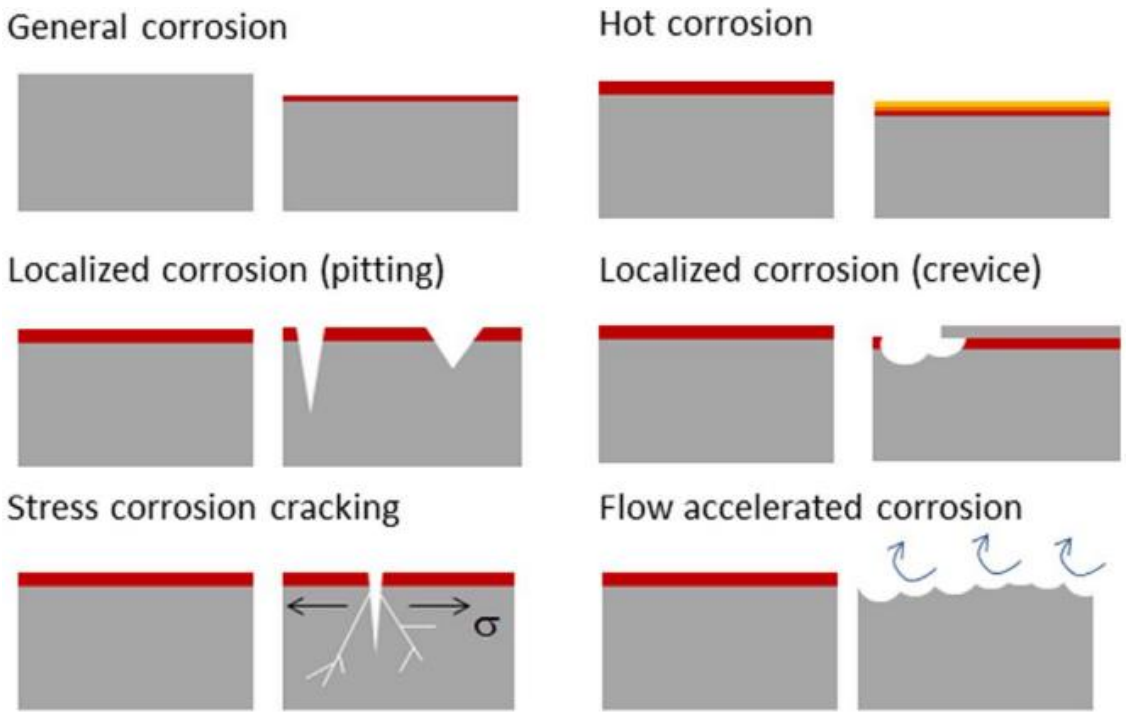

Figure 2-4. Summary of corrosion mechanisms identified for metallic alloys exposed to molten salts (Walczak et al., 2018)

2.3.1 General corrosion

General corrosion is the most common form of corrosion. General corrosion causes a uniform mass loss of the material, which is characterised by corrosion attack proceeding evenly same rate over the exposed metal area without localised attack. The thickness or mass loss due to corrosion is determined from the weight difference before exposure and after cleaning. General corrosion is easier to predict than any other types of corrosion introduced later, and the corrosion failures are not likely caused by general corrosion. This kind of corrosion was the mainly failure category in the CSP molten salt corrosion.

2.3.2 Hot corrosion

Hot corrosion has a definition as “accelerated corrosion of metal surfaces that results from the combined effect of oxidation and reactions with sulphur compounds and other contaminants, such as chlorides, to form a molten salt on a metal surface that fluxes, destroys, or disrupts the normal protective oxide” (R.A. Rapp, 1994).

Hot corrosion can be divided in two types of attacks (Kutz, 2018). Type I hot corrosion usually occurs at higher temperatures (between ~800 and 950°C): when the salt deposit on the metal or alloy is in a liquid state. Under these conditions, the corrosion rate is very high, right from the beginning of the corrosion process, and the kinetics are mainly linear. In Type II hot corrosion, the reaction in the beginning is very slow, until the rate increases suddenly, at a certain point, and follows linear kinetics. In other words, there is an incubation period before the corrosion rate rises with fast linear kinetics. This type of hot corrosion usually occurs at low temperatures (observed between ~600 and 800°C).

The degree to which corrosion resistance of the alloy is compromised depends on the actual conditions at the salt/metal interface. The electrolytic nature of molten salt enables electrochemical reactions at the metal/salt interface, oxidation of alloy components and reduction of salt components as well as dissolved impurities (Walczak et al., 2018). To understand the mechanism of hot corrosion better, all of the anodic and cathodic reactions taking place at the interface have to be taken into account. Because these aspects are specific to the particular salt and alloy, there is no general description of hot corrosion (Walczak et al., 2018). Hot corrosion often occurs at relatively high oxygen partial pressures and at specific areas of a component due to temperature, geometry or fluid dynamics, leading to localised attack. For TES based molten salts, availability to oxygen will likely be reduced at salt-metal interfaces, likely reducing corrosion, and localised attack will probably be due to inhomogeneity in the metal surface. Also, the large volume of salt used for TES

will form a significant sink for any compounds which are soluble, even if that solubility is comparatively lower than that of the hot corrosion deposits (Bell et al., 2019).

2.3.3 Localised corrosion

Localised corrosion is mostly understood as the occurrence of relatively small and deep indentations (pitting corrosion) or preferential degradation of metals around confined volume of electrolyte (crevice corrosion), both associated with the breakdown of a passive film, although crevice corrosion may also affect active metals (Walczak et al., 2018, Bell et al., 2019). The localised corrosion in molten salt always includes pitting corrosion and intergranular attack. The pitting corrosion is always featured by the breakdown of passive film with the presence of aggressive ions, such as Cl^-, Br^-, SO_4^{2-} and NO_3^-. And localised corrosion, characterised by the preferential corrosion of grain boundaries (intergranular corrosion), is often observed in alloys exposed to molten chlorides in oxidizing atmospheres. Kondo (Kondo et al., 2009) has investigated that FLiBe salt preferentially attacked grain boundaries of 304 and 316L stainless steel alloys tested at 500 and 600°C for 1000 h. They determined that the attack was due to fluorination of the chromium oxides present in the grain boundaries by HF present in the salt. Intergranular corrosion was also found in nickel alloys after 500-hour immersion in FLiNaK salt at 850°C (Olson et al., 2010) due to the removal of chromium oxides in GBs which is more susceptible to dissolve in fluoride salt. The temperature, salt species and environmental condition (e.g., impurities) are critical factors determining the occurrence of intergranular corrosion.

2.3.4 Stress corrosion cracking

Stress cannot be ignored in thermal energy storage systems because there are many likely stress sources. The weight of the storage media in large tanks, induced stresses from thermal cycling and expansion of the storage media, and residual stresses from manufacturing techniques such as welding are all potential sources of mechanical stress (Bell et al., 2019). Stresses, in combination with a corrosive environment, present a real and valid risk of stress corrosion cracking in the materials. There are few researches into stress corrosion cracking since no standard tests method can be used when the metal tokens submerged in molten salt (Bell et al., 2019). But the post test on the corrosion layers has been proved successfully to explain the spallation behaviours of layers caused by thermal stress between layers and bulk material (Ramos et al., 2021, Yin et al., 2021).

2.3.5 Flow accelerated corrosion

The mechanism of accelerating corrosion by agitating of molten salt electrolyte depends on the flow velocity. At lower velocities, the convention and diffusion to mass transfer is lower, preventing depletion of cathodic reactants and accelerating removal of soluble corrosion products. At higher velocities, erosion of the protective deposits may take place and attack the base material (Walczak et al., 2018). X. zhang (Zhang et al., 2020) investigate the dynamic corrosion behaviour of 316 and 321 stainless steels in Solar Salt with the velocity of 1 m/s, 2 m/s and 3 m/s at 565 ˚C under air atmosphere and found the weight loss of studied alloys increases with the increasing of molten salt flow velocity. They also found that the eroding and accelerated dissolution of flowing molten salt for the protective corrosion products, like $MgFe_2O_4$ and Fe_3O_4 attached to the surface, might be one of prime reasons of increasing corrosion in this study. It can be concluded that the dynamic flow of the molten salt in the pipeline could take the poor adherence layer and lead to the fresh metal or inner layer directly exposed to molten salt his study.

2.4 Fundamentals aspects of high temperature material degradation

Apart from the chemical reaction of metal with the aggressive environment, the material degradation could not be neglected during the manufacture process and long-term service, which also poses a great influence on the material performance. In this section, we will introduce the material degradation mechanism at high temperature, which include intergranular corrosion (the most dominant), sensitization, high temperature induced thermal fatigue and creep.

2.4.1 Intergranular corrosion

Heat treatment (including welding) of corrosion resistant alloys can lead to formation of particles, such as chromium carbides in the case of 304SS or σ phase (Fe-30-50%Cr) binary system intermetallic compound transformed from of delta ferrite) in duplex stainless steels. This will lead to local depletion of alloying elements, unless replenished by matrix diffusion, the extent of which will be temperature dependent. This process is commonly referred to as sensitization because deleted zones have an intrinsic lower resistance to localised corrosion and, where appropriate, to stress corrosion cracking. The extent to which these damage mechanisms develop and propagate will depend on the extent of depletion and the density of depleted zones.

Certain alloys, when exposed to a temperature characterised as a sensitizing temperature, become particularly susceptible to intergranular corrosion. In a corrosive atmosphere, the

grain interfaces of these sensitised alloys become very reactive and intergranular corrosion results. This is characterised by a localised attack adjacent to grain boundaries with relatively little corrosion of the grains themselves. Once the area around the grains has corroded, the grain will literally fall out. The schematic mechanism of sensitization in stainless steel is shown in Figure 2-5.

Intergranular corrosion is caused by the segregation of impurities at the grain boundaries or by enrichment or depletion of one of the alloying elements in the grain boundary. In the case of austenitic stainless steels, when they are sensitised by heating to about 900 to 1500°F (482-815°C), depletion of chromium in the grain boundary occurs. This results in susceptibility to intergranular corrosion. Several methods have been used to control or minimise the intergranular corrosion of susceptible alloys, particularly of the austenitic stainless steels.

- High temperature solution heat treatment. Sensitised material can be by heating to a temperature, known as solution anneal, to dissolve the carbides and eliminate the chromium-depleted regions. The carbon is then kept in solution by rapid cooling through the sensitizing temperature range.
- Incorporate strong carbide formers or stabilizing elements such as niobium or titanium in the stainless steels. These stabilizing elements tend to form carbides that are more stable than chromium carbide in the sensitization temperature range. Examples of stabilised grades include 321H and 347H stainless.
- Reduce carbon content below 0.03 percent so that insufficient carbon is available for carbide formation. The higher alloyed, more corrosion resistant stainless steels have very low carbon contents and susceptibility to Intergranular corrosion is typically not a concern.

The working temperature range for molten salt have partly overlaid with the sensitisation temperature, so the effect of sensitisation on corrosion degradation in molten salt condition cannot be negligible and there will be one chapter to investigate the sensitization behaviour of the corrosion resistant alloys with or without molten salt at high temperature.

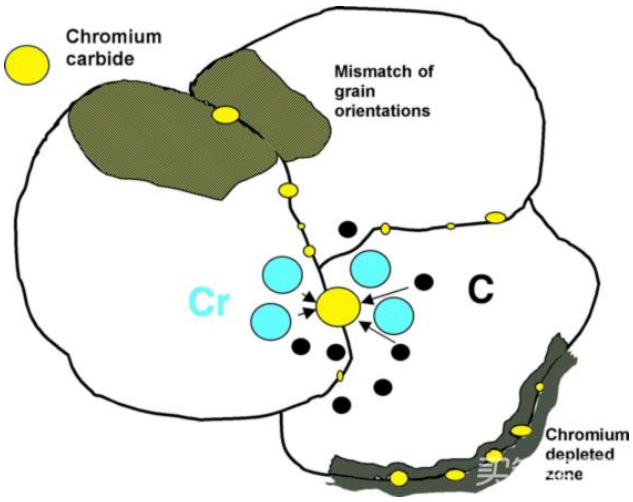

Figure 2-5. Mechanism of sensitization in stainless steel [access in July 2022] https://www.ssina.com/education/corrosion/intergranular-corrosion

2.4.2 Sensitisation in alloy manufacturing process and the relevance to material performance in molten salt systems

Intergranular corrosion is a form of localised corrosion that starts from the surface and develops inwards along the grain boundary to reduce cohesive stress, causing strength loss of material. It is linked with the segregation of impurities and/or depletion of one of the alloying elements along the grain boundaries (GBs). This is known as sensitisation and often used in reference to austenitic stainless steels and Ni-based alloys when operating in temperature range between 482-815°C (Lima et al., 2005). Many researchers have concluded that the mechanisms and rate controlling step of classical intergranular corrosion is the chromium depletion and/or carbide precipitation (Trillo and Murr, 1998). Among reported theories in literatures, it was widely accepted that Cr carbides was the main cause of intergranular corrosion (Wilson, 1971). It is also believed that the process of precipitation of Cr carbide may be divided into reaction theory (Yin et al., 2010) and kinetic theory (Sahlaoui et al., 2002). $M_{23}C_6$ carbide is the most prevailing carbide in stainless steels and its formation follows the reaction:

$$\mathbf{M_{23}C_6 \leftrightarrow 23M + 6C} \qquad \text{Equation 2}$$

The precipitation process of $M_{23}C_6$ includes the diffusion and reaction of Cr and C at the $M_{23}C_6$/matrix interface and the growth of $M_{23}C_6$ (Qian et al., 2016). The diffusion coefficient of carbon is 10^4 larger than that of chromium due to the fact that carbon is present interstitially and chromium substitutionally (Gellings and De Jongh, 1967). S. Kolli (Kolli et al., 2020) deduced that the preferential precipitation along the GBs is controlled by two factors, thermodynamics of the $M_{23}C_6$ formation and the difference in the diffusivities of Cr

and C. After the formation of $M_{23}C_6$ at the grain boundaries, they become a kind of crystal defects with a higher Gibbs energy (Qian et al., 2016). To reduce the Gibbs energy of the system, GBs tended to interact with other lattice defects (dislocations, vacancies and foreign atoms) (Lejček, 2010) and thus lower the corrosion resistance of the material. Efforts and techniques have been taken to control or mitigate sensitisation of susceptible alloys, such as high temperature solution heat treatment, reducing carbon content to reduce carbide formation and incorporating strong carbide formers or stabilising elements such as niobium or titanium (Pardo et al., 2007, Kim et al., 2014, Kokawa et al., 2000, Li et al., 2013, Trillo and Murr, 1998). Thorvaldsson and Dunlop (Thorvaldsson and Dunlop, 1982, Thorvaldsson and Dunlop, 1980, Thorwaldsson and Dunlop, 1979) found that $M_{23}C_6$ was more stable than TiC and less than NbC, which is consistent with the finding formation of $M_{23}C_6$ in 321 after long term aging by Grot (Grot and Spruiell, 1975). It is very important to determine the stabilised temperature to cause effective (Ti/Nb)C precipitation. Perrard (Perrard et al., 2006, Perrard et al., 2007) found the kinetic of NbC precipitation depend strongly on temperature and he built time–temperature transformation diagram to reveal the reaction rate between 600-800°C.

There has been limited research focused on characterising and understanding the relationship between molten salt chemistries, conditions encountered in CSP systems, the occurrence of sensitisation and the propensity for intergranular corrosion to occur in materials used in CSP systems. Chromium-depletion theory suggest that annealing at critical temperature or cooling slowly leads to the precipitation of carbides along the GBs (Gellings and De Jongh, 1967), thus resulting in the local Cr content dropping below a critical level of 12 wt.% (Kim et al., 2014, Li et al., 2013). In the region adjacent to GBs after precipitation, a minimum chromium content is unavailable to provide the passive Cr_2O_3 layer for corrosion resistance (Kolli et al., 2020). The working temperature range for molten salt is partly overlaid with the sensitisation temperature. This provides the basis for material degradation to be driven by the synergy of high temperature degradation and molten salt corrosion. The occurrence of sensitisation has been well researched for most alloys under high temperature conditions (Kim et al., 2014, West et al., 2013); particularly relating to alloy metallurgical and manufacturing processes (Zhang et al., 2019). Some authors have also reported intergranular corrosion attack in molten chloride (Hofmeister et al., 2015a, Grégoire et al., 2020) and nitrate (Goods et al., 1994b) salts. However, the propensity for sensitisation to occur in materials used with molten salt under real conditions in CSPs has not been researched and accurately characterised. Whilst the corrosion mechanism between chloride

and nitrate salts has some similarities in terms of chromium removal from the alloy (Bell et al., 2019), the role of impurities in these salts introduces some distinct effect on material degradation; particularly for chloride molten salts (Hamdy et al., 2021). Such research information is vital to guide material design and selection processes, improve CSP plant efficiency and lower energy production costs. Various standard tests have been developed to characterise the intergranular corrosion behaviour of stainless steels at different conditions. However, as a quick material selection filter, the double loop electrochemical potentiokinetic reactivation **(**DL-EPR) test can be used to quickly assess the synergy of electrochemical activity of molten salt and high temperature degradation of alloys used in CSP systems.

2.4.3 Thermal fatigue and creeping

Thermal fatigue is a type of fatigue failure mechanism that is induced by cyclic stresses from repetitive fluctuations in the temperature of equipment. The degree of damage is affected by the magnitude and frequency of the temperature swings. Damage typically appears in the form of one or more cracks at the surface of the component. Unless remedied, cracks may propagate through the material eventually leading to failure. All materials of construction used in CSP plants can be affected by thermal fatigue, because they go through the high temperature or high temperature gradients. Moreover, the different thermal expansion of the corrosion product on the metal surface in contact with molten salt may result in thermal fatigue. Another question to be solved about thermal fatigue is that whether the corrosion layer serve as protective role to reduce the depletion of chromium at metal/salt surface or not.

Creep, also creep deformation, is a time-dependent formation under a certain applied load especially occurring at high temperature (thermal creep). The behaviour of creep is often affected by the state and service environment of the materials, involving various defects, dislocation cores or grain boundary, dislocation density, grain size, grain shape, stress and temperature. The Figure 2-6 is a plot of creep strain. The terms “Primary”, “Secondary” and “Tertiary” creep are widely used. At a simple level, they are often associated respectively with the concepts of: (i) setting up some kind of mechanistic balance, (ii) steady state (constant strain rate) deformation occurring once this balance has been set up and (iii) the breakdown of this balance, often with defects starting to appear and failure rapidly following. Creep in service is usually affected by changing conditions of loading and temperature.

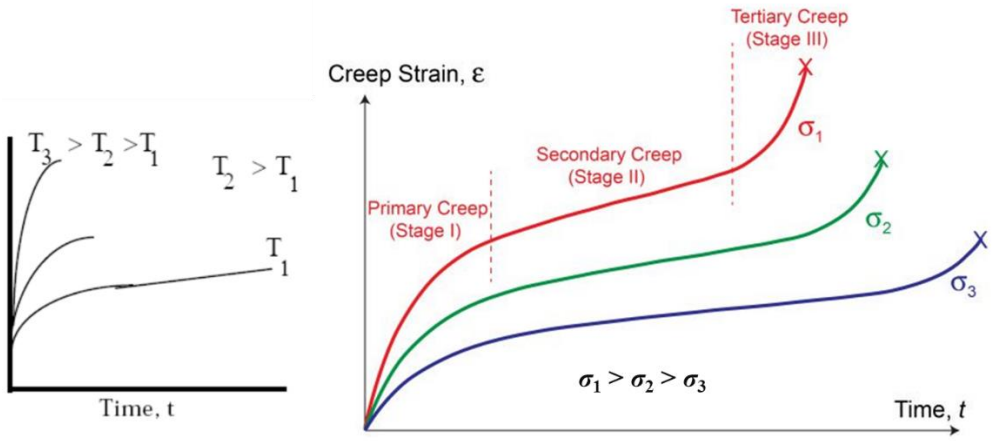

Figure 2-6. Schematic creep curves, for 3 different levels of temperature and applied stress (de la Roche et al., 2020)

There are 4 types of creep mechanisms involving Nabarro-Herring creep, Coble creep, Dislocation creep and Thermal activated glide. Diffusion and dislocation motion are the main mechanisms by which the creep of materials occurring and as such limiting them is key to designing creep resistant materials. The method for diffusion limiting is applying homologous temperature and controlling grain structure and crystal structure. Creep deformation is a common phenomenon for metallic material used in CSP plant because creep generally occurs in hot tank and heat transfer pipe at elevated temperatures and thermal cycling.

2.5 Common inspection techniques useful for corrosion study of materials used with TES

To predict and verify the corrosion performance of materials accurately, some methods are proposed, either prior or in parallel with the actual implementation. These techniques, summarised in Table 2-3, need further implemented by surface analysis, SEM-EDX and XRD (Walczak et al., 2018).

The gravimetric techniques of weight loss (WL) and weight gain (WG) consist in monitoring the weight change before and after exposure to aggressive environment. For accurate results any corrosion products must be removed from the metal surface by acid washing and the rate of weight loss is reported normalised, i.e., in units of mass per unit of area per unit of time. Weight gain is observed in environments where corrosion products are strongly adherent and difficult to remove by standardised procedure according to standard (Institution, 2009). A common procedure for the intermittent control of mass change is given by the standard ASTM G1-03 (G1-03, 2017). The typical weight change figure adapted from

(Soleimani Dorcheh et al., 2016) was shown in Figure 2-7. The corrosion rate can be obtained by the following equation:

$$\mathbf{CR} = \frac{\mathbf{87600}\Delta \boldsymbol{M}}{\boldsymbol{\rho}\, \boldsymbol{T}} \qquad \text{Equation 3}$$

Where Δ M is descaled mass loss per unit area (mg/cm^2), ρ is alloy density (g/cm^3) and T time hours.

Table 2-3. Common method useful for corrosion study in molten salt (Walczak et al., 2018)

Inspection technique	Advantage	Disadvantage
Weight loss (WL)	Simple, inexpensive	Requires long time of exposure
Weight gain (WG)	Simple, inexpensive	Requires long time of exposure
Weight loss (DGA)	Minimised human error	Higher cost compared with WL/WG
Electrochemical polarization (EP)	Fast, sensitive, accurate	Destructive or difficult to implement for being non-destructive
Electrochemical impedance spectroscopy (EIS)	Fast, sensitive, accurate	Complex analysis of data

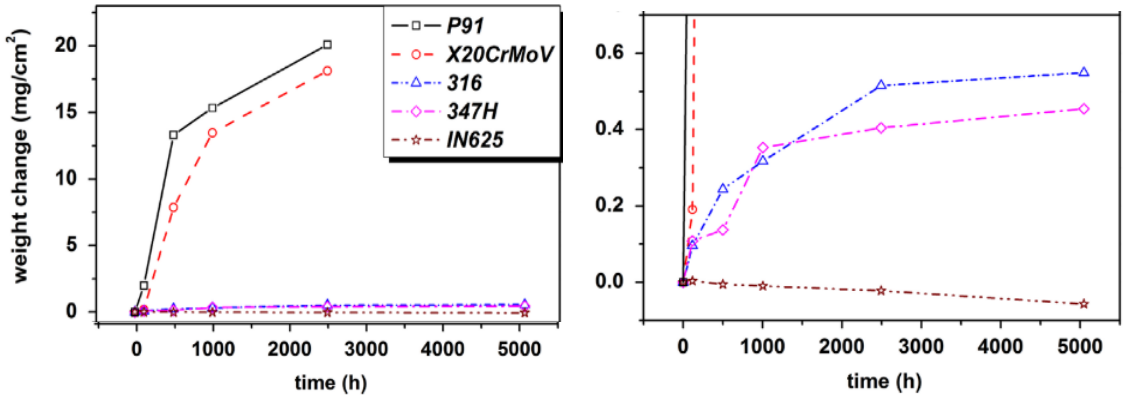

Figure 2-7. Weight changes of alloys exposed in molten salt (Soleimani Dorcheh et al., 2016)

A new version of the gravimetric technique is referred as dynamic gravimetric analysis (DGA), which is more accurate and relying on continuous monitoring of weight (Liu et al., 2016). But it brings with high cost compared with WG/WL. The electrochemical corrosion reactions was mainly taking about the thermodynamics and kinetic aspects of corrosion of metallic substrates, which defines the spontaneity for the corrosion reactions to occur and the rate at which corrosion reactions and substrate metal degradation occurs (Pessu, 2015b). The relevant concepts and theories with respect to electrochemical test in this study include:

Open circuit potential is the natural potential difference between the two electrodes half-cell of an electrochemical cell. It is the potential of an electrode relative to the reference standard electrode when no potential or current driving force is being applied to the cell (Pessu, 2015b). It can provide a useful way to differentiate conditions of active corrosion and passive corrosion.

Tafel polarisation is an electrochemical technique that records non-equilibrium potential and current response of a corrosion cell in a potential-current plot. It is usually applied for understanding the anodic and cathodic behaviour at the substrate metal and a corrosive environment surface. This is conducted by using a computer-controlled potentiostat and using a 3-electrode cell, including;

Working electrode (WR): the specimen

Reference electrode (RE): single Ag/AgCl electrode

Counter electrode (CE): a platinum wire

Tafel slopes are used in this study to calculate the corrosion rate I_{corr} and the potential of the corrosion system, E_{corr}. The cyclic potentio-dynamic polarization (CPDP) technique is a suitable way for evaluating the susceptibility of a metal to localised corrosion by analysing the beginning of passivity, breakdown of the oxide film, susceptibility to repassivation and calculation of the rate pf pitting corrosion. General shape of CPDP curve is as shown Figure 2-9 (Bellezze et al., 2018).

The determination of Tafel constants is completed at ±50 mV(Barker, 2012), where Tafel behaviour becomes linear. An example of a Tafel plot is shown in Figure 2-8 highlighting how Tafel constants and corrosion current density, I_{corr}, is determined from the intersection of the linear anodic and cathodic Tafel branches.

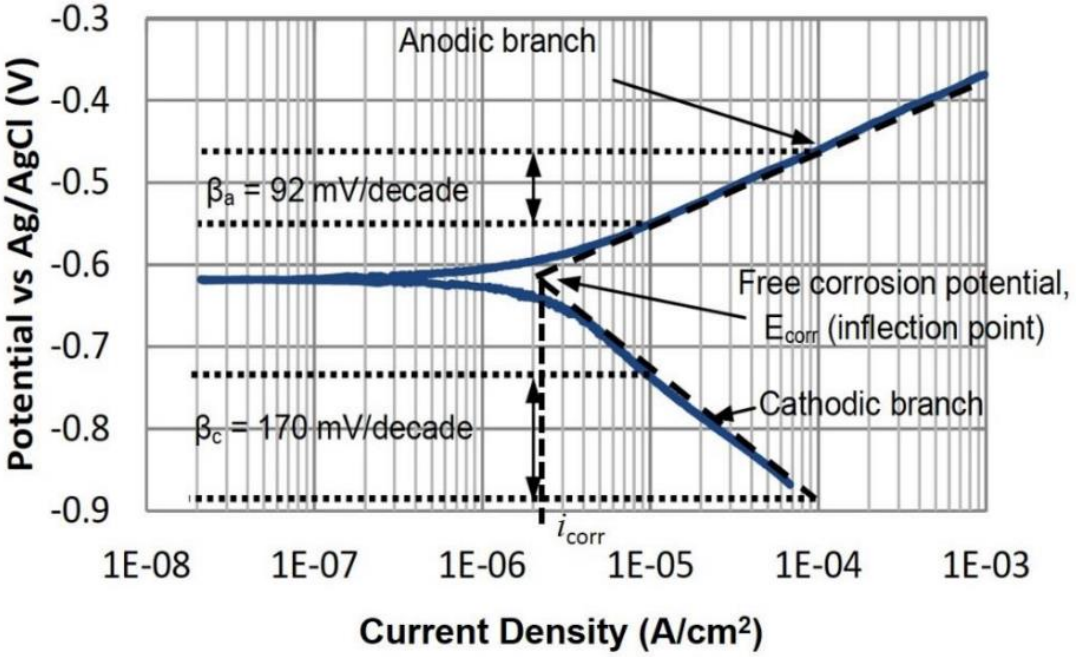

Figure 2-8. Tafel plot showing the relationship between potential and current showing how β_a, β_c and i_{corr} are determined, adapted from (Barker, 2012)

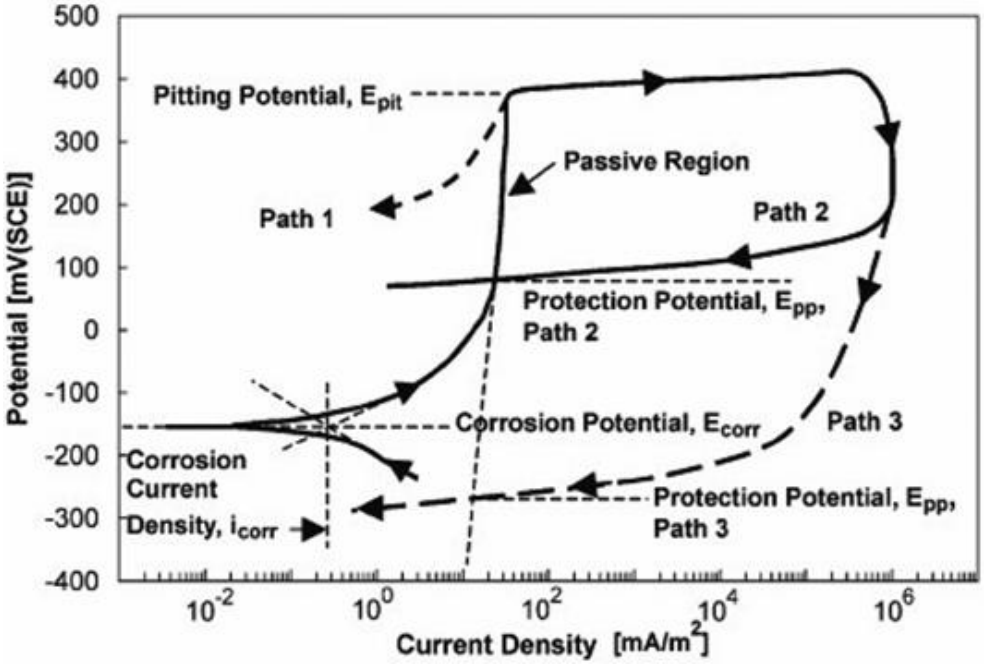

Figure 2-9. General shape of CPDP curve (Bellezze et al., 2018)

The electrochemical test such as polarization and electrochemical impedance spectroscopy (EIS) can provide information of corrosion rate and corrosion processes helping to identify the cathodic and anodic reactions in the special test conditions (Walczak et al., 2018). Electrochemical polarization analyses de metal/electrolyte interface by measuring electric current generated by an externally applied potential. The corrosion potential and corrosion

current can be obtained from potentiodynamic polarization curves (shown in Figure 2-10 (Zhu et al., 2018)) and corrosion rate can be calculated employing the principle of proportionality between charge and mass according to:

$$\mathbf{CR} = \frac{\boldsymbol{Icorr \cdot K}}{\boldsymbol{A\,\rho\ \sum(\frac{fi \cdot ni}{MWi})}} = K\frac{icorr}{\rho}EW \qquad \text{Equation 4}$$

Where CR is corrosion rate, mm/yr, ρ is alloy density, the alloy density of SS321, SS347, IN625 and IN 825 is 7.94, 8.03, 8.14 and 8.14 g/cm^3, respectively. K is constant 3.27*10-3, mm g/μA cm yr. I_{corr} is corrosion current (μA/cm^2), f_i is weight fraction of elezment i, n_i is number of electrons being transferred in i, i is 2, 3 and 2 for Fe, Cr and Ni respectively in this study. MW_i is atomic weight of i. The alloy equivalent weight, EW, is considered dimensionless in these calculations. The EW of SS 321, SS347, IN 625 and IN 825 is 25.13, 25.29, 25.89 and 25.52 respectively.

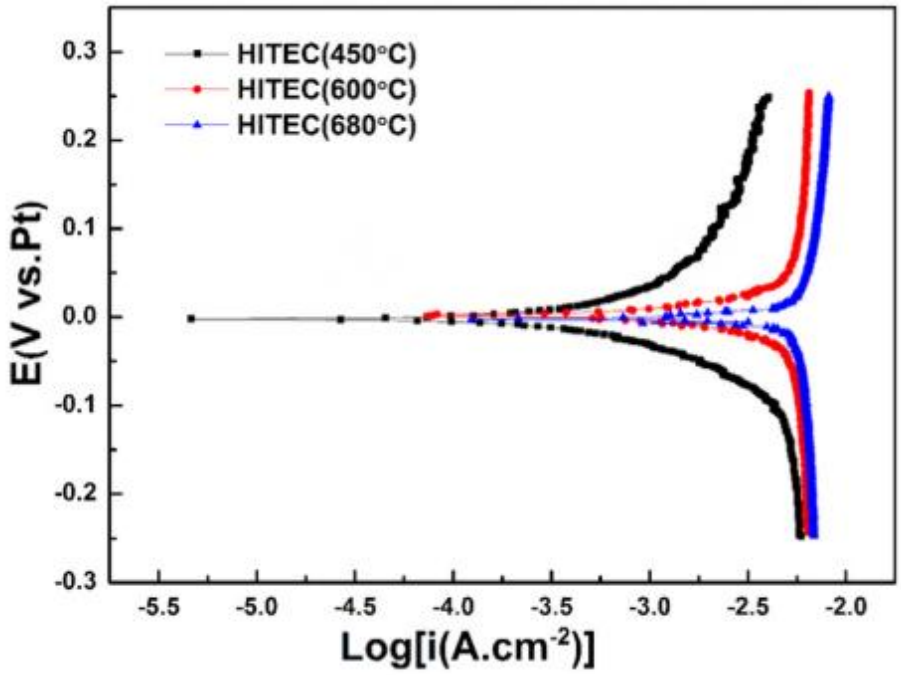

Figure 2-10. The potentiodynamic polarization curves of 316SS under air in molten salt (Zhu et al., 2018)

Electrochemical impedance spectroscopy (EIS) is an electrochemical technique used for characterising the dynamics of a corrosion process by measuring the electrical responses to non-linear excitation in potential signal to help unravel complex corrosion process at a corrosion interface (Pessu, 2015b). Some results of EIS in molten salt corrosion shows that for short immersion tests, the corrosion process was under diffusion control, but for longer

exposure times, the presence of a protective scale was evident (Gonzalez-Rodriguez et al., 2009).

EIS consists in applying a small amplitude signal, typically a voltage between 5 and 50 mV about the potential of equilibrium, or other potential of interest, and measuring the induced current, while the voltage is modulated at the frequencies from 0.001 Hz to 100,000 Hz (Walczak et al., 2018). The results of EIS are typically represented as a set of graphics recorded simultaneously: the Nyquist plot indicating the real and imaginary components of system's impedance, and the Bode plots indicating the modulus and phase angle of the real and imaginary components in function of the applied frequency range.

Taking into account the chemical stability and scaling features of metals, there are four electrochemical impedance models were proposed to represent their electrochemical impedance responses in molten-salt systems at the open-circuit potential (Zeng et al., 2001), as shown in Figure 2-11. Electrochemical charge transfer for the non-active metals is the rate-limiting process. For the active metals, the transfer of ions in the scale and the diffusion of oxidants in melts become increasingly important as compared with the electrochemical process. When a non-protective scale forms on the metal surface, the impedance diagram may present the characteristics typical of a diffusion-controlled reaction, i.e., a semi-circle at high frequency and a line at low frequency. When a protective scale forms on the metal surface, the Nyquist plot is composed of double capacitance loops, and the transfer of ions in the scale is rate limiting (Zeng et al., 2001). In the case of localised corrosion, the Nyquist plot also consists of double capacitance loops, which can be described by an equivalent circuit of double layer capacitance parallel to oxide capacitance.

Although EP or EIS allows for rapid and accurate determination of corrosion rate and the nature of passive film (porous or dense), they have limitations. When the polarization curve does not present a linear Tafel region, EP is not applicable. The probability of pitting corrosion from the EIS data relies on the choice of electric model and electrochemical constants so that the use of complementary characterization techniques such as SEM, TEM, XRD or GD-OES, is required for proper interpretation of electrochemical data (Walczak et al., 2018).

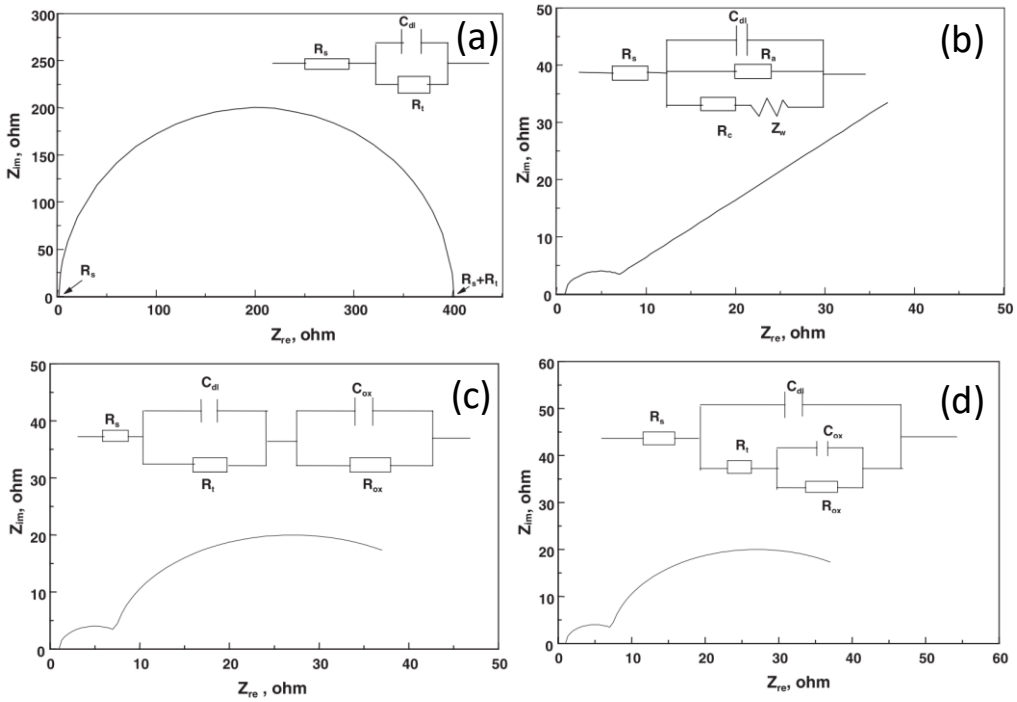

Figure 2-11. Equivalent circuit representing (a) non-active metal electrode, (b) the corrosion of metals forming a porous scale, (c) the corrosion of metals forming a protective scale and (d) metals suffering from localised corrosion in molten salts and its schematic impedance spectrum (Zeng et al., 2001)

2.5.1 Evaluation of mechanical properties of metal – molten salt interface

Nano-indentation has been a commonplace tool for the measurement of micromechanical properties at small scales. It is introduced to this research to investigate the mechanical properties (e.g., elastic modulus, nanohardness) of the sample or the corrosion layer/film of corrosion product. Figure 2-12 presents the working principle of a nanoindenter (He et al., 2015). The key measured quantities are the peak load, Pmax, the displacement at peak load, hmax, the initial unloading contact stiffness, S = dP/dh (i.e., the slope of the initial portion of the unloading curve), and the displacement found by linearly extrapolating the initial portion of the unloading curve to zero load, h_0 (Pharr and Oliver, 1992b). The measurement of nanohardness and elastic modulus are using the equation below (Pharr and Oliver, 1992b);

$$\mathbf{s} = \frac{\boldsymbol{dP}}{\boldsymbol{dh}} = \frac{\mathbf{2}}{\sqrt{\boldsymbol{\pi}}}\boldsymbol{Er}\sqrt{\boldsymbol{A}} \qquad \text{Equation 5}$$

$$\frac{\mathbf{1}}{\boldsymbol{Er}} = \frac{(\mathbf{1}-\boldsymbol{\nu_f}^{\mathbf{2}})}{\boldsymbol{Ef}} + \frac{(\mathbf{1}-\boldsymbol{\nu_i}^{\mathbf{2}})}{\boldsymbol{Ei}} \qquad \text{Equation 6}$$

Where A is projected contact area, Er the reduced modulus, Ef and ν_f are the elastic modulus and Poisson's ratio for the film, and Ei and ν_i are the same quantities for the indenter.

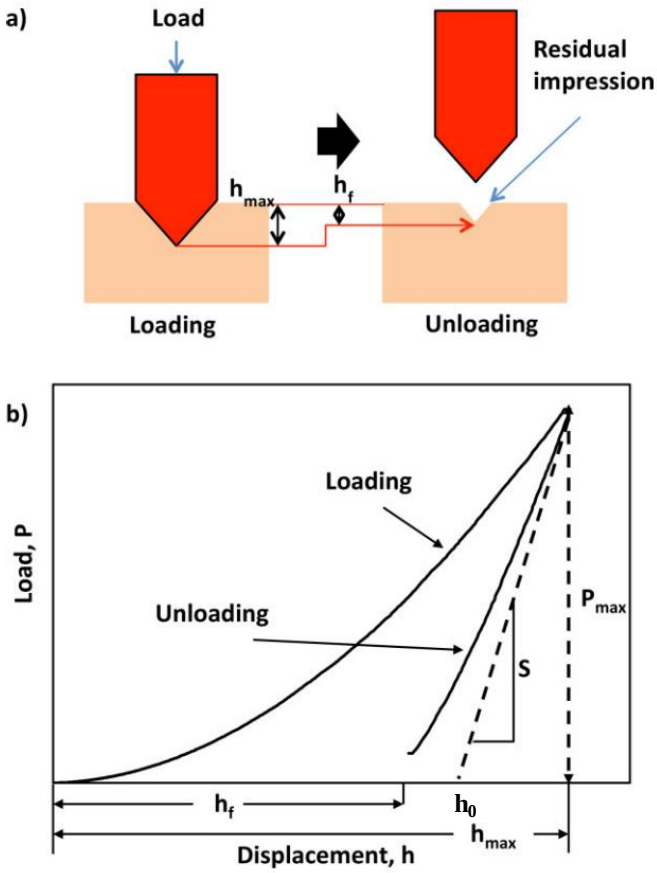

Figure 2-12. Nano-indentation schematic (a) Diagram showing working principles (b) load–displacement curve showing the process of loading and unloading. S the contact stiffness of unloading (He et al., 2015)

There are no literatures available on investigating the change of nano-mechanical properties of corrosion product and substrate metal on the field of molten salt corrosion.

Few literatures have reported the sensitization, thermal fatigue and creep behaviour of material used as heat transfer pipe and hot tank used in Concentrated Solar Power plants where the material exposed to high temperature and high temperature gradient and molten salt.

An atom that gains thermal energy and begins to vibrate behaves as though it has a larger atomic radius. The average distance between the atoms and therefore the overall dimensions of the materials increase. The change in dimensions of the materials Δl per unit length is given by the linear coefficient of thermal expansion α:

$$\alpha = \frac{l_f - l_0}{l_0(T_f - T_0)} = \frac{\Delta l}{l_0 \Delta T} = \frac{\varepsilon}{\Delta T} \qquad \text{Equation 7}$$

Where T_0 and T_f are the initial and final temperatures and l_0 and l_f are the initial and final dimensions of the material and ε is the strain.

When material is slowly and uniformly heated, the material expands uniformly without creating any residual stress. If, however, the material is restrained from moving, the dimensional changes may not possible and, instead, stresses develop. These thermal stresses are related to the coefficient of thermal expansion, the modulus of elasticity E of the material, and the temperature change ΔT:

$$\sigma_{thermal} = \alpha E \Delta T \qquad \text{Equation 8}$$

Thermal stresses can arise from a variety of sources. Changes in temperature cause different amounts of contraction or expansion in the different materials. This disparity leads to thermal stresses that may cause the protective coating or corrosion product spall off. In this study, the different thermal expansion of corrosion product may develop thermal stresses under thermal cycling condition, where the temperature gradient is significant.

2.6 Common salts chemistries used in CSP and their effects on the structural integrity of materials used.

As mentioned earlier, molten salts are the preferred heat transfer fluids and heat storage medium mainly due to their favourable thermos-physical properties (Alva et al., 2018) and thermal stability (Vignarooban et al., 2015a), including high working temperature and large temperature range, high specific heat capacity, high heat transfer coefficient, low viscosity, low vapour pressure, low cost, and good thermal stability.

2.6.1 Nitrate/nitrite salts

As shown in Table 2-2, most of the currently used salts are based on nitrates/nitrites among various molten salts. It consisted of “Solar salt” (60 wt% $NaNO_3$ and 40 wt% KNO_3), “Hitec” (7 wt% $NaNO_3$, 53 wt% KNO_3, 40 wt% $NaNO_2$) and “Hitec XL” (7 wt% $NaNO_3$, 45 wt% KNO_3 and 48 wt% $Ca(NO_3)_2$). The equilibrium phase diagrams of Solar Salt (for this study) is shown in Figure 2-13.

Solar Salt is one commonly used commercial molten-salt in modern CSP systems. Second generation CSP favour nitrate salts to store heat due to their relatively low melting points (Bell et al., 2019). Due to its wide use in CSP plants, corrosion in nitrate salts has been

studied at both the laboratory scale and industrial scale. The corrosive effect of nitrate salts is based on the following reduction reaction:

$$\mathbf{N}O_3^- + 2e^- \leftrightarrow \mathbf{N}O_2^- + O^{2-} \qquad \text{Equation 9}$$

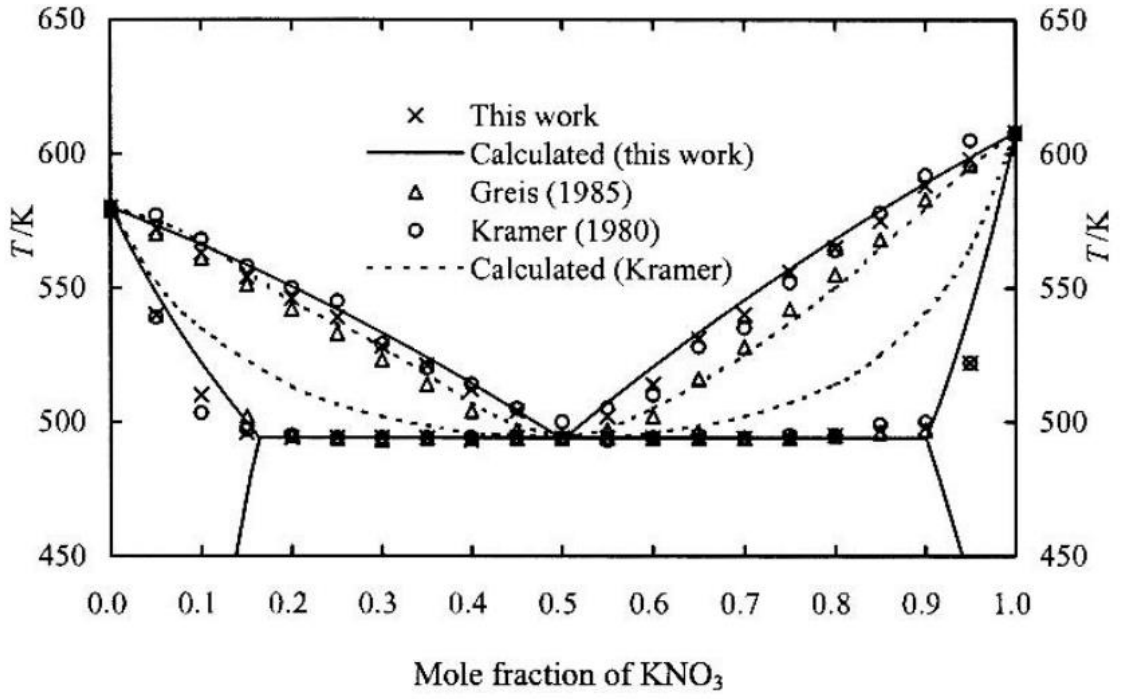

Figure 2-13. The phase diagram for the $NaNO_3$-KNO_3 system (Zhang et al., 2003)

As shown in Figure 2-14 The nitrite concentration of melts in equilibrium with air is about 3 wt.% at 565°C and 5.5 wt.% at 600°C, the decomposition is supressed by increasing the pressure of oxygen in the cover gas (Bradshaw and Goods, 2001a).

Which results in oxidation of iron from the alloy (Fernández and Cabeza, 2019b):

$$\mathbf{Fe} + O^{2-} \leftrightarrow FeO + 2e^- \qquad \text{Equation 10}$$

$$\mathbf{3FeO} + O^{2-} \leftrightarrow Fe_3O_4 + 2e^- \qquad \text{Equation 11}$$

Oxide layers on 316 stainless steel were reported to consist of primarily magnetite (Fe_3O_4) outer layers which protect an iron spinel inner layer and limit chromium depletion from the metal (Bell et al., 2019). Above 600°C, the reaction (1) from nitrate to nitrite becomes more favourable. As a result, the protective Fe_3O_4 outer layer is converted to a sodium ferrite ($NaFeO_2$) which is non-protective and corrosion rate increases rapidly. Soleimani et al. (Soleimani Dorcheh et al., 2016) conducted the test with ferritic steels, austenitic steels (SS316 and SS347H) and Ni-based alloy (IN625) immersed in nitrate solar salt at 600°C up to 5000 h. The ferritic steels were completely destroyed and dissolution of the oxide corrosion products in the molten salt was observed in austenitic stainless steels. IN625

exhibited the best corrosion performance among the alloys, showing a linear weight loss with slow kinetics (Figure 2-7). They (Soleimani Dorcheh et al., 2016) concluded that a multiphase oxide layer composed of iron-chromium spinel, iron oxides and sodium ferrite was formed on SS347H, and a denser NiO layer was primarily found on the surface of IN625, as shown in Figure 2-15.

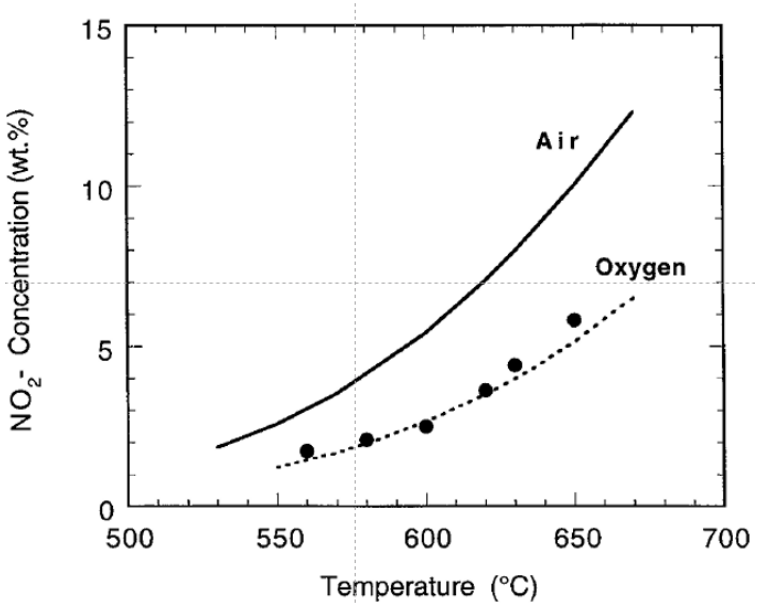

Figure 2-14. Nitrate/Nitrite Equilibrium concentration of nitrite in molten nitrate salt vs. temperature. (Bradshaw and Goods, 2001a)

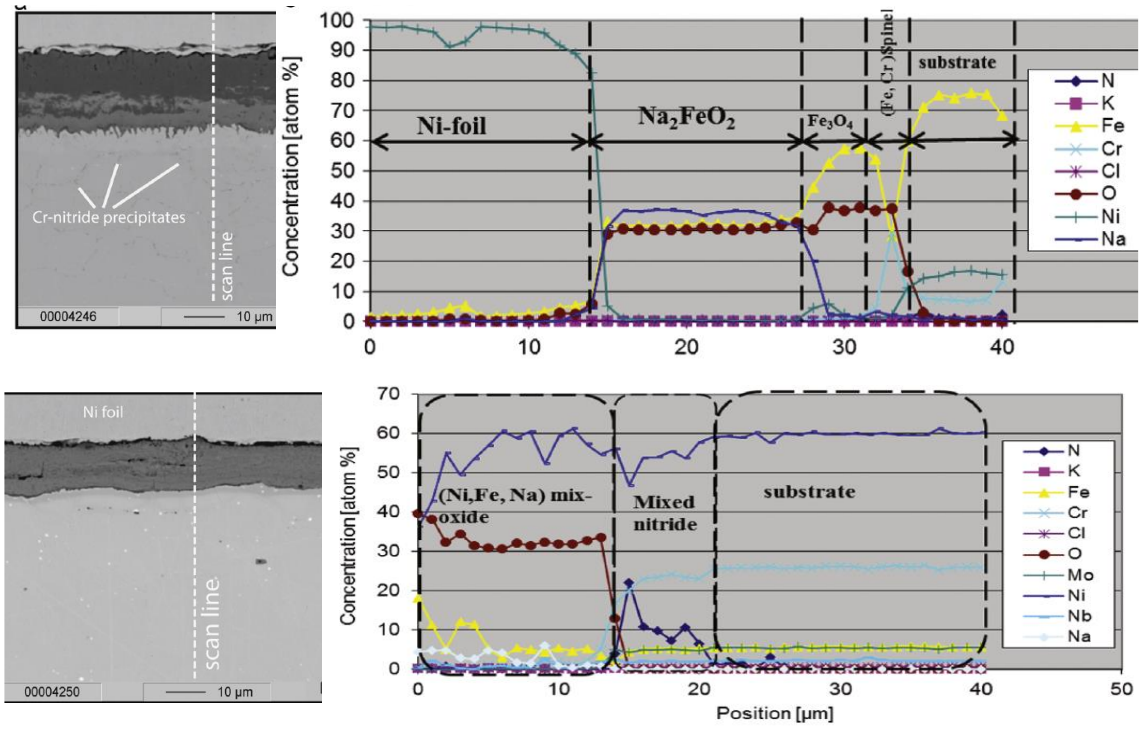

Figure 2-15. Line scans of the oxide scale and substrate in SS347H and IN625 immersed for 5000h at 600 °C in molten nitrate salt. (Soleimani Dorcheh et al., 2016)

Severe spallation was observed when austenitic stainless steels were immersed in nitrate salts at 680°C (Kruizenga et al., 2013), so the Ni-based materials are proposed as corrosion resistance alloys (CRA) at temperature above 600°C (Fernández and Cabeza, 2019b).

In addition to solar salt, the corrosion mechanism evaluation of ternary alkali nitrate mixtures has been studied. Hitec and Hitec XL salts have a relatively lower melting point and lower stability limit temperature than solar salt, thus reducing the risk of freezing for molten salt and decreasing the heat transfer efficiency. The layer of corrosion products in Hitec was found to be compact, adherent and composed mainly of magnetite and hematite (Walczak et al., 2018). These new salt mixtures reported a better corrosion performance compared to binary solar salt (Fernández and Cabeza, 2019b). A corrosion study conducted by Fernandez (Fernández et al., 2015b) analysed the insoluble and corrosion products formed (Table 2-4), yielding lower corrosion rates in Hitec XL salt containing $Ca(NO_3)_2$, due to a lower Cl^- content (Fernández and Cabeza, 2019b). In a recent research, Grosu (Grosu et al., 2018) analysed the formation of two corrosion mechanisms in Hitec XL, oxidation (corrosion) and carbonization (protection). Their finding proposed a simple method to control the corrosion issue of carbon steel in contact with nitrate salt by spray graphitization.

At low temperature below 600°C nitrate salts have relatively low corrosivity for stainless steels as iron oxide is not soluble and forms a stable oxide film, resulting in minimal corrosion rate below 15 µm over 4000h (Bell et al., 2019). Above 600°C however, nitrate salts become significantly more corrosive, even for high nickel alloys. Apart from temperature, chloride ions and moisture are the main important impurities that tend to drive corrosion on nitrate molten salts due to the enhancement of Cr dissolution.

Table 2-4. Corrosion products formed in Hitec XL and solar salt in contact with commercial carbon steels (Fernández and Cabeza, 2019b)

Molten salts	Steel	Corrosion products		Corrosion rate (µm/h)
		Steel	Salt	
Solar salt	A1	$MgFe_2O_4$, Fe_2O_3, MgO	Fe_2O_3, Na_2O, $MgFe_2O_4$	0.1108
	T22	Fe_3O_4, Fe_2O_3, FeCr	Fe_2O_3, Na_2O, $MgFe_2O_4$	0.0081
Hitec XL salt	A1	Fe_3O_4, Fe_2O_3, $NaFeO_2$	$KFeO_2$, $NaFeO_2$, Na_2O	0.00075
	T22	$MgCr_2O_4$, Fe_2O_3	Na_5FeO_4	0.00044

2.6.2 Fluoride salts

Fluoride salts have been widely studied in nuclear industry where they are used as heat transfer fluids in nuclear reactors. Hastelloy grades N and X were both studied with fluoride

salt mixtures, such as lithium, sodium, and potassium fluoride salt mixture (referred as FLiNaK) (Bell et al., 2019). Fluoride salts have attractive properties for use in TES with high working temperature range, comparable densities and thermal conductivities to other salt (Bell et al., 2019). However, fluoride salts are generally expensive than other salts considered for TES, particularly chloride and carbonate salts (Kenisarin, 2010).

The likelihood of fluoride salt reacting with containment metals has been discussed by Sridharan (Sridharan and Allen, 2013a). As all metals will react to form a metal fluoride, fluoridation of structural metals depends upon the relative free energy of formation of the metal relative to the salt anions. Transition metals such as iron, chromium or nickel are unlikely to react with the fluoride ions in the molten salt, as the fluoride ions will preferentially react with the alkali or alkali earth metals present in the salt (Bell et al., 2019). They concluded that corrosion is highly dependent upon temperature and thermal gradients in the container will cause thermally driven corrosion (Sridharan and Allen, 2013a).

Some researchers (Ouyang et al., 2013) investigated the effect of moisture content on corrosion behaviour of nickel alloys, mainly Hastelloy-N and Hastelloy-B3. They found that higher moisture content produces higher mass losses and causes intergranular and pitting corrosion as predicted by the HF mechanism for fluoride corrosion (Bell et al., 2019).

Corrosion in fluoride salts is primarily due to impurities in the salt. After the impurities are used up, the corrosion rate is reliant upon mass transfer of susceptible elements, particularly chromium and aluminium. Corrosion is best controlled by using very pure salts and reducing access to oxidants, particularly moisture. Long term, mass transfer based corrosion can also be mitigated by coatings which prevent migration of chromium into the salt (Bell et al., 2019).

Fluoride molten salts are attractive option for PCM based TES when considering handling these salts in nuclear section and their thermophysical properties, especially at higher temperature.

2.6.3 Carbonate salts

Carbonate salts are of great interest for solar thermal energy storage, particularly PCM storage, as they are relatively inexpensive and able to form eutectics with melting temperatures between 400 and 800°C (Bell et al., 2019). Apart from the favourable melting points, carbonate salt eutectics offer latent heats of fusion from 150 to 300 J/g, comparable to chloride salts but with higher thermal conductivities (Kenisarin, 2010).

Nishikata's research of the electrochemistry in molten salts demonstrates that the carbonates ions will not react with metals directly, because the reduction potential of carbonate ions to carbon is more negative than the corrosion potential of metals (Nishikata et al., 1991). Another researcher Kruzenga (Kruizenga, 2012) identified that the corrosion in molten carbonate salts proceeds in five steps: (1) oxidant dissolving into melt, (2) oxidant transport in melt, (3) corrosion reactions at metal/salt surface, (4) oxide scale dissolution into melt, and (5) preferential dissolution of soluble products. They conclude that the alloying elements in the metals and impurities are critical factors in carbonate salt corrosion. The effect of temperature, atmosphere and additives are clear areas for future investigation for carbonate salts to be used as sensible and latent heat storage media (Bell et al., 2019).

2.6.4 Chloride salts

Chloride salts are gaining more interest as thermal energy storage media in recent years due to low cost and acceptable thermophysical properties (Kenisarin, 2010). Similar to fluoride salts, the free energy of formation for transition metal chlorides is less favourable than for the alkaline metal and alkaline earth metal chlorides which form salt. It means that the corrosion is dependent on the unfavourable chlorination of transition metals, or on the presence of impurities (Sridharan and Allen, 2013a).

Kruizenga (Kruizenga, 2012) demonstrated the effect of O_2 addition to a chloride salt by comparing the mass loss of 316L, Inconel 600 and 625 under 100% Ar and 90%Ar-10%O_2. The 316L lost 12% mass in O_2 containing atmosphere compared to 0.25% under pure Ar. The Inconel alloys see the same difference between pure Ar and O_2-containing environment. Other review of metallic alloys in molten chloride salts concluded that temperature, atmosphere and impurities have significant effect on corrosion rates, Ni-based alloys are generally more corrosion resistance than stainless steels (Ding et al., 2018). The corrosion rates can be mitigated by salt purification, addition of corrosion inhibitors and formations of protective coatings (Ding et al., 2018).

2.6.5 Sulphate salts

Sulphate salts are not commonly considered for TES applications (Bell et al., 2019). But the sulphate salts have advantageous properties, especially mixed with other salt species, which draw the attention of many researchers. The sulphates do present a risk of sulphur penetrating the metal, causing embrittlement and affecting the high temperature performance of the steel.

2.6.6 Summary

In conclusion, among all these types of salts, nitrate salts are relatively benign and have acceptable corrosion rate at temperature below 600°C in 304 and 316 grade alloys. To prevent substantial de-alloying and corrosion in chloride and fluorides, the salts must be pure, free from moisture, and an inert atmosphere must be maintained (Bell et al., 2019). Pre-forming oxide layers may help. Carbonate salts also require purification and inert atmosphere. Using sulphate salts may induce additional corrosion mechanism via sulphidation. High nickel alloys and coatings are most likely to be resistant to attack. The solubility and/or diffusion of chromium can be reduced or limited via microstructure modification, alloying, surface coating or the use of low chromium alloy to mitigate the dissolution of chromium into salt (Bell et al., 2019).

2.7 Assessment of the corrosion performance of common metallic materials used in CSPs

Most of the CSP components, especially those of TES system, are made of metallic alloy, which are inevitably susceptible to corrosion, especially exposed to molten salt (Vignarooban et al., 2015a, Barlev et al., 2011, Papaelias et al., 2016, Fernández et al., 2015b). Stable and safe operation and long service life are the basic requirements of CSP plants system, some high-temperature corrosion resistant materials are urgently needed. In this section, we will focus on the most common and recently considered grades of carbon steels, stainless steel and Ni-based alloys and compare their corrosion performance.

2.7.1 Carbon and low alloy steels

Carbon and low alloy steels are most common materials employed in engineering. Sufficient mechanical properties and low cost ensures both carbon and low-alloy steel to be early candidates considered for TES components in contact with molten salt. First study about corrosion performance of carbon steel was carried out by Baraka since the 1970s (Baraka et al., 1976), reporting the effect of temperature on the corrosion rate for carbon steel exposed to salt mixture of $NaNO_3$ and KNO_3 for 8h at 250, 300, 350, 400 and 450°C. The corrosion rate followed parabolic and linear rate laws at the lower and higher temperatures, respectively. The Sandia National Laboratories started to study the most common structural steel, i.e. A36, in now-commercial salt mixture, Solar Salt (Goods et al., 1994a). The adherent oxide layer compose of magnetite was observed by SEM and XRD after corrosion test. Consequently, A36 was recommended for the components of CSP plants. Another materials evaluated for use in Solar Salt is the T22 with low-Cr grade, tested for 2000h at

390 and 550°C (Fernández et al., 2012). Corrosion products were identified as a mixture of $MgFe_2O_4$, $FeCrO_4$ and Fe_2O_3 at both temperatures, indicating the importance of alloying elements in the formation of oxide layer. While tested at 550°C, corrosion damage observed was classified as “catastrophic” because of severe intergranular corrosion. T22 alloy was also evaluated in Hitec and Hetic XL, in which corrosion rate showed at least twice slower than that in Solar Salt, which was explained by the formation of protective layer of K_2CrO_4 spinel in Hitec (Fernández et al., 2015a) and $MgCr_2O_4$ spinel in Hitec XL (Fernández et al., 2015b), indicating the diffusion of Cr into the outer zone of the corrosion layer. The corrosive effect of Hitec and Hitec XL at 390 °C has also been evaluated on carbon low-alloy grade A516 (Vignarooban et al., 2015b), low-Cr alloy grade T11 (Fernández et al., 2015b) , and low-carbon grade A1 (Fernández et al., 2015b), in the respective order of increasing relative corrosion resistance.

The main drawback of carbon steel and low alloy steel is their corrosion rate increases when operating temperatures increases. Protective nitrogen atmosphere is needed to control corrosion rate during exposure to molten salt (Walczak et al., 2018). Still they can be applied at temperature not exceeding 390°C, which are favourable due to their mechanical properties and low relative cost.

2.7.2 Stainless steels

Stainless steel was discovered as resistance alloy to atmospheric corrosion and now was defined to prevent rusting in aqueous environment with 12% Cr (Walczak et al., 2018). For stainless steel, corrosion resistance relies on the formation of thin and dense Cr-oxide, protective properties of which can be further improved by the alloying with Ni and Mo. Compared with carbon steels, their mechanical properties and corrosion resistance which can be maintained to higher temperature triggered their application in TES systems (Walczak et al., 2018).

Although the various stainless steels differ in chemical composition and microstructure, a general trend of faster corrosion with increasing temperature can be observed in Figure 2-16 below (Walczak et al., 2018). It should be noted that the AISI 321 and 347 tested at 680°C showed exceptional high corrosion rate, which is related with the onset of additional reactions, once the salt’s stability limit of 600°C is surpassed. As shown in Figure 2-16(a), stainless steels in solar salt are affected by the presence of chloride, accelerating localised corrosion. The corrosion products formed in Solar salt for stainless steel are $FeCrO_4$, Fe_2O_3, and $MgFe_2O_4$ with the presence of Mg impurities, also a porous outer layer of $NaFeO_2$ was

observed (Fernández et al., 2015b, Xu et al., 2015). The Fe-Cr spinel, formed at the inner layer of corrosion products, controls the rate of corrosion (Bradshaw and Goods, 2001b).

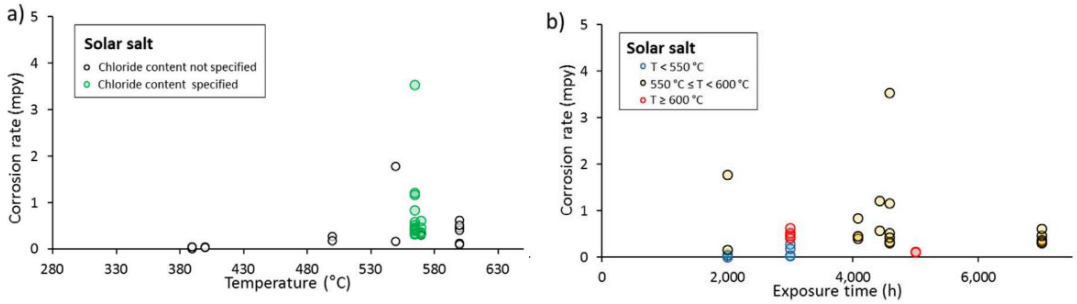

Figure 2-16. Scatter plots of corrosion rates of stainless steels tested in Solar Salt at different condition, presented in function of: (a) temperature, with effect of chloride content, (b) exposure time, considering temperature range of exposure (Walczak et al., 2018), 1 mpy (Mils per Year) = 25.4 um/y

Some researchers studied the corrosion performance of stainless steels in carbonate salts mixtures (K_2CO_3-Na_2CO_3) at 750°C (Gomez-Vidal et al., 2016). They reported unacceptably high corrosion rates for the alloys 310, 321 and 347. Chloride salts represent another alternative mixture used for increasing operational temperatures of TES. AISI 316L shows unacceptably high corrosion rates in binary mixture of LiCl-KCl associated with rapid formation and spallation of the corrosion products (Shankar et al., 2010). Further binary mixture tested at 650 and 700 °C on AISI 310 and 347 was NaCl–LiCl. The low Ni content of alloy 347 resulted in high corrosion rate at the lower temperature, whereas alloy 310 was almost as good as the Ni-based alloy In800H, but the increase of temperature from 650 to 700 °C doubles the rate of corrosion and also localised corrosion associated with preferential dissolution of chromium and iron is observed rendering the alloy not applicable (Gomez-Vidal and Tirawat, 2016). In ternary mixture of LiCl-KCl-CsCl, the alloys 304L and 321 exhibited another disappointing corrosion performance. Although the higher Ni alloy showed no corrosion at 400°C, but other corrosion damage at 500°C and 600°C showed unacceptable intergranular corrosion (Figure 2-17) (Hofmeister et al., 2015b).

The most promising ternary chloride salt mixture is NaCl-KCl-$ZnCl_2$ tested on the alloy 304, proposed by (Walczak et al., 2018). The researchers reported that the 304 showed the similar corrosion rate compared to Ni-based alloys under inert atmosphere (Vignarooban et al., 2015b).

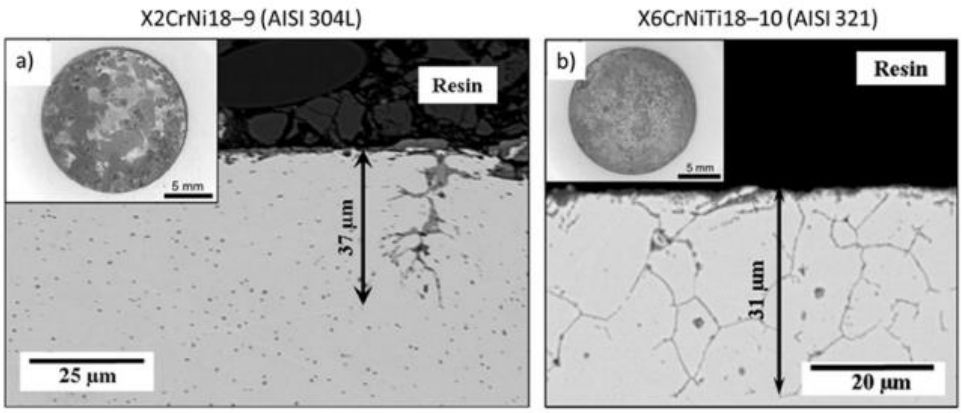

Figure 2-17. Cross-sectional SEM micrographs of a) X2CrNi18-9 (AISI 304L) and b) X6CrNiTi18-10 (AISI 321) with the corresponding light microscopic top-view of the corroded samples (insert) after 3 h exposure to LiCl–KCl–CsCl at 600 °C. The arrows indicate depth of corrosion (Hofmeister et al., 2015b)

2.7.3 Ni-based alloys

Ni-based alloys are based on nickel and exhibit good mechanical properties and high corrosion resistance and oxidation resistance. Most of these alloys qualify as superalloys for their mechanical strength and resistance to thermal creep deformation. Despite high price, alloys based on Ni has overwhelming superiority at high temperature conditions due to their resistance to pitting corrosion, reducing acids, crevice attack and stress corrosion cracking as compared with stainless steels (Walczak et al., 2018).

Due to the good performance of stainless steels in nitrate salts, the necessity of implementing Ni-based alloys is little justified so that only In625 and HA230 were tested in Solar Salt at 600 and 680 °C (McConohy and Kruizenga, 2014, Soleimani Dorcheh et al., 2016), In800 in Solar Salt at 560 °C (Zhang et al., 2014), and In600 was tested in Hitec at 530 °C (Federsel et al., 2015). The corrosion rate of Ni-based alloys in Solar Salt at 600 °C are practically the same as those of AISI 316, 321 and 347 tested at the same conditions and showing analogous increase of corrosion rate at 680 °C (Kruizenga and Gill, 2014, Goods et al., 1994a) associated with build-up of additional corrosion products at the higher temperature (Walczak et al., 2018). More attention of the corrosion behaviours of Ni-based alloys are diverted to molten carbonate, chloride salts. Electrochemical data for In625 and In800H tested in the eutectic K_2CO_3–Na_2CO_3 at 750 °C reported by Gomez-Vidal et al. (Gomez-Vidal et al., 2016) shows unacceptably high corrosion rates. Corrosion rates of determined in LiCl-KCl at 400, 500 and 600 °C for alloys In600, In625, In690 and In800H are considerably higher than those observed in nitrite salts but in the same range as those

determined for AISI 316 (Shankar et al., 2010, Shankar et al., 2012). Figure 2-18 shows the morphology of the scales and descaled surfaces observed after 2 h exposure to LiCl-KCl at 600 °C for In600 and In800H (Shankar et al., 2012). Although morphology and chemical composition of the scales formed on the alloys were distinctive, surface of the metal become porous as a result of selective dissolution of alloying elements producing enrichment of Ni and depletion of Cr and Fe content. In case of IN 625, enrichment of Mo was observed in addition (Walczak et al., 2018). Notably, the corrosion rates of Ni-based alloys in chloride salts are too high to meet the requirement of restraining corrosion to 50 µm/year (Gomez-Vidal et al., 2016). A more promising performance of Ni-based alloys was shown for ternary mixtures NaCl-KCl-$ZnCl_2$ of varying molar fractions at temperatures between 250 and 800 °C with corrosion rate from negligible to admissible 48.9 µm/year (Vignarooban et al., 2015b), the lowest corrosion rate were observed in the mixture NaCl-KCl-$ZnCl_2$ of 13.4/33.7/52.9 mol% (Walczak et al., 2018).

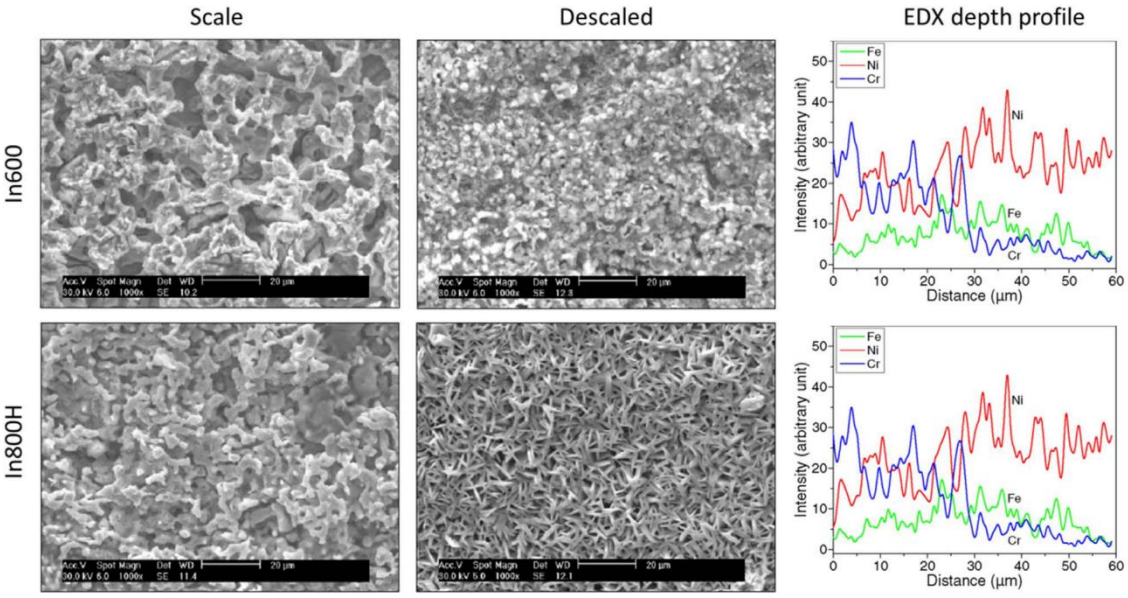

Figure 2-18. Morphology and elemental depth profiles determined by SEM-EDX on alloys In600 and In800 after 2 h exposure to LiCl-KCl at 600 °C (Shankar et al., 2012)

From the discussion above, amongst all the alloys, Ni-based alloy shows best corrosion performance in all salts. It shows the linear and very slow weight loss and its oxide scale remains protective for long contact with the molten salts. Considering the higher price of these alloys, it is still favourable to use cheaper stainless steels than the expensive Ni-based alloy. Development of protective coatings for low alloyed steels can be an alternative and economic solution to prolong the lifetime of installations in solar power plants against molten salt corrosion (Soleimani Dorcheh et al., 2016).

2.8 Factors influencing the corrosion process and corrosion mechanism

According to openly literatures, there are many factors influencing the corrosion performance of studied alloy in molten salt and corresponding to different mechanisms.

2.8.1 Temperature

Generally, higher temperatures cause a further increase in mass loss due to enhanced kinetics and thermodynamics (Bell et al., 2019). Zhu (Zhu et al., 2018) has investigated the corrosion behaviours of SS 316 in Hitec salts at 450, 600 and 680°C to demonstrate how the temperature influences the corrosion behaviours. They concluded that SS316 showed good corrosion resistance in Hetic at 450°C and the oxide scale could not be distinguished on the surface. Corrosion density increased at 600°C with thick, loose and porous oxide scale formed on the surface of SS 316. Corrosion rate of the tested sample increased considerably with the increase of test temperature from 600°C to 680 °C. The temperature also has effect on the corrosion rate-limiting step, the corrosion process was controlled by outward diffusion of metal ions, electrons, and oxygen vacancies at 450 and 600°C while at 680 °C, the Warburg impedance was observed at low frequency region of the impedance spectrum indication that inward diffusion of oxygen ions controlled the rate of corrosion (Zhu et al., 2018).

2.8.2 Thermal cycling and thermal shock

Another corrosion mechanism named thermal driven corrosion occurs when there are temperature gradients in the molten salts (Bell et al., 2019). The melt ion solubility can be temperature dependent, the alloy dissolved preferentially in the hotter area or hotter period of the melt. The dissolved ions may then diffuse to cooler areas where solubility is lower and precipitate out of solution (Sridharan and Allen, 2013b). This diffusion process is promoted by thermal driven convection resulting in material removal from one area and deposition in another. A recent study (Cho et al., 2015) shows that the corrosion rate of Alloy 230 in $MgCl_2$/KCl salt under a thermal gradient between 800°C and 950°C was 2–3 times higher than the corrosion rates at those temperatures without the thermal gradient. They concluded that this was due to the thermally driven flow promoting Cr^+ removal from the metal surface. Thermally driven corrosion is a particular problem for thermal energy storage systems which incorporate temperature variations.

The effect of thermal cycling on the corrosion is not neglected. Due to the diurnal nature of CSP plants, the receiver tubes must tolerate many excursion between its maximum operating temperature and ambient temperature (Bradshaw and Goods, 2001b). Thermal

cycling generally aggravates high temperature oxidation, but the degree to which a particular material may be affected in any given environment is difficult to predict (Walter et al., 1993, Mevrel and Technology, 1987). The primary effect of thermal cycling on corrosion is to damage protective surface oxide layers mechanically, thereby compromising the barrier to corrosion such layers provide (Bradshaw and Goods, 2001b).

The temperature/time profile used in Ref (Bradshaw and Goods, 2001b) for the thermal cycling tests is shown in Figure 2-19 and consisted of a cycle time of 8 hours with coupons immersed in molten salt at 560°C for 7.5 hours and cooled in air for 0.5 hour. The effect of thermal cycling on corrosion in nitrate salts was tested and found moderately increase the corrosion rate (Bradshaw and Goods, 2001b), as shown in Figure 2-20. This protocol cannot simulate the specific conditions of CSP plants. In this study, we make a modified protocol and the samples are kept at temperature at 250°C, 600°C and controlled to fluctuate between 250 and 600°C representing peak time heating of molten salt and night time cooling of molten salt in CSP flow lines. The detailed discussion is shown in the following statements.

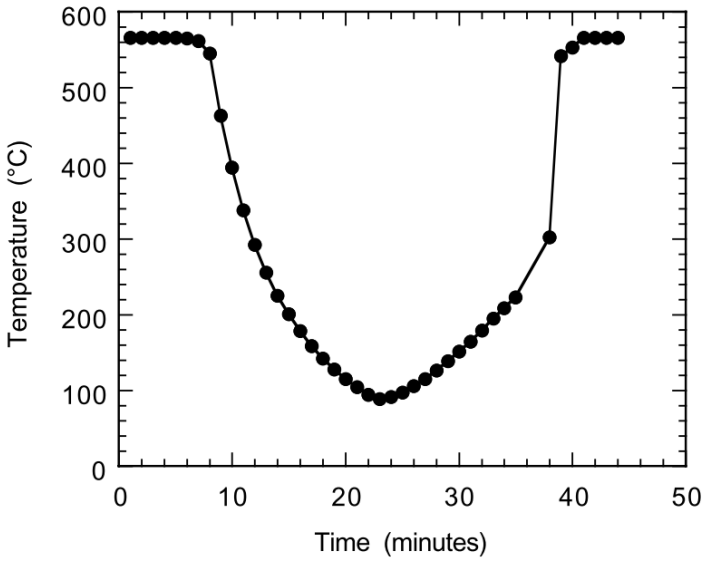

Figure 2-19. Temperature profile experienced by molten salt corrosion coupons during thermal cycling (Bradshaw and Goods, 2001b)

As we know, the availability of sunlight could highly affect the capacity and efficient of electric energy generation. Besides, according to the operating and maintenance experience from one power plant in China, it can also affect the receiver panels when a cloud comes or gust of wind blows through suddenly to either cut off the solar irradiation from mirrors (heliostats) or take away the heat on the surface of pipe panels. The threat of thermal shock is significant

and is always contributed to deformation and expansion of the receiver pipes, causing final failure of it and leading to the collapse of the system.

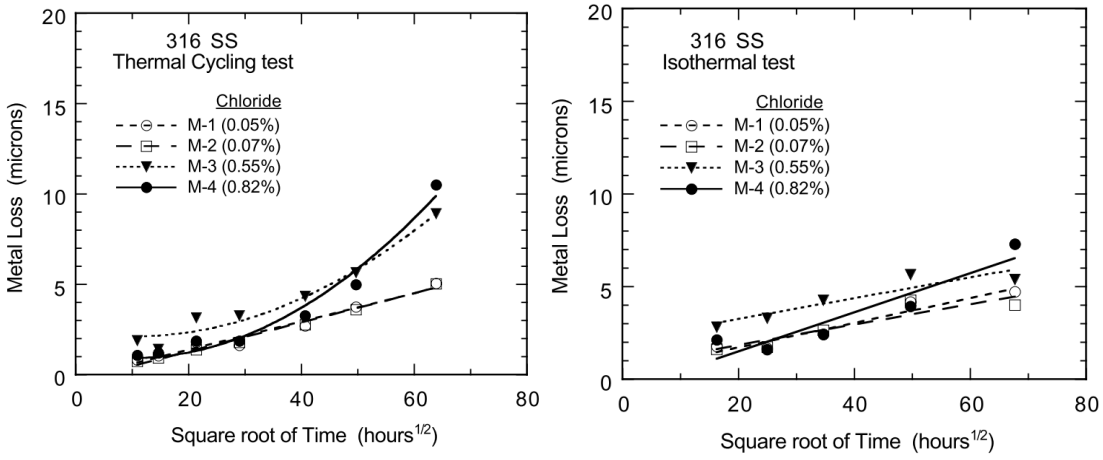

Figure 2-20. Descaled metal losses of Type 316 SS during corrosion in molten nitrate salt mixtures at 565˚C, Data for four levels of dissolved chloride are shown for thermal cycling (left) and isothermal corrosion (right) (Bradshaw and Goods, 2001b)

2.8.3 Impurities

Impurities such as oxygen, moisture, oxides and hydroxides can be present in salts and are potential oxidants. Other salts, such as chlorides in carbonate and nitrate salts, are also impurities which affect corrosion. These impurities are often difficult to remove (Sridharan and Allen, 2013b), leading to an initially high corrosion rate until the impurities are exhausted and corrosion becomes driven by a different mechanism (Figure 2-21).

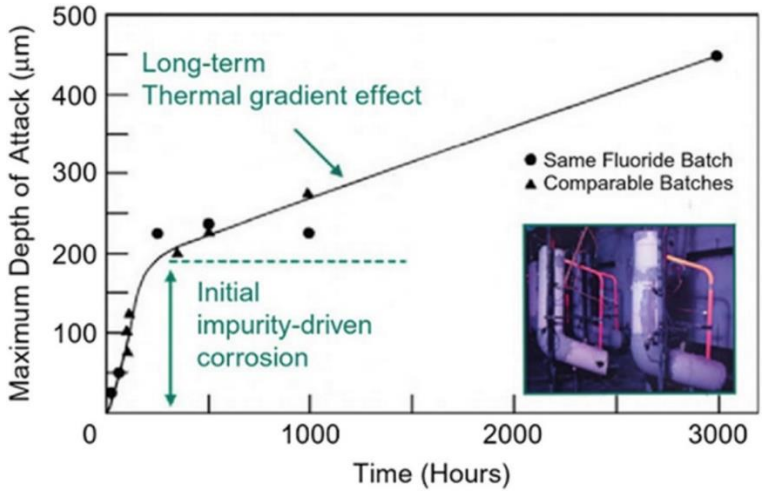

Figure 2-21. Two regimes of corrosion; early, impurity driven corrosion, and; long term, linear corrosion (Sridharan and Allen, 2013b)

Ouyang, Fan-Yi (Ouyang et al., 2013) has investigated the effect of moisture on corrosion of Hastelloy in molten alkali fluoride FLiNaK salt environments. As shown in Figure 2-22 (a),

the mass loss of the Hastelloy-N in the purified FLiNaK salts were significantly lowered by at least 25 times, even though the corrosion tests in the purified salts were run at higher temperature and longer exposure time. The introduction of moisture in fluoride salts would significantly increase the corrosion rates of the alloys that are exposed to it. They came to the conclusion that the mass loss of the samples is primarily determined by the purity of FLiNaK salts. But, once a minor amount of H_2O is introduced in the salts, the effect of temperature become more significant on the mass loss of the samples.

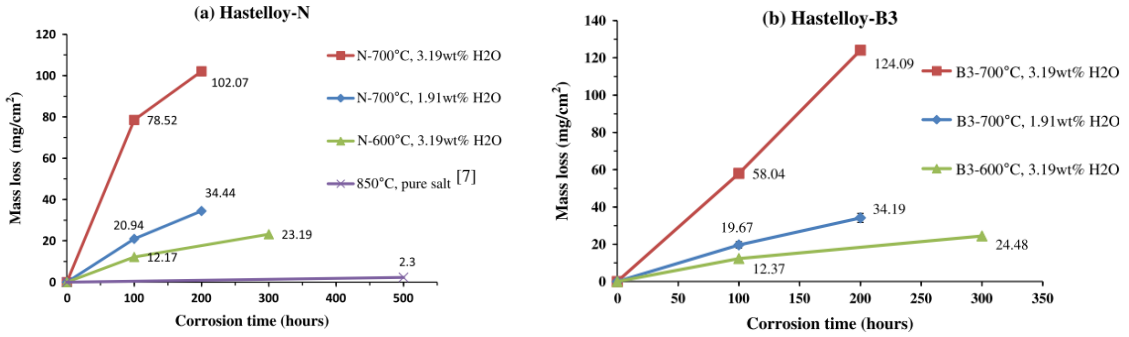

Figure 2-22. The comparison of mass loss of (a) Hastelloys-N and (b) Hastelloys-B3 after different periods of corrosion tests for different moisture contents and temperatures. (Ouyang et al., 2013)

2.8.4 Cover gas

Although in most cases, the corrosion often occurred beneath liquid salt and the cover gas seems not important to control the corrosion process. While the covering gas atmosphere does play an important role in regulating the corrosiveness, stability and oxidation of salt at high temperature. From the previous studies, the oxygen availability is a critical factor influencing the corrosion behaviours by altering the acidity/basicity of the salt thus affecting the chromium dissolution and selective oxidation processes of steels in molten salts (Bell et al., 2022).

S.bell (Bell et al., 2022) has found that the oxidation state of Fe and Cr was affected by the basicity and oxygen content, where lower oxidation state was found in argon and higher oxidation state in air. They also found the presence of greater proportion of Fe^{3+} and the absence of Cr and thus implying the solubility of the Cr^{3+} phase in the salt (Bell et al., 2022). Vignarooban (Vignarooban et al., 2015b) found that corrosion rate of C-276 in open container at 500 ˚C showed as 10 times higher as that in sealed container even at 800 ˚C, shown in Figure 2-23 for comparison. While S.Bell (Bell et al., 2021) found that the corrosion was even more server when C-276 tested with chloride/sulphate eutectic salt in argon. Therefore, they concluded that the atmospheric air plays a big role in inducing the corrosion

in the molten-salt/alloy systems. From a recent research (Bonk et al., 2020), the decomposition from nitrate ions to nitrite ions are more favourable at higher temperature in open atmosphere, thus resulting in higher content of oxide ions, shown in the Figure 2-24 (adapted from Ref (Bonk et al., 2020)). As we discussed before, the oxide ions formed from Equation 13 can increase the basicity of the solar salt and are believed to enhance the corrosion effects toward metallic components (storage tanks, pipes, receivers and valves) (Bradshaw and Meeker, 1990, Siegel et al., 2011, Goods et al., 2004, Olivares and Edwards, 2013). To what extent the differences of salt chemistry affect the corrosion performance of steels/alloys and the reason of it are our concern.

$$NO_3^- \rightleftharpoons NO_2^- + \frac{1}{2}O_2(g) \qquad \text{Equation 12}$$

$$2NO_2^- \rightleftharpoons NO_2(g) + NO(g) + O^{2-} \qquad \text{Equation 13}$$

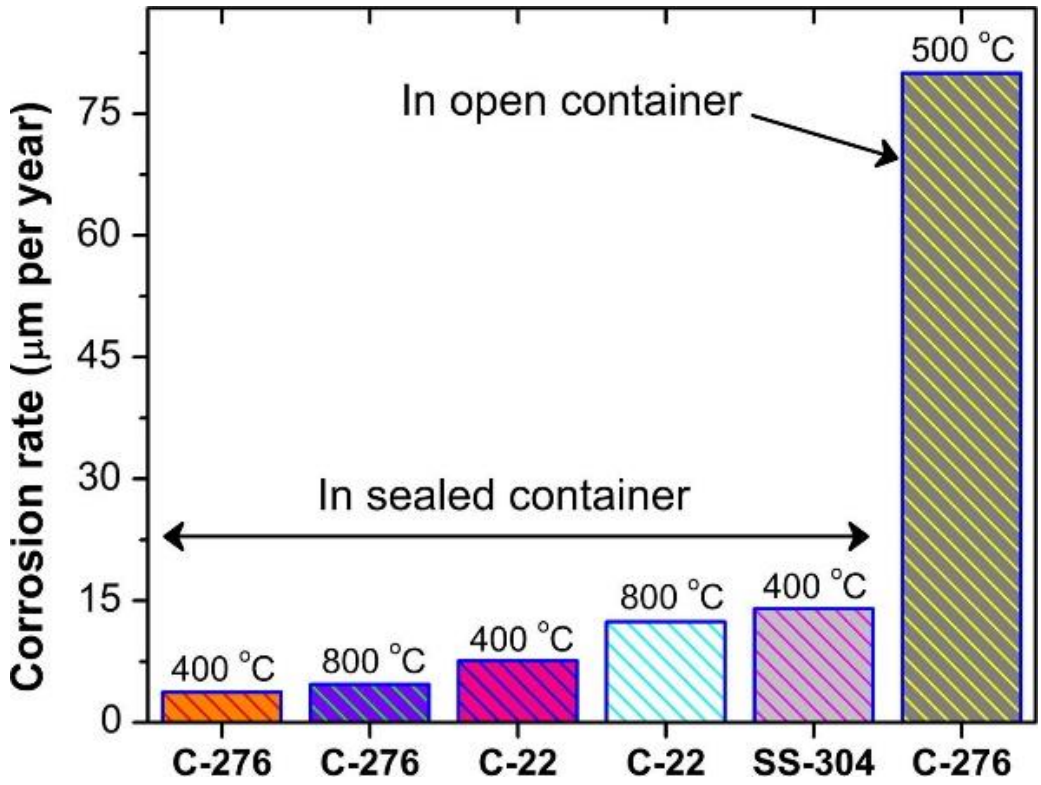

Figure 2-23. Corrosion rate values from immersion method for C-276, C-22 and SS-304 alloys at 400 and 800 °C in the absence of air along with CR value for C-276 at 500 °C in the presence of air in 13.4 NaCl: 33.7 KCl: 52.9 $ZnCl_2$ molten salt (Vignarooban et al., 2015b)

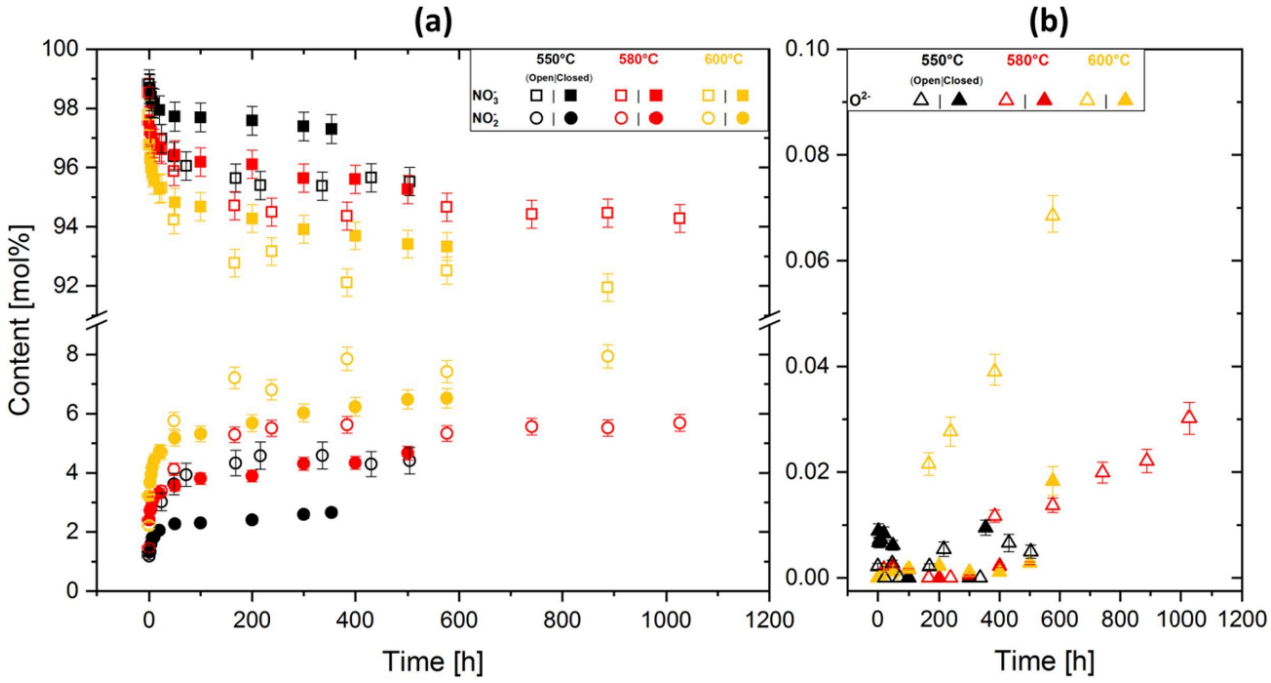

Figure 2-24. Nitrate and nitrite content in Solar Salt stored in open atmosphere (open symbols) and closed atmosphere (closed symbols) at 550 °C, 580 °C and 600 °C. Adapted from Ref (Bonk et al., 2020)

2.8.5 Oxygen and aggressive ions

The oxidation was found (Sarvghad et al., 2017a) as the primary attack to the alloy in molten salt environment when exposed to air. Sarvghad et,al. started the static corrosion test using the corrosion vessel in Figure 2-25, the bottom half of metal coupons were submerged into the molten salt and top half of that was exposed to air. Such a configuration enabled them to make a comparison between the impact of salt and the oxygen from the environment, as well as the corrosive impact of decomposition gases of salt. They proved that the availability of O_2 controls the degree of oxidation and the molten salts proved to reduce the degree of oxidation when the materials were submerged. In another literature reported by Sarvghad (Sarvghad et al., 2017c) the availability of oxygen controlled its rate. NaCl + Na_2SO_4 and NaCl + Na_2CO_3 salts at 700 °C were found protecting further oxidation through limiting the oxygen available to the metal. For the metal in carbonate salt at 450 °C, oxidation was further assisted by corrosion from molten salt. The effect of vapour depends on the temperature and salts.

Corrosion testing (Bradshaw and Clift, 2010) demonstrated that dissolved chloride in molten binary Solar Salt (60-40 wt.% $NaNO_3$-KNO_3) has a significant effect on corrosion of carbon steel at 400°C and above. The change of mass loss implies that corrosion rate increase with the increase of chloride content and temperature. The tendency of oxide scale layers to spall

depended on the concentration of dissolved chloride and such tendency was exacerbated at relatively high temperature.

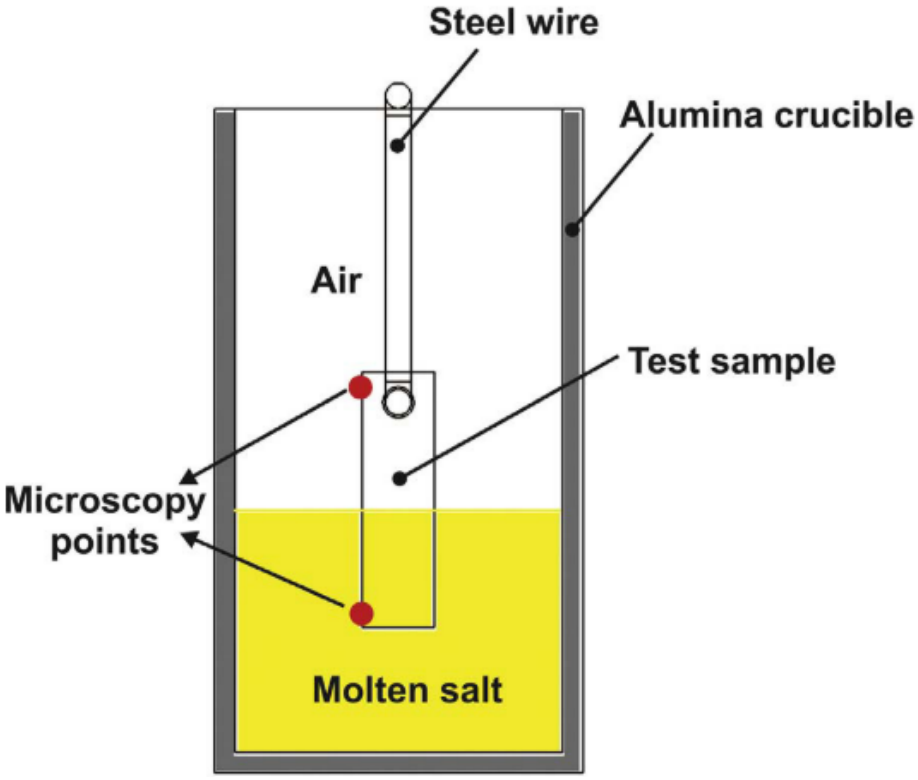

Figure 2-25. Schematic of the corrosion vessel and a sample inside the furnace (Sarvghad et al., 2017a)

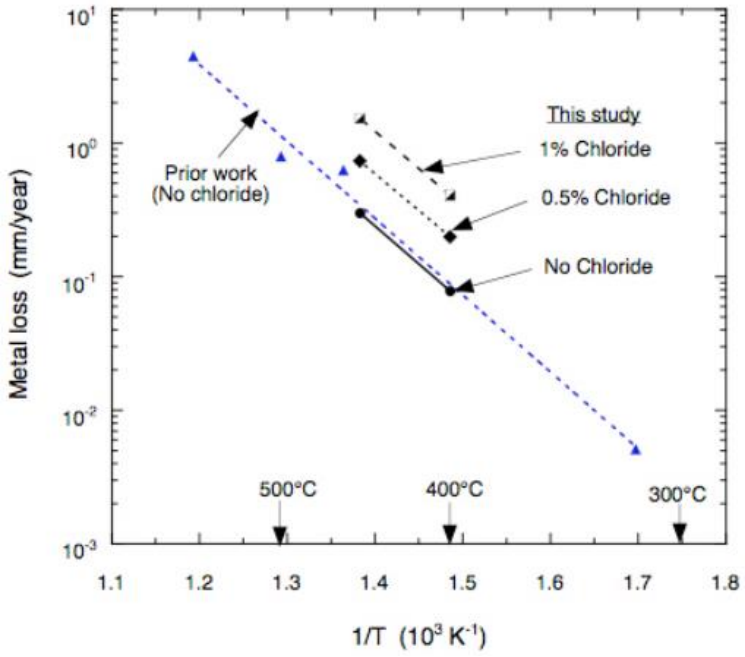

Figure 2-26. Corrosion rates of several carbon steels vs. temperature in a 60-40 wt% nitrate molten salt mixture (Bradshaw and Clift, 2010)

Some authors (Federsel et al., 2015) demonstrated the important role of chlorides in the corrosion mechanism, affecting the adherence between oxide layers and the steel tested. As shown in Figure 2-27, two stainless steels, AISI 321 and 316Ti, show similar results that the weight loss stopped after 1000-2000 hours exposure to Solar Salt due to the initial formation of a protective oxide layer. They concluded that the formation of iron chloride below the oxide layer with even a small concentrations of chloride can lead to a permanent spalling of the oxide layer due to the relatively high volatility of iron chloride.

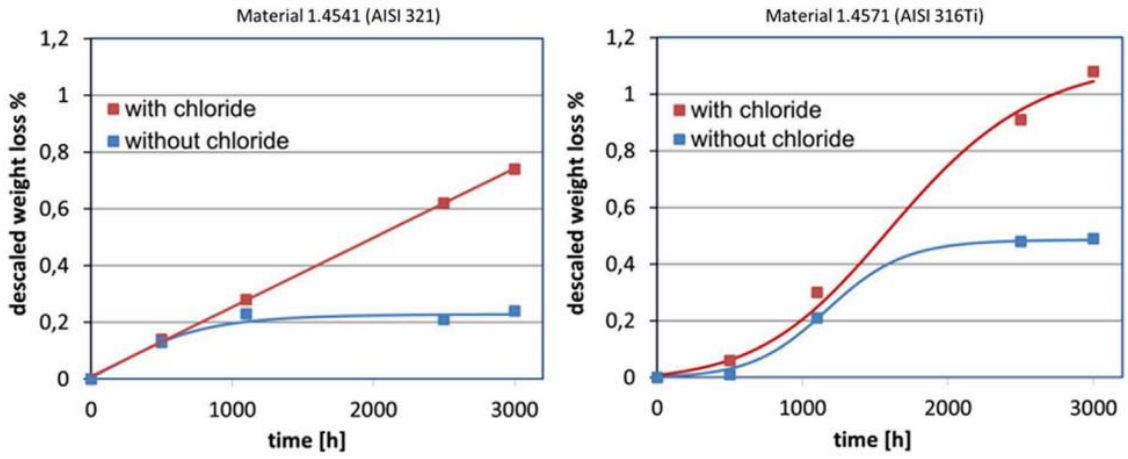

Figure 2-27. Effect of chloride impurity on weight loss evolution in Solar Salt at 565 °C for the indicated stainless steels (Federsel et al., 2015)

2.8.6 Salt vapour

Considering the flowing behaviour and static storage behaviour of molten salt in the flow lines and storage tanks, it is easy to imagine that the metallic parts are either immersed in the salt or above the liquid line of the molten salt, whereas the air or salt vapour.

From recently reported literature (Sarvghad et al., 2017b), the research designed a corrosion vessel to have the samples half-immersed in liquid salt to compare not only the impact of salt and the oxygen from the environment, but also the gases decomposed from carbonate salt which are expected to worsen the corrosiveness of system in this atmosphere. They found that the oxidation was the primary attack to alloys in molten salt or vapour environment and confirmed that the availability of oxygen could control the degree of oxidation/corrosion. They also found evidence to confirm that the molten salts can slow down the oxidation on the submerged samples.

Another research (Liu et al., 2021b) carried out by Chinese Academy of Sciences investigated the corrosion behaviours of GH3535 (Ni-based alloy: NiMoCr) alloy in NaCl-

$KCl\text{-}MgCl_2$ salt and vapour at 700°C. The chloride salt has high vapour pressure and easily lead to evaporation of the salt. The samples were divided into two groups, upper samples were totally suspended above the liquid salt and bottom samples were completely immersed into liquid salt, shown in Figure 2-28. They found that the fully immersed samples exhibited regular and smooth surface without intergranular corrosion, while vapour-exposed samples formed double-layered structures of easily exfoliated oxides. A loose oxide layer formed on the surface of the corroded alloy, which had poor adhesion to the substrate and was easily exfoliated from substrate metal of GH3535 (NiMoCr alloy). Also, some new peaks appeared in the XRD spectra of the alloy surfaces in vapour. Further analysis indicated that these new peaks were diffraction peaks of Mg-Cr and Ni-Mo oxide, the Ni-Mo-Cr alloy surface tended to be oxidised and form oxides when exposed to high-temperature molten salt vapour.

They also investigated the corrosion behaviours of stainless steels (Liu et al., 2022c) at the same condition and found that the Fe and Cr were preferentially corroded at the grain boundary and thus resulted in the formation of corrosion holes, where the oxide substance entered into the material and reacted with inner metal. As for the chemistry of the multi-layer, they found that the farther away from the substrate, the lower content of Fe and Ni and higher Cr and Mg content was observed on the oxide layer.

From the introduction above, we can easily draw a conclusion that the material exposed to mixed environment with molten salt vapour and oxygen would suffer a higher degree of corrosion. Because of the relative low vapour pressure of the nitrate salt, there was few open literatures reported the salt vapour of nitrate salt. Another reason is the pursuit of higher temperature in CSP plant, and the nitrate salt is proven not stable at temperature higher than 600°C due to its decomposition. However, the corrosion performance of metallic material in nitrate salt vapour should be investigated before the large-scale use of newly type salts to figure out corrosion or protection dominates the corrosion behaviour in this condition.

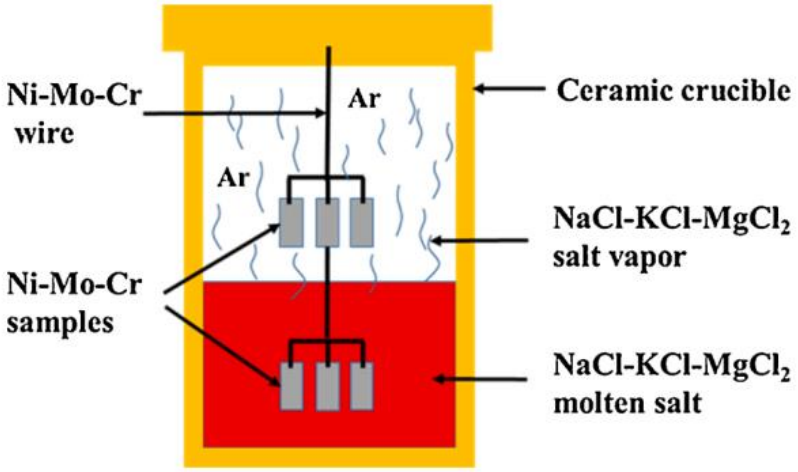

Figure 2-28. Schematic of the salt vapour corrosion experiment set-up

2.8.7 Alloy element

Sun et.al (Sun et al., 2018) claimed that no systematic studies have been performed to clarify the relationship between the alloying elements and the corrosion behaviour of Ni-based alloys in molten salts. But the alloying elements can affect the resistance of Ni-based alloy against molten salt. They concluded that the effect of alloying elements on corrosion have a strong temperature dependence (Sun et al., 2018), which is attributed to the temperature induced the increase of Cr diffusion coefficient.

The data available for stainless steel is insufficient to verify how the actual amount of Cr in a stainless alloy affects the composition of the oxide layer (Walczak et al., 2018). All the stainless steels have Cr content above 12-13wt %. With the increasing Cr content, the main effect is to improve corrosion resistance and stabilise the ferrite phase. It is acknowledged that the corrosion of alloys in molten chloride salts are attributed to selective dissolution and/or oxidation of the element Cr.

The content of Ni can influence the corrosion resistance, as Ni is known to stabilise the oxides at high temperatures and its enrichment was found after exposure of AISI 321 and 347 to Solar Salt at 680 °C (Kruizenga and Gill, 2014). Ti (titanium) and Nb (niobium), as stabilizing elements, are usually added into stainless steel to form strong carbide to avoid sensitization, which we mentioned in 2.2. And their effect on the corrosion behaviours in molten salts is not clear.

As for the effect of Mo, which is known to improve the resistance to localised corrosion in aqueous media, its benefit on corrosion rate in Solar Salt could not be established (Walczak et al., 2018), considering that corrosion resistance of AISI 316, 317L and OC-4 does not differ significantly from that of Mo-free alloys. In a recent study (Sun et al., 2018), the Ni-Mo-

Cr alloys exhibited better corrosion resistance than the Ni-W-Cr alloy. The corrosion resistance can be increased with an increase of Mo and a decrease of Cr. The authors (Sun et al., 2018) claimed the elements Mo and W show different ability in restricting the outward diffusion of Cr, Mo can diffuse from the alloy to surface in Mo-containing alloys and be then segregated around the viods as a form of Mo-rich phase, restricting the outward diffusion of Cr from the alloy base due to the nobility of Mo element, shown in Figure 2-29. While it is difficult for W to diffuse and segregate around the voids due to the large atom size of W.

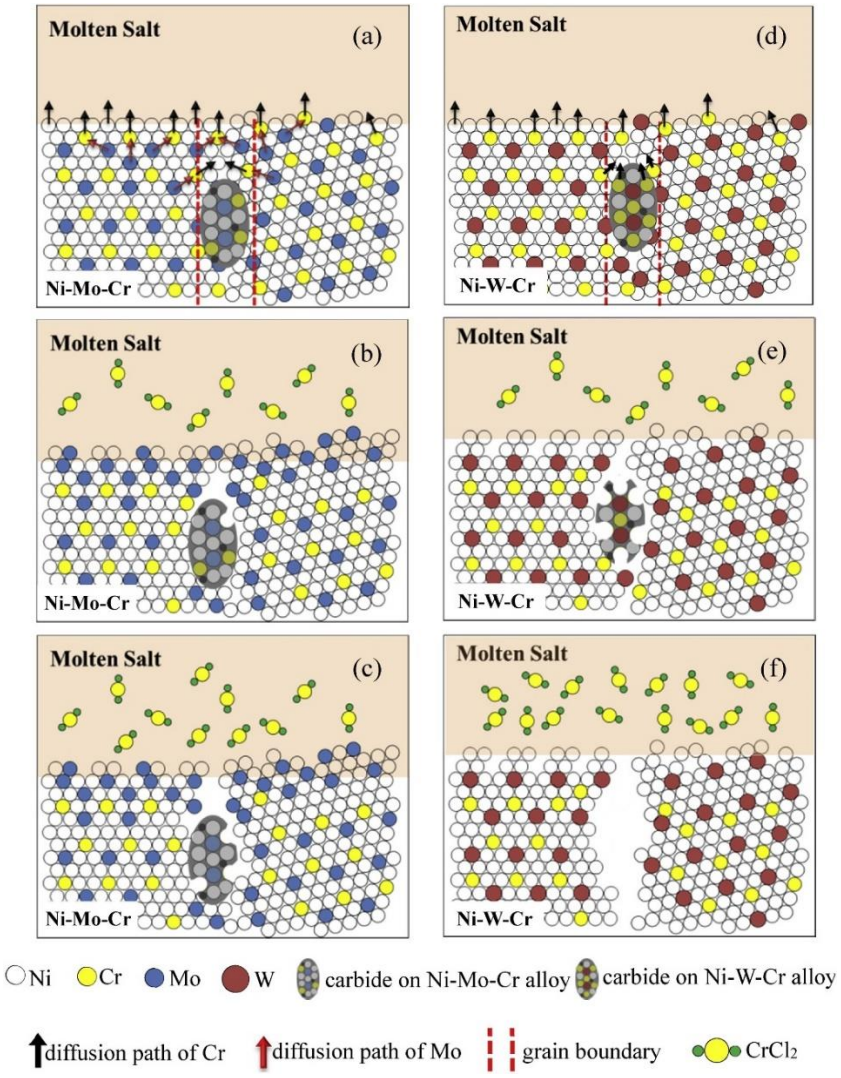

Figure 2-29. Schematic of corrosion of the Ni-based alloys in molten NaCl-KCl-$MgCl_2$ under Ar gas: (a,d) the early stage of corrosion; (b,e) the later stage; (c,f) observed situation (Sun et al., 2018)

Fabre et al. (Fabre et al., 2013) applied linear voltammetry to investigate the several pure metals in the LiF-NaF salts at 900 °C, and observed that oxidation potentials of metals can be classified in increasing order: Cr < Fe <Co < Ni < Mo < W, which is in good agreement with the Gibbs energies order.

2.9 Summary the gap between literature and the novelty of this study

To bridge the gap as stated above, we systematically investigated the corrosion mechanism in different thermal profiles compared to isothermal ones including: the corrosion products evolution, the corrosion rate controlling steps and the corrosion degree under the different gas covering in this study. I simulated the real thermal profile in the CSP plants where the temperature change with the alternation of day and night like thermal cycling and thermal shock. Also new characterization method has been raised to identify the corrosion products, the formation, different protectiveness, and spallation behaviour by analysing the nanomechanical properties of them and calculating the inner thermal stress between multi-layers and substrate material. Further I investigated the formation Gibbs free energy of the crushing products to better understand formation mechanism of these oxide at initial oxidation stage.

Chapter 3. Experimental methods and characterization methodology

This chapter is divided into five main sections; the first sections describe the material and salt used in the study, the general samples and salt preparation. The next section of this chapter introduces the electrochemical assessment of corrosivity of the salts dissolved in water: this was done in reference to typical 3.5 wt. % NaCl solution. The third section describes the test set up for sensitization experiments, including designs for test sample and solution, details of experiment conditions and procedures. The fourth section introduce the immersion corrosion test setup, including the static test, post-test analysis and the descaled method for gravimetric analysis. The final section describes the post-experiment surface analysis techniques used in this work.

3.1 Sample and salt preparation

3.1.1 Sample description with micrograph and microstructural features

The material used in this research study are two kinds of austenitic stainless steels and Ni-based alloys are investigated in this study, AISI 321, AISI 347, Inconel 625 and Incoloy 825 (or SS 321, SS 347, IN 625 and IN 825), and their compositions are showing in the Table 3-1.

Table 3-1. Elemental compositions of stainless steel and Ni-based alloys tested (wt. %)

Alloy	N	C	Mn	Si	P	Cu	Cr	Ni	Ti	Nb	Mo	Fe
AISI 316L	0.05	0.02	1.50	0.60	0.03	-	17.5	10.2	-	-	2.0	Bal.
AISI 321	0.08	0.018	1.44	0.519	0.035	-	17.33	9.24	0.225	-	-	Bal.
AISI 347	0.02	0.049	0.95	0.402	0.026	0.11	17.35	9.65	-	0.656	-	Bal.
IN 625	-	0.018	0.04	0.142	0.001	0.03	21.69	62.36	0.211	3.31	8.65	3.06
IN 825	0.15	0.008	0.67	0.258	0.012	1.75	22.6	40.18	0.943	0.025	2.88	30.32

Before the test, the microstructure of material needs to be checked to better understand its significant effect on its mechanical properties and corrosion behaviours. The samples were shaped into discs with dimension of 10mm x 10mm, thickness of 4mm. The samples were grounded and prepared no more than 30 minutes prior to microstructure observation.

According to the standard ISO 4969:2015, the etchant for stainless steels is HCl: HNO_3: H_2O=1:1:1 in vol % and the etchant for Ni-based alloy is nitrohydrochloric acid (HCl:HNO_3=3:1 vol %), the procedure is to immerse the samples into the etchant for 15-30

seconds at room temperature and wash the samples with distilled water, or swab the etchant on the surface of samples for 1-3 minutes (depends on the reaction on the surface of sample).

Figure 3-1 shows the optical images of SS321 and SS347, containing an austenitic field with equiaxed grains. Austenite is characterised with high toughness and ductility, but low strength. The grain size is about 50 μm +/- 4 μm and the annealing twins can be observed with red arrows. The austenitic stainless steel show high ductility by Twining Induced Plasticity. Annealing twins, along with deformation twins during tensile process, can divide up austenite matrix and lead to Hall-Petch reaction to strengthen material by refining grain. From Figure 3-1, a smaller grain size has been observed.

To have a better understanding of the microstructure of stainless steels, SEM-EDX observation was conducted. SEM-EDX profile of SS 321 are shown in Figure 3-2, there are some precipitations along the grain boundary, which is demonstrated to be TiN by element analysis of Spectrum 2. The addition of Ti is to incorporate strong carbide/nitride former to avoid the depletion of chromium. SEM-EDX profile of SS347 are shown in Figure 3-3, the element is distributed homogenously. According to spectrum 2 in Figure 3-3, some precipitations can be observed along the grain boundaries (red arrows) which is demonstrated to be NbC. The microstructure of SS 321 and SS 347 was consisted with coarse carbon/nitrides precipitation of titanium and niobium, as well as a higher content of δ-ferrite and γ-austenite.

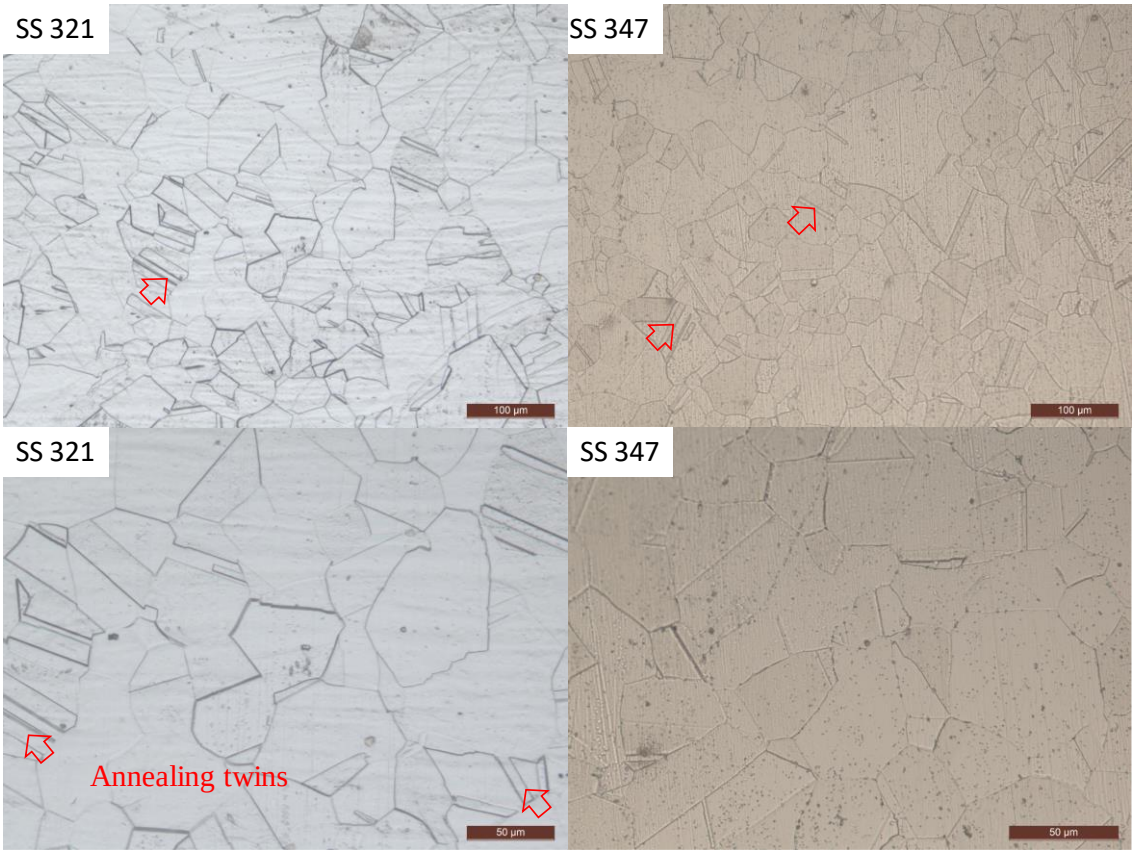

Figure 3-1. The microstructure of SS321 and SS347

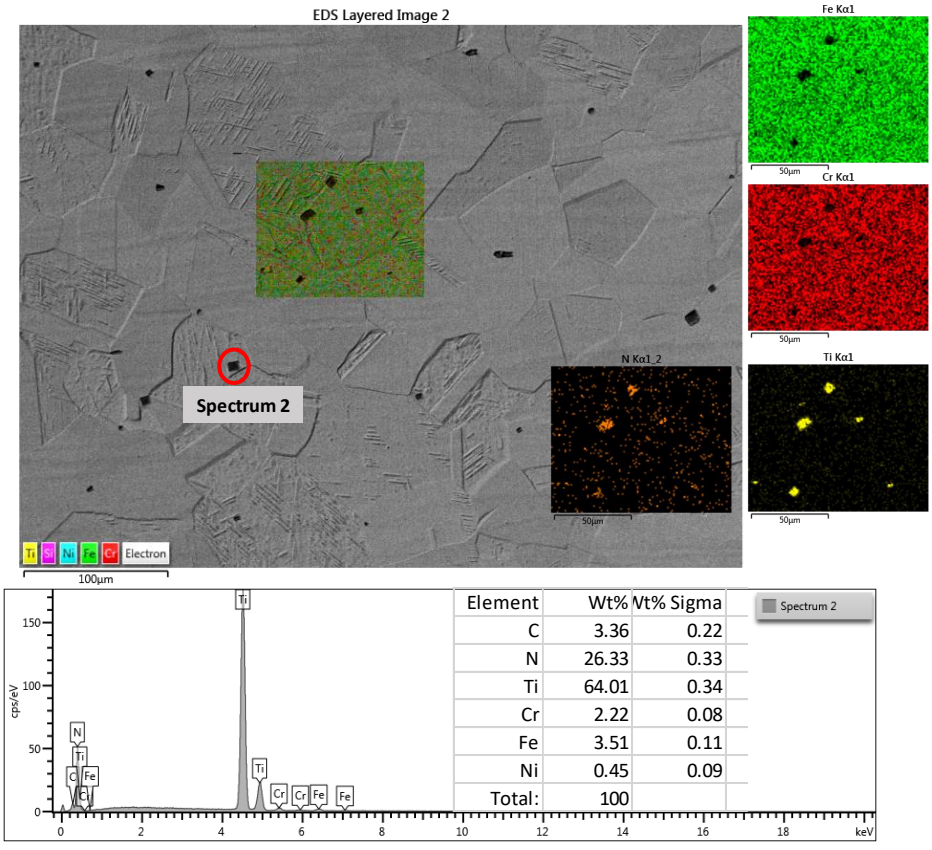

Figure 3-2. SEM-EDX profile of as-received SS 321

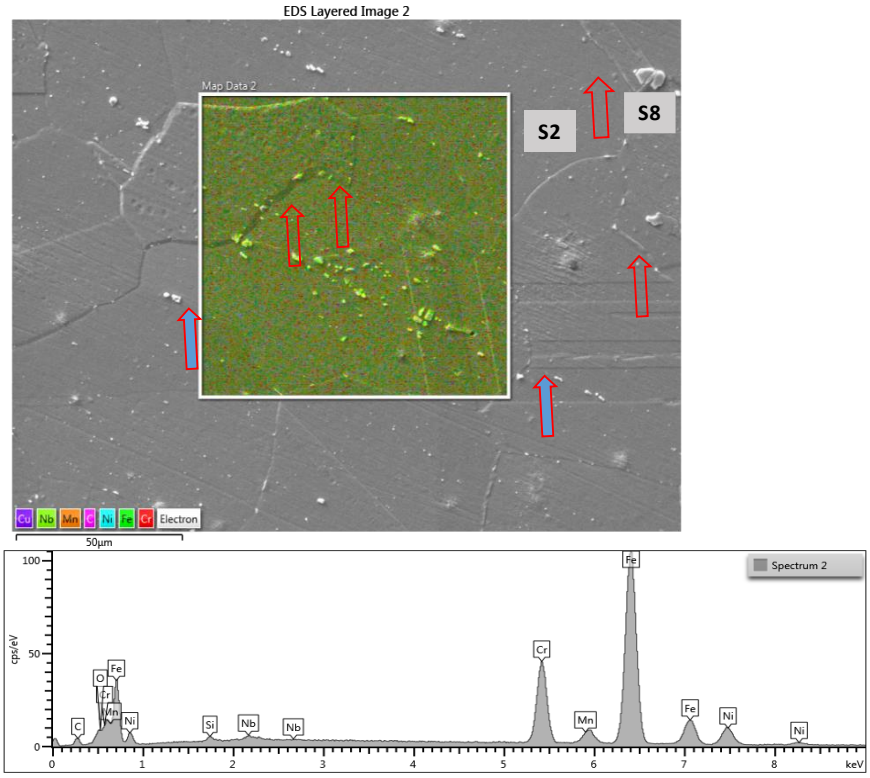

Figure 3-3. SEM-EDX profile of as-received SS347

Figure 3-4 shows the microstructure of IN 625 and IN 825 at different magnification under optical microscope. From the Figure 3-4, the IN 625 and IN 825 indicated different equiaxed grains and their growth had no fixed direction. The average grain size of IN 625 and IN 825 are 50 µm +/- 3 µm and 45 µm +/- 4 µm, respectively. They are both the Fe and Ni solution strengthening nickel alloys and many annealing twins are clearly seen in some grains. This type of twins are frequently encountered in metal and alloys with face centred cubic structures. When analysed under a microscope, annealing twins are characterised by straight lines extending across a grain boundaries (Gunen and Kanca, 2017).

The specimens were annealed at 1200°C for 30 min followed by water quenching to room temperature to obtain a fine homogeneous γ phase with carbides solute in the matrix (Li et al., 2011). The micrograph shows primary carbides in IN 625, especially precipitated at grain boundary (GB); Carbides include MC, $M_{23}C_6$ and M_6C type where M denotes metals like Ti, Nb, and Mo. IN625 is a prominent alloy of solid solution strengthening (compared with precipitation hardening). Both Cr and Mo partition preferentially to the γ phase where they reduce the matrix solubility for the precipitation strengthening elements like Ti, Al and Nb. Though the alloy was designed mainly as solid solution strengthened, the presence of alloying elements like Nb, Mo, Ti assists in generating either precipitate or carbides and

contribute in strengthening (Sukumaran et al., 2017). The precipitation was also observed along the grain boundary of IN 825, which was demonstrated as TiN.

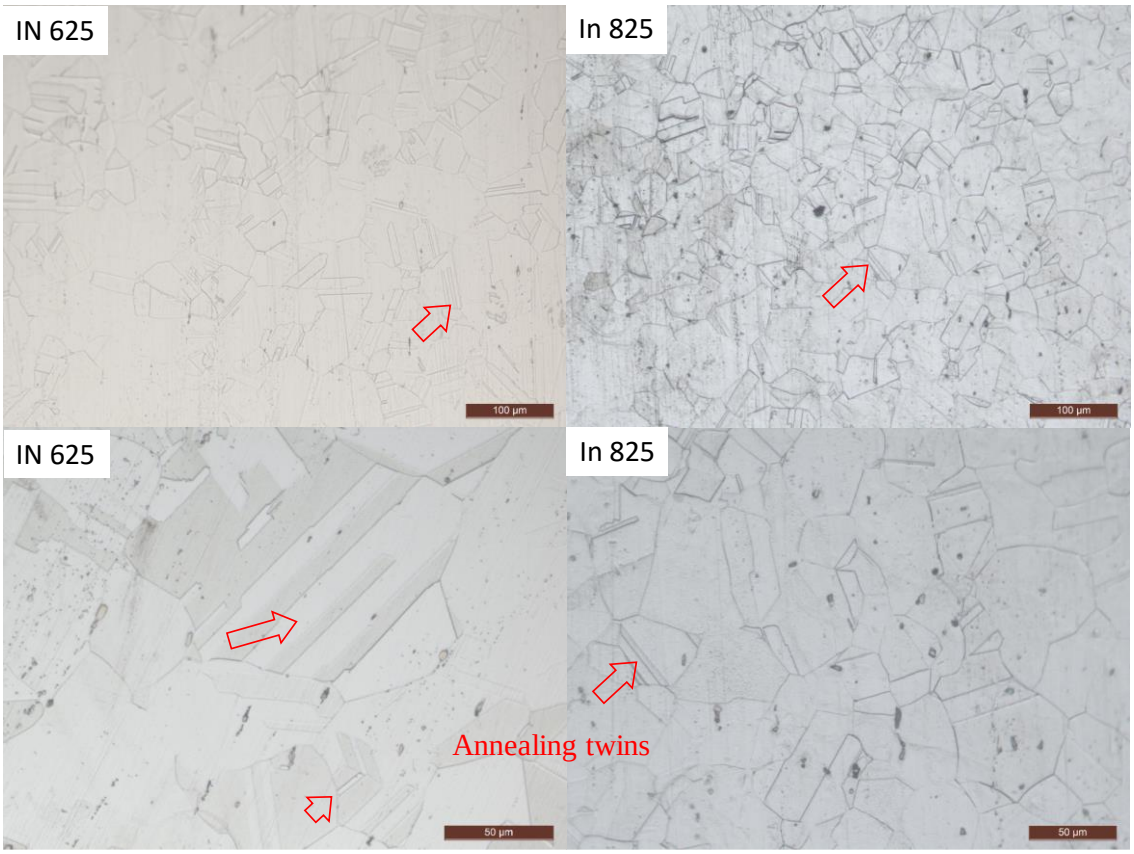

Figure 3-4. The microstructure of IN 625 and IN 825

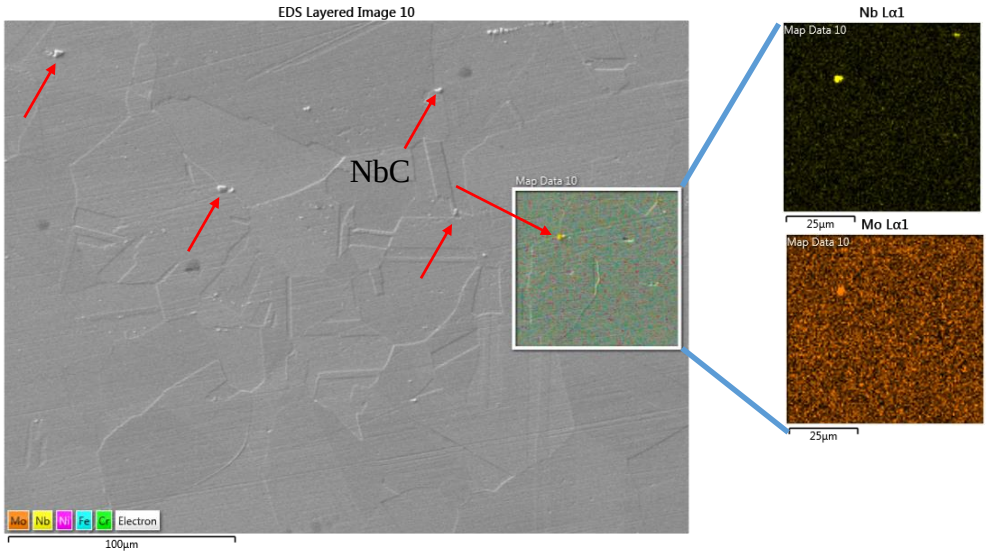

Figure 3-5. SEM-EDX profile of IN 625

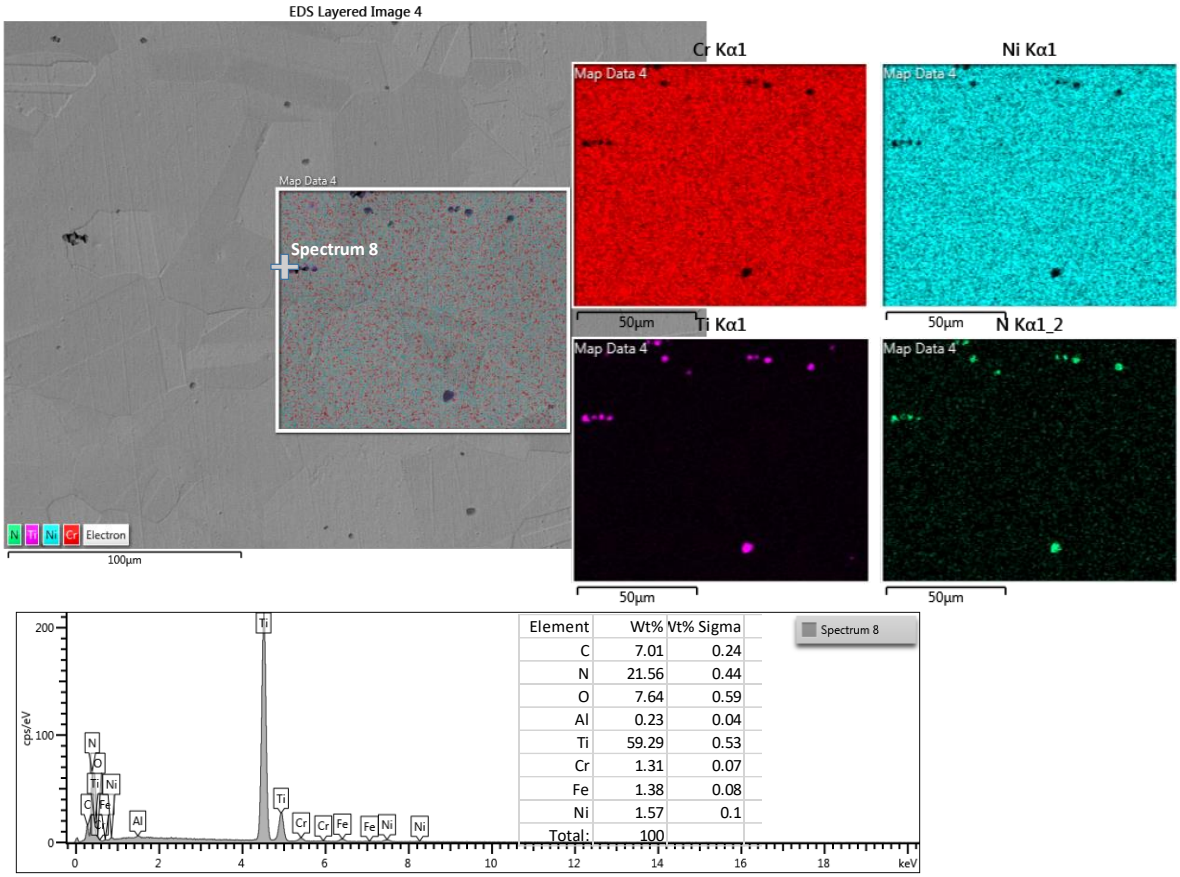

Figure 3-6. SEM-EDX profile of IN 825

3.1.2 Salt chemistry and properties

Thermal and physical properties of some selected molten salts used as HTF was summarised in Table 2-2 (Walczak et al., 2018). Some molten salts mixtures, based on nitrates and nitrites, have been commercially implemented. The Solar salt is widely used for its high thermal stability, consisting of 60% $NaNO_3$ and 40% KNO_3. And Hitec is a ternary mixture of 53% KNO_3, 40% $NaNO_2$ and 7% $NaNO_3$, characterised by lower melting point and lower thermal stability than the Solar Salt.

Other molten salts mixture based on nitrate, carbonates and chlorides have also been given consideration and their compatibility is still under study due to technical and economic implications such as corrosion issues of involved materials (e.g., carbon and low-alloy steels, stainless steels and Ni-based alloys) (Walczak et al., 2018). In this study, Solar salt (60 wt.% $NaNO_3$ and 40 wt.% KNO_3) was selected for this study and was purchased from Alfa Aesar with analytical reagent purity (99.5% KNO_3 and 99.5% $NaNO_3$), and the components and purities of the salt were provided in Table 3-2. The salts were weighed to achieve the required ratio, homogeneously mixed and dried at 120 °C for 24 h in a furnace before the experiments. The amount of corrosive molten salt in each crucible are required

to be at least 20ml per 1cm^2 of samples' area according to British Standard ISO 17245:2015. The solar salt density at 565°C was 1.72 g/cm^3, which is obtained by extrapolating data from literature (Wei et al., 2020). After referring to the surface area, the amount of solar salt for each crucible is 413g (248g $NaNO_3$ and 165g KNO_3).

Table 3-2. Main component contents and purity of the test salt (wt%), from supplier data.

Components	KNO_3	$NaNO_3$
Main component, %	99.5%	99.5%
Insoluble, %	0.002	0.002
IO_3^-, %	<0.0005	<0.0005
SO_4^{2-}, %	0.003	0.003
NO_2^-, %	<0.001	<0.001
Ca, %	0.004	0.005
Mg, %	0.002	0.002

3.2 Electrochemistry assessment of corrosivity of salt using cyclic potentiodynamic polarization technique in brine of solar salt mixture

Three types of salt solution have been selected to investigate the corrosivity and corrosion behaviour of the materials above. The salt solutions are 3.5 and 5 wt. % NaCl, Hitec salt (7%$NaNO_3$+53%KNO_3+40%$NaNO_2$) and solar salt (60%$NaNO_3$+40%KNO_3). While the sample preparation process involves cutting samples, soldering wire to back of samples, mounting into resin, grounding, and polishing following with cleaning. The stainless steels and Ni-based alloys are cut to a dimension of 10mm x 10mm x 4mm with an exposed area of 1 cm2. Conductive wires (Cu wire) are soldered to the back of samples to make sure good electricity conductivity before embedding in resin. The sample preparation for CPDP was performed by encapsulating the samples in epoxy resin. The encapsulated samples were progressively polished using up to a 1200-grit SiC abrasive paper followed by 6-μm, 0.5-μm diamond suspension. The polished surface of samples was rinsed with distilled water and dried with compressed air before putting it into the test solution. The sample was well-embedded in resin as shown in Figure 3-7.

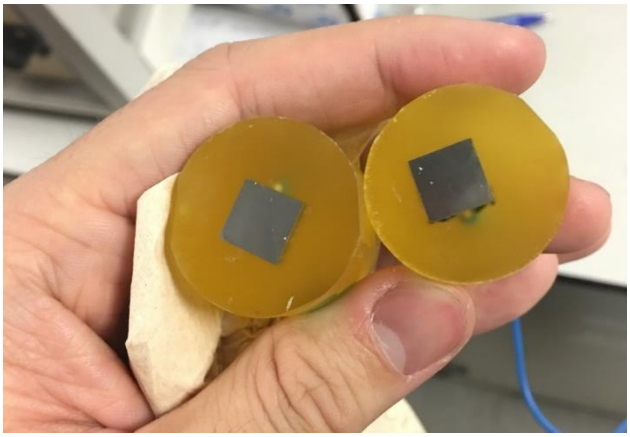

Figure 3-7. Schematic of already prepared test samples used for sour corrosion experiments.

The cyclic potentio-dynamic polarization was used in this study to record the electrochemical responses. The three-electrode cell was used to measure the OCP and corrosion current density (Icorr). The three-electrode cell used in this work contained an Ag/AgCl reference electrode with 0.1M Cl^- and a platinum counter electrode. The E_{corr} and I_{corr} were used to evaluate the aggressiveness of the brines and determine the corrosion rate of the test samples. Cyclic potentio-dynamic polarization was performed on freshly polishing samples in separate conditions after reaching a stable OCP and corrosion current. The test start from -100mV from OCP and scan anodically to 5mA/cm^2 and reverse scan. The test was carried out at 25 and 80 ˚C and the scan rate was chosen 25 mV/min. Other tests are also to be conducted to investigate the corrosion rate as function of the concentration of solar salt. The experiment protocol is shown in Table 3-3.

Table 3-3. The salt solutions for cyclic potentio-dynamic polarization test

Solution	Concentration	T (˚C)	Scan rate
NaCl	3.5 and 5 wt. %	25 and 80	25 mV/min
Solar	3.5 and 5 wt. %	25 and 80	25 mV/min
Hitec	3.5 and 5 wt. %	25 and 80	25 mV/min

The electrochemical test such as polarization and electrochemical impedance spectroscopy (EIS) can provide information of corrosion rate and corrosion processes helping to identify the cathodic and anodic reactions in the special test conditions (Walczak et al., 2018). Electrochemical polarization analyses the metal/electrolyte interface by measuring electric current generated by an externally applied potential. The corrosion potential and corrosion

current can be obtained from potentiodynamic polarization curves and corrosion rate can be calculated employing the principle of proportionality between charge and mass according to:

$$\mathbf{CR}=\frac{\boldsymbol{Icorr}\cdot\boldsymbol{K}}{\boldsymbol{A}\,\boldsymbol{\rho}\,\sum(\frac{\boldsymbol{fi}\cdot\boldsymbol{ni}}{\boldsymbol{MWi}})}=\boldsymbol{K}\frac{\boldsymbol{icorr}}{\boldsymbol{\rho}}\boldsymbol{EW} \qquad \text{Equation 14}$$

Where CR is corrosion rate, mm/year, ρ is alloy density, the alloy density of SS321, SS347, IN625 and IN 825 is 7.94, 8.03, 8.14 and 8.14 g/cm^3, respectively. K is constant 3.27*10-3, mm g/μA cm yr. I_{corr} is corrosion current (μA/cm^2), f_i is weight fraction of elezment i, n_i is number of electrons being transferred in i, i is 2, 3 and 2 for Fe, Cr and Ni respectively in this study. MW_i is atomic weight of i. The alloy equivalent weight, EW, is considered dimensionless in these calculations. The EW of SS 321, SS347, IN 625 and IN 825 is 25.13, 25.29, 25.89 and 25.52 respectively. The detailed information about how K was derived was shown in appendix file.

3.3 Sensitization experiment and electrochemical characterization methods

As we describe before, intergranular corrosion is a form of localised corrosion which starts from the surface and develops inwards along the grain boundary to reduce cohesive stress, causing strength loss of material. It is linked with the segregation of impurities and/or depletion of one of the alloying elements along the grain boundaries (GBs). This is known as sensitisation and often used in reference to austenitic stainless steels and Ni-based alloys when operating in temperature range between 482 and 815 °C (Liu et al., 2021a). So there was a need for a simple laboratory test to rapidly identify potentially deleterious thermal effect on stainless steel and alloys. Here we list 2 methods to detect the degree of sensitization.

According to the ASTM A262-15, the oxalic acid etch test can be used for acceptance of austenitic stainless-steel material but not for rejection of material. This test is used in connection with other evaluation tests to provide a quick method for identifying qualitatively those specimens that are certain to be free of susceptibility to rapid intergranular attack in those tests. The preparation of etching solution is following. Dissolve 100 g of reagent grade oxalic acid crystals ($H_2C_2O_4.2H_2O$) in 900mL of reagent water. Stir until all crystals are dissolved. Then etch the polished specimen at 1 A/cm^2 for 1.5 min. Examine the etched surface on a metallurgical microscope at 250x for steels. The etched surfaces, shown in Figure 3-8 (International, 2015a), would be classified into three types including (a) step structure in which there is not any ditches at the grain boundaries, (b) dual structure in which

there are some steps and ditches at the grain boundaries but none of the grains are completely surrounded by the ditches; and (c) ditch structure in which at least, one of the grains is completely surrounded by the ditches.

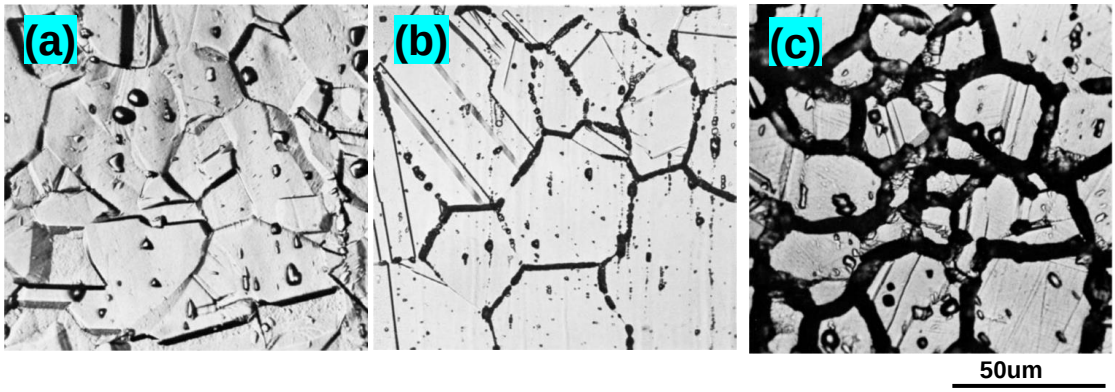

Figure 3-8. Classification of sensitised microstructure according to ASTM A262: (a) step structure: with no ditches at grain boundaries; (b)“dual” structure, with some ditches at grain boundaries; (c) “ditch” structure, with one or more grains completely surrounded by ditches. 500X Magnification

Another effective method to evaluate the degree of sensitization is electrochemical potentiokinetic reactivation measurement using the double loop method (DLEPR), according to BS EN ISO 12732. The specimen is immersed in an acid solution such that it is in the active state under freely corroding conditions, but then anodically polarised into passive domain. As surface features are dissolved during initial immersion under active corrosion conditions, the likelihood of surface preparation having an impact diminishes. From the passive state, the specimen is polarised at a controlled scan rate in the cathodic direction. A schematic illustration is shown in Figure 3-9 (Aydoğdu and Aydinol, 2006).

In the double loop test, specimen is first polarised anodically through the active region then the reactivation scan in the reverse direction is carried out. When it is polarised anodically at a given rate from the corrosion potential to a potential in the passive area, this polarization leads to the formation of a passive layer on the whole surface. Then when scanning direction is reversed and the potential is decreased at the same rate to the corrosion potential, it leads to the breakdown of the passive film on chromium depleted areas (Aydoğdu and Aydinol, 2006). During decreasing the potential, the protective passive film over chromium-depleted areas is more easily dissolved than that over undepleted (non-sensitised) surfaces. The electrochemical potentiokinetic reactivation (EPR) test is based on the assumption that only

sensitised grain boundaries become active, while grain bodies are unsensitised (Aydoğdu and Aydinol, 2006).

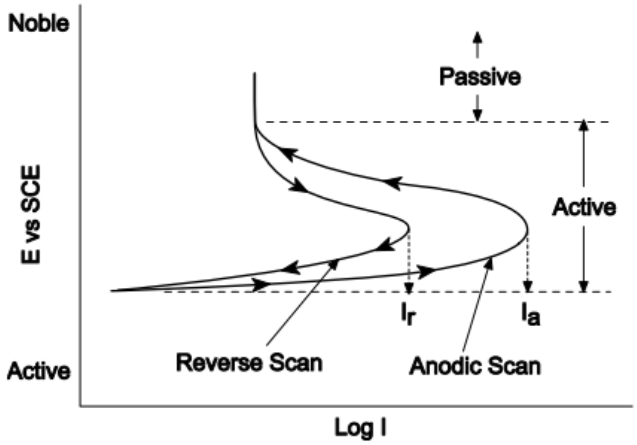

Figure 3-9. Diagram for the procedures of double loop EPR test method (Aydoğdu and Aydinol, 2006)

In Figure 3-9 two loops are generated, an anodic loop and a reactivation loop. A ratio of maximum current generated in the double loop test (Ir:Ia) is used as a measure for the degree of sensitization. As for the determination of the optimum condition of the test, Aydogdu (Aydoğdu and Aydinol, 2006) has determined the optimum DLEPR test conditions to be electrolyte of composition of 0.5M sulphuric acid and 0.01M potassium thiocyanate (used as an activator) at a scan rate of 1.667mV/s, and other researchers obey this standard (Morshed-Behbahani et al., 2018). It is worthy noted that there was an increase not only in intergranular corrosion but also in general corrosion when lower scan rate is used (Aydoğdu and Aydinol, 2006).

Prior to the DL-EPR test, the test samples were grounded with SiC paper up to 2000 grit, polished with 9 μm, 6 μm, 1 μm and 0.25 μm diamond suspension and then degreasing with acetone before experiments. According to the literature (Padilha et al., 2003), the as-received materials were each solution heat treated at 1150°C for 0.5 h to dissolve all the potential NbC(N)/TiC(N), as the time-temperature phase transformation diagram shown in Figure 3-10. Followed by water quenching to get homogenised austenite field and destroy the sensitivity to intergranular corrosion due to the carbides entering into solution (Gellings and De Jongh, 1967). The treated samples were held and aged for 2 h at temperatures 550, 650 and 750°C in air without molten salt and in air with molten salt to simulate the temperature conditions in current and future CSP plants. It should be worth noting that the temperature chosen in this study is based on the two key operational considerations. Firstly,

although the decomposition of nitrate salt (Bonk et al., 2020) limits its use above 560˚C, the temperature at receiver panels (mainly made of Ni-based alloy) can reach to 650 ˚C when all the mirrors are engaged in reflecting solar irradiation at noon in the real solar power plants. A slightly higher limits are also possible with solar salt to realise a higher CSP plant efficiency targets (Mehos et al., 2017). Secondly, scientists are considering higher operation temperature (650 to 750˚C) of CSP plants in future (Mehos et al., 2017) where hot tank, heat transfer pipes and receivers are made of Ni-based alloys in contact with other chloride and carbonate salts. The assessment of sensitization behaviours for Ni-based alloys or Stainless steels at higher temperature will provide theoretical basis and guidance for the characterisation and selection of the materials in the future.

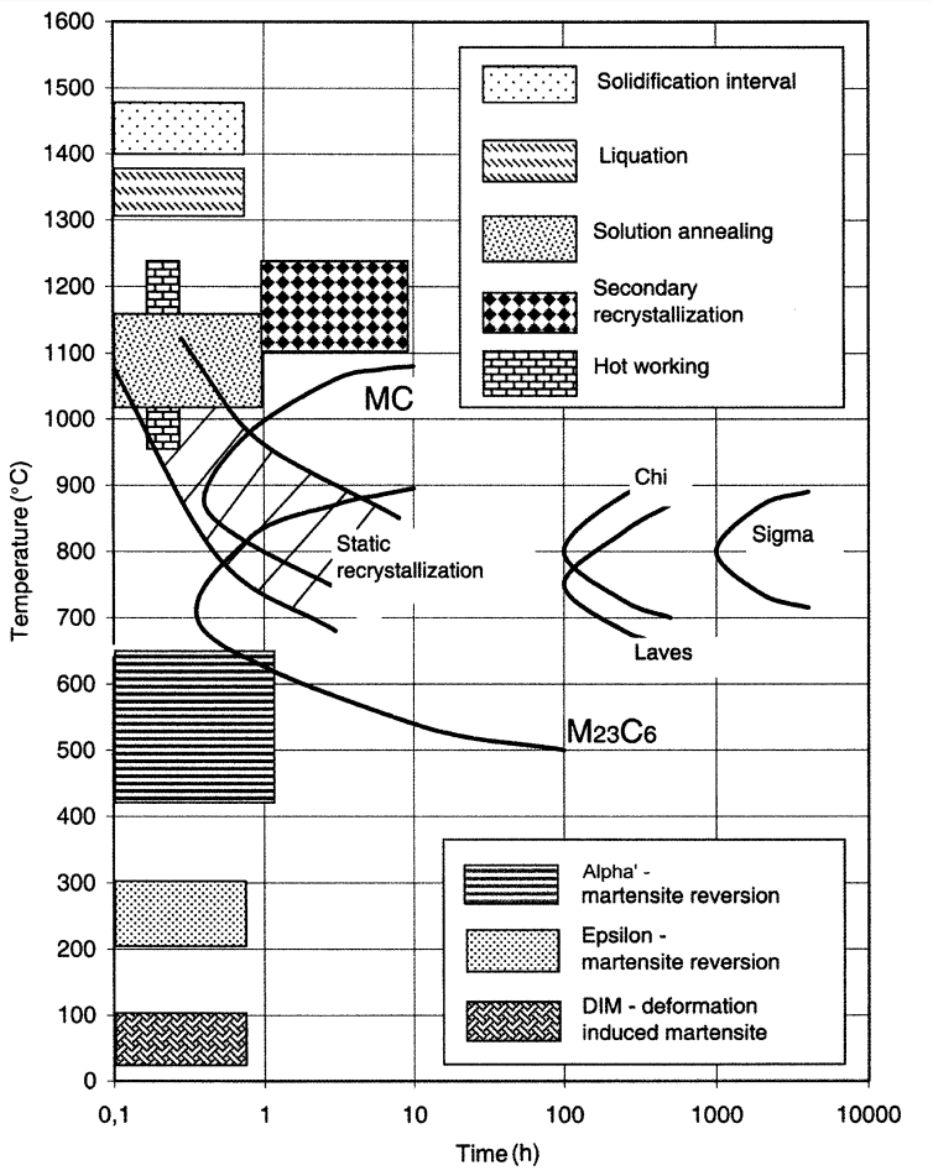

Figure 3-10. Main thermal treatments and transformations that occur in austenitic stainless steels between room temperature and the liquid state. (Padilha et al., 2003)

As shown below, the heat treatment methodology was shown in Table 3-4, the studied material was first solution treated at 1150°C for 0.5 hour followed by water quenching to get homogenised samples. After this, these samples have been subjected to aging treatment at 550-850°C for aging time from 0.5 to 24 hours. The exposure temperature for tests with molten salt were 550, 650 and 750°C, simulating the real operating conditions in various CSP plants.

Table 3-4. Time-temperature profile for sensitisation test

Materials	Heat treatment	Temperature (˚C)	holding time(h) Without salt	holding time(h) With molten salt
SS321 SS347 IN 825 IN 625	Solution and water quenching	1150	0.5	-
	After solution and quenching treated, sensitization	550	2	2
		650	2	2
		750	0.5	2
			1	
			2	
			4	
			8	
			12	
		850	2	
	As-received	-	-	

The oxalic acid etch test has used for classification of etch structures in austenitic stainless steels according to ASTM A262 (International, 2015a). This test can only be used for acceptance of wrought or cast austenitic stainless steel material but not for rejection of material (International, 2015a). Need to be used in conjunction with other evaluation test to provide a quick method identifying qualitatively whether a specimen is free of susceptibility to intergranular corrosion. 10% oxalic acid solution ($H_2C_2O_4.2H_2O$) was used to etch the polished specimen at 1 A/cm^2 for 1.5 min to see the microstructure changes. The

microstructures obtained were classified into three types: “step” structure with no ditches at grain boundaries; “dual” structure, with some ditches at grain boundaries; and, “ditch” structure, with one or more grains completely surrounded by ditches (Lima et al., 2005). Those specimens with “ditch” structure are more prone to IGC (Morshed-Behbahani et al., 2018). These classified microstructures are adapted from ASTM A-262 and shown in Figure 3-8 (International, 2015a).

DL-EPR tests were conducted in a three-electrode cell using a saturated calomel electrode (SCE) as reference electrode and platinum plate as counter electrode. The sample materials were embedded in epoxy resin and served as working electrode. The degree of sensitization (DOS) of the aged samples were investigated in a solution of mixture of 2 M sulfuric acid (H_2SO_4) and 0.05 M potassium thiocyanate (KSCN) at 30°C (Wu and Tsai, 2003). The specimen was polarised anodically into passive region at 100 mV/min after exposure at open circuit potential (OCP) for 5 minutes. Once the passivation potential (typically 0.3V SCE) is reached, the scan was reversed from forward scan to reverse scan (cathodic direction) back to OCP at the same rate. The schematic curve of DL-EPR was shown in Figure 3-9 .

The peak current for the reverse scan and forward scan is recorded and named as reactivation current density (i_r) and activation current density (i_a) respectively. The ratio of reactivation (i_r) and activation (i_a) current density is defined as the degree of sensitisation. This is presented in Equation 15. After DL-EPR test, visual evidence to characterise materials susceptibility to IGC is obtained. The schematic DL-EPR curves is shown in Figure S2 obtained from the BS EN ISO 12732:2008 standard.

$$DOS = (i_r/i_a) \times 100\% \qquad \text{Equation 15}$$

The correlation of anodic current and reactivation current with DOS is classified to three levels. DOS value less than 1% is an indication that material is ‘unsensitised’, 1%-5% means material is ‘slightly sensitised’ and higher than 5% indicates that material is ‘sensitised’(BS EN ISO 12732:2008 standard).

3.4 Immersion corrosion test setup

3.4.1 Test apparatus for static gravimetric corrosion assessment

According to BS ISO 17245:2015, crucibles shall be baked in air to remove volatile compounds before their first use. The recommended baking conditions are at least 24 h at a temperature of 1 000 °C. If water absorption is suspected to have occurred, used crucibles shall be dried at significantly above 100 °C. The amount of corrosive substance in each

crucible shall be at least 20 ml per 1 cm^2 of the surface area of a test piece. The corrosive substance shall be placed in a manner that the depth between the surface of the corrosive substance and the surface of the test piece will be at least 5 mm in the liquid phase. The volume shrinkage of the corrosive substance during melting shall be determined in a separate test using the same powder loading procedure as will be used in the corrosion test. The test pieces in their crucibles shall be placed in the furnace at room temperature, and heating shall be carried out in the test gas. The time to reach the test temperature shall be recorded.

Four samples of each alloy were placed horizontally in each Al_2O_3 crucible. The homogeneous salts were poured into each sample-containing crucible before being transferred into the furnace to dry under air/argon atmosphere for 12 h at 180 °C. Then start the heating procedure. Heating shall be carried out using as fast a heating rate as possible, up to the temperature of 30 °C below the liquids temperature of the corrosive substance. Further heating shall be conducted at a slower rate (e.g., 2 °C per minute) up to the temperature of 30 °C above the liquids temperature of the corrosive substance. A fast heating rate can then be used to achieve the test temperature. The test is defined to commence when the test piece temperature exceeds 97 % of the desired test temperature Tdwell. The test duration shall be relevant to the intended application and agreed upon between the parties concerned.

3.4.2 Post-experiment analysis

The test ends when the temperature of the test piece falls below 97 % of the desired test temperature. Depending on requirements, the test pieces can be cooled in the furnace, or they can be removed, and the corrosive liquid decanted from the crucible. All necessary health and safety requirements should be met when handling hot corrosive liquids.

3.4.3 Descaled method & Weight loss

After immersion test in molten salt, specimens extracted from each crucible were retrieved and cleaned in deionised water and acetone to remove the residual salt on the surface. Three parallel coupons were used for mass change test.

As described in ASTM G1-03 (G1-03, 2017) and international standard BS ISO 17245:2015, the coupons were descaled to remove the corrosion product using a standardised procedure of 20-min washing with 10% HNO_3 at 60°C for austenitic stainless steels (G1-03, 2017). Weight change before and after immersion test were calculated via Equation 16 and thus

corrosion rate was estimated by Equation 17, assuming the uniform corrosion occurred on the interface between salt and metal.

$$\frac{\Delta m}{S} = \frac{m_0 - m_1}{S} \qquad \text{Equation 16}$$

$$CR(\mu m/y) = \frac{87600\,\Delta m}{\rho\, S\, t} \qquad \text{Equation 17}$$

Where m_0 represents the initial weight and m_1 is the weight of specimen after corrosion. S the surface area (cm^2). Δm is descaled mass loss (mg). ρ is alloy density (g/cm^3): the density of AISI 321 and 347 are 7.94 and 8.03g/cm^3, respectively. t is the immersion time (h). Three parallel samples were used to determine the mass loss data to ensure accuracy.

3.5 Surface analysis techniques

The most important part of post-analysis was surface analysis where the morphology and composition of the corrosion products formed on the surface of test material with a combination of the surface analysis techniques, including X-Ray diffraction (XRD), Raman spectroscopy, scanning electron microscopy (SEM), Energy-dispersive X-ray spectroscopy (EDX) and NPFLEX (NPFlex 3D OPTICAL PROFILOMETER). Nano-indentation technique was also employed to investigate nano-mechanical properties across the corroding metal-oxide-molten salt interface. If there was no special statement, all the data obtained from these techniques was analysed by Origin Pro.

3.5.1 X-ray diffraction (XRD) technique for characterization of corrosion oxide layers

A Bruker D8 X-ray diffractometer was used for X-ray diffraction analysis of alloys to identify crystalline structure so can identify the corrosion product on the surface using monochromatic Cu Kα radiation (λ=1.5418 Å). XRD patterns were collected in the 2θ range from 10° to 90° using a step size of 0.033 per seconds and with a scan rate of 1.5°/min. The stainless steels and Ni-based alloy samples required no preparation beforehand and could simply be inserted onto a sample holder and then be analysed using the Bruker D8, shown in Figure 3-11. The XRD consists of an X-ray tube, an X-ray detector and a sample holder. The cathode X-ray tube generates X-rays which are then filtered, collimated and then directed towards the surface of the sample (Hofmeister et al., 2015a). The incident rays then interact with the surface and produces constructive interference as well as a diffracted ray when the conditions meet and satisfy Bragg's law which relates the electromagnetic wavelength to the diffraction angle and the lattice spacing. The diffracted rays are then

detected by the X-ray detector where they get counted. The further data was analysed by X'pert Highscore software provided by LEMAS.

$$n\lambda=2d\sin\theta \qquad \text{Equation 18}$$

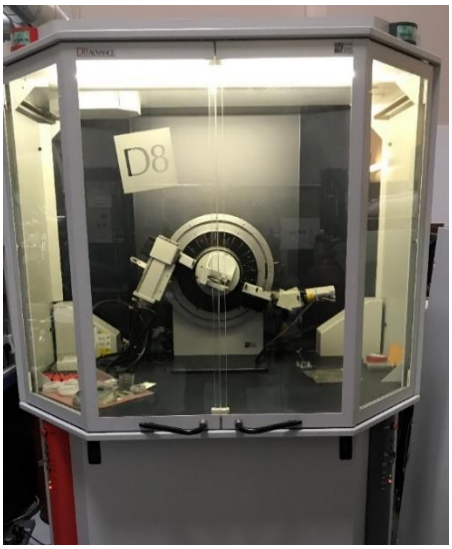

Figure 3-11. Bruker D8 Advance X-ray diffractometer (XRD) used in this study, LEMAS University of Leeds

3.5.2 Raman spectroscopy

Raman spectra was used in this study as a supplement and confirmation of the results obtained from XRD. For example, the FexOy can be identified by XRD but the overlapped peaks of FexOy should be confirmed by Raman spectra. Also some oxides formed on the Ni-based (Fe_2O_3-NiO, also as Fe_2NiO_4) only shows on the Raman spectra. The Renishaw InVia spectrometer (UK) was used in this study. 488 nm wavelength laser operates at a laser power of 0.1 and 0.5 mW respectively using 50x short distance objectives.(Hua, 2015).

3.5.3 Scanning electron microscope (SEM) technique for surface and subsurface characterisation of corrosion oxide layers.

The surface morphology and cross-sections analysis of samples were investigated using a Zeiss optical microscope (OM) (Axio Imager 2) and Carl Zeiss EVO MA15 scanning electron microscope (SEM). The SEM was integrated with an Oxford Instruments Aztec Energy dispersive X-ray (EDX) system with an 80mm X-max SDD detector which provided secondary and backscattered imaging, EDX elemental mapping and line scans. The incident beam voltage of 20 keV was employed and working distance of 8-9 mm. The picture of the SEM-EDX used in this study is shown in Figure 3-12.

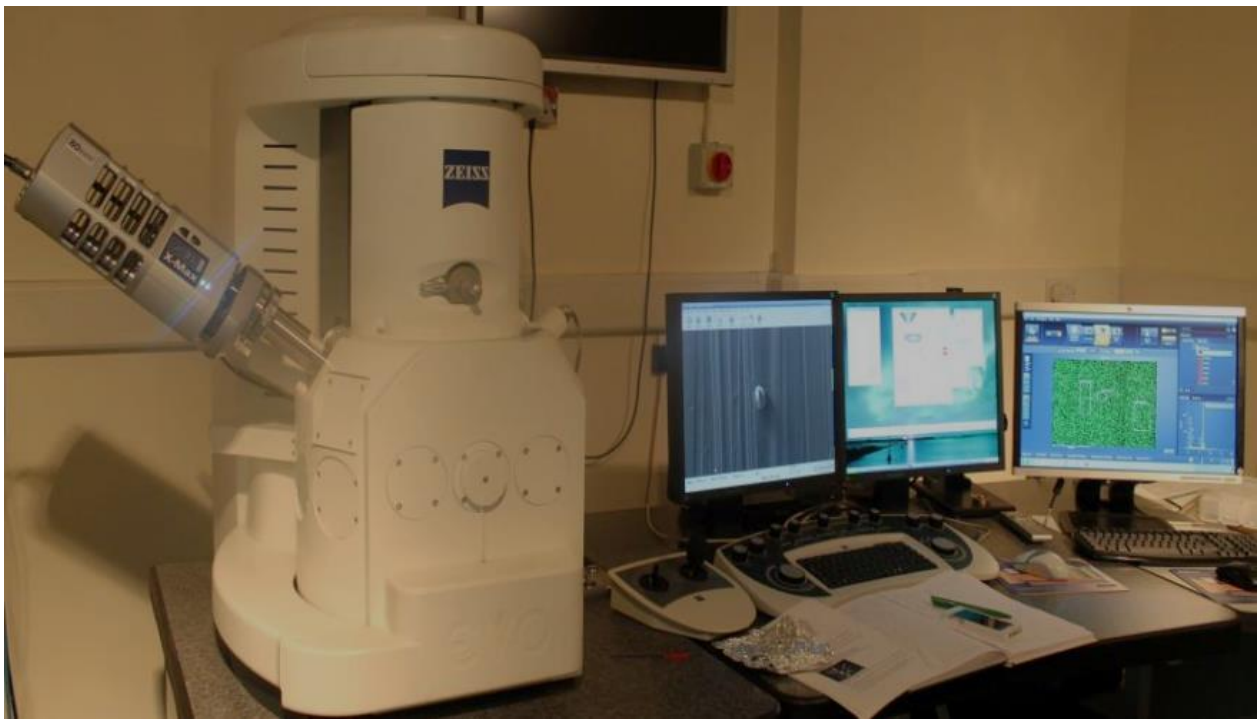

Figure 3-12. Scanning electron microscopy (SEM) with energy dispersive X-ray (EDX) analysis used in this study, LEMAS centre in University of Leeds.

3.5.4 NPFLEX 3D analysis for investigating pitting corrosion

From the previous study (Pessu, 2015a), the white light interferometry has been employed in the fields of surface profiling to measure the small surface irregularities and investigate the corrosion damages on corroded surfaces. The NPFLEX interferometer can divide a beam of white light into two beams and recombines and superimpose them to extract information about the original state of the source wave and to create interference patterns (Pessu, 2015a).

Contactless process for NPFLEX was based on use of white light interference and intuitive software to characterise surface texture, roughness, depths, and pits at angstrom-level accuracy. For example, the samples to be analysed should be firstly cleaned thoroughly by Clarke's solution (a combination of hydrochloric acid and inhibitors is one of the standard techniques used for removal of corrosion products from iron and steel) to remove contaminations on the surface to enable the pits can be accurately quantified. All the pits' profiles are analysed according to Standard ASTM G46-94, where regulates that every 10 deepest pits with the maximum depth should be used for characterizing pits damage of the selected area.

The picture of the Bruker NPFLEX 3D interferometer was shown in Figure 3-13.

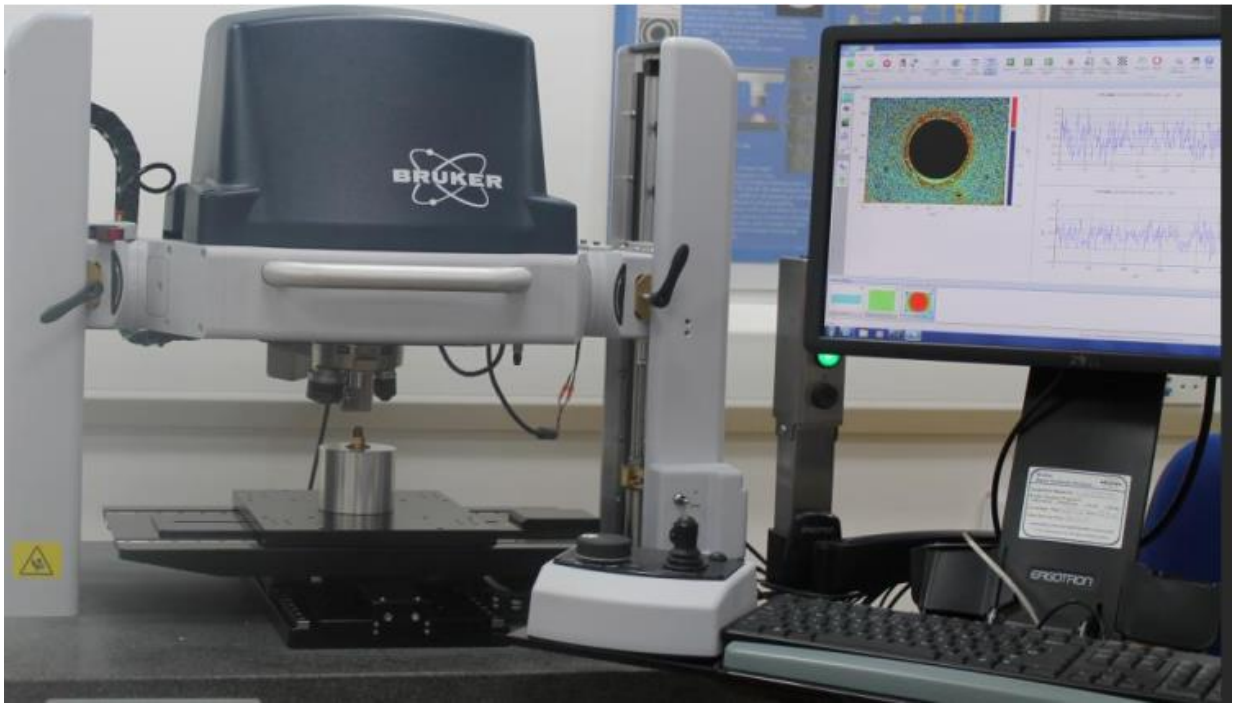

Figure 3-13. NPFLEX 3D interferometer used in this study, school of mechanical engineering in University of Leeds.

3.5.5 Nano-indentation technique for characterising the micro-mechanical properties of corrosion oxide layers

The Nano-mechanical properties of corrosion layers and base material were analysed after Nano-indentation test. The tests were performed using a Micromaterials Vantage platform equipped with a Berkovich tip. Indentations were made at selected points at 20mN maximum load. Loading and unloading were at fixed time of 15 seconds, with a dwell time of 5 sec to allow elastic relaxation of the materials before unloading. Hardness (H) and reduced modulus (E_r) were determined using the Oliver and Pharr method (Pharr and Oliver, 1992b). The Young's modulus of the material being measured can then be determined using following equation,

$$\frac{1}{E_r} = \frac{(1-v^2)}{E} + \frac{(1-v_i^2)}{E_i} \qquad \text{Equation 19}$$

Where E_r is the reduced modulus, v_i and E_i are the Poisson's ratio and modulus of the indenter tip respectively, and v and E are the Poisson's ratio and modulus of the sample. The diamond Berkovich indenter tip was assumed to have E_i=1141 GPa and v_i=0.07.

3.5.6 Subsurface Analysis Using a Focused Ion Beam (FIB) and Transmission Electron Microscope (TEM)

For TEM, thin lamellae of sample (<80 nm thick) were prepared via the in-situ lift-out method using a FEI Helios G4 CX DualBeam - High resolution monochromated, field emission gun, scanning electron microscope (FEGSEM) with precise Focused Ion Beam (FIB). Ion Beam deposited, Pt layer (1 µm) using the FIB (at 30 kV, 80 pA for the liquid Ga ion source). A bulk lamella was initially cut (by the FIB at 30 kV, 9.3 nA), before a final cut-out was performed (at 30 kV, 0.79 nA). In-situ liftout was then performed using the Easylift needle. The lamellae were attached, using Ion Beam Pt(at 30 kV, 80 pA), to a copper FIB lift-out grid (Omniprobe, USA) mounted within the SEM chamber (in-situ) and then stored under vacuum before TEM analysis. Thinning and polishing of the lamellae to electron translucency was performed with a final polish/clean with a gentle ion beam (5 kV, 41 pA).

TEM analysis was carried out on the FEI Titan Themis Cubed X-FEG operated at 300kV and fitted with a Monochromator, as shown in Figure 3-14. Bright field TEM images were collected using the Gatan OneView 16 Megapixel CMOS digital camera using Digital Micrograph (GMS3) software. The TEM is fitted with the Super-X EDX system with windowless 4-detector design. Elemental maps were collected at a probe current of 200 pA and a dwell time of 20 microseconds.

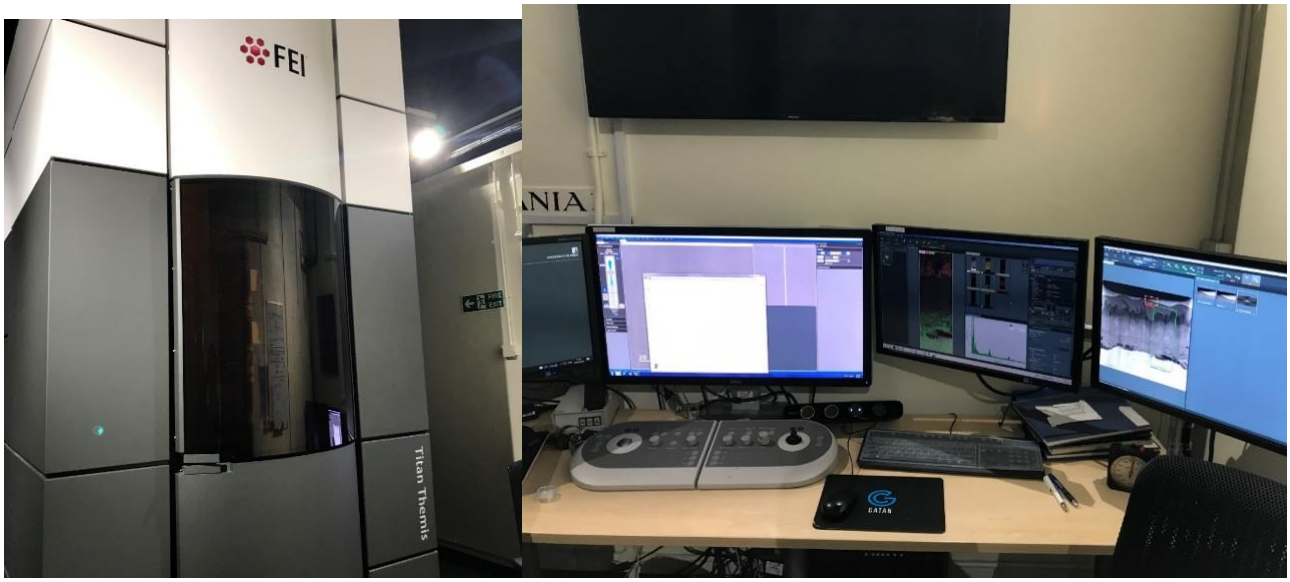

Figure 3-14. FEI Titan used in this study, School of Chemical and Processing Engineering in University of Leeds.

3.5.7 Summary

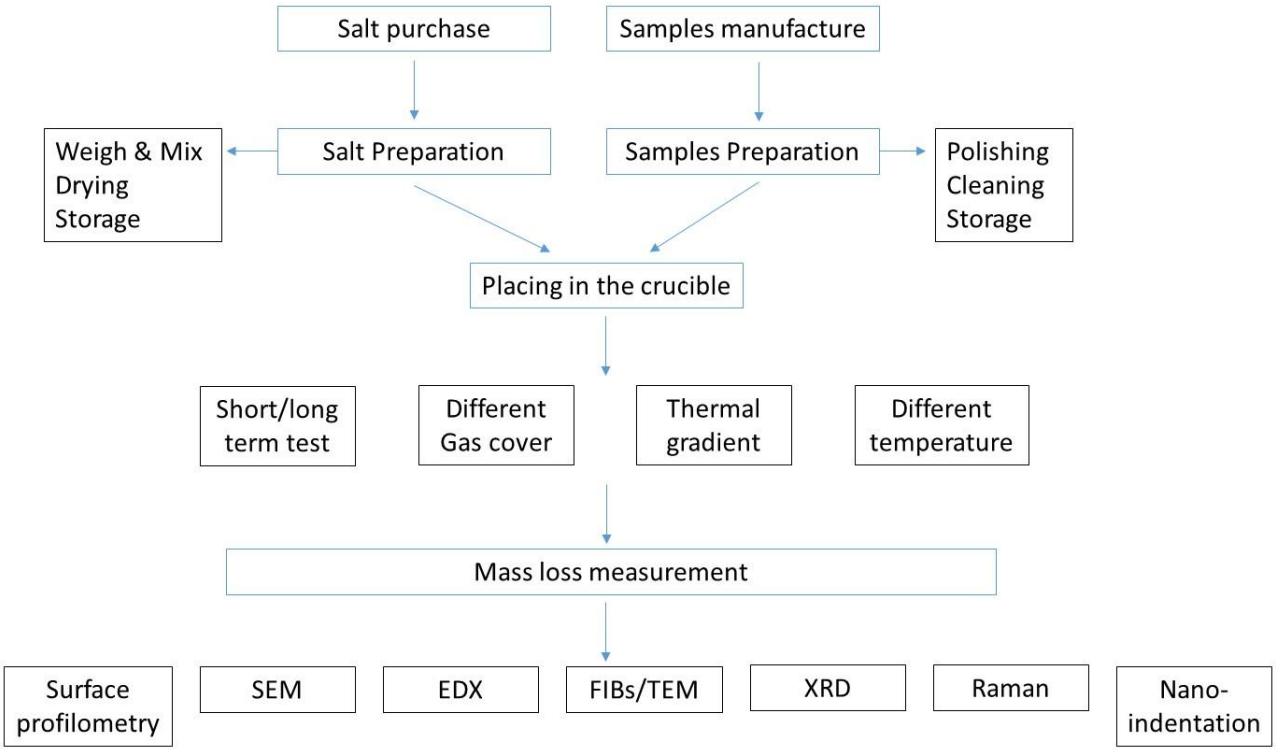

Figure 3-15. Procedures of experimental work outlined.

Chapter 4. Case Study of electrochemical polarization of stainless steels and Ni-based alloys in salt aqueous environments

4.1 Overview & Introduction

Molten salt corrosion at high temperature and molten salt-related material degradation has been well documented in solar and solar energy industry. However, the pitting corrosion and other localised corrosion in the salt solution has not been reported, which is common corrosion type occurring on the stainless steels. What remains a point of debate is a convincing link of the corrosiveness of the salt between salt solution and molten salt. While it is not comparable of the salt solution with molten salt, it is still essential to investigate the corrosion behaviour of focused alloys in the salt solution. This chapter includes three main sections; firstly, introduce the effect of the temperature and salt chemistry as critical environmental factors on the corrosion and pitting corrosion behaviours of stainless steels and Ni-based alloys in salt brines. The second part is to evaluate the effect of salt concentration on the corrosion behaviours by conducting the test in different salt concentration conditions.

Prior the molten salt corrosion, the preliminary test has been done to investigate the salt corrosivity in aqueous environment and also to have an initial knowledge on corrosion resistance of materials.

The corrosivity of salt or corrosion resistance of alloys will be characterised by measuring the corrosion potential and observing the corrosion surface (localised corrosion, pitting) after polarization. In this part, SS 321 samples are using to characterise its pits formed during electrochemical polarization test. As one of the localised form of corrosion attack, pitting takes place in relatively rapid penetration at small area (Yi et al., 2013). The reason why pits are observed in NaCl solution is that chloride ions break down the passivity and prevent the formation of passive layer in stainless steels or Ni-based alloys (Yi et al., 2013). Cheng studied that the role of Cl^- in metastable pitting and pointed out that Cl^- is to increase the breakdown chance of the passive film rather than inhibited the surface repassivation (Cheng et al., 1999).The evaluation of the pitting susceptibility are using the critical pitting potential, Epit, which is defined as a potential above the rapid current increase on CPDP curves and accompanied with random pits formation (Yi et al., 2013). The pits formed above the Epit are defined as stable pits and continue to grow, while the metastable pits are the initiation and repassivation of micropits without stable growth (Moayed and Newman, 2006). The Epit has been determined by different electrochemical techniques such as potentiodynamic

polarization in this study. The process was called passive region between E_{corr} and Epit, and during this process, the occurrence of small current fluctuation are the result of metastable pit nucleation, growth and repassivation (Tang et al., 2014). In this study, the pitting corrosion in chloride and nitrate salt solution exhibited significant differences due to the nature of pitting promotion of chloride and pitting-inhibiting of nitrate.

The method used in electrochemical test include Electrochemical Impedance spectroscopy and Cyclic Potentio-dynamic Polarization (CPDP) test. The CPDP test is widely used to determine resistance to localised corrosion and degradation rate in a short time. Thus this technique is applicable as a method for the prediction of localised corrosion also beneficial for alloys that are passivized spontaneously and underwent localised corrosion.

4.2 Temperature-induced corrosion for stainless steels and Ni-based alloys in salt solution

As shown in Table 3-3, the test was conducted under different temperature and different salt solution and different salt concentration. To start with, the effect of temperature on the polarization test was investigated in 3.5 wt% salt solution at 25 and 80°C, the CPDP curves of the samples in salt as shown in Figure 4-1 and Figure 4-2 respectively.

As shown in Figure 4-1 and Table 4-1, the corrosion rates of all alloys in NaCl are normally higher than these in Solar salt and Hitec salt, while the corrosion potential of four material are lowest in NaCl among three salt solutions. It means that the corrosion reactions are most likely occurring in NaCl with the highest corrosion rate. It can be concluded that the NaCl shows the severer corrosivity than solar salt and Hitec salt at 25°C. Similarly, as shown in Figure 4-2 and Table 4-2 for the result tested at 80°C, same conclusion can be drawing that the corrosion potential of four alloys are lowest with higher corrosion current density, indicating the corrosion is most like occurring in NaCl with the highest corrosion rate.

Figure 4-1 (a) and Figure 4-2 (a) shows the CPDP curves of SS 321 in NaCl, Solar salt and Hitec salt at 25 and 80°C respectively. The corrosion potential (E_{corr}) of SS 321 in NaCl, Solar salt, and Hitec are -246, -89.3 and -166 mV with corrosion current density (Icorr) are 0.268, 0.039 and 0.472 μA/cm^2 at 25°C. Lower carrion rate exhibited higher corrosivity in NaCl with the aggressive ions Cl. Meantime, the corrosion potential (E_{corr}) in NaCl, Solar salt, and Hitec are -439, -337 and -33.8 mV with corrosion current density (Icorr) are 0.81, 0.38 and 0.043 μA/cm^2 at 80°C. The corrosion potential in NaCl is lowest, and corrosion current density is highest, which means the corrosion is most likely occurring in NaCl and the corrosion rate is the highest. In Hitec, SS 321 exhibited best corrosion resistance with

the highest corrosion potential and lowest corrosion current density. For SS321 at 25 and 80°C, 1.5 pits/mm^2 and 2.3 pits/mm^2 were observed on the samples after test in NaCl due to the breakdown of oxide film and occurrence of pitting corrosion in the presence of aggressive ions, Cl^-, as shown in Figure 4-3. It's worth noted that the deepest depth of the pits is relatively close, about 160 μm. It can be inferred that the temperature plays an important role on the formation of pits during pit corrosion. No pitting was observed on the sample after test in in solar salt and Hitec salt due to the formation of stable passive film over the electrode potential of O_2 evolution without aggressive ions.

Figure 4-1 (b) and Figure 4-2 (b) show the CPDP curves of SS 347 in NaCl, Solar salt and Hitec salt at 25 and 80°C respectively. The E_{corr} of SS347 in NaCl, Solar salt, and Hitec are -382.9, -364 and -298 mV, with I_{corr} are 0.39, 0.12 and 0.13 μA/cm^2 at 25°C. The E_{corr} exhibited small fluctuation from -298 to -382.9 mV, still lowest E_{corr} and highest I_{corr} in NaCl among these salt solutions. For SS 347 at 80°C, the E_{corr} of SS 347 at 80°C are -459.1, -277 and -132mV and I_{corr} are 1.78, 0.16 and 0.079 respectively. Still, the corrosion is most likely occurring in NaCl and the corrosion rate is the highest. In Hitec salt, SS 347 showed the best corrosion resistance with highest corrosion potential and lowest corrosion current density than that in other two salt solution. Pits were observed on the sample after test in NaCl. No pitting was observed on the sample in Solar Salt and Hitec salt due to the absence of aggressive ions.

As the Ni-based alloys are known as corrosion resistant alloys, the analysis of salt brine focus on temperature at 80°C. For IN625, the corrosion potential is lowest in NaCl, while highest in Hitec. The corrosion current density in NaCl is one order of magnitude higher than that in solar salt and Hitec. There is no pitting in any salt solution. For IN 825, the corrosion potential is lowest in NaCl, while highest in Hitec. Notably, the corrosion current density in NaCl is much lower than that of other steels in NaCl; the corrosion current density of IN 825 in NaCl, Solar salt and Hitec keep stable at a same order of magnitude.

According to Figure 4-4, the effect of temperature on the corrosion rate is bigger for stainless steels than in Ni-based alloy. The corrosion rate of stainless steels in NaCl exhibited a significant growth with the increase of temperature from 25°C to 80°C. The corrosion rate of stainless steels is much higher than that of Ni-based alloys at 25 and 80°C. The Ni-based alloys show better corrosion resistance than stainless steels due to the addition of more alloy element like: Cr, Mo and Cu.

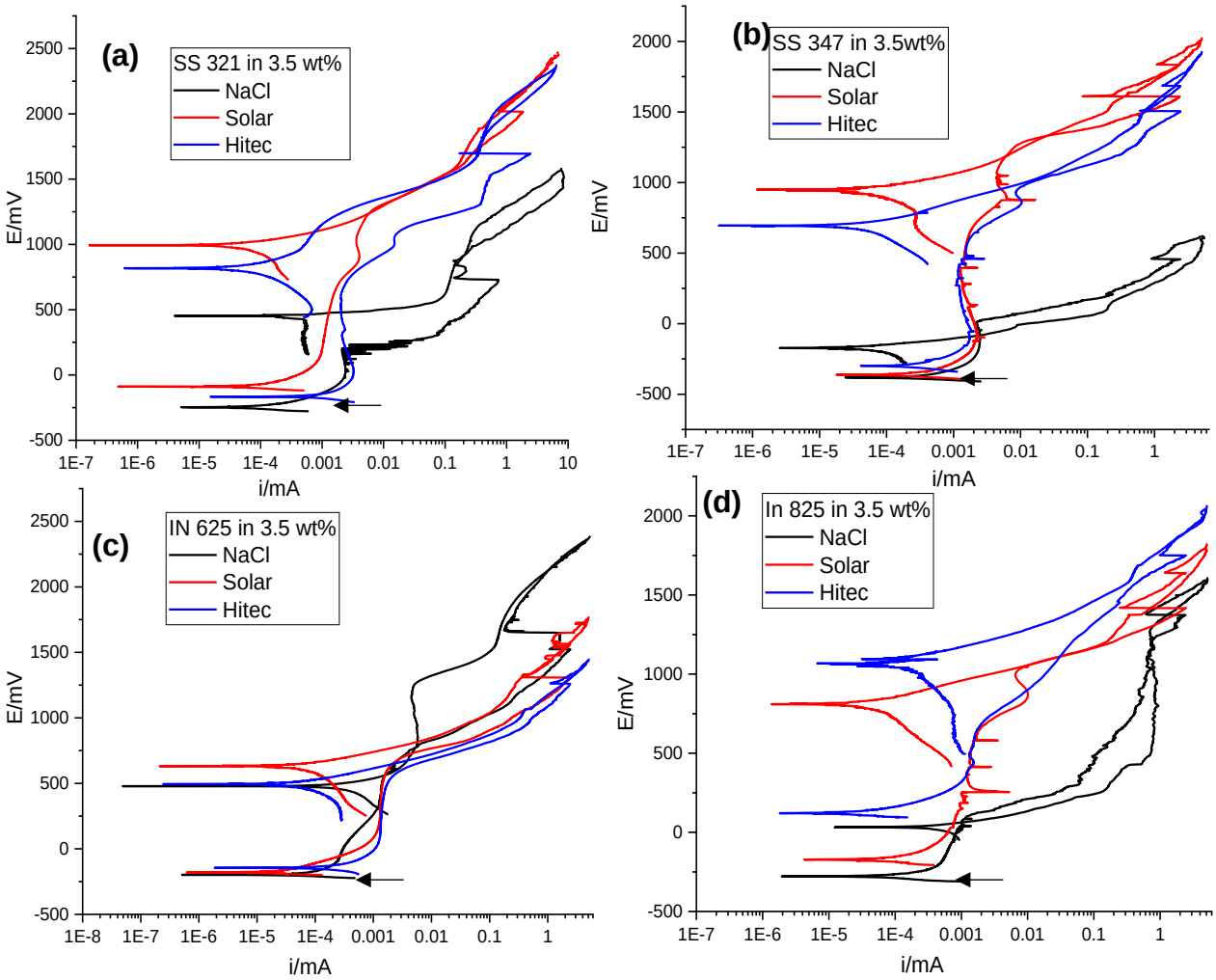

Figure 4-1. The CPDP curves of (a) SS321, (b) SS347, (c) IN625 and (d) IN 825 in 3.5 wt. % NaCl, Solar salt and Hitec salt at 25°C (the curve start from the arrow at the bottom of each image)

From the curve in Figure 4-1 and Figure 4-2, it's difficult to obtain the data from these figures directly. The Tafel approach was applied to get these values by extending the linear polarization area range from +50 mV OCP and -50 mV OCP. The intersection of the extended lines with OCP was set as I_{CORR}. The relatively low value of corrosion density is difficult to measure (10-20 nA/cm^2 for example), so the uncertainty was added in these tables to make the values more accurate.

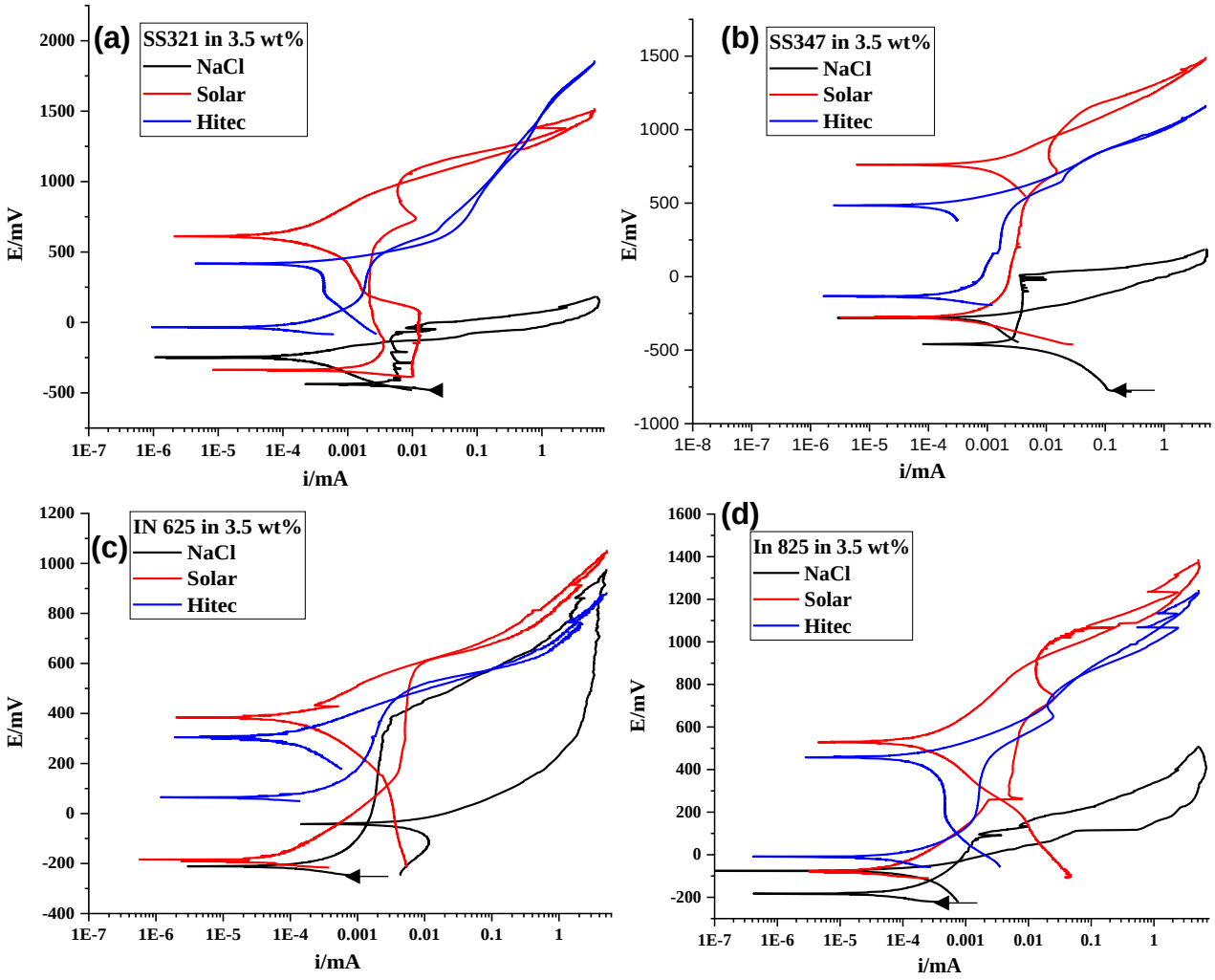

Figure 4-2. The CPDP curves of (a) SS321, (b) SS347, (c) IN625 and (d) IN 825 in 3.5 wt. % NaCl, Solar salt and Hitec salt at 80°C (the curve start from the black arrow at the bottom of each image)

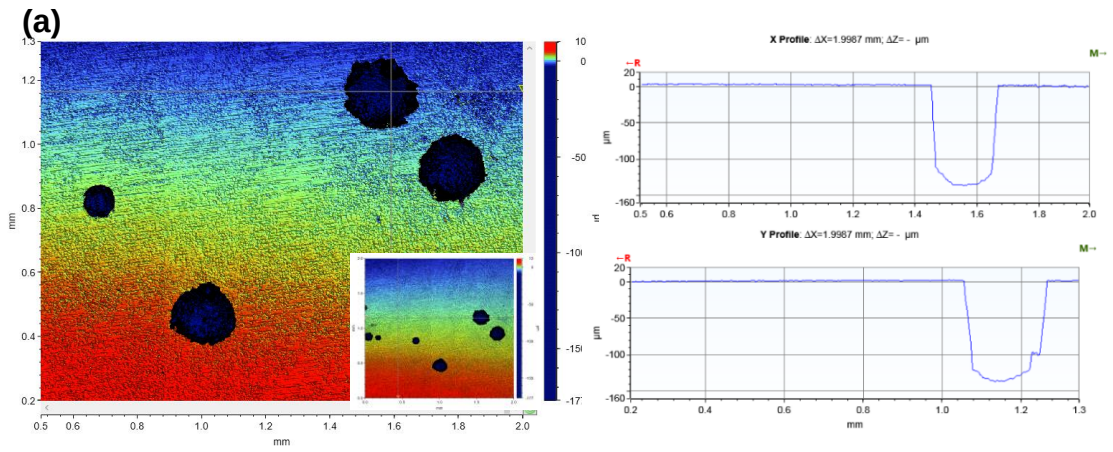

(Figure 4-3 to be continued)

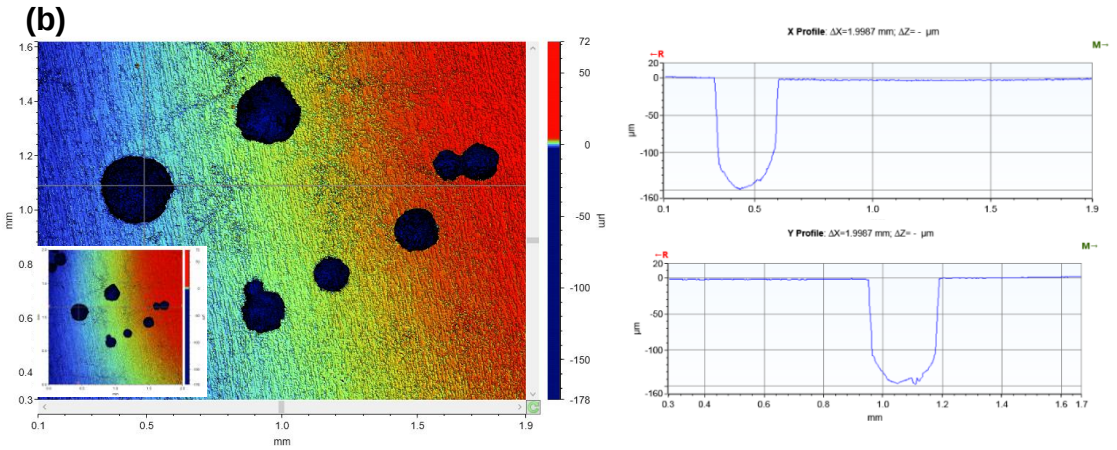

Figure 4-3. 2D images of deepest pit (relative to corroded surface) on SS 321 after CPDP test in 3.5 wt.% NaCl at (a) 25°C; (b) 80°C

Table 4-1. Corrosion potential/current density and corrosion rate of 4 materials from CPDP tests at 25°C

25°C	E_{corr}: mV	Icorr: $\mu A/cm^2$	Corrosion rate: µm/yr	Epit: mV	Erep: mV
SS 321 NaCl	-246	0.268	2.77	260	850
SS 321 solar	-89.3	0.04±0.01	0.403	1250	-
SS 321 Hitec	-166	0.472	4.88	1151	-
SS 347 NaCl	-382.9	0.39	4.02	30.8	-85.2
SS 347 solar	-364	0.12	1.24	1303	-
SS 347 Hitec	-298	0.13	1.34	1014	-
IN 625 NaCl	-198	0.04 ± 0.02	0.416	812.2	-
IN 625 solar	-179	0.01 ± 0.005	0.114	788.7	-
IN 625 Hitec	-144.7	0.07 ± 0.02	0.728	708.3	-
IN 825 NaCl	-277.2	0.072 ± 0.02	0.738	121	58
IN 825 solar	-172.3	0.052	0.533	1094	1175
IN 825 Hitec	122	0.021 ± 0.01	0.215	702	-

Table 4-2. Corrosion potential/current density and corrosion rate of 4 materials from CPDP tests at 80°C

80°C	E corr mV	I corr μA/cm^2	Corrosion rate μm/yr	E pit mV	E rep mV
SS 321 NaCl	-439	0.81	8.38	-1.19	-135.5
SS 321 solar	-337	0.38	3.93	1050	980
SS 321 Hitec	-33.8	0.043±0.01	0.445	510	500
SS 347 NaCl	-459.1	1.78	18.33	15.2	-237
SS 347 solar	-277	0.16	1.65	1150	960
SS 347 Hitec	-132	0.079	0.81	751	770
IN 625 NaCl	-211.1	0.154	1.60	383.8	-37.5
IN 625 solar	-184.2	0.032	0.333	615	-
IN 625 Hitec	64.8	0.079	0.822	550	-
IN 825 NaCl	-182.7	0.04±0.01	0.41	113	-33
IN 825 Solar	-79.5	0.02 ±0.01	0.21	1100	915
IN 825 Hitec	-9.4	0.04±0.01	0.41	800	-

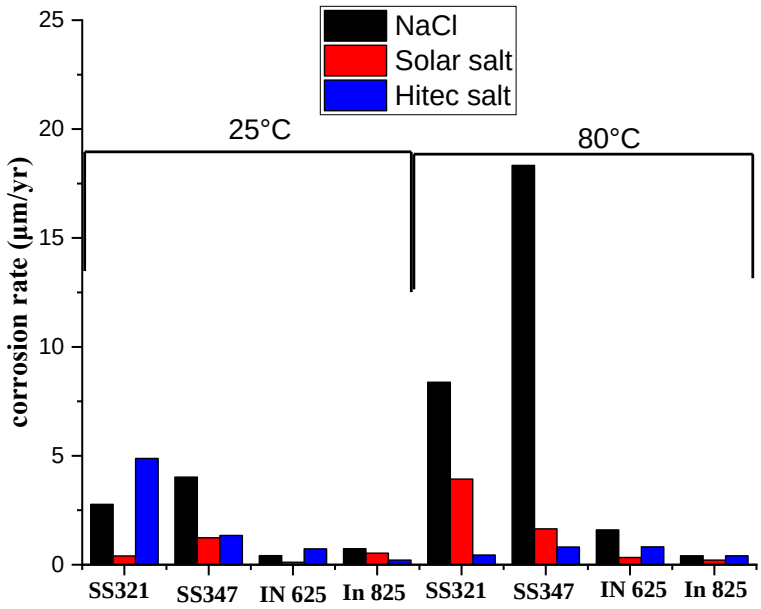

Figure 4-4. The comparison of corrosion rate for 4 materials at 25 and 80°C

4.2.1 Evaluation in NaCl salt

Except the comparison of salt corrosivity, the corrosion resistance of alloys needs to be confirmed. The results shown above has been replotted by comparing different alloys in the same salt conditions. These results are the same as those presented in the previous section and only presented in another way to clearly show how the different corrosion behaviour of focused alloys exhibit in three independent salt solutions. Figure 4-5, Figure 4-6 and Figure 4-7 show the CPDP curves of four material at 25 and 80°C in NaCl, Solar salt and Hitec salt respectively.

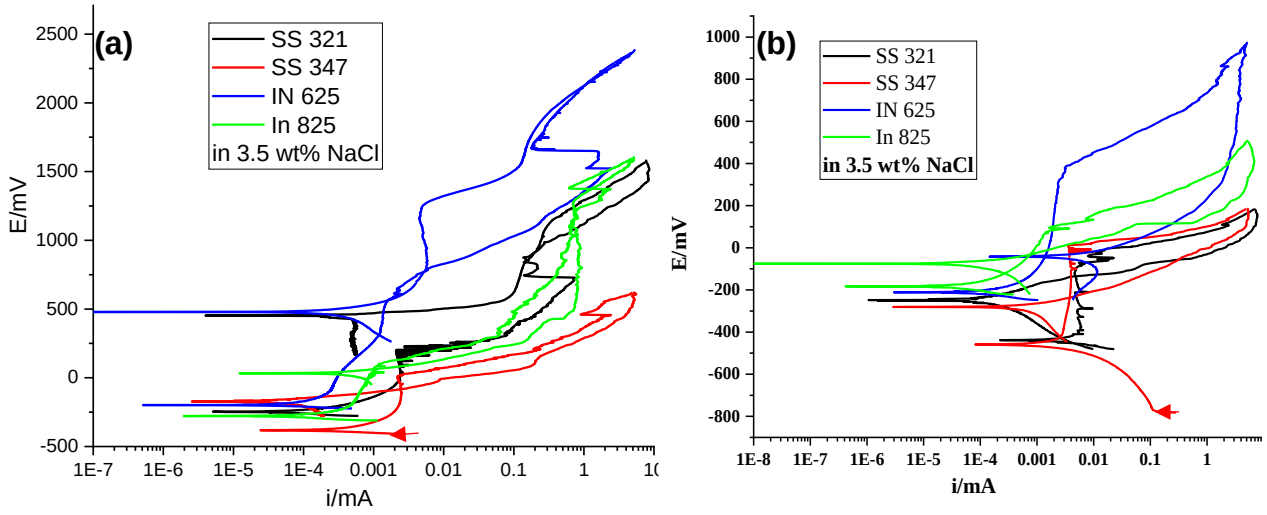

Figure 4-5. The CPDP curves of SS321, SS347, IN625 and IN 825 in 3.5 wt. % NaCl at (a) 25 °C and (b) 80 °C

As shown in Figure 4-5 (b) at 80°C, SS347 showed lowest corrosion potential, the corrosion potential of SS321 is close to that of SS347 in NaCl. IN 825 showed highest corrosion potential. SS 347 showed the highest corrosion current density in NaCl, and SS 321 ranked second, one order of magnitude higher than that of IN 625 and 2 orders of magnitude higher than that of IN 825 in NaCl. SS347 showed the worst corrosion resistance in 3.5 wt.% NaCl with lowest corrosion potential and highest corrosion current; the corrosion behavior of SS 321 is a bit better than SS 347. Notably, the corrosion current in NaCl is much lower than that of other steels in NaCl; IN 825 showed the best corrosion performance in 3.5 wt.% NaCl, then IN625.

4.2.2 Evaluation in Solar salt

As shown in Figure 4-6 (b), the CPDP curves in Solar salt show different shape with that in NaCl. The forward curve is mostly overlaid with the reverse scanning curve and the small difference of current density at higher potential. The corrosion potential of SS 321 exhibited

the lowest corrosion potential but highest corrosion current, which means the severest corrosion is believed to occur on the surface of SS 321. The result is a little different from the results in NaCl where SS 347 has been identified as the most vulnerable to corrosion. The corrosion resistance result of Ni-based alloys shows good agreement with that in NaCl, IN 825 shows best corrosion resistance with highest corrosion potential and lowest corrosion current density. It's noteworthy that solar samples show current spikes right in the passive region indicates the inhibitor nature of nitrate salt to prevent the occurrence of pitting corrosion.

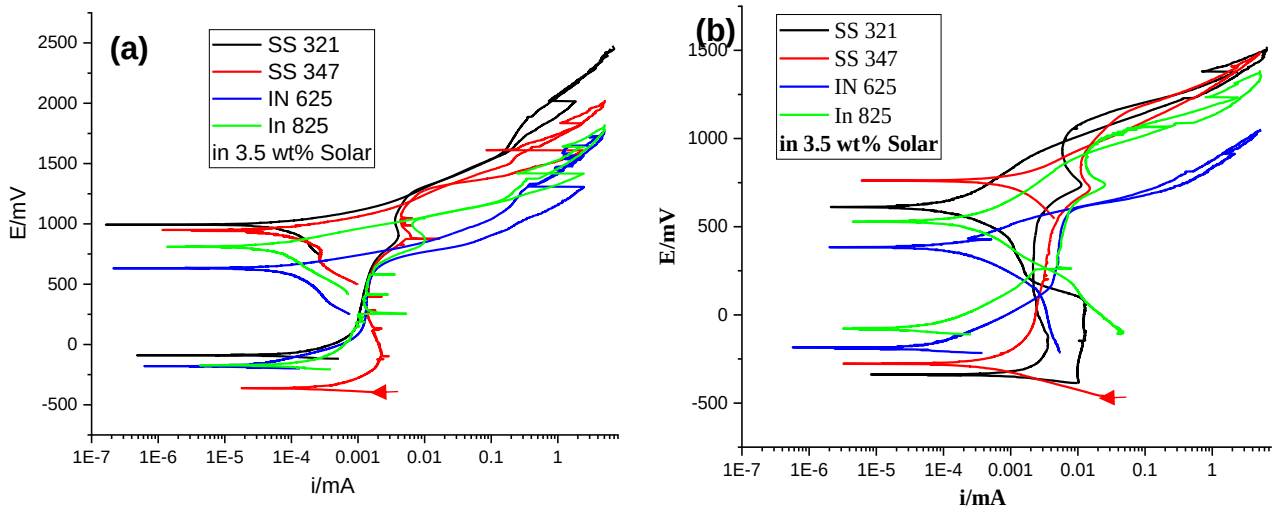

Figure 4-6. CPDP curves of SS321, SS347, IN625 and IN 825 in 3.5 wt. % Solar salt at (a) 25 °C and (b) 80 °C

4.2.3 Evaluation in Hitec salt

As for the CPDP curves in Hitec salt in Figure 4-7, the forward curve is mostly overlaid with the reverse scanning curve, similar with that in Solar salt. The difference between forward and reverse current density is relatively small at high potentials in the CPDP curve which means the localised corrosion does not take place or effect of the disruption of the surface passivity is very small.

4.2.4 Summary

As we discussed before, the temperature plays an important role on the corrosion behaviour of stainless steels and Ni-based alloy by increasing the corrosion rate as shown in Figure 4-4, especially on stainless steels.

Among three salts, the samples exhibit the best corrosion resistance in Hitec salt, then in solar salt, samples show the most corrosive in NaCl than in other salts. According to the result above, we can draw the conclusion that at 80°C, the corrosion resistance order of four materials obeys the following order: IN 825 > IN 625 > SS 321 > SS 347, and the corrosivity of the salts obey the order, Hitec < Solar salt < NaCl. The ranking was based on the critical pitting potential and the corresponding corrosion rate shown in the Table 4-2**.**

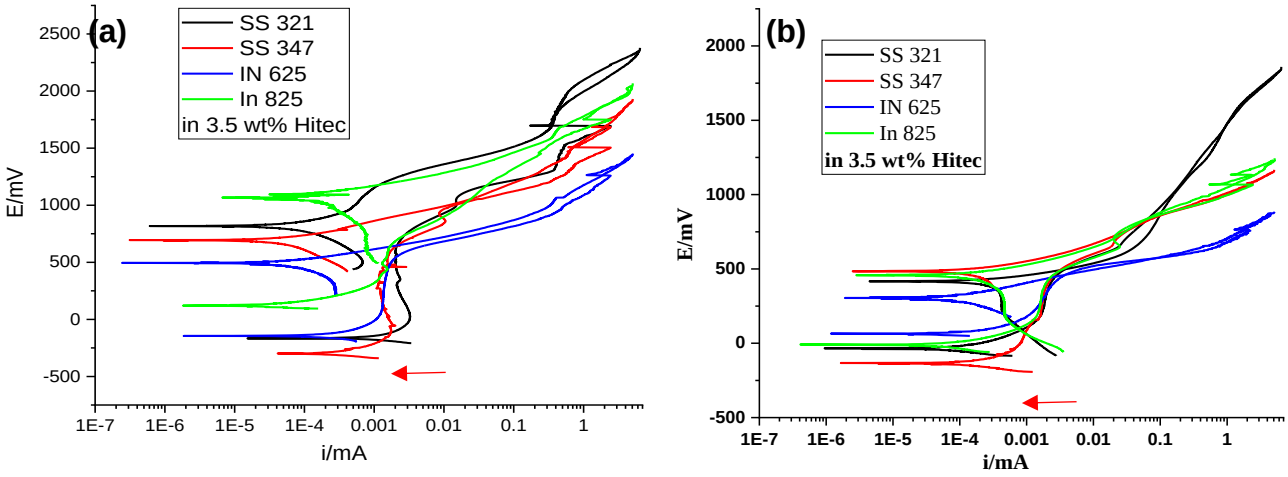

Figure 4-7. CPDP curves of SS321, SS347, IN625 and IN 825 in 3.5wt. % Hitec salt at (a) 25 °C and (b) 80 °C

4.3Salt concentration influencing the corrosion process

Except from the effect of temperature, the salt concentration could also affect the corosion performance of selected alloys. This section will discuss the elctrochemical behaviours as influenced by the salt ion concentration (Cl^-, NO_3^-). The discussion will be focused on three different brine systems (NaCl. Solar salt, Hitec salt) at concentration of 3.5 and 5 wt.%. However, the results presented in this part are aimed at estblishing a theory explaining how differnet salt ions affect the corrosion behaviour of stainless steels. In this part, SS 316L was only investigated in 3.5 and 5 wt. % NaCl, Solar salt and Hitec salt due to its better pitting corrosion resistance by adding Mo alloy element than SS 321 and SS 347.

Figure 4-8 shows the cyclic potentiodynamic polarization curves for focused alloys samples exposed to the following conditions. It should point out that each of the polarization tests were repeated at least two times to ensure the reliability of the data and ensure the accuracy of the corrosion rate. The summary of corrosion potential and current density were shown in Table 4-3.

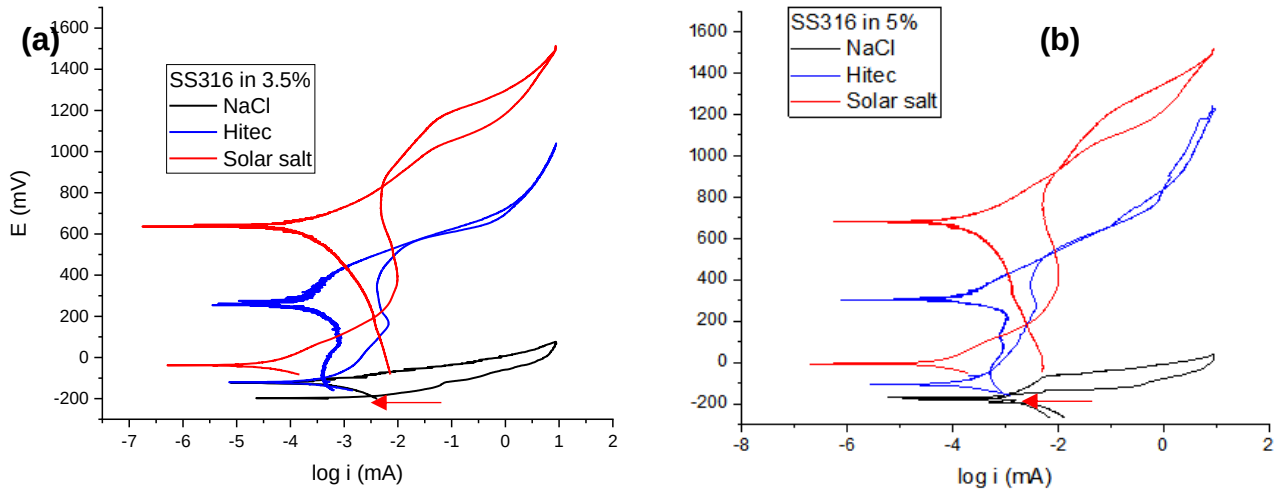

Figure 4-8. CPDP curves of SS 316L in (a) 3.5 wt.%; and (b) 5 wt.% NaCl, Hitec and Solar salt at 80˚C.

Table 4-3. Corrosion potential and corrosion current density of SS 316L CPDP tests in 3.5% (left) and 5% (right) NaCl, Hitec and Solar salt at 80°C.

In 3.5% salts	E corr mV	I corr μA/cm^2	E pit mV	E pp mV
SS 316L NaCl	-122	0.32	-122	-187
SS 316L Hitec	-120.6	0.22	566	--
SS 316L Solar	-38	0.021	909	827
In 5% salts	**E corr mV**	**I corr μA/cm^2**	**E pit mV**	**E pp mV**
316 NaCl	-177	0.79	-55	-152
316 Hitec	-136	0.29	516	837
316 Solar	-36.7	0.042	862	928

Cyclic potentio-dynamic polarization tests presented in this part are to show the electrochemical behaviour of SS316L in three salt brine at 80°C. According to Figure 4-8, the typical polarization curves shows similar shape with those of other stainless steels in Figure 4-2 (a) and (b). From the corrosion potential and corrosion density extrapolated from potentiodynamic curvces, the SS326L exhibited severest corrosion in NaCl and mildest in Solar salt.

In NaCl, the corrosion potential decreased from -122 to-177 mV and the corrosion current density increased from 0.32 to 0.79 μA/cm^2 when salt ion concentration increased from 3.5 to 5 wt.%. Figure 4-9 also provides the 2D and 3D pits morphologies of samples for the tests conducted in 3.5 and 5 wt.% NaCl. In Figure 4-9 (a), 9-13 pits above a depth of 100μm were observed on the samples tested in 3.5 wt.% NaCl, while more than 15 pits above a depth of

130 µm were observed on the samples tested in 5 wt.% NaCl solutions. The results shows that the localised corrosion was occurred when the test was conducted in a Cl^- ions containing solution. More pits with a deeper penetration at 5 wt.% NaCl than 3.5 wt.% NaCl indicates that the higher Cl^- ions is believed to lead to a more severe corrosion/localised corrosion on the surface of SS 316.

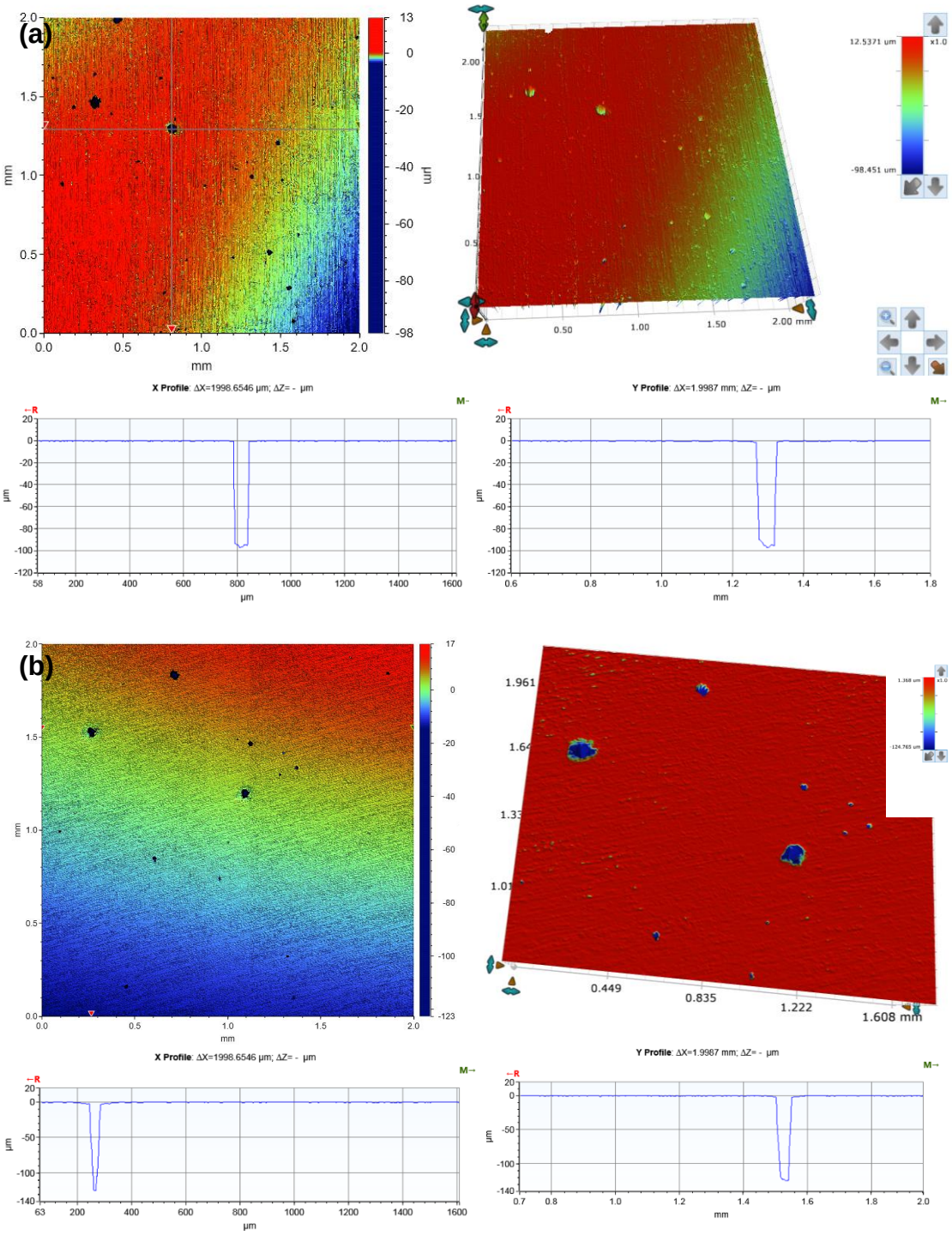

Figure 4-9. 2D and 3D images of deepest pit (relative to corroded surface) on SS 316L after CPDP test in (a) 3.5 wt.% and (b) 5 wt.% NaCl at 80°C.

The similar trend has been observed in the other salt conditions. The corrosion potential drops slightly while the corrosion current density increased significantly: 0.22 to 0.29 μA/cm^2 in Hitec salt and 0.021 to 0.042 μA/cm^2 in Solar salt when the corresponding ion concentration increase. However, the corrosion rates obtained from the corrosion current density in solar salt and Hitec salt are much lower in comparison with the results from NaCl. Figure 4-10 provides the 2D images of the pits formed on the surface during polarization test in Solar salt. Only 3 pits with a depth of 4 μm are observed on the surface in 3.5 wt.% solar salt, while 7-10 pits with a depth of 10 μm are observed on the surface in 5 wt.% solar salt solution. The results show good agreement with that in NaCl that higher salt concentration increase the degree of corrosion by increasing the corrosion current density (corrosion rate) and aggravating the pit penetration. Even so, considering the pit depth and corrosion rate, the corrosiveness of solar salt (and Hitec salt) is not as comparable as that of NaCl.

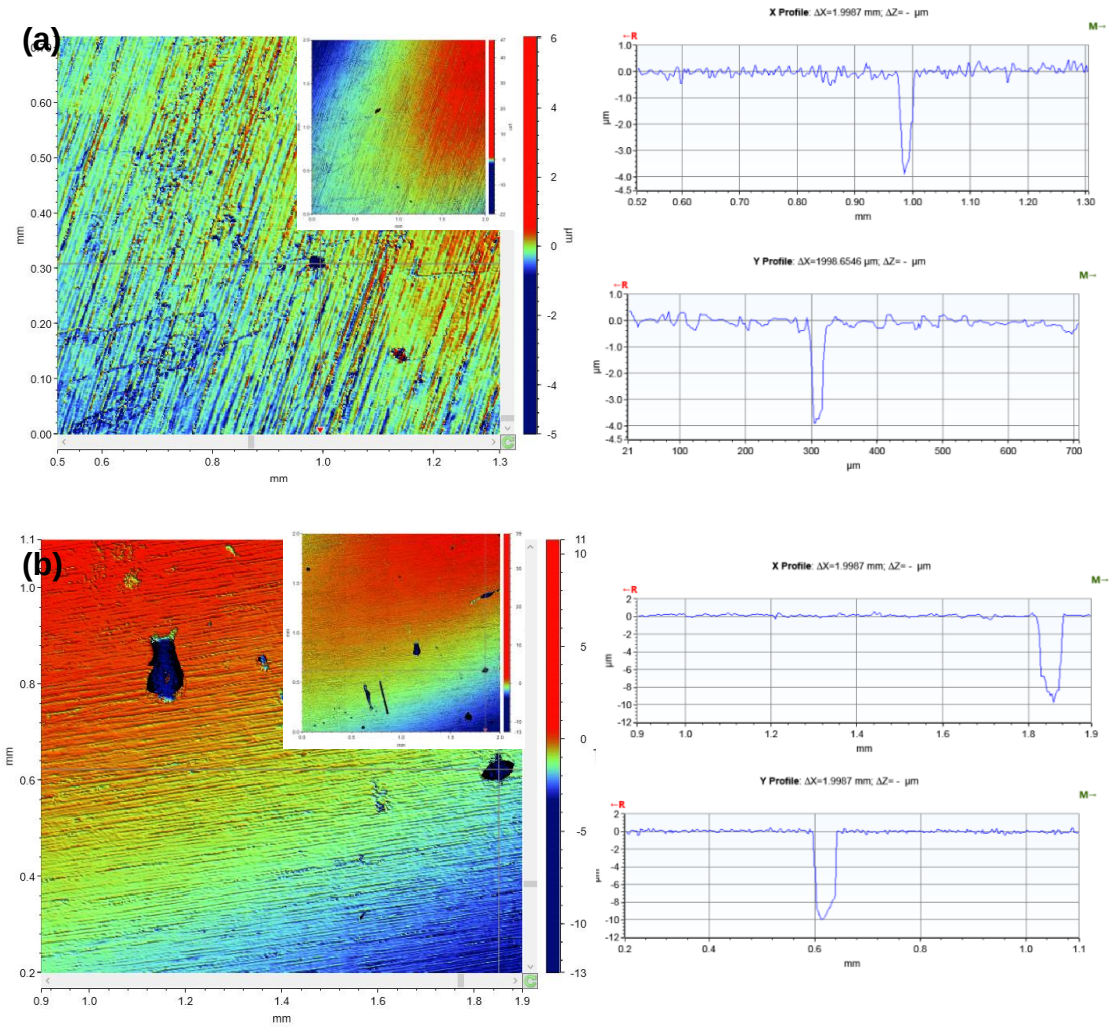

Figure 4-10. 2D images of deepest pit (relative to corroded surface) on SS 316L after CPDP test in (a) 3.5 wt.% and (b) 5 wt.% Solar Salt at 80°C

4.3.1 Summary

These findings confirm the conclusion we draw in previous section about the corrosiveness of salt and highlight the effect of salt concentration influencing the corrosion progress. Additionally, the results also highlight the importance of controlling the corrosive Cl- ions on the solar salt to mitigate the localised and pitting corrosion in solar salt system to ensure the integrity.

4.4 Summary and conclusions

In this chapter, we investigated the corrosion behaviour of these four materials in NaCl, Solar salt and Hitec salt at different temperature and studied the corrosiveness of these two salts which were widely used as Heat Transfer Fluids and Heat Storage medium in Concentrated Solar Power plants. The key findings in this section can be summarised as follows.

1. Ni-based alloy shows better resistance than stainless steel with higher corrosion potential and lower corrosion current density, the corrosion resistance following the ascending order: SS 347<SS 321< IN625<IN 825.
2. And the corrosivity of the salts obey the descending order: NaCl>Solar salt>Hitec salt.
3. The temperature plays an important role on the corrosion behaviour of stainless steels and Ni-based alloy by increasing the corrosion rate.
4. Higher salt concentration increases the degree of corrosion by increasing the corrosion current density (corrosion rate) and aggravating the pit penetration.
5. The Cl^- ions are too aggressive and need to be controlled to mitigate the localised and pitting corrosion in solar salt system to ensure the integrity.

Based on the discussion above, the conclusions can give us the reference of the corrosion behaviour of these steels at high temperature in contact with molten salt. The materials selection and salt selection can be given based on the results.

Chapter 5. Sensitization behaviours of stainless steels and Ni-based alloys at high temperature with/without molten salt

This chapter was originated from paper “Application of double loop electrochemical potentio-kinetic reactivation for characterizing the intergranular corrosion susceptibility of stainless steels and Ni-based alloys in solar nitrate salts used in CSP systems” in Engineering Failure Analysis, Volume 129, November 2021, 105717.

https://doi.org/10.1016/j.engfailanal.2021.105717.

Engineering Failure Analysis 129 (2021) 105717

Contents lists available at ScienceDirect

Engineering Failure Analysis

journal homepage: www.elsevier.com/locate/engfailanal

Check for updates

Application of double loop electrochemical potentio-kinetic reactivation for characterizing the intergranular corrosion susceptibility of stainless steels and Ni-based alloys in solar nitrate salts used in CSP systems

Qingyang Liu [a,b,*], Jiong Qian [b,c], Richard Barker [a,b], Chun Wang [a,b], Anne Neville [a,b], Frederick Pessu [a,b]

[a] Institute of Functional Surface, School of Mechanical Engineering, University of Leeds, Leeds LS2 9JT, United Kingdom
[b] Jiuli Corrosion and Integrity Centre Laboratory (University of Leeds), Leeds LS2 9JT, United Kingdom
[c] Engineering Research Centre of High-Performance Nuclear Power Pipe Forming of Zhejiang Province, Huzhou 313028, China

ARTICLE INFO

Keywords:
Intergranular corrosion
Molten salt
Stainless steels & Ni-based alloys
Carbides pricipitation

ABSTRACT

In this study, the sensitivity of four corrosion resistant candidate alloys; austenitic stainless steels (AISI 321 and AISI 347) and Ni-based alloys (IN 625 and In 825) to degrade by intergranular corrosion when used with molten salts in conditions of CSP systems were investigated at different temperatures. This was achieved by implementing the Double loop electrochemical potentiokinetic reactivation (DL-EPR) technique to quantitatively measure the degree of sensitisation (DOS) in the selected alloys by aging in air with and without Solar Salts (60 wt% $NaNO_3$ and 40 wt% KNO_3) at 550–750 °C for 2 h. Electrochemical etching technique was implemented further to verify the results from DL-EPR. The results show that DL-EPR and microstructural evaluation techniques can be used to assess the synergy of temperature and molten salt electrochemical activities on the tendency for intergranular corrosion attack to occur in CPS systems. IN 625 showed the highest intergranular corrosion resistance among the alloys investigated in both air and molten salt; especially at temperatures higher than salt stability temperature. Samples aged in molten salts showed higher DOS than samples aged in air across all temperatures and linked to Cr-consuming corrosion and chemical reactions that drives molten salt – alloy interaction in CSP plants.

5.1 Introduction

Considering the compatibility and likelihood of corrosion occurrence, the optimal combination selection of molten salt and metallic materials might become a critical aspect

because of risk of developing catastrophic failure of an entire CSP plants. Stainless steels and Ni-based alloys are widely served in CSP plants due to their good mechanical properties, high corrosion resistance and oxidation resistance. Ni-based alloys have overwhelming superiority on resistance to pitting corrosion, crevice attack and stress corrosion cracking compared with stainless steels (Walczak et al., 2018). Efforts and techniques have been taken to control or mitigate sensitization of susceptible alloys, such as high temperature solution heat treatment, reducing carbon content to reduce carbide formation and incorporating strong carbide formers or stabilizing elements such as niobium or titanium for stabilization (Pardo et al., 2007, Kim et al., 2014, Kokawa et al., 2000, Li et al., 2013, Trillo and Murr, 1998).

To the best of the author's knowledge, there is no literatures comparing sensitization behaviour at high temperature with and without molten salt. In this study, the stainless steels and Ni-based alloys were sensitised at a large temperature range for different aging time to simulate as closely as actual working conditions in CSP plant. Various standard tests have developed to characterise the intergranular corrosion behaviour of stainless steels at different conditions. Electrochemical etching in oxalic acid was first employed to give a quick filter of material and double loop electrochemical potentiokinetic reactivation **(**DLEPR) test can quantitatively access the degree of sensitization of stainless steels (Morshed-Behbahani et al., 2018).

This chapter introduces the evaluation of the degree of sensitization, which is related to the potential occurrence of intergranular corrosion of stainless steels and Ni-based alloys in CSP molten salt system. The sensitization behaviour of the focused alloys has been investigated the effect of different aging temperature and aging hours with/without molten salt. The results from this study could provide data to support and guide the material selection process in molten salt CSP plant.

The test methodology for DLEPR test (Cihal's in particular) is shown in Chapter 3.

5.2 Sensitization behaviour under different temperature with and without molten salt

The materials used in this study were AISI 321 and AISI 347 austenitic stainless steels, and Inconel 625 and Incoloy 825 with nominal composition provided in Table 3-1. The as-received samples were heat treated by supplier at stabilised temperature for 5 h to cause effective (Ti/Nb) C precipitation as described in the literature (Morshed-Behbahani et al., 2018). These materials represent the main candidate materials used in CSP plants for

molten salt transport and thermal collector pipes and accessories. The samples were cut from as – received pipes supplied by Zhejiang JIULI Hi-tech Metals Co., Ltd, China. In this study, Solar salt (60 wt.% $NaNO_3$ and 40 wt.% KNO_3) was selected as experimental salt, which was purchased from Shanghai Chemical Reagents Limit Company with analytical reagent purity. The main impurities in this salt mixture includes 0.004% insoluble, 0.0001% IO_3^-, 0.004% Ca^{2+} and 0.001% NO_2^-. The salts were weighed according to the ratio and separately dried at 120 ˚C for 24 h in a furnace. Afterwards, they are heated at 300˚C for 24 h to a homogeneously mix of salt for further use.

As shown in the Figure 3-1 to Figure 3-6, Titanium stabilised AISI 321 and Niobium stabilised AISI 347 austenitic stainless steels have an austenite phase with equiaxed-grain size about 45 +/- 4 μm prior to sensitisation treatment. Referring to the backscatter image, there are some precipitates distributed along the GBs or inner grain. SEM/EDX element mapping shows that the (Fe, Ni and Cr) depleted precipitate are identified as TiN and TiC in AISI 321 and NbN in AISI 347 at the grain boundaries, which is consistent with the reports by A.Pardo (Pardo et al., 2007). IN 625 and IN 825 show the austenitic phase with equiaxed grains and some annealing twins formed during the heat treatment process. There is also some precipitation along the GBs or inner grain, which was identified as NbN or TiN. Precipitation of intermetallic γ″ and $Ni_2(Cr,Mo)$ phases and the inter and intragranular carbides were found to be responsible for higher strength of the IN 625 (Shankar et al., 2001). For IN 825, it has been shown that these precipitates are mainly $Cr_{23}C_6$, Mo_6C and TiC or a combination of them.

5.2.1 Double loop electrochemical potentiokinetic reactivation test

The DL-EPR curves of sensitised samples of AISI 321 AISI 347 IN 625 and IN 825 were shown in Figure 5-1, Figure 5-2, Figure 5-3 and Figure 5-4, respectively. The critical current and DOS values determined from the DL-EPR curves are summarised in Table 5-1 and plotted in Figure 5-5 and Figure 5-6 as function of temperature and effect of molten salt on degree of sensitisation.

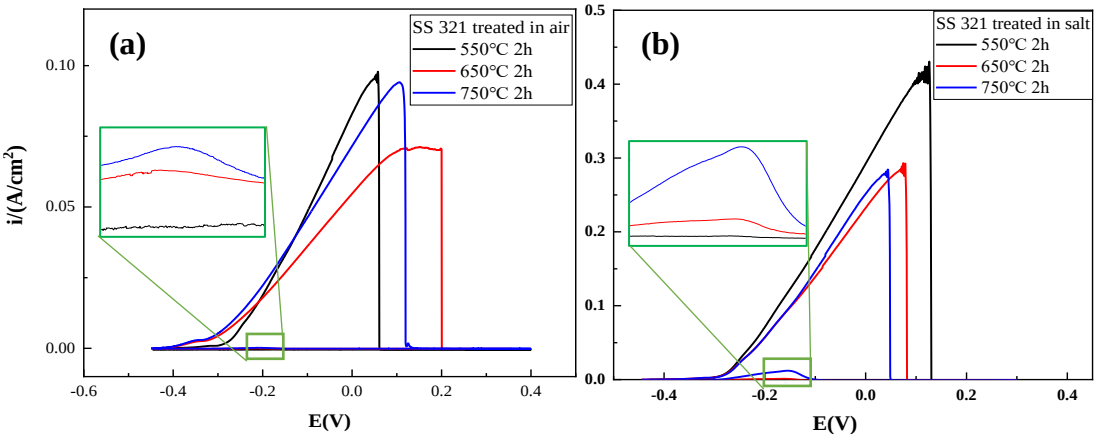

Figure 5-1. DL-EPR curves of AISI 321 sensitised at 550, 650 and 750 for 2 h in air and molten salt

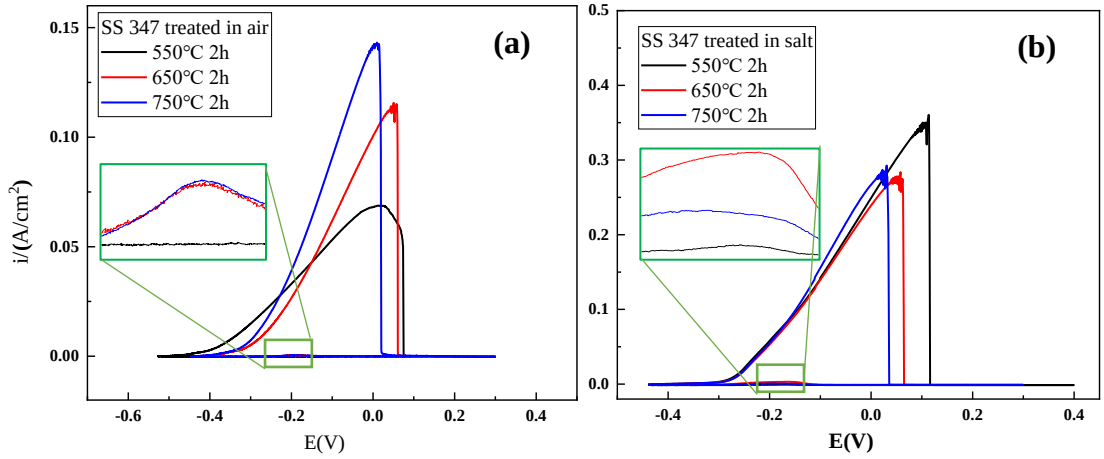

Figure 5-2. DL-EPR curves of AISI 347 sensitised at 550, 650 and 750 for 2 h in air and molten salt

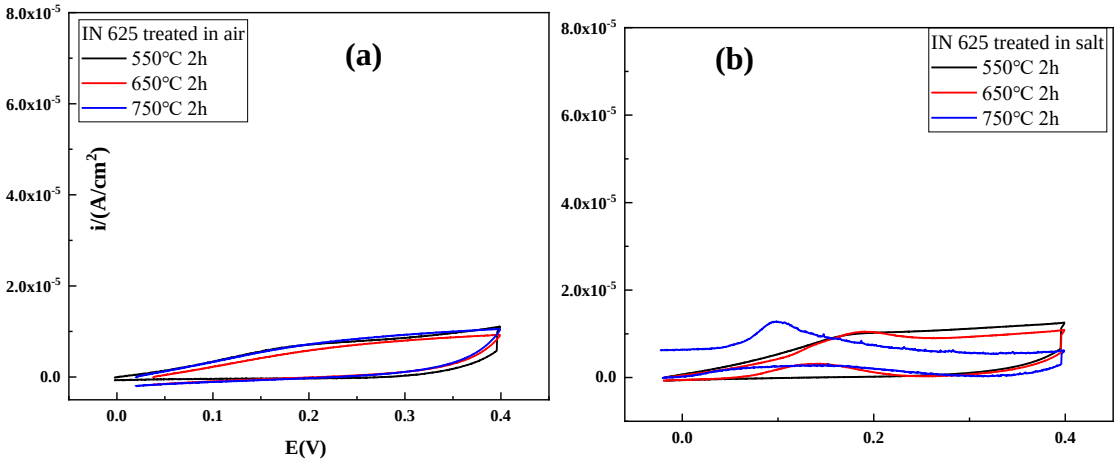

Figure 5-3. DL-EPR curves of IN 625 sensitised at 550, 650 and 750 for 2 h in air and molten salt

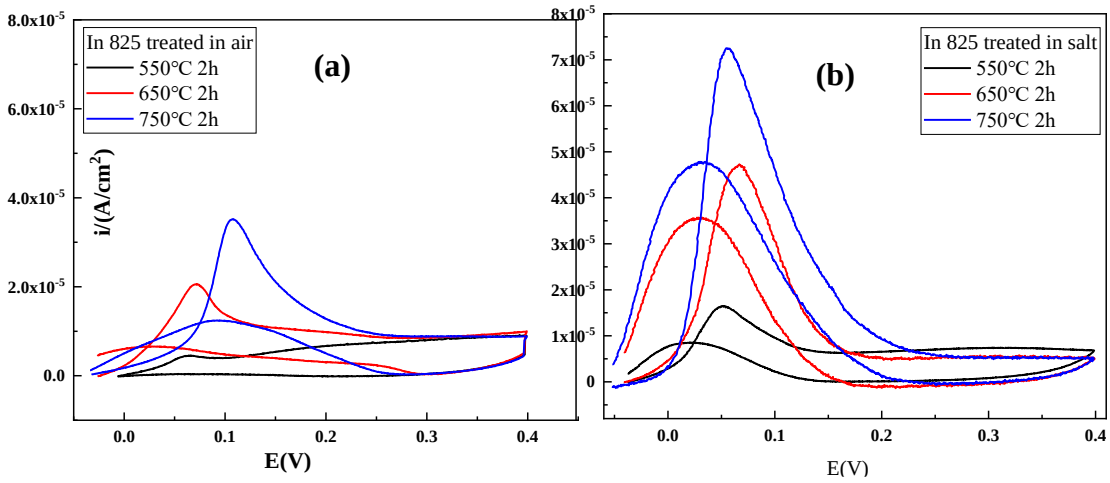

Figure 5-4. DL-EPR curves of IN 825 sensitised at 550°C, 650°C and 750°C for 2 h in air and molten salt

Table 5-1. DOS values of the material under different aging conditions in air (: %)

Condition		550°C			650°C			750°C		
Material		I_r	I_a	DOS	I_r	I_a	DOS	I_r	I_a	DOS
AISI 321	In air	10^{-5}	0.097	0.1	10^{-5}	0.071	0.14	1.6×10^{-4}	0.094	0.18
	In salt	0.001	0.427	0.23	0.001	0.291	0.34	0.012	0.282	4.26
AISI 347	In air	2×10^{-4}	0.068	0.29	3.7×10^{-4}	0.11	0.34	3.3×10^{-4}	0.14	0.24
	In salt	1.1×10^{-3}	0.36	0.3	3.1×10^{-3}	0.28	1.09	1.3×10^{-3}	0.29	0.45
IN 625	In air	0	1.1×10^{-5}	0	0	0.9×10^{-5}	0	0	1.1×10^{-5}	0
	In salt	0	1.0×10^{-5}	0	3×10^{-6}	1.0×10^{-5}	30.4	0.3×10^{-5}	1.3×10^{-5}	23.1
IN 825	In air	5×10^{-7}	0.5×10^{-5}	10.0	6.5×10^{-6}	2.1×10^{-5}	31.6	1.2×10^{-5}	3.5×10^{-5}	35.2
	In salt	8×10^{-6}	1.6×10^{-5}	49.4	3.6×10^{-5}	4.7×10^{-5}	76.0	4.8×10^{-5}	7.3×10^{-5}	65.5

Notes: I_r I_a represents current density of reactivation and anodic scan process in mA/cm^2, and DOS is degree of sensitization in %.

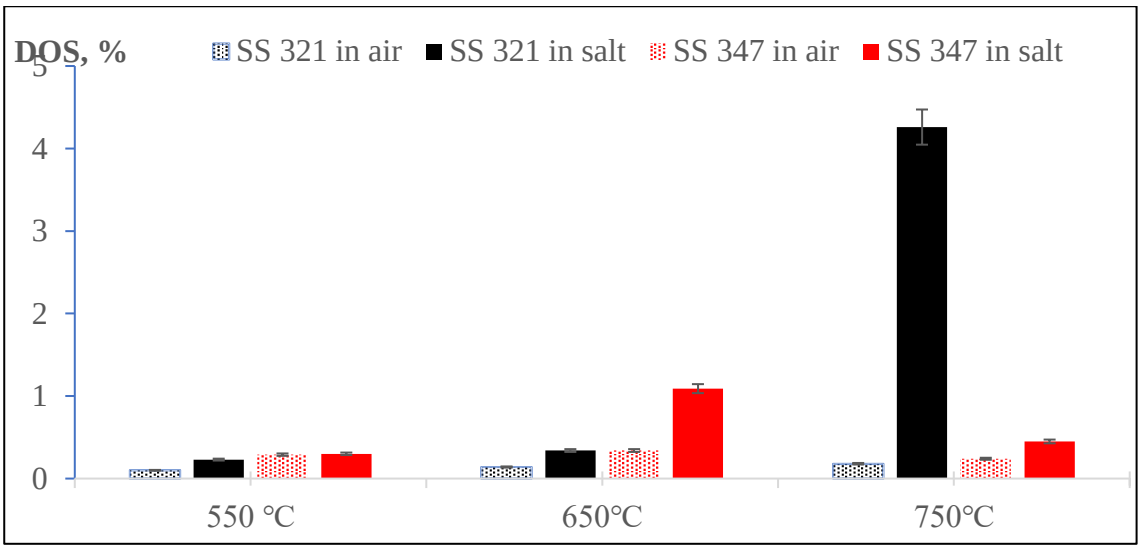

Figure 5-5. Bar chart of DOS value as function of temperature and molten salt for AISI 321 and AISI 347

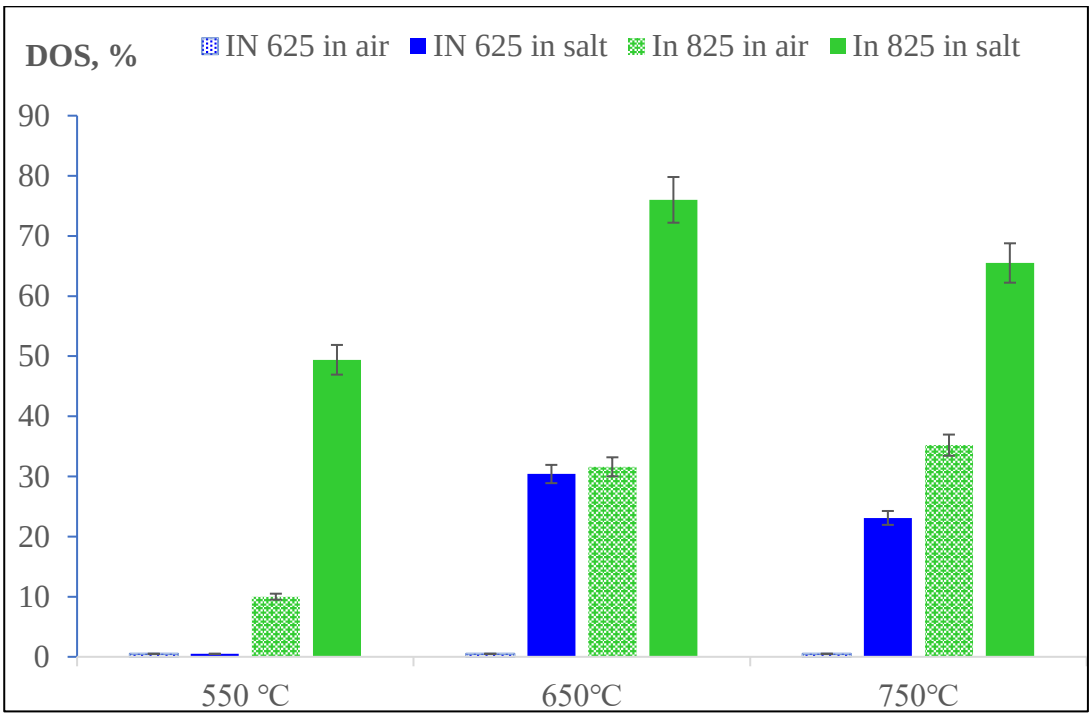

Figure 5-6. Bar chart of DOS value as function of temperature and molten salt for IN 625 and IN 825

5.2.2 Microstructure observation

The oxalic etching microstructure of the focused alloys are presented in Figure 5-7, Figure 5-8, Figure 5-9 and Figure 5-10.

AISI 321

According to the DL-EPR curve shown in Figure 5-1, air-sensitised AISI 321 samples show a relatively small reactivation current density at the temperatures under focus. Referring to Figure 5-5, DOS value increase gradually from 0.1% to 0.18% with increase of temperature from 550˚C to 750˚C. In air, the AISI 321 clearly exhibited no tendency for intergranular corrosion to occur after 2 h heat treatment at 750˚C with a DOS value of 0.18%. These results are consistent with the results of microstructure observation. In Figure 5-7 (a, b, c), the samples exhibited 'step' structure without any Cr-depletion or Cr precipitation evidence at GBs. Ti-stabilised AISI 321 steels are less prone to IGC and exhibited no obvious change in microstructure with increase in aging temperature in air. However, the specimens exhibited higher tendency for IGC to occur in solar salt than in air from the result of DL-EPR at same temperature in Figure 5-5. The DOS value of samples in solar salt increases to 0.23% and 0.34% at 550˚C and 650˚C, respectively. However, these samples remained 'unsensitised' as the DOS values are less than 1%. The results of microstructure also confirm this conclusion as samples exhibited 'step' structure when aged at 550˚C and 650˚C in molten salt, as shown in Figure 5-7 (d) and (e). It is worth mentioning that there is significant increase in DOS value from 0.18% in air to 4.27% in solar salt at 750˚C. At 750˚C and in solar salt, the microstructure of AISI 321 samples exhibited 'dual' structure with some ditches at GBs as shown in Figure 5-7 (f), indicating the highest tendency for IGC to occur.

In this study, the DOS of AISI 321 increases with increasing temperature while the synergy of high temperature and the aggressive nature of solar salt significantly increases the tendency for AISI 321 to degrade by IGC. As reported in the literature (Mahmoudi et al., 2012), chromium carbides precipitate most when aging at temperature between 750-800 ˚C without any effective TiC precipitation in AISI 321 samples (Morshed-Behbahani et al., 2018). On one hand, the increase of temperature can enhance the formation of chromium carbide thermodynamically and kinetically, resulting in significant increase of DOS value. On the other hand, the chemical reaction with molten salt is also a Cr-consuming process that leads to the formation of corrosion products such as iron chromium spinel and chromium nickel oxide [(Fe, Ni) Cr_2O_4] (Gomes et al., 2019, Walczak et al., 2018, Bradshaw and Goods, 2001a). Therefore, the degree of sensitisation, and hence the likelihood for AISI 321 to degrade, could be enhanced by the synergy of increase of temperature and molten salt chemistry.

AISI 347

Figure 5-2 shows the DL-EPR curves of AISI 347 sensitised at 550, 650 and 750 for 2 h in air and molten salt. The DOS value of air sensitised AISI 347 samples is 0.29%, 0.34% and

0.24% when held at 550˚C, 650˚C and 750˚C. Although this was slightly higher than the DOS of AISI 321 samples, AISI 347 also show lower tendency for IGC to occur with DOS less than 1% and therefore considered as ‘unsensitised’, even at 750°C. These conclusions are consistent with the results from microstructure observation. Air sensitised AISI 347 specimen shows ‘step’ structure in Figure 5-8 (a), (b) and (c) for test at 550˚C, 650˚C and 750˚C, respectively.

In the molten salt system, AISI 347 samples show the ‘step’ structure at 550˚C and 750˚C and ‘dual’ structure when aged at 650˚C in Figure 5-8 (d), (e) and (f). As mentioned before, specimens tend to have a higher tendency for IGC to occur when they have ditch structure than dual structure and step structures. The DOS value of samples in solar salts were 0.36%, 1.09% and 0.45%, which is slightly higher than when samples were aged in air at corresponding temperature. The sample aged at 650˚C in molten salt also shows a ‘dual’ structure (shown in Figure 5-8 (e)) with highest DOS value, indicating highest tendency of IGC to occur. This indicates that samples aged at 650 ˚C in both air and molten salt showed higher DOS values and hence higher tendency for IGC to occur than samples aged at 550˚C and 750˚C in both air and molten salt. This threshold effect with respect to DOS is linked to the preferred temperature limit for NbC precipitation suggested by Perrard (Perrard et al., 2007, Perrard et al., 2006) and Stopher (Stopher et al., 2016). Both authors (Perrard et al., 2006, Stopher et al., 2016) came to the conclusion that NbC precipitation depends strongly on temperature and precipitation occurred fastest between 700-800°C (973K-1073K). More stable NbC (Sourmail, 2001) precipitation could retard the precipitation of Cr carbides and thus reduce the IGC tendency. From this study, it is clear that there is a “critical sensitisation” temperature of 650˚C in molten salts at which AISI 347 samples exhibited highest DOS and tendency for IGC to occur. This is consistent with the findings of Perrard (Perrard et al., 2007) and Stopher (Stopher et al., 2016). The trend of increase in DOS values in molten salt in AISI 347 is similar to AISI 321 to highlight the contribution of molten salt chemistries to the Cr-consuming interfacial phenomenon that increases the tendency for IGC to occur.

IN 625

In addition to testing austenitic stainless steels, electrochemical test and etching method was also used to investigate Ni-based alloy. These tests have been shown to be suitable for characterising the DOS in Ni-based alloys (Kekkonen et al., 1985, Číhal and Štefec, 2001). Referring to Figure 5-3 and Figure 5-4 for IN 625 and IN 825 respectively, the DL-EPR curves and results of Ni-based alloys were significantly different from austenitic stainless steels in terms of current density and reactivation process. The results indicate that alloy

composition has a strong effect on anodic and reactivation process even though sensitisation may lead to similar chromium depletion.

IN 625 exhibited the lowest tendency for IGC to occur in air at 550-750°C without any reactivation peaks (shown in Figure 5-3 (a)). The samples remained passive during anodic and reactivation scan. The microstructure of IN 625 samples after aging in air shows a shallow ‘step’ structure in Figure 5-9 (a), (b) and (c) to confirm the results obtained from DL-EPR test. The DL-EPR curves of IN 625 samples aged in solar salt is shown in Figure 5-3 (b). Two reactivation peaks to obtain increase in DOS values of 30.4% and 23.1% at 650°C and 750°C respectively between air and molten salt can be observed. ‘Step’ structure for IN 625 at 550°C and ‘ditch’ structure at 650°C and 750°C is a clear indication that IN 625 samples remained unsensitised at 550°C even with molten salt but severely sensitised at 650°C and 750°C. This result shows that temperature plays a decisive role on sensitisation behaviour of IN 625 in molten salt. More detailed analysis is provided in section before.

IN 825

Similar to IN 625, IN 825 samples exhibited relatively small anodic and reactivation current in the DL-EPR curves. In comparison with IN 625, DL-EPR tests on IN 825 samples in air show the anodic peaks and reactivation peaks at all temperature in Figure 5-4 (a). The DOS values were 10.0%, 31.6% and 35.2% at 550, 650 and 750°C respectively, indicating that IN 825 samples are “sensitised” in air. ‘DL-EPR results and Ditch’ structure in Figure 5-10 (a), (b) and (c) for IN 825 aged in air show relatively higher tendency for IGC to occur. For DL-EPR tests with molten salt, the DOS value of IN 825 samples was 49.4%, 76% and 65.5% at 550, 650 and 750°C, respectively in Figure 5-4 (b). These values are significantly higher than the DL-EPR test results on IN 825 samples aged in air at all temperatures. Similarly, IN 825 samples aged in solar salts exhibited ‘ditch’ structure after electrochemical etching as shown in Figure 5-10 (d), (e) and (f). The width of Cr-depleted zones are the largest and indicate the highest tendency for IGC to occur (Yin et al., 2010) among all the alloys investigated. IN 825 samples exhibit high sensitivity to temperature when aged in air and in molten salt. From these results, it is believed that IN 825, though a Ni-based alloy, exhibited a significantly higher tendency for IGC to occur than Ti and Nb – alloyed austenitic stainless steels.

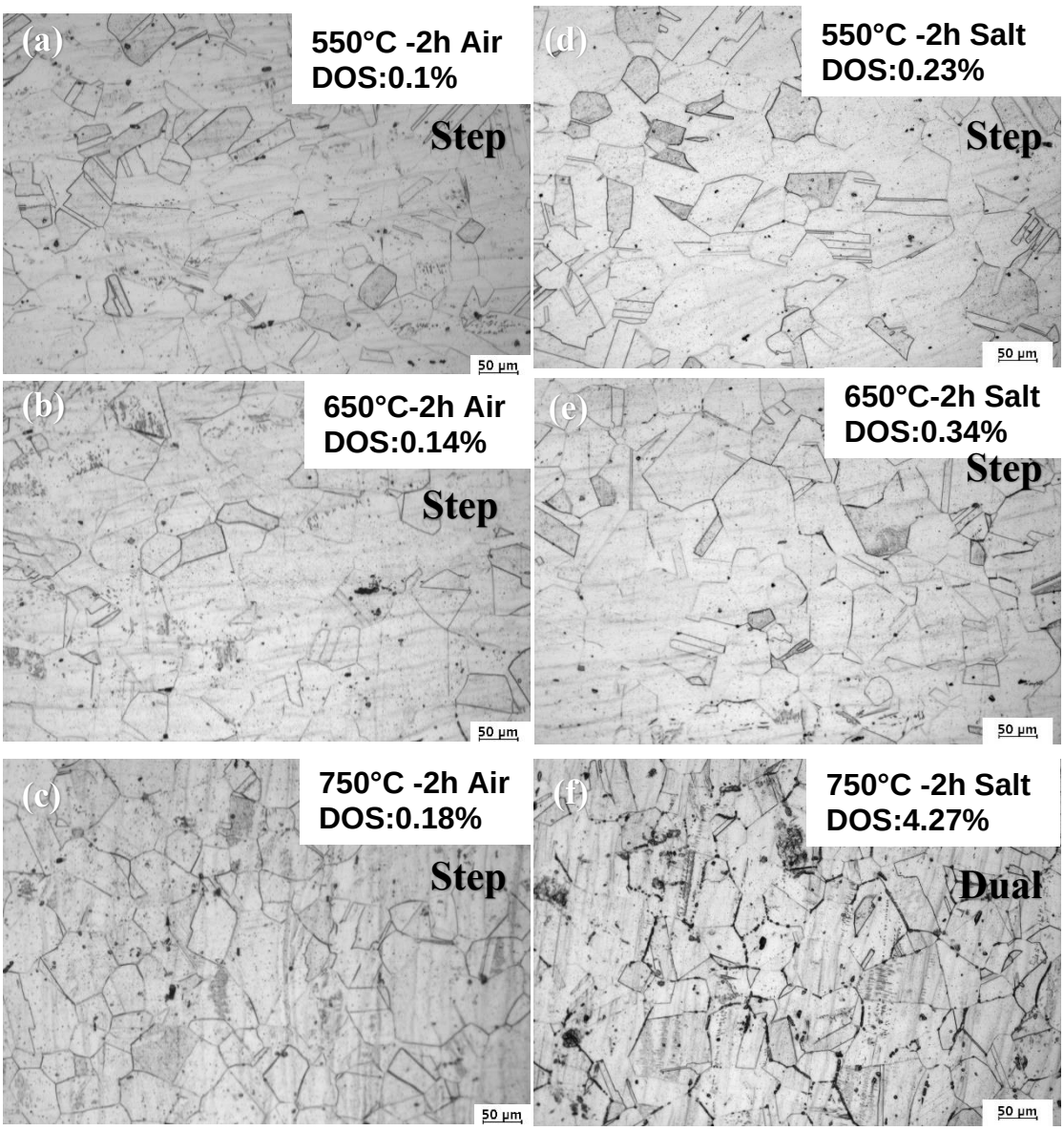

Figure 5-7. Oxalic etching microstructures for AISI 321 treated by (a) 550°C for 2 h in air; (b) 650°C for 2 h in air; (c) 750°C for 2 h in air; (d) 550°C for 2 h in molten salt; (e) 650°C for 2 h in molten salt; (f) 750°C for 2 h in molten salt, respectively.

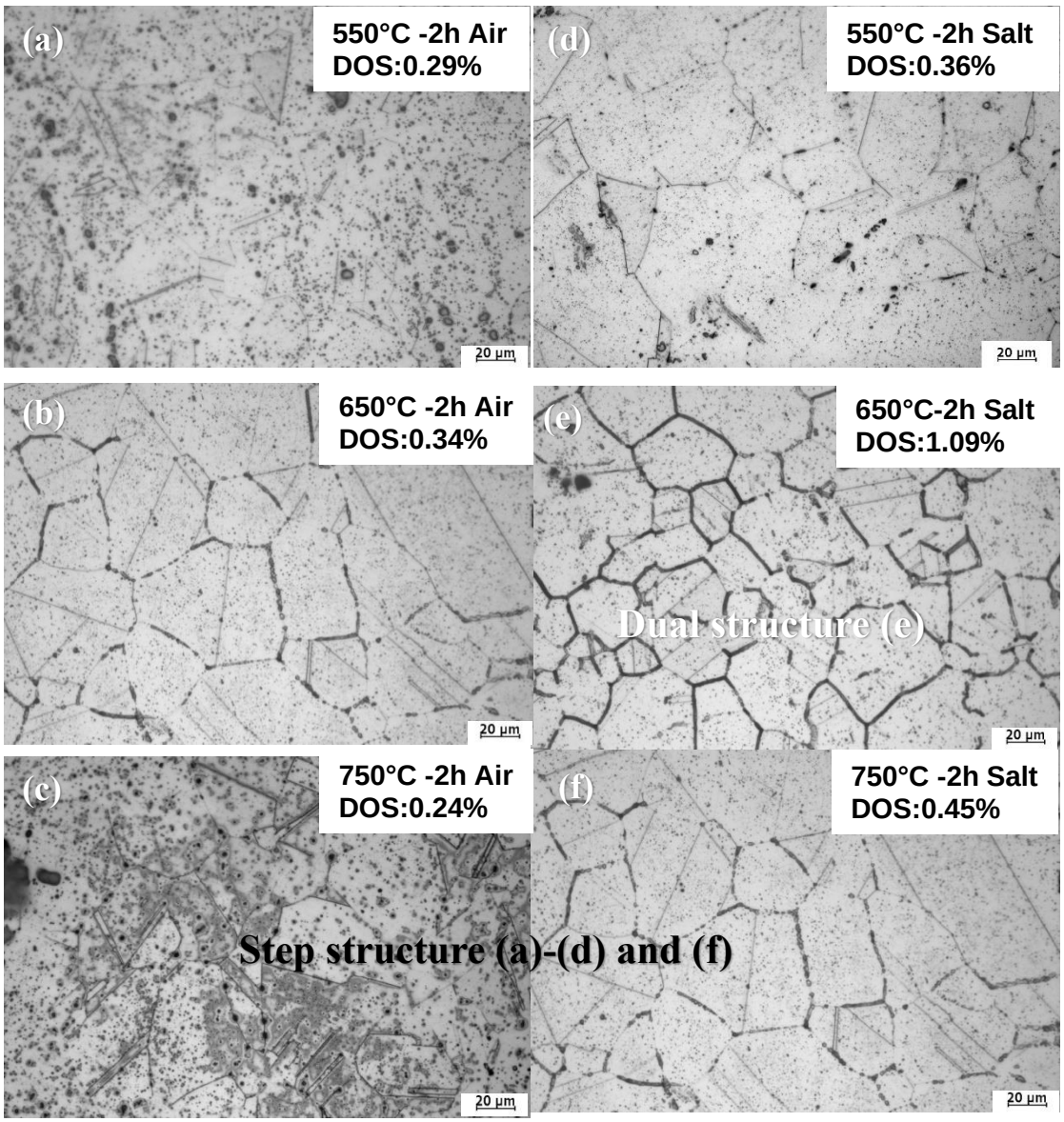

Figure 5-8. Oxalic etching microstructures for AISI 347 treated by (a) 550°C for 2 h in air; (b) 650°C for 2 h in air; (c) 750°C for 2 h in air; (d) 550°C for 2 h in molten salt; (e) 650°C for 2 h in molten salt; (f) 750°C for 2 h in molten salt, respectively**.**

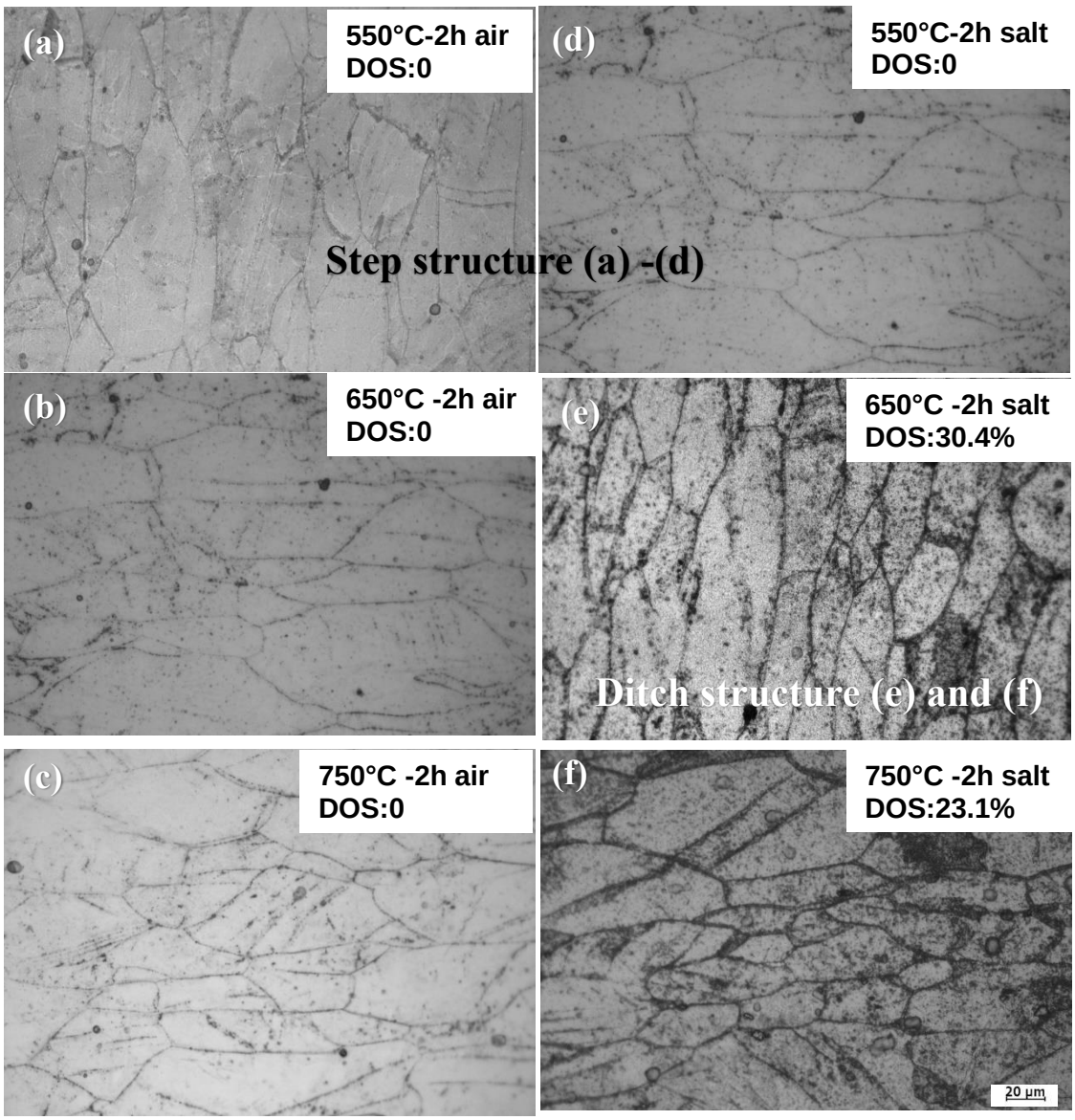

Figure 5-9. Oxalic etching microstructures for IN 625 treated by (a) 550°C for 2h in air; (b) 650°C for 2h in air; (c) 750°C for 2h in air; (d) 550°C for 2h in molten salt; (e) 650°C for 2h in molten salt; (f) 750°C for 2h in molten salt, respectively.

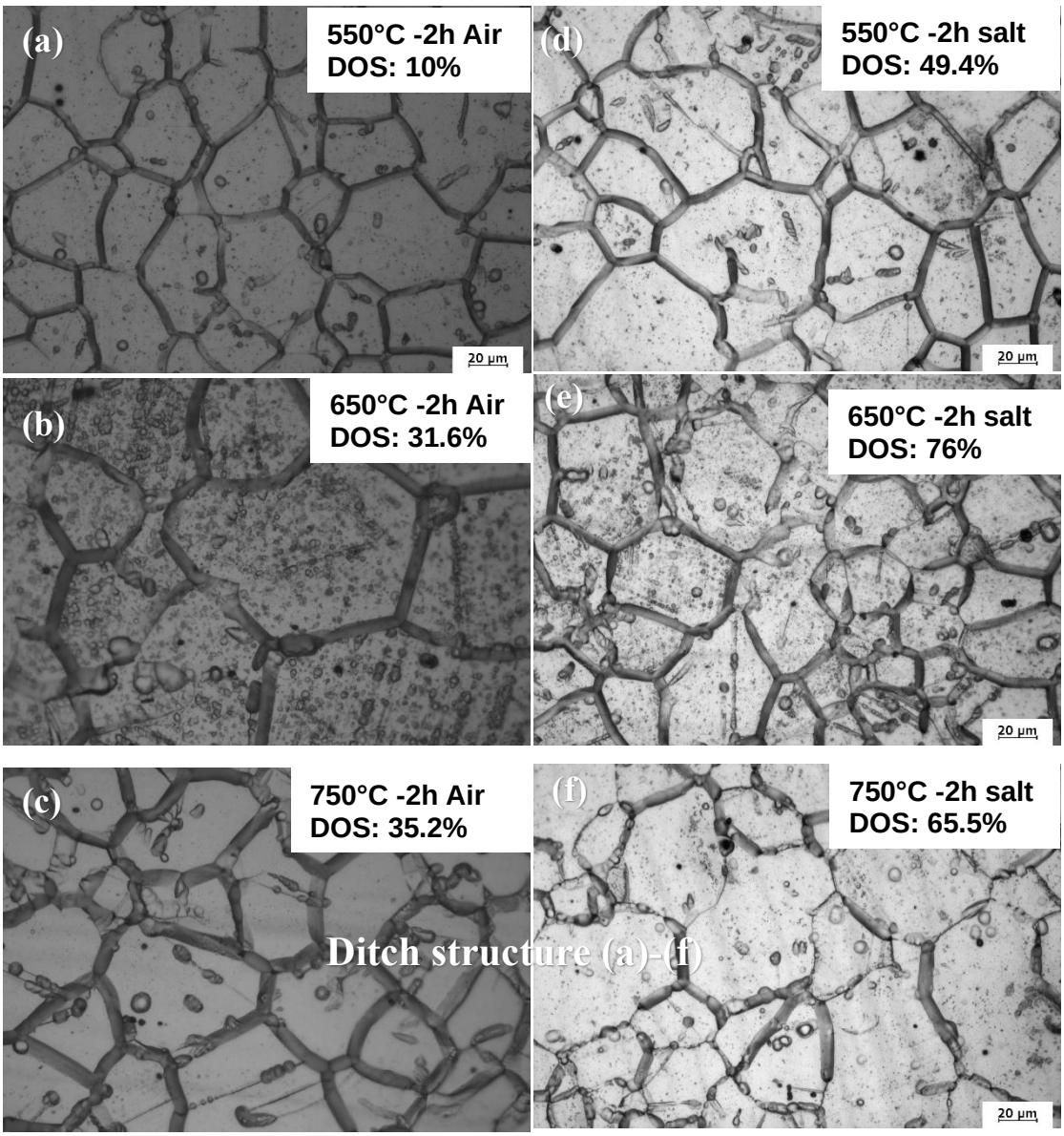

Figure 5-10. Oxalic etching microstructures for IN 825 treated by (a) 550°C for 2 h in air; (b) 650°C for 2 h in air; (c) 750°C for 2 h in air; (d) 550°C for 2 h in molten salt; (e) 650°C for 2 h in molten salt; (f) 750°C for 2 h in molten salt, respectively.

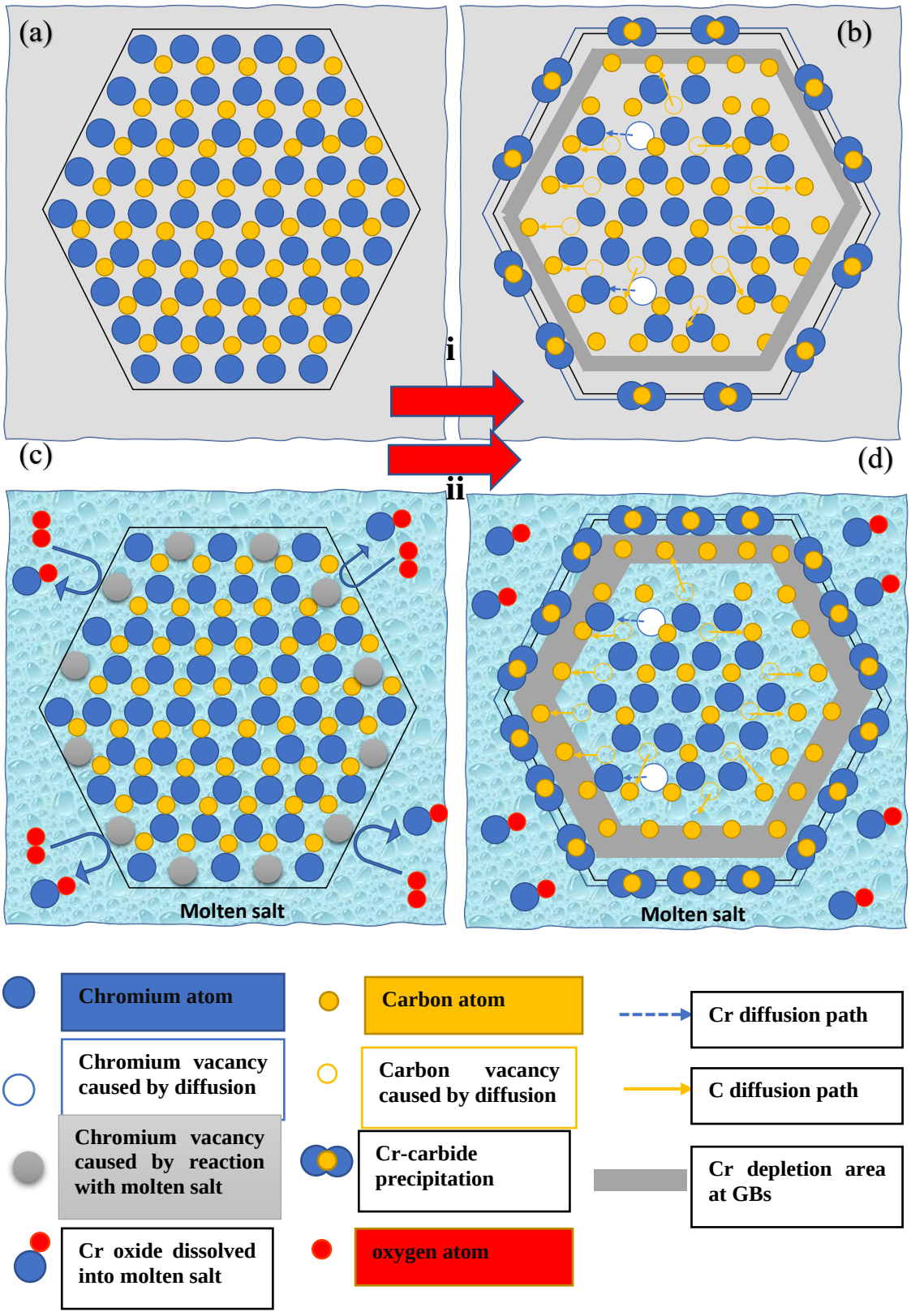

Figure 5-11. Schematic of sensitization mechanism on the surface of stainless steels/Ni-based alloys (a) and (b) in air, (c) and (d) in molten salts.

5.3 Comparison of salt effect on the sensitization behaviours of stainless steels and Ni-based alloys

As earlier discussed, the sensitisation behaviour of stainless steels and Ni-based alloys are often due to the precipitation of chromium carbides at grain boundaries. This therefore leads to a chromium depleted area at/near the GBs, where a minimum chromium content is unavailable to provide the passive film or passive films break during the reactivation process. Both scenarios could cause the depleted area to be vulnerable to intergranular corrosion, exhibiting the rise of reactivation current and high DOS value. For austenitic stainless steels, the most accepted explanation for sensitisation is the Cr-depletion theory. Other researchers (Was et al., 1981) have suggested that the size and Cr content of the Cr-depleted zone are the main factors driving intergranular corrosion. Yin (Yin et al., 2010) later reported that the degree of sensitisation of stainless steels is only determined by the width of Cr-depleted zone. The formation of Cr-depleted area is due to the lower diffusion coefficient of chromium than that of carbon.

In this study, the width of Cr-depleted area was not investigated, however, the results from post experiment analysis shows evidence of the tendency for IGC to occur along the grain boundaries. This has been observed in this study to increase with increasing of temperature and in synergy with molten salt for AISI 321 (see Figure 5-7). The effect of temperature on sensitisation behaviour for stainless steels is linked to the degree of carbide precipitation ($Cr_{23}C_6$, TiC or NbC in Figure 3-2 to Figure 3-6) at critical temperature. The higher degree of sensitisation in molten salt was due to the corrosion and chemical reaction kinetics that consumes Cr content. Solar salt is known to remain stable at temperatures ≤ 565°C and decomposes at higher temperatures into nitrite and oxygen ions (Bell et al., 2019), which enhanced the corrosivity of salt. This process in synergy with the high temperatures triggers aggressive reaction with bulk material to form corrosion products, such as mixed oxides of (Cr, Fe and Ni) (Soleimani Dorcheh et al., 2016). Chromium rich corrosion products could result in Cr-depleted zones, where passive film breakdown occurs and are likely to corrode actively. For IN 825, the reason why molten salt causes the increased degree of sensitisation is similar with that of stainless steels. From Figure 5-8, Figure 5-9 and Figure 5-10, the corrosion products are found on the microstructure, indicating the occurrence of the corrosion in this condition.

The sensitization mechanism is presented as a schematic illustration in Figure 5-11 to summarise the mechanism of sensitisation behaviour and synergy of temperature and

molten salt to influence the tendency for IGC to occur. When “sensitised” samples precipitate Cr-carbide along GBs, inner chromium is hindered more significantly in its ability to diffuse outwards than carbon, thus leading to a Cr-depleted area. More Cr carbides aggregate at the grain boundaries due to the higher diffusion coefficient of Cr with the increase of temperature, thus increasing the width of Cr-depleted area and the tendency for IGC. While in molten salt, according to literature (Sarvghad et al., 2017a, Bell et al., 2019, Walczak et al., 2018), oxidation was the primary attack to the alloys and the formation of Cr and Fe oxides may protect the bulk material against the corrosion. However, the subsequent dissolution of the Cr oxides into molten salt (Bell et al., 2019, Ahmed, 2013) causes the breakdown of this protective film and facilitates the interaction between molten salt and bare metal/alloy to accelerate the consumption of Cr emanating from bulk material as temperature increase. This corrosion/oxidation and dissolution process will remove chromium from the GBs first. Then, due to faster diffusion through GBs at temperatures below about 800 °C, it will lead to higher sensitisation near the exposed surface. The dissolution of Cr-oxide into molten salt resulted in higher DOS in molten salt than that in air by consuming chromium adjacent to GBs.

It is worth mentioned that the anodic and reactivation current of Ni-based alloy is almost four orders of magnitude lower than that of stainless steels, indicating that the passive film is more stable than that on stainless steels. We can conclude that the passive film on the surface of Ni-based alloys is containing mixture oxides of chromium and nickel due to its higher nickel content, which exhibited a more stable oxide layer at higher temperature; particularly for IN 625, than the chromium oxide film on the surface of stainless steels. Further long-term immersion tests in molten salt are needed to investigate the IGC behaviour to confirm this conclusion.

5.4 Summary and conclusions

As a non-destructive and time saving test method, Double loop electrochemical potentiokinetic reactivation test has been successfully deployed to quantitatively evaluate the degree of sensitisation and characterise material susceptibility to intergranular corrosion.

The following conclusions have been deduced from this chapter:

1. The tendency for intergranular corrosion to occur in molten salt was shown to be influenced by the synergy of temperature and molten salt chemistry for different alloys; AISI 321, AISI 347, IN 625 and IN 825. Degree of sensitisation was higher for samples aged in molten salt than for samples aged in air and linked to the relationship between

the kinetics of metal carbide precipitation and aging temperature in synergy with molten salt corrosion and chemical activities.

2. The higher DOS value of samples aged in salts than samples aged in air is linked to can be linked to the underpinning Cr-consuming reactions that drives electrochemical and chemical interactions metals and molten salt. Therefore, more chromium was consumed both in the inner grains and along GBs, increasing width of Cr-depleted area and promoting the likelihood for intergranular corrosion to occur.
3. A temperature threshold effect was also observed for AISI 347 above which DOS and hence the tendency for IGC to occur reduces. This was also observed in the microstructure change for AISI 347 from a dual structure at 650°C to a step structure at 750°C in molten salt and linked to the threshold effect of temperature on the kinetics of NbC precipitation. Increase in the kinetics of NbC precipitation at 750°C decreases the kinetics of Cr-C precipitation and hence decreased tendency for IGC to occur.
4. IN 625 has highest IGC resistance among these steels from the results of microstructure observation and DL-EPR with or without molten salt in this study. Stainless steels exhibited higher intergranular corrosion tendency when employed at sensitised temperature with molten salt.

Chapter 6. Evaluation the corrosion performance of stainless steels and Ni-based alloys in molten salt isothermal and thermal cycling condition

This chapter was originated from paper “The corrosion behaviour of stainless steels and Ni-based alloys in nitrate salts under thermal cycling conditions in concentrated solar power plants” in Solar Energy, Volume 232, 15 January 2022, Pages 169-185. https://doi.org/10.1016/j.solener.2021.12.072

Solar Energy 232 (2022) 169–185

Contents lists available at ScienceDirect

Solar Energy

journal homepage: www.elsevier.com/locate/solener

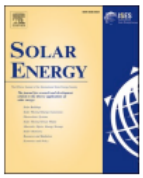

The corrosion behaviour of stainless steels and Ni-based alloys in nitrate salts under thermal cycling conditions in concentrated solar power plants

Qingyang Liu [a,b,*], Richard Barker [a,b], Chun Wang [a,b], Jiong Qian [b,c], Anne Neville [a,b], Frederick Pessu [a,b]

[a] Institute of Functional Surface, School of Mechanical Engineering, University of Leeds, Leeds LS2 9JT, United Kingdom
[b] Jiuli Corrosion and Integrity Centre Laboratory (University of Leeds), Leeds LS2 9JT, United Kingdom
[c] Engineering Research Centre of High-Performance Nuclear Power Pipe Forming of Zhejiang Province, Huzhou 313028, China

ARTICLE INFO

Keywords:
Molten salt
Thermal cycling
Stainless steels
Ni-based alloys
Multi-corrosion layer

ABSTRACT

Molten nitrate salts are widely used as heat transfer fluids and heat storage media for concentrated solar power (CSP) plants due to their favourable thermo-physical properties. The corrosion of alloys in nitrate salts used in CSP plants poses a critical challenge to the safety, cost and efficiency of their operations under high temperature. In this study, the corrosion behaviour of stainless steels; 321 and 347, and Ni-based alloy; IN 625 and In 825, in Solar (nitrate) salts has been experimentally investigated under isothermal (at 600 °C) and thermal cycling (between 600 °C and 250 °C) conditions, and under argon atmosphere. Corrosion assessment of test materials was achieved using gravimetric measurements in a simulated metal – molten salt environment in a furnace for 7 days. The micro-morphology and cross-sectional analysis of the corroding interface was carried out using a combination of scanning electron microscopy, energy dispersive X-ray spectroscopy and X-Ray diffraction techniques. Compared with isothermal condition, thermal cycling between the 250 °C (for 12 hrs) and 600 °C (for 12 hrs) reduces the corrosion rate of test materials, the severity of corrosion attack and the thickness of corrosion product layers. The result also shows that corrosion product breakdown due to spallation was also reduced by lower time at maximum temperature and cooling effect during thermal cycling, especially in stainless steels when compared with isothermal conditions at 600 °C. The spallation process became prominent with the formation of a Na-Fe oxide layer at the corrosion interface. Ni-based alloys show better corrosion resistance than stainless steels under both isothermal and thermal cycling conditions due to the superior passivation behaviour from combined Cr and Ni enrichment. Cr_2O_3 and NiO were formed as an inner layer in a multi-layered corrosion products on the metal surface from reaction with oxygen. Oxygen was made available from the decomposition of nitrate ions at 600 °C.

6.1 Introduction

Electricity generation from solar irradiation is achieved by photovoltaic (PV) and photothermal conversion (Desideri and Campana, 2014), Compared with photovoltaic technologies, concentrating solar power (CSP) has gained particular interest for large scale applications due to its advantage in terms of potential efficiency, low operation cost and low

environmental impact. It also has the advantage of being able to integrate thermal energy storage (TES) systems (Alva et al., 2018) to mitigate the intermittence of power supply. In CSP systems, molten salts (especially mixture of $NaNO_3$ and KNO_3) are currently widely used as heat transfer fluids (HTF) and sensible heat storage material to collect, transfer and store energy in heat collector, heat transfer pipes and hot tanks, respectively. This inevitably poses significant threat to all the metallic components, which are exposed to molten salts at extremely high temperature gradients (typically ranging from 550 -850°C) (Bell et al., 2019) and are more vulnerable to high temperature fatigue and intergranular corrosion (IGC) at metal/salt interface.

Considering potential for corrosion to occur, the optimal combination of molten salt and metallic materials is critical for mitigating the risk of catastrophic failure of metal components used in CSP plant. Stainless steels and Ni-based alloys are widely used in CSP plants due to their good mechanical properties, high corrosion resistance and oxidation resistance. Ni-based alloys have overwhelming superiority in relation to resistance to pitting corrosion, crevice attack and stress corrosion cracking compared with stainless steels (Walczak et al., 2018).

Therefore research that helps to develop improve understanding of metal molten salt interactions are needed to mitigate molten salt induced material degradation in CSP plants. This has not received the needed research attention, particularly research under thermal cyclic stress. A summary of corrosion studies on molten salt (solar salt) corrosion is shown in Table 6-1. The focus of some of these studies are on the effect of temperature and molten salt chemistry on the corrosion rate of the selected alloy. It was shown that SS321 exhibited higher and higher corrosion rate from 1 to 460 μm/year as the temperature increase from 400 to 680 °C (isothermal) with the largest increase in corrosion rate occurring between 600 and 680°C from 15.9 to 460 μm/year respectively (Kruizenga et al., 2013) (Gomes et al., 2019). Similar trend was also found for Ni-based alloy in solar salt (Kruizenga et al., 2013). Bradshaw (Bradshaw and Goods, 2001b) first started thermal cycling test in air with a 7.5-hour hot and 0.5-hour cold cycle and found that thermal cycling moderately increased the corrosion rate of three stainless steels compared with isothermal condition. The methodology provided by Bradshaw cannot simulate the real condition for CSP which includes day-time heating and night-time cooling. The results presented by Bradshaw (Bradshaw and Goods, 2001b) mainly focused on characterizing the corrosion rate and corrosion layer without providing persuasive evidence to explain the increase in corrosion rate due to thermal cycling.

Table 6-1. Summary of corrosion data for alloys in solar salt under isothermal and thermal cycling condition ('ISO' indicates isothermal corrosion, 'TC' indicates thermal cycling, 7.5 hours immersion in molten salt at maximum temperature and 0.5-hour cooling in ambient air at 95˚C, for a total cycle time of 8 hours).

Author and Ref	Alloy	Molten Salt	Temperature (˚C)	Exposure time (h)	Corrosion rate (μm/year)
Goods and Bradshaw 2004	304	Solar salt	570-ISO	7008	7.9
Goods and Bradshaw 2001		Solar salt-0.05% NaCl	565-ISO	4584	11.5
		Solar salt-0.05% NaCl	565-TC	4432	15.6
Goods and Bradshaw 2004	316	Solar salt	570-ISO	7008	9.4
Goods and Bradshaw 2001		Solar salt-0.05% NaCl	565-ISO	4584	8.96
		Solar salt-0.05% NaCl	565-TC	4084	10.72
(Bradshaw and Goods, 2001b)	316L	Solar salt-0.05% NaCl	565-ISO	4584	8.41
		Solar salt-0.05% NaCl	565-TC	4084	12.2
(Kruizenga et al., 2013) & (Gomes et al., 2019)	321	Solar salt	400-ISO	3064	1
			500-ISO	3064	7.1
			550-ISO	3064	9
			600-ISO	3064	15.9
			680-ISO	3064	460
(Kruizenga et al., 2013)	347	Solar salt	400-ISO	3064	0.7
			500-ISO	3064	4.6
			600-ISO	3064	10.4
			680-ISO	3064	447

Table 6-1 to be cont.

(Kruizenga et al., 2013)	IN 625	Solar salt	400-ISO	3064	0.17
			500-ISO	3064	1.8
			600-ISO	3064	12.7
			600-TC	3200	21.7
			680-ISO	3064	554

To the best of the authors′ knowledge, the studies on corrosion behaviour of alloys in molten-salt mixtures under inert atmosphere and thermal cycling conditions are very limited. This study focuses on thoroughly investigating the corrosion performance of two stainless steels and two Ni-based alloys under isothermal and thermal cycling conditions. Argon was chosen as inert protective atmosphere to minimise the influence of unwanted O_2 gas on corrosion behaviour and isolate and characterise the true effect of thermal cycling. The test protocols were developed to closely simulate real solar power tower from the industrial scale CSP that accounts for conditions during day-time heating and night-time cooling in heat transfer pipes or heat storage tanks. The results and findings in this study could provide a new theoretical basis and guidance for characterization and selection of the materials with molten salt in CSP plants.

6.2 Experiment methodology and test protocol

6.2.1 Experimental material

The materials used in this study were AISI 321, AISI 347 austenitic stainless steels, and Ni-based Inconel 625 and Incoloy 825 alloys. The composition of these alloys is provided in Table 3-1. The as-received pipes were supplied by Zhejiang JIULI Hi-tech Metals Co., Ltd China. Samples of approximately 1 cm2 area were obtained from seamless pipes as shown in Figure 6-1. They are first grounded with SiC paper up to 2000 grits and followed by polishing with 9 μm, 6μm, 1μm and 0.25 μm diamond suspension. Polished samples are then degreased with acetone before commencement of experiments. The initial dimensions and weight of coupons were recorded by electronic calibre and analytical balance. The samples for cross-section analysis were encapsulated in epoxy resin before being abraded and polished. Prior to cross section analysis, the prepared samples were sprayed with either Au or Pt to enhance the conductance of the specimens.

Solar salt (60 wt.% $NaNO_3$ and 40 wt.% KNO_3) is the most common molten salts used in CSP plant and therefore was selected for this study. The solar salt used was purchased

from Shanghai Chemical Reagents Limit Company with analytical reagent purity as shown in Table 6-2. The salts were weighed according to the ratio and separately dried at 120°C for 24 h in a furnace, heated at 300°C for 24h to achieve a homogeneous mix of salt before the experiments.

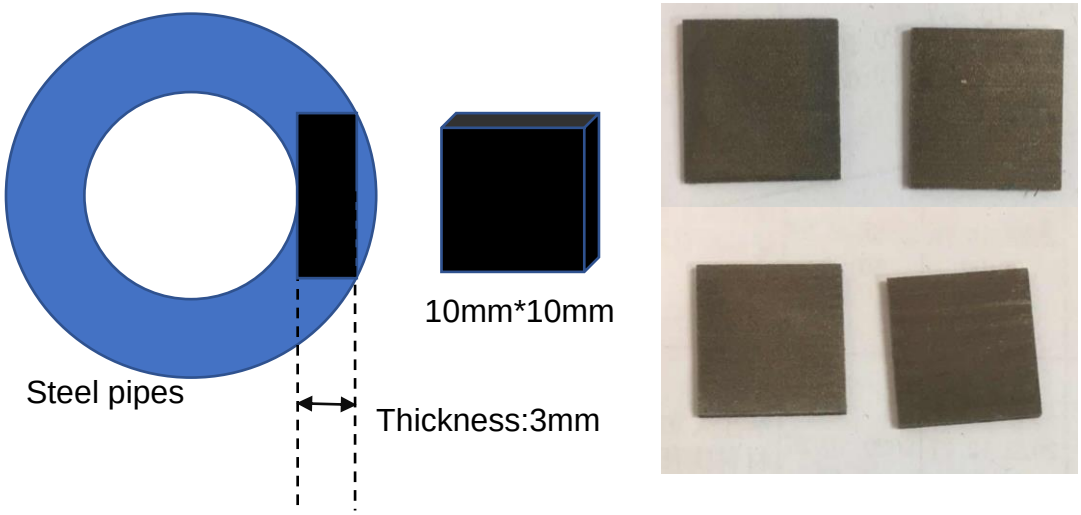

Figure 6-1. Geometry of samples obtained from the pipes and the dimensions**.**

Table 6-2. Main component contents and purity of the test salt (wt%).

Components	KNO_3	$NaNO_3$
Main component, %	99.0	99.0
Insoluble, %	0.004	0.004
IO_3^-, %	0.0005	0.0005
SO_4^{2-}, %	0.003	0.003
NO_2^{2-}, %	0.001	0.0005
Ca, %	0.004	0.005
Fe, %	0.0002	0.0001
Mg, %	0.002	0.002

6.2.2 Specimens preparation and test procedure

Tubular furnace was used to provide stable and accurate high temperature environment with argon atmosphere in horizontal direction. Figure 6-2 shows the photo of the furnace and

basic assembly drawing of the oven. In this test, the samples containing crucibles are placed in the middle of the tube and the preparation procedure are as follows.

Four specimens of each alloy were placed horizontally in each Al_2O_3 crucible in order to ensure the same contact surfaces between the specimens and the molten salt. The homogeneous solid salts were poured into each sample-containing crucible before being transferred into the furnace to dry under argon atmosphere for 12 hours at 180°C. The furnace is gradually heated up to test temperature, with test commencing when the test piece temperature exceeds 97 % of the desired test temperature. It should be noted that the test chamber was filled inert argon gas in this study.

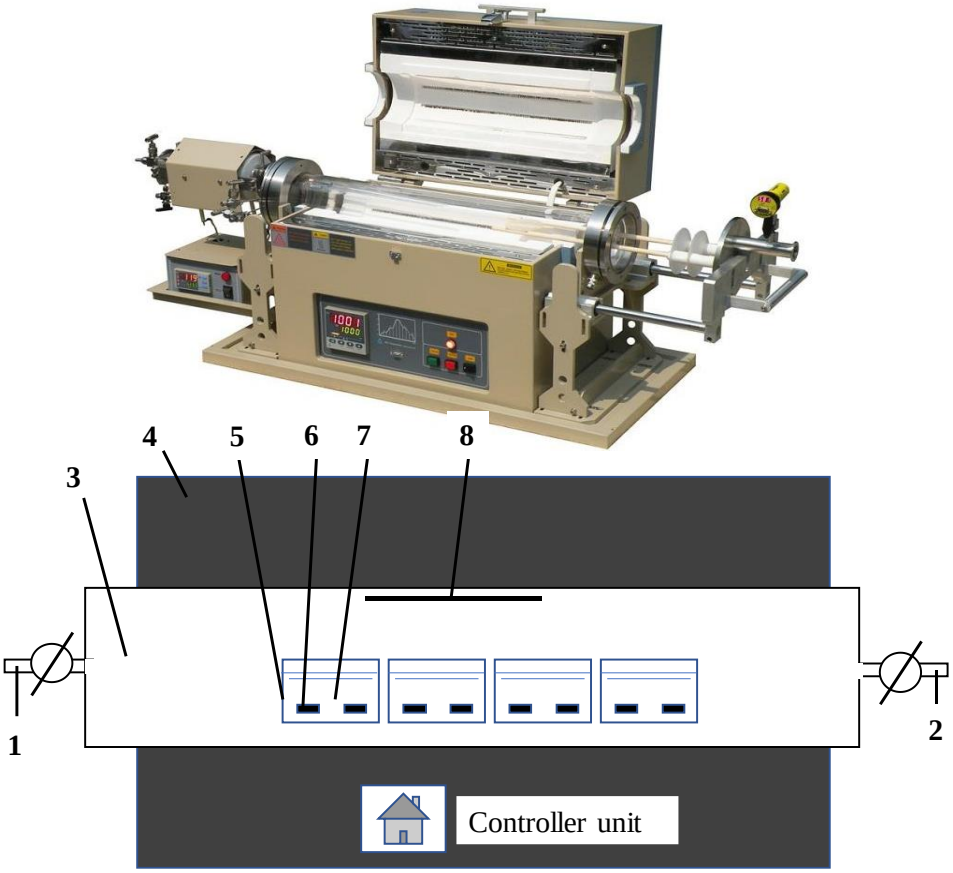

Figure 6-2. The structure of tubular furnace whole and part. 1 gas inlet; 2 gas exit; 3 test chamber; 4 heating unit; 5 crucible; 6 specimen; 7 molten salt; 8 thermocouple**.**

In order to investigate the corrosion behaviour of test samples under thermal cycling conditions, tests were initially performed at a constant temperature of 600°C for isothermal corrosion. Under thermal cycling conditions, the temperature was controlled to fluctuate between 250 and 600°C, representing peak time heating of molten salt and night time cooling of molten salt in CSP storage tanks and flow lines. The selection of duration of

exposure of materials to molten salts in these configurations are designed to replicate as closely as possible the real time cycle between daytime 12-hour heating and night-time 12-hour cooling. The chosen temperatures range to be explored are chosen based on the melting point at 220°C and stability limit at 600°C for the molten salt (solar salt). The thermal cycling profile are shown in Figure 6-3.

The tested specimens were characterised using Scanning Electron Microscope (SEM), Energy Dispersive Spectrometer (EDS) and X-ray diffraction (XRD) to investigate the corrosion products and corrosion surface and cross-section morphology in detail.

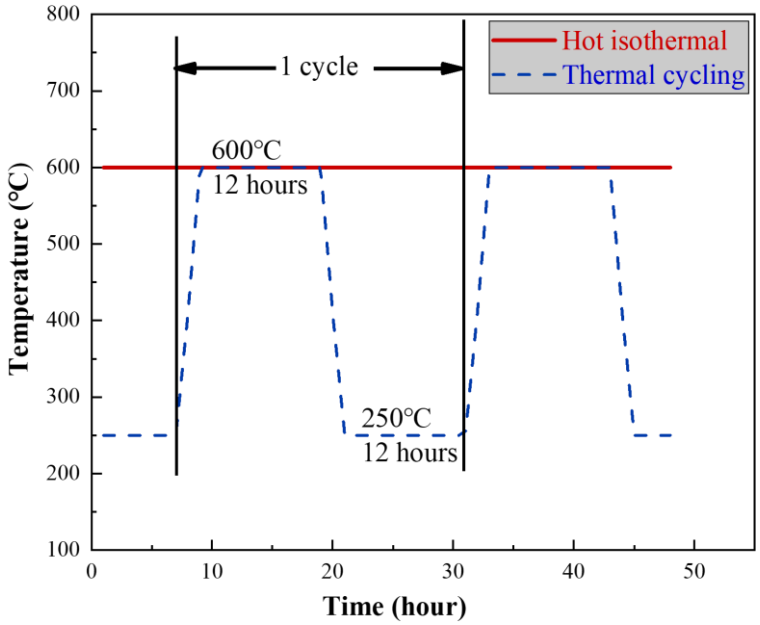

Figure 6-3. Time-temperature profile of isothermal immersion and thermal cycling (heating and cooling rate at 10°C /min with 25-min interval)

6.2.3 Weight loss measurement and corrosion rate calculations

After the test and cooling process, the specimens were retrieved and cleaned ultrasonically in deionised water and alcohol to remove the residual salt. Three of four specimens were used in weight loss test and the fourth specimen was used to characterise the corrosion products using techniques such as Scanning Electron Microscope (SEM), Energy Dispersive Spectrometer (EDS) and X-ray diffraction (XRD) and other morphology and composition characterisation tests. The specimens were then dried and weighed to obtain the weight changes using an analytical balance with 0.00001g precision.

As described in ASTM G1-03 (G1-03, 2017) and international standard (2015), the coupons were descaled to remove the corrosion product using a standardised procedure of 2-min washing with 10% H_2SO_4 at 20-25°C and 20-min washing with 10% HNO_3 at 60°C for Ni-

based alloys and austenitic stainless steels, respectively (G1-03, 2017). After removal of corrosion product, the samples were weighed to for weight loss analysis.

Weight changes before and after the corrosion test were used to estimate the corrosion rate via the Equation 20 and Equation 21, assuming uniform corrosion:

$$\frac{\Delta m}{S} = \frac{m_0 - m_1}{S} \qquad \text{Equation 20}$$

$$CR(\mu m/y) = \frac{87600\,\Delta m}{\rho\, S\, T} \qquad \text{Equation 21}$$

Where m_0 represents the initial weight and m_1 is the weight of specimen before and after corrosion, respectively. Δm is descaled mass loss per unit area (mg/cm^2), ρ is alloy density (g/cm^3): the density of AISI 321, 347, IN 625 and IN 825 are 7.94, 8.03, 8.14 and 8.14 g/cm^3, respectively., T is the immersion time (h). The weight loss data was obtained after 3 times measurements to ensure the results more accurate.

6.2.4 Microstructure analysis and surface characterization

The Bruker D8 X-ray diffractometer was used for X-ray diffraction analysis of alloys to identify the corrosion product on the surface using a monochromatic Cu Kα radiation (λ=1.5418 Å). And XRD patterns were collected in the 2θ range from 10° to 90° with a 1.5 °/min scan rate. The surface morphology and cross-sections analysis of samples were investigated using a Zeiss optical microscope (OM) (Axio Imager 2) and Carl Zeiss EVO MA15 scanning electron microscope (SEM). The SEM was integrated with an Oxford Instruments Aztec Energy dispersive X-ray (EDX) system with an 80mm X-max SDD detector which provided secondary and backscattered imaging, EDX elemental mapping and line scans. The incident beam voltage of 20 keV was employed and working distance of 12–13 mm.

6.3 Corrosion evaluation of stainless steels and Ni-based alloys under Argon

6.3.1 Weight loss measurements

Results from weight loss measurements of AISI 321, AISI 347, IN 625 and IN 825 after 7 days immersion test are shown in Figure 6-4. Weight change was measured after deionised water sonication and acid washing in turn. Ultrasonic washing with deionised water was used to remove the remained salt and loose oxides on the sample surface (Hua et al., 2019). Corroded samples were taken to acid washing to remove all corrosion products and the

subsequent weight loss measured is used to compute the corrosion rate according to the ASTM G1 standard (Villada et al., 2018). From Figure 6-4, both stainless steel samples exhibited higher total corrosion rate than Ni-based alloys in both isothermal and thermal cycling immersion experiments. The corrosion rate of AISI 321 and 347 is 434 µm/y and 317 µm/y after 7 days from isothermal immersion tests respectively. These values are 3-4 times higher than that of IN 625 and IN 825 at same condition. Thermal cycling resulted in lower corrosion rate values of up to 25 – 50% less than corrosion rate from isothermal immersion tests for these alloys. Thermal cycling cycles between 600 and 250°C attenuated the corrosion rate to values ranging from 57.7 µm/y in IN 625 to 124 µm/y in AISI 347 from 317 µm/y after isothermal test. Mass change measurements after ultrasonic washing consistently show weight gain for samples from thermal cycling experiments while samples from isothermal experiments show weight loss. This is an indication of improved protective properties from dense oxide layers. Under isothermal conditions, it has been reported that a high initial corrosion rate is needed to drive the formation of dense corrosion product layer (oxide layers). This could protect the metal substrate or easily undermined with time to promote transition from dense oxide layers to loose/porous oxides (Bell et al., 2019). The latter can be linked to sustained molten salt – metal interaction at a high temperature of 600°C.

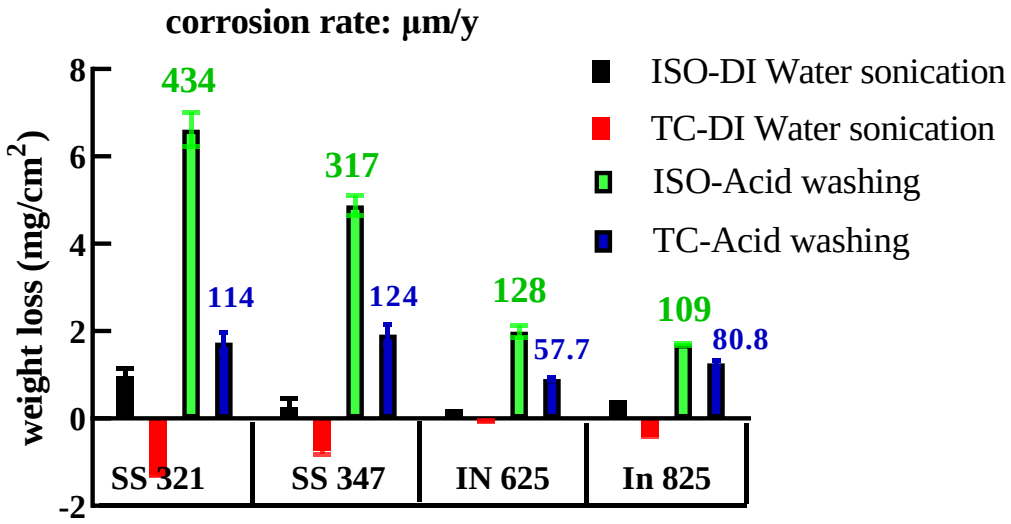

Figure 6-4. Mass loss of 321 347 IN 625 and IN 825 coupons at isothermal and thermal cycling in Solar salt for 7 days (and corrosion rate)

The higher corrosion rate from isothermal tests than from thermal cycling tests is mainly linked to the lower time (12 hours per 24 hours experiment time) at maximum temperature of 600°C under thermal cycling conditions. This is due to the effect of the 12 hours of cooling

process per thermal cycle. Under isothermal condition, the continuously formed oxide layers have more potential to breakdown and spall off due to the instability of the layers at high temperatures (Encinas-Sánchez et al., 2019). The sustained period of thermal effects under isothermal conditions is substantially tempered by intermittent cooling process under thermal cycling conditions over an interval of 12 hours per cycle. This period of cooling is long enough to limit the potential impact of thermal fatigue linked to thermal shock and reduce the impact of thermal cycles on the integrity of oxide layers. The corrosiveness of the molten salt system is also continuously and progressively increased by the decomposing nitrate salt into nitrite and oxide ions (Walczak et al., 2018) with longer residence time at 600 °C, resulting in higher corrosion rate and oxide formation. The process of molten salt decomposition also takes place under inert gas atmosphere as is the case in this study (Bonk et al., 2020). The outwards diffusion of alloy elements from the base material to form oxides at the molten salt-metal interface is also promoted by high temperature (in this case, 600°C) and duration (Bataillou et al., 2018). This is sustained under isothermal conditions but interrupted under thermal cycling conditions to limit material loss rate. Based the statements above, under the thermal cycling conditions explored in this study, the range of temperature used for the cooling phase is believed to help to slow down the kinetics of outward diffusion active atoms of key alloying elements in the base material, slow down the formation of corrosion oxide, thereby reducing material loss rate. The intermittent cooling effect during thermal cycling could also provide a way of limiting the progressive increase in the corrosiveness of molten salt linked to the thermal stability of molten salts at high temperature. This indirectly helps to improve the adherence of initially formed corrosion oxide layers at 600°C under thermal cycling conditions. This has been shown to restrict the potential transformation from dense oxide layers to loose/porous oxide layers, and detailed evidence and analysis are discussed after.

6.3.2 2-week thermal cycling test as extra data

Considering to different immersion time at 600 ˚C between 1-week isothermal with 1-week thermal cycling, 2-week thermal cycling test in argon have been performed to better explain and understand the synergic effect of thermal cycling and immersion temperature time at maximum temperature on the corrosion mitigation process. A two-week thermal cycling experiment represents an equivalent of 1-week Isothermal test at 600°C and additional 1-week Isothermal test at 250°C in argon. Referring to Figure 6-5 the weight loss of alloys from thermal cycling tests (between 600°C and 250°C) after 14 days is slightly (~ 1.5 times) higher than that after 7 days, but much lower than alloys from isothermal tests at 600°C after

7 days (except for IN 825). Comparing the results after continuous and intermittent 7-day immersion at maximum temperature, the cooling process during thermal cycling is clearly central to the overall corrosion behaviour of the alloys.

Compared with the isothermal and thermal cycling tests after 7-day immersion, higher corrosion rate recorded from isothermal test was due to consistent exposure at maximum temperature of 600°C. If we introduce the test results from 2-weeks thermal cycling test with an equivalent of 1-week isothermal exposure at 600°C, corrosion rate data in Figure 6-5 is a clear evidence that the intermittent cooling for an equivalent of 1 week isothermal exposure at 250°C helps to retard the corrosion and corrosion product kinetics.

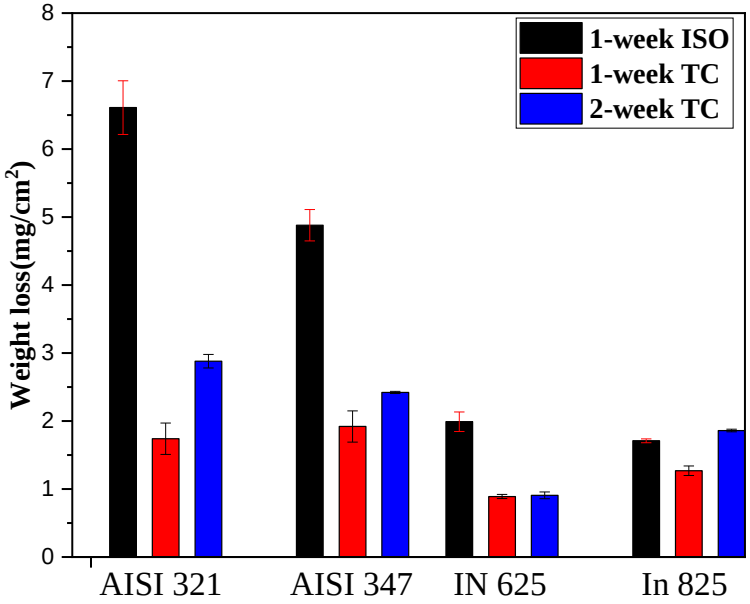

Figure 6-5. Weight change of 7-day isothermal and thermal cycling and 14-day thermal cycling samples after acid washing (in mg/cm^2)

6.3.3 Post-experimental salt characterization

Except from the thermal effect on the samples itself, the aggressiveness of salt system need to be checked after different test conditions to figure out how the salt chemistry change influencing the corrosion degradation of material.

In relation to the salt chemistry, X-ray Diffraction patterns of the salt before and after 7-day isothermal and thermal cycling test are presented in Figure 6-6. The as-received salt was identified as only mixture of (Na, K) NO_3, while the salts after Isothermal and thermal cycling immersion tests showed peak of (Na, K) NO_2 around 30.001 (100 % intensity) degree and 32.065 degree (55% intensity, according to Reference code 00-006-0392). This indicates the presence of nitrites in the form of (Na, K) NO_2 from the decomposition of (Na, K) NO_3

after 7-day immersion. It's worth noting that the peak at 32.065 degree (not main peak for $NaNO_3$ with 14% intensity and main peak for $NaNO_2$ (6000 a.u.) with 55% intensity) in Figure 6-6 (b) for 1 week isothermal test shows higher intensity (0-2000 a.u.) than that in Figure 6-6 (a), (c) and (d) for as received, 1 week and 2 weeks thermal cycling test respectively. Other researchers (Han et al., 2021) also reported that the $NaNO_2$ was found in Solar salt after 500 thermal cycles, thus influencing the thermal physical properties of molten salt. The reported (Han et al., 2021) XRD patterns of thermal cycled salt show agreement with the results in our study. This supported results published by Bonk. (Bonk et al., 2020), which shows that the chemistry of nitrate salts changes to produce nitrite in a nitrate-nitrite ratio of 94-6% after isothermal test at 600°C in a closed atmosphere the ratio will keep stable with increasing immersion time. This is clear evidence to confirm that the salt aggressiveness after 1-week isothermal is higher than that even after 2-week thermal cycling due to increase in nitrite concentration from solar salt decomposition. The detailed comparison of peak intensity of $NaNO_2$ after different test conditions are shown in Table 6-3.

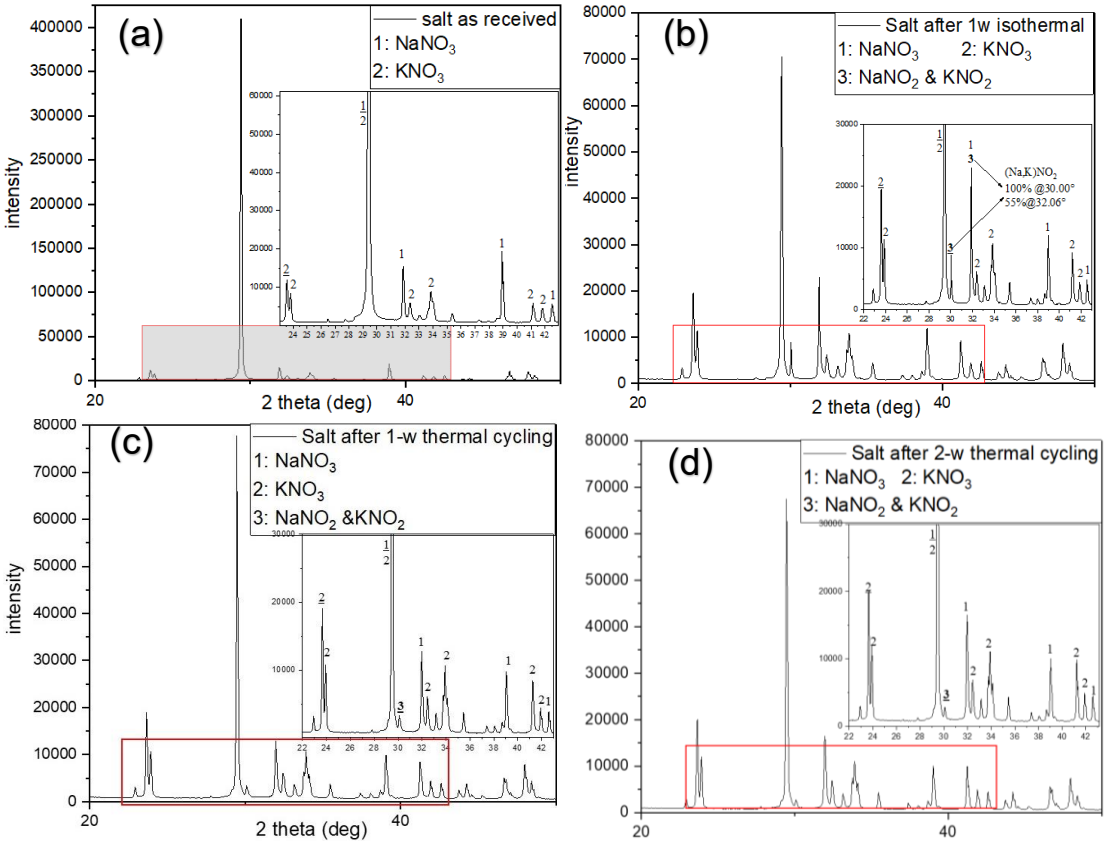

Figure 6-6. XRD results of solar salt before and after immersion test, (a) as received; (b) after 1-week isothermal; (c) after 1-week thermal cycling and (d) after 2-week thermal cycling (Reference code 00-006-0392, 00-036-1474 and 00-05-0377)

Table 6-3. Main peaks intensity of $NaNO_2$

	$NaNO_2$ intensity at 30 2theta (100% intensity)	$NaNO_2$ intensity at 32 2theta (55% intensity)
As-received salt	0	0
1-week isothermal	9800	6000
1-week thermal cycling	3200	0
2-week thermal cycling	3500	2000

6.3.4 Corrosion Product characterisation

6.3.4.1 XRD analysis

To have a better comparison of the formation of the corrosion products formed on the surface before and after immersion test, the XRD was employed on the as-received samples prior to the experiment and the XRD patterns of these alloys are shown in Figure 6-7.

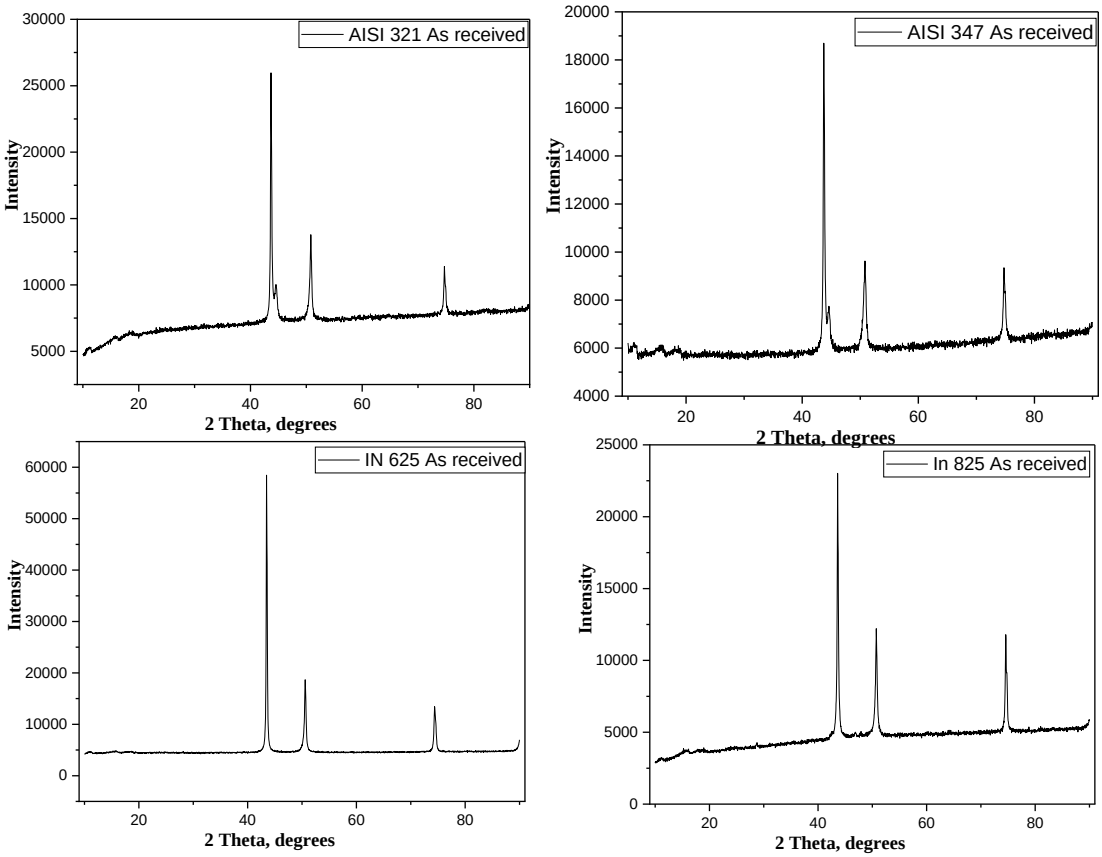

Figure 6-7. XRD patterns for as-received samples

Figure 6-8 (a) (b) (c) and (d) show the XRD patterns of the corrosion surface of AISI 321, AISI 347, IN 625 and IN 825 after 7-day immersion in Solar salt under isothermal and thermal

cycling condition, respectively. Referring to the XRD patterns, it is confirmed that the oxides layers formed on surface of AISI 321 and AISI 347 in Solar Salt are $FeCr_2O_4$, Fe_2O_3, and a less dense, and less protective outer layer of $NaFeO_2$ (Walczak et al., 2018). In this study, the main corrosion products formed on surface of stainless steels during corrosion process included iron oxide, sodium iron oxide and iron chromium spinel. Nickle oxide formed on the corrosion surface of Ni-based alloy, as well as iron chromium spinel and iron oxide, shown in Figure 6-8 (c) and (d). Compared with the products formed on IN 625 samples, more iron oxide mixtures were found on the surface of IN 825 due to its higher iron content and lower nickel content. These results have a good agreement with those observed from SEM images and EDS analysis presented later.

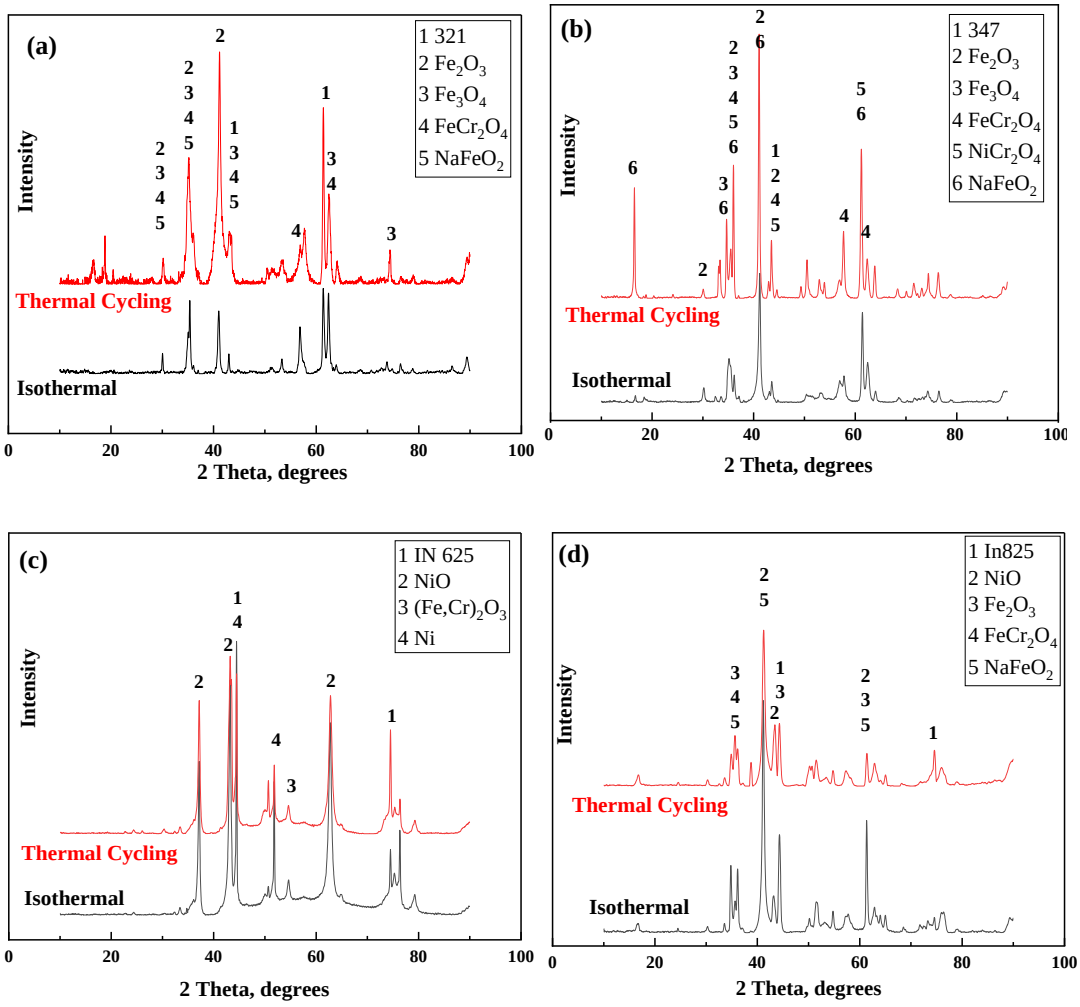

Figure 6-8. XRD patterns of (a) AISI 321; (b) AISI 347; (c) IN 625 and (d) IN 825 after isothermal and thermal cycling immersion in Solar salt for 7 days

6.3.4.2 SEM surface analysis

The corrosion surface was examined using SEM after immersion test to characterise the properties of the corrosion products layers. This is shown in Figure 6-9. The complimentary

EDS results is provided in Table 6-4. Referring to Figure 6-9, the corrosion products from isothermal and thermal cycling experiments in stainless steel samples show distinct properties. As shown in Figure 6-9 a1 and a2 for AISI 321 samples after isothermal tests, loose corrosion products appear to have spalled off due to the poor cohesiveness and adherence to bulk material. The Ni and Cr rich area was confirmed to be the fresh metal by the EDS mapping and data shown in Figure 6-9 a1. After spallation of the loose oxide layer, large area of fresh metal was directly exposed to molten salt and grain boundaries attack took place in this area. The dark deposit on region A-1 was confirmed as Al_2O_3, which Al element could come from the alumina crucible. The block product on region A-6 was identified as porous $NaFe_2O_4$, Fe_2O_3, which was also found as the primary corrosion products on the surface of samples from thermal cycling experiments in Figure 6-9 (a3) and (a4) (region A-3, 4, 5). A more protective inner layer of $FeCr_2O_4$ (Fe-Cr spinel region A-2) and other Cr-enriched layer were identified in Figure 6-9 a3 after spallation of sodium – iron oxides on test samples from thermal cycling experiments. Figure 6-9 (b1-b2) and (b3-b4) show the corrosion surface of AISI 347 after isothermal and thermal cycling immersion test respectively. Non-protective porous oxide layer was observed in region B-1, B-2 and B-4, and believed to be iron oxide and sodium ferrite from EDS data analysis and data in Table 6-4. It is evident from Figure 6-9 (b1 and b2) that the iron oxide and sodium ferrite is non-adherent and easily detachable during the test (see region B-3 in Figure 6-9 b1). The spalled area is shown from EDS data in Table 6-4 to have higher Cr and Ni content than other area in Figure 6-9 b1. Referring to the EDS data in Table 6-4, the corrosion products on AISI 347 samples from thermal cycling experiments is believed to be sodium ferrite and iron oxides. They are formed as dispersed and porous layer across corroding surface without no evidence of spallation as shown in Figure 6-9 b3-b4. The spallation behaviours of corrosion products on stainless-steel surfaces has been reported by several researchers (Gomes et al., 2019, Trent et al., 2016a, Stott and Wei, 1989, Bradshaw and Goods, 2001b), and attributed to the stress due to the mismatch of thermal expansions and Young's module between the bulk steel and corrosion scales. Referring to Ni – based alloys, the corrosion products formed are more uniform with consistent distribution of elements across the corrosion surface (see Table 6-4) for samples from isothermal and thermal cycling experiments. Samples from isothermal tests exhibited larger crystal of corrosion products as shown in Figure 6-9 c1 and d2 for IN 625 and 825 respectively, when compared with corrosion products formed under thermal cycling condition in Figure 6-9 c3 and d4 for IN 625 and 825 respectively. The main corrosion products of IN 625 is believed to be NiO from EDS data in Table 6-4. NiO is known to be protective as shown by the corrosion rate data

in Figure 6-4. The SEM images in Figure 6-9 (d1-d4) also shows that the protectiveness of NiO is also linked to how well adhered to the substrate metal at 600°C (Soleimani Dorcheh et al., 2016). The EDS data also show evidence of the potential for mixed oxide of Fe, Cr and Ni being formed as corrosion product on the corroding surface of IN 825.

The results presented clearly show that the corrosion rate recorded for stainless steel samples is always higher than Ni-based alloys under isothermal and thermal cycling conditions are due to the loose and porous properties of oxides formed on the stainless-steel surface. These oxides are less protective than NiO against the combination of chemical and redox activities from molten salt, and thermal stress. This induced stresses could be due to differences in the coefficient thermal expansion and elastic modules between the metal and oxide layers, causing cracking and spallation between protective oxides (Bell et al., 2019). Referring to the stainless-steel samples, it is evident that more severe spallation occurs under isothermal condition than under thermal cycling conditions. The spallation behaviour of the oxide layers would certainly affect the protectiveness of corrosion layer, thus affecting the corrosion rate. However, the cooling effect of lower temperature during thermal cycling and the residence time of 12 hrs per cycle at test temperature is capable of tempering the thermal stress and help to lower corrosion rate after thermal cycling tests. It is also believed that this helps to improve the thermal stability and adherence of the oxide layers and to avoid spallation of protective dense corrosion layer. This is reflected in the higher corrosion rate and severer layer spallation in samples from isothermal tests than samples from thermal cycling tests in Figure 6-4 and Figure 6-9.

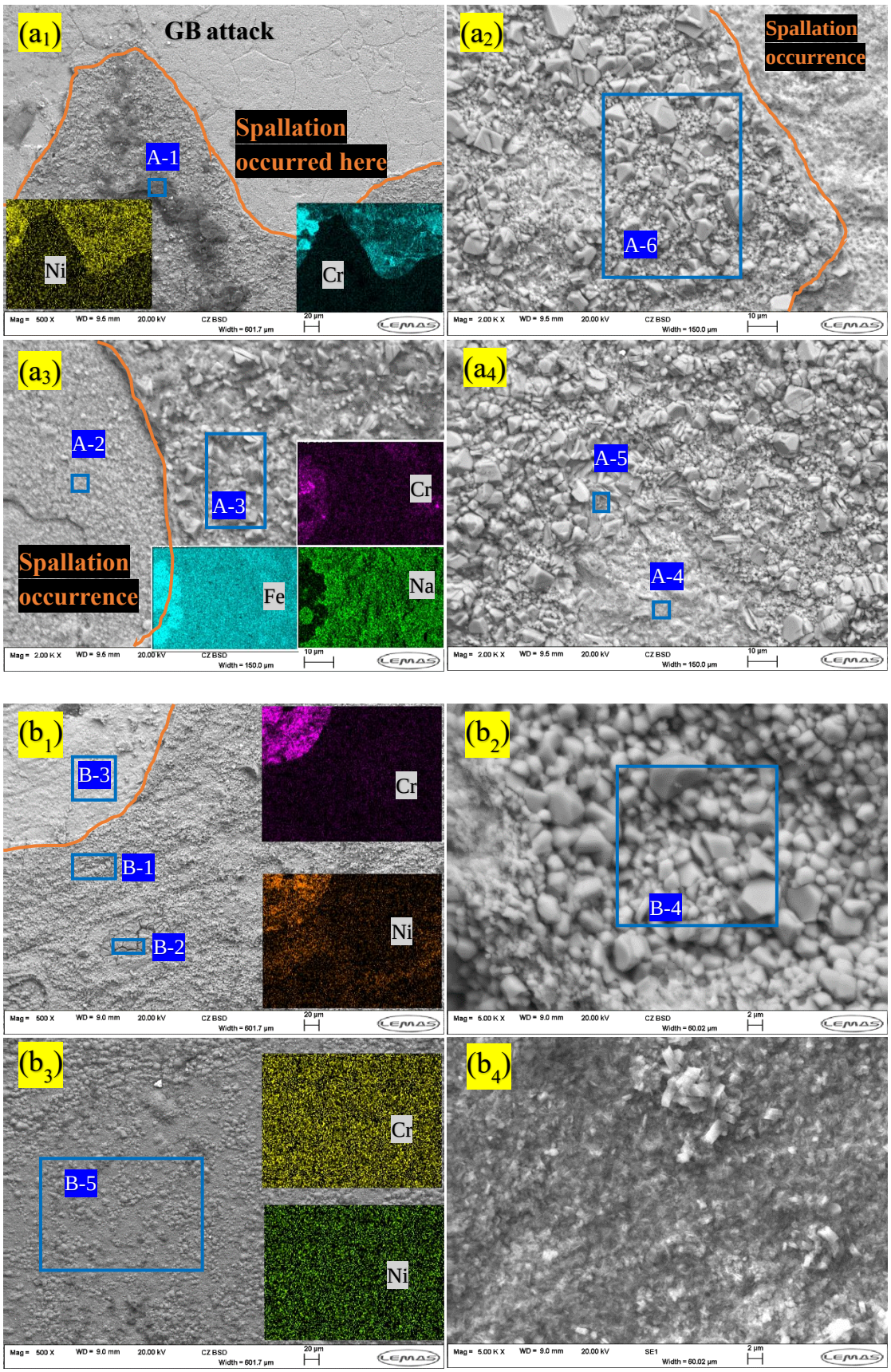

(Figure 6-9 to be continued)

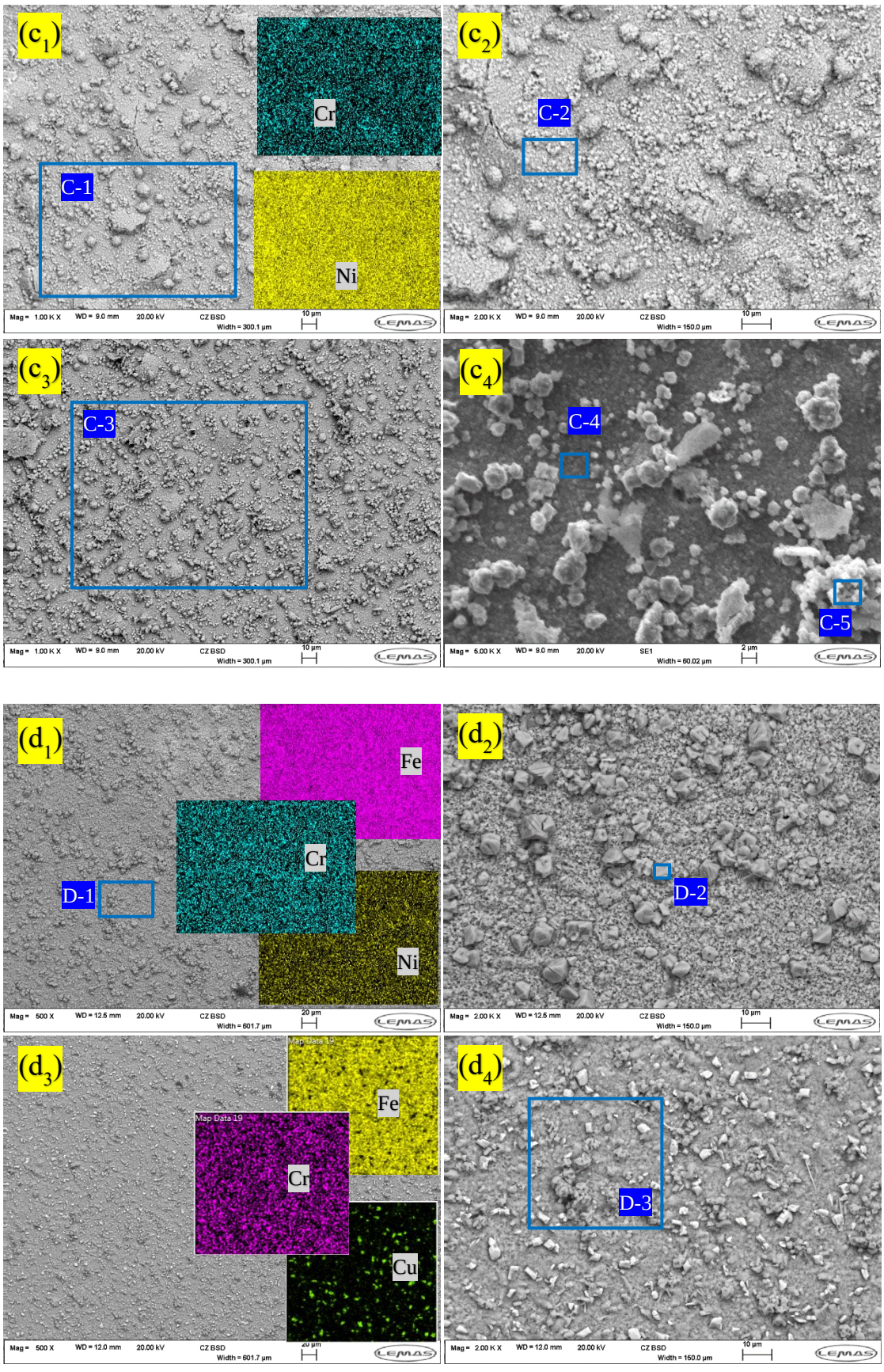

Figure 6-9. SEM top surface of the oxide scales formed on (a) AISI 321; (b) AISI 347; (c) IN 625; (d) IN 825 after 7-days immersion test in Solar Salt; isothermal (1) (2) and thermal cycling (3) (4)

Table 6-4. EDS data for regions in Figure 6-9

Region (wt.%)	Possible phases	O	Fe	Cr	Na	Ni	other
A-1	Al_2O_3	57.94	1.88	0.17	1.48	-	22.72 Al
A-2	$FeCr_2O_4$, Fe_2O_3	28.97	48.36	8.13	0.99	1.19	1.03 Al
A-3	$NaFeO_2$, Fe_2O_3	32.8	43.25	0.86	8.37	0.36	0.74Al
A-4	$NaFeO_2$, Fe_2O_3	29.44	57.7	1.21	5.36	-	-
A-5	$NaFeO_2$, Fe_2O_3	26.06	66.2	1.05	6.53	-	-
A-6	$NaFeO_2$, Fe_2O_3	32.39	49.99	0.62	6.73	0.32	0.26Al
B-1	$NaFeO_2$, Fe_2O_3	29.86	50.64	0.62	9.99	2.99	-
B-2	$NaFeO_2$, Fe_2O_3	36.06	45.64	0.69	6.15	0.44	0.74Al
B-3	$FeCr_2O_4$, Fe_2O_3	28.78	51.29	8.52	1.43	4.71	-
B-4	$NaFeO_2$, Fe_2O_3	30.15	56.73	0.91	10.88	0.76	0.18Al
B-5	$NaFeO_2$, Fe_2O_3	30.5	41.25	1	10.03	0.68	0.53Al
C-1	NiO, $(Fe, Cr)_2O_3$	21.71	7.36	0.62	1.89	60.98	-
C-2	NiO, $(Fe, Cr)_2O_3$	21.53	7.45	1.1	2.08	60.86	-
C-3	NiO, $(Fe, Cr)_2O_3$	19.77	6.88	1.71	1.98	62.61	-
C-4	NiO, $(Fe, Cr)_2O_3$	14.88	4.57	1.08	1.66	70.93	-
C-5	NiO, $(Fe, Cr)_2O_3$	20.02	5.16	1.3	1.45	59.96	-
D-1	NiO, $NaFeO_2$, Fe_2O_3	31.77	43.54	1.25	10.17	5.17	0.55Cu
D-2	NiO, $NaFeO_2$, Fe_2O_3	34.19	39.6	1.04	9.11	6.78	1.14Cu
D-3	NiO, $NaFeO_2$, Fe_2O_3	32.74	40.63	1.34	7.43	3.8	4.49Cu

6.3.4.3 Cross-sectional analysis

Referring to the XRD and SEM results in Figure 6-8 and Figure 6-9 respectively, it is evident that different oxide layers were formed on the surface of alloys specimens after immersion test. Loose oxide layer of Sodium-iron oxide spalls off during the test while others with good adherence was shown to protect based metal against further molten salt – substrate metal interactions. This section presents results from cross-section analysis using SEM-EDS techniques to provide detailed insights into the depth and mechanism of corrosion attack and interfacial oxide formation.

Figure 6-10 shows the cross-sectional images of AISI 321 samples after isothermal immersion test. Continuous oxide layers presence is observed along the interface but with non-uniform oxide layer thickness across the interface as shown in Figure 6-10 (c). From the result of EDS line scan and mapping in Figure 6-10 (b) (d) (e), it is evident that the composition of the double corrosion layer included an outer 12 – 39 µm iron oxide layer and inner 13µm iron/nickel chromium spinel layer. As shown in Figure 6-11, AISI 321 from thermal cycling tests shows uniform thickness of corrosion layer of about 10 µm along the interface, with 4.2 µm iron chromium spinel at the interface of layer/metal and 5.8 µm outer iron oxide layer. The reason of differences in the thickness of the outer iron oxide layer is the spallation behaviour of poorly adherent oxide layer formed from isothermal corrosion tests.

For AISI 347, a double oxide layer with thickness of 16.48 µm was formed on the surface of sample from isothermal immersion tests. The double oxide layer is made up of 8.4-µm outer iron oxide layer and 8-µm inner iron chromium spinel layer as shown in Figure 6-12. Figure 6-13 presents the cross-sectional image of AISI 347 after 7-day of thermal cycling corrosion test. A corrosion product layer of thickness of 9.56 µm was found on the surface and comprising of an outer iron oxide layer and an inner layer of oxides of iron and chromium. A thin Ni enrichment layer was observed at the alloy/oxide interface, which has been reported to be the result of the depletion of chromium from the bulk metal (Kruizenga and Gill, 2014). No obvious spallation behaviours were found from the cross-sectional analysis of AISI 347 samples. However, and the main difference between isothermal and thermal cycled samples are the formation of thicker corrosion layer and the presence of thin Ni-enrich layer after thermal cycling.

The cross-section analysis of IN 625 after 7-day isothermal corrosion test at 600 °C is shown in Figure 6-14. The double corrosion product layer was formed as a continuous layer along the corrosion interface. However, this layer is not uniform across the corrosion interface with thickness ranging from 9.5-16.5 µm. The inner layer was identified as a chromium enriched layer with oxygen and outer layer identified as a mixture oxide of Ni and Fe with uneven thickness between 3 and 10 µm. As shown in Figure 6-15, corrosion product layer formed on IN 625 samples from thermal cycling experiment consist of a thinner inner corrosion oxide layer (with thickness of 4.5 µm in average) than that under isothermal condition. Cr-enrich layer was found at the interface of alloy/oxide, together with external Ni-rich layer were considered as protective layer against further corrosion from molten salt.

Referring to IN 825, the thickness of corrosion oxide layer formed from isothermal immersion experiment ranges from 9-13.6 μm, and consist of outer iron oxide layer and inner mixed oxides of Cr and Ni. Referring to the EDS line scan (Figure 6-16 a) and literature (Kruizenga and Gill, 2014), sodium was present in the oxidation products in the form of $NaFeO_2$. This is a typical corrosion oxide layer at temperature above 600°C (Bradshaw and Goods, 2001a). Sodium iron oxide provides little protection and is easily removed and/or spalled by slightly sanding the surface. The non-uniformity of the corrosion layer thickness observed after isothermal corrosion test for IN 825 in this study is caused by the loose iron oxide layer (Walczak et al., 2018). The spallation of iron oxide layer was found in Figure 6-16 b, where iron oxide tended to spall due to its poor porosity and bad adherent with bulk material. Fe depleted area was found at the interface of oxide/alloy, where oxides of Ni and Cr were present as a protective layer from further metal interactions with molten salt. Thinner and more uniform corrosion layer was found without spallation on cross-section of samples from thermal cycling experiments when compared with samples from isothermal immersion test on IN 825. In Figure 6-17, double corrosion layer, with the thickness of around 6.5μm is observed, and consisted of inner iron oxide and Ni oxide (Cr oxide).

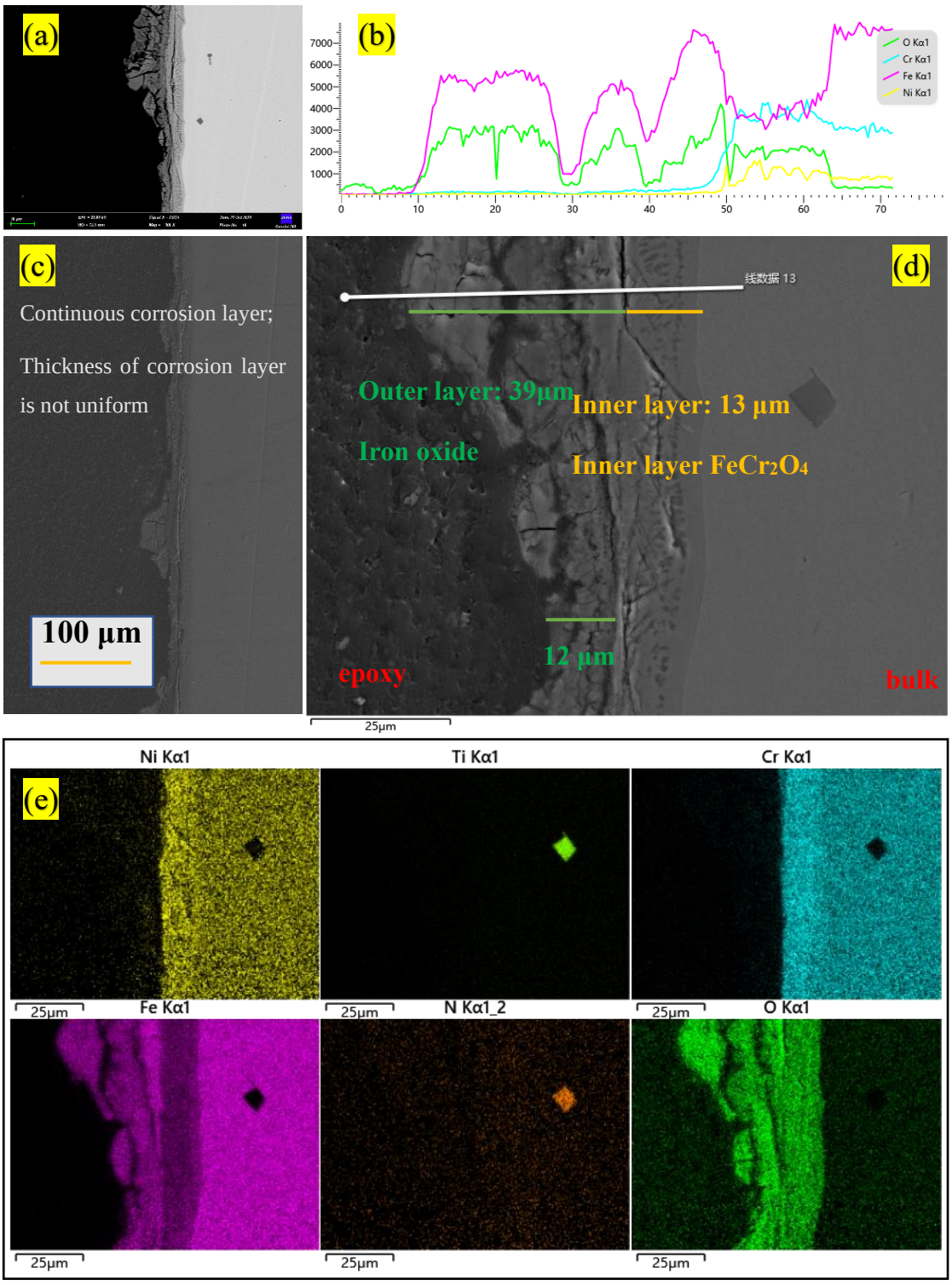

Figure 6-10. SEM-EDS profile of AISI 321 after 7-day isothermal immersion in Solar salt at 600°C

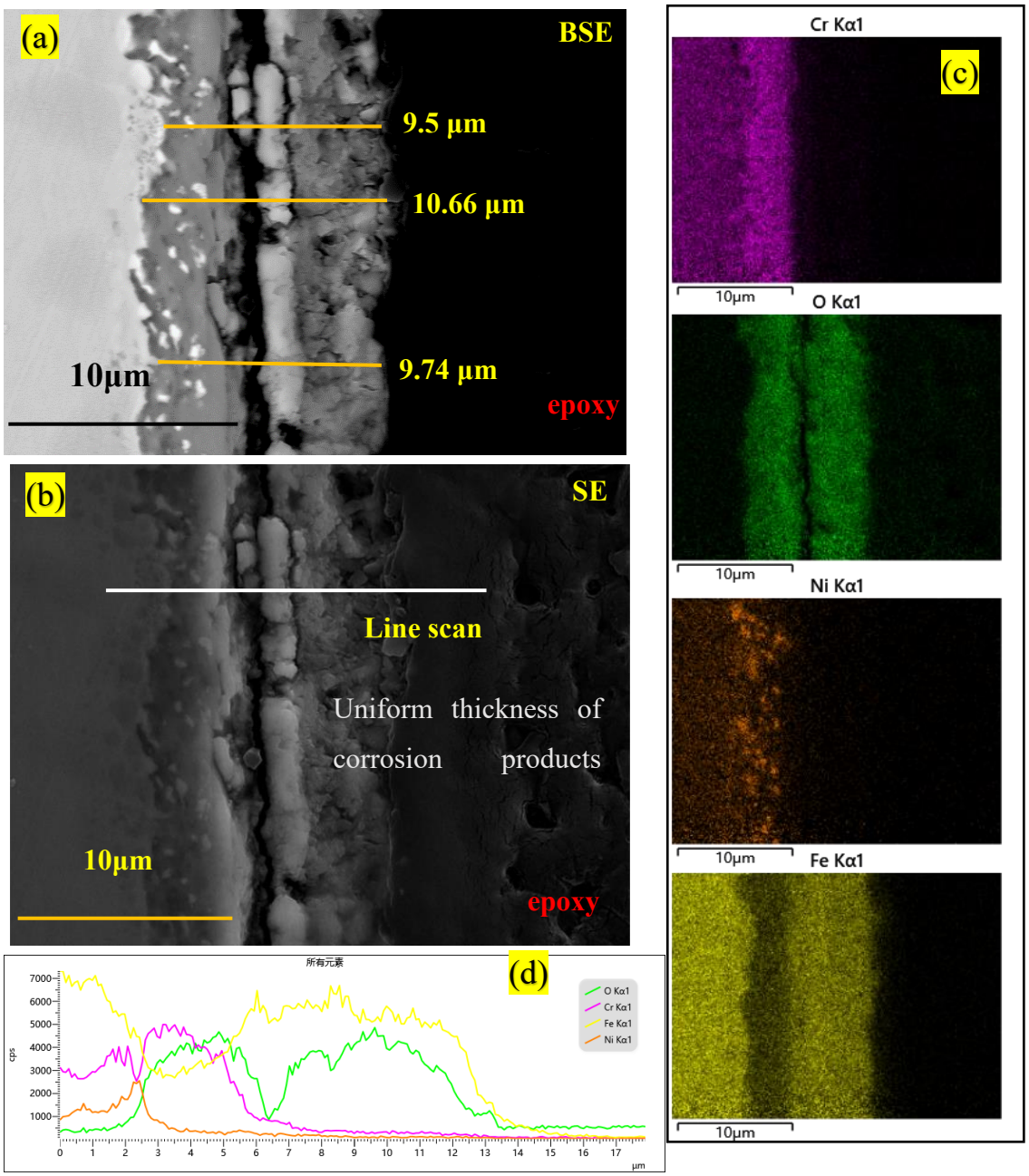

Figure 6-11. SEM-EDS profile of AISI 321 after 7-day thermal cycling immersion in Solar salt at 600°C

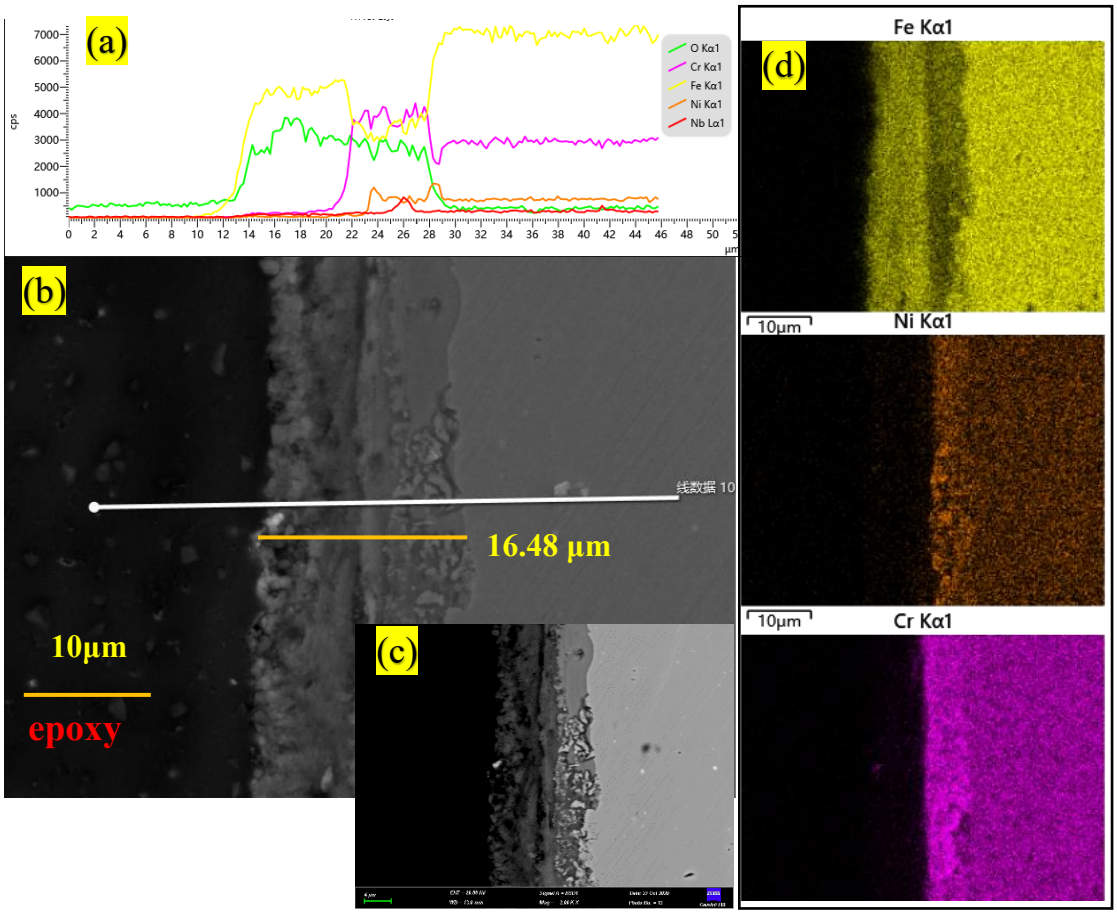

Figure 6-12. SEM-EDS profile of AISI 347 after 7-day isothermal immersion in Solar salt at 600°C

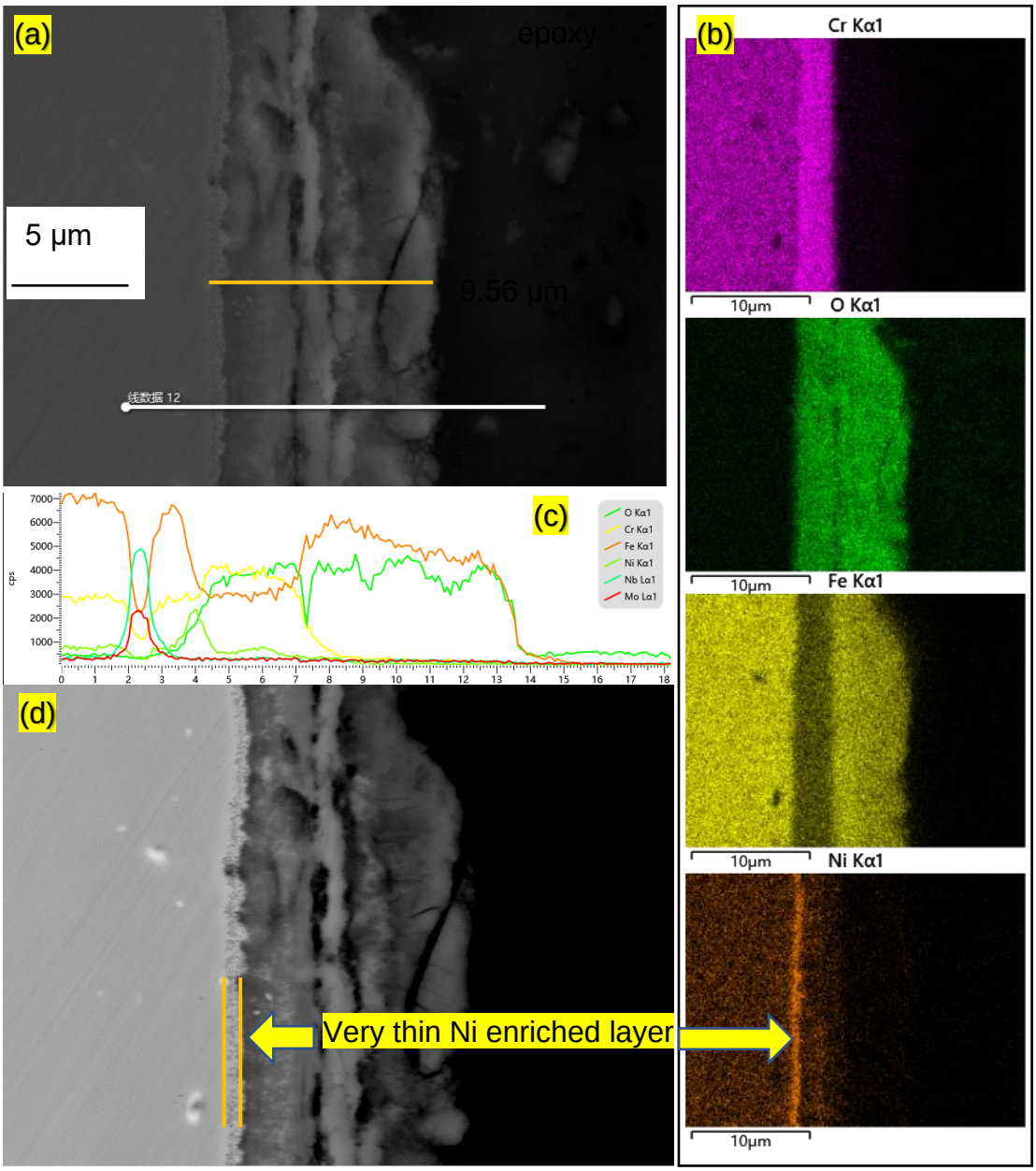

Figure 6-13. SEM-EDS profile of AISI 347 after 7-day thermal cycling immersion in Solar salt at 600°C

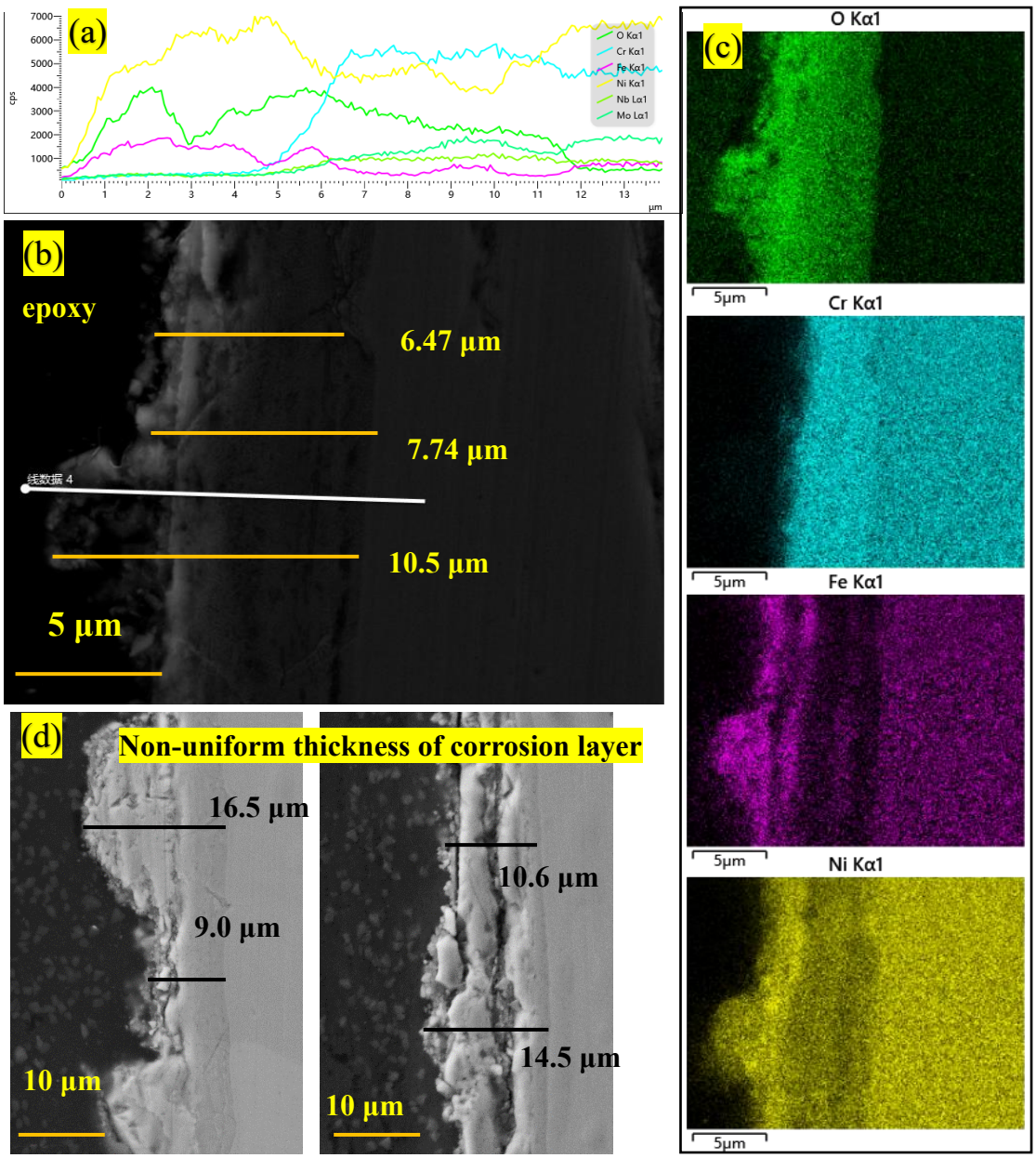

Figure 6-14. SEM-EDS profile of IN 625 after 7-day isothermal immersion in Solar salt at 600°C

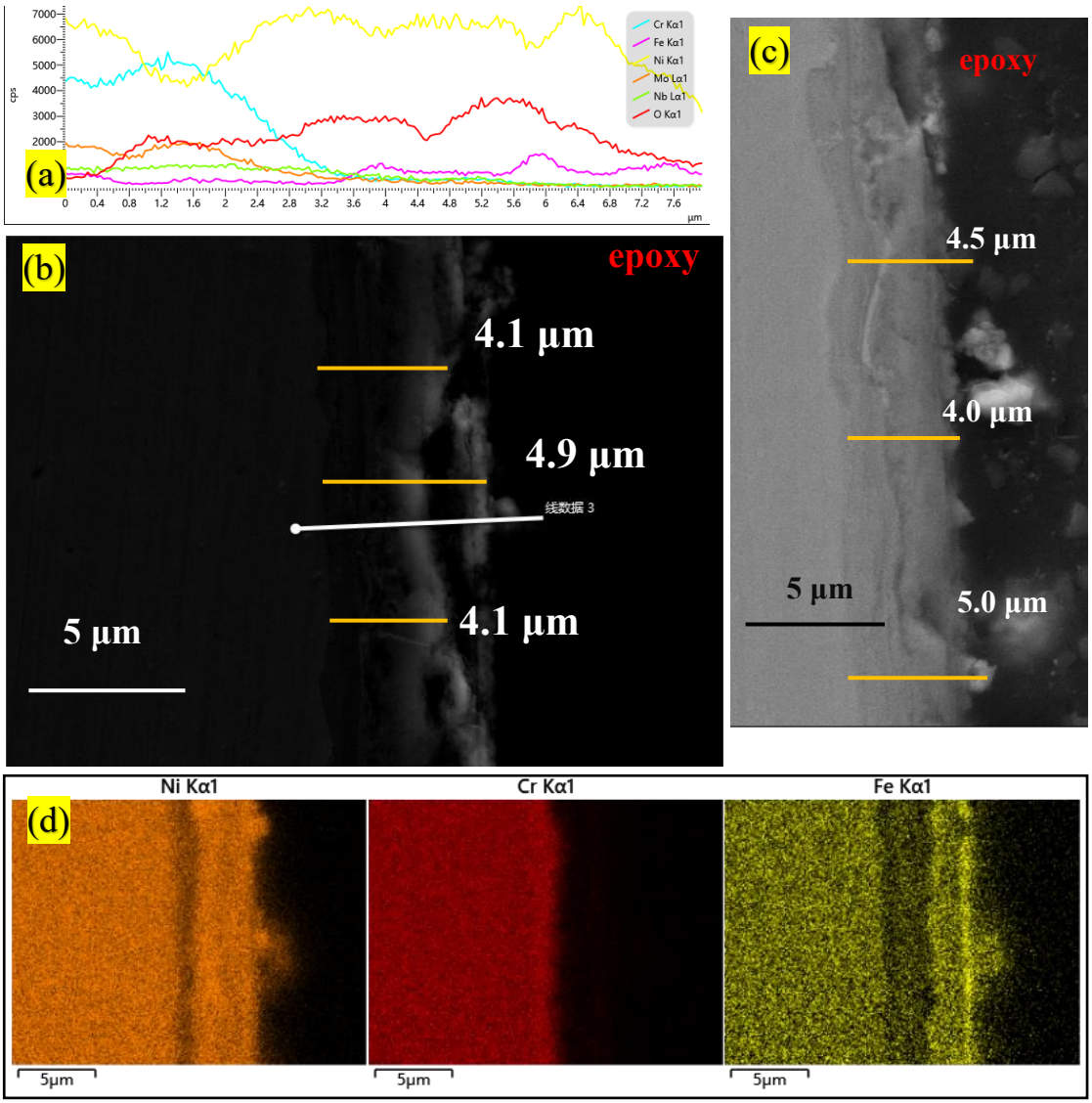

Figure 6-15. SEM-EDS profile of IN 625 after 7-day thermal cycling immersion in Solar salt at 600°C

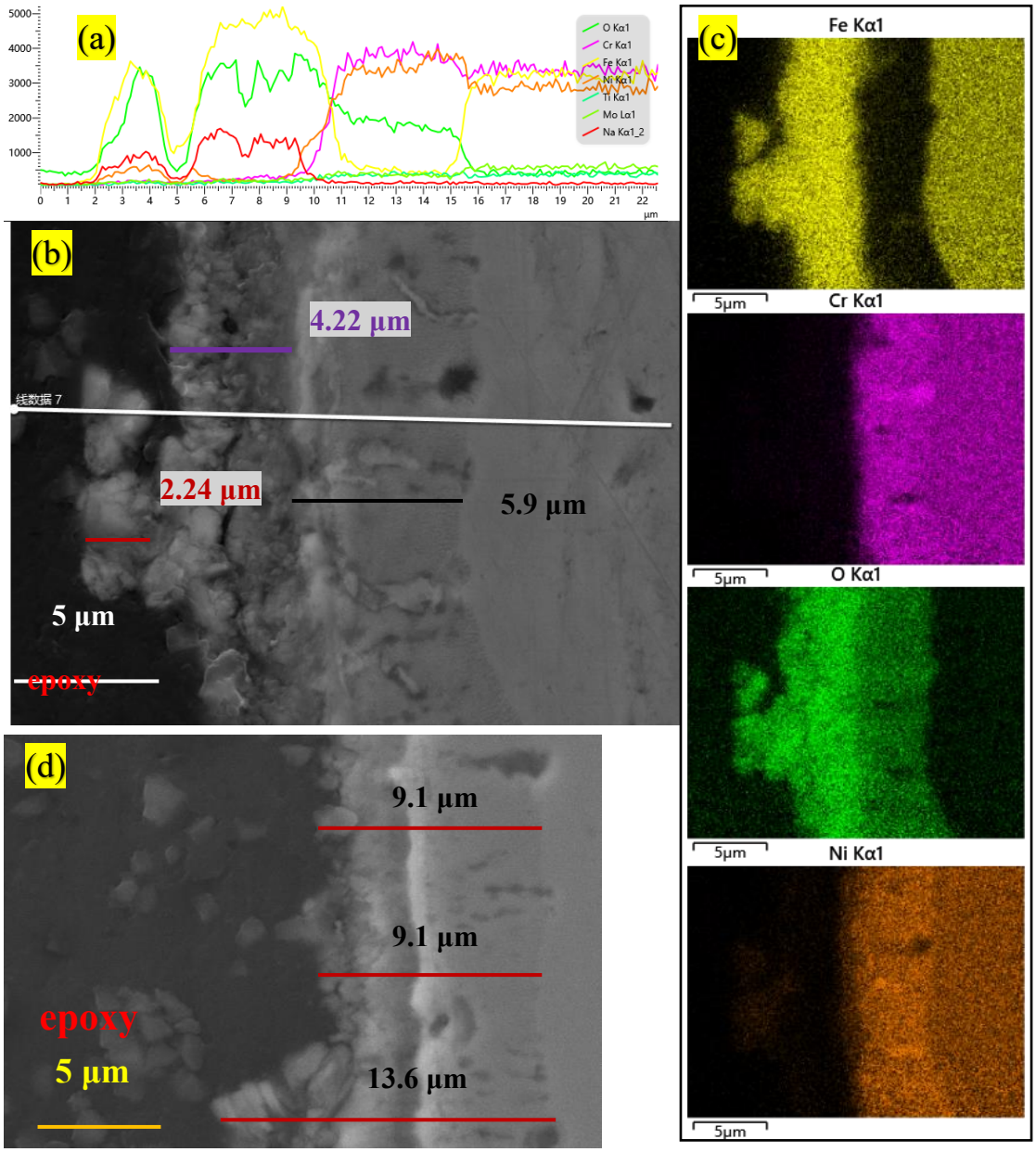

Figure 6-16. SEM-EDS profile of IN 825 after 7-day isothermal immersion in Solar salt at 600°C

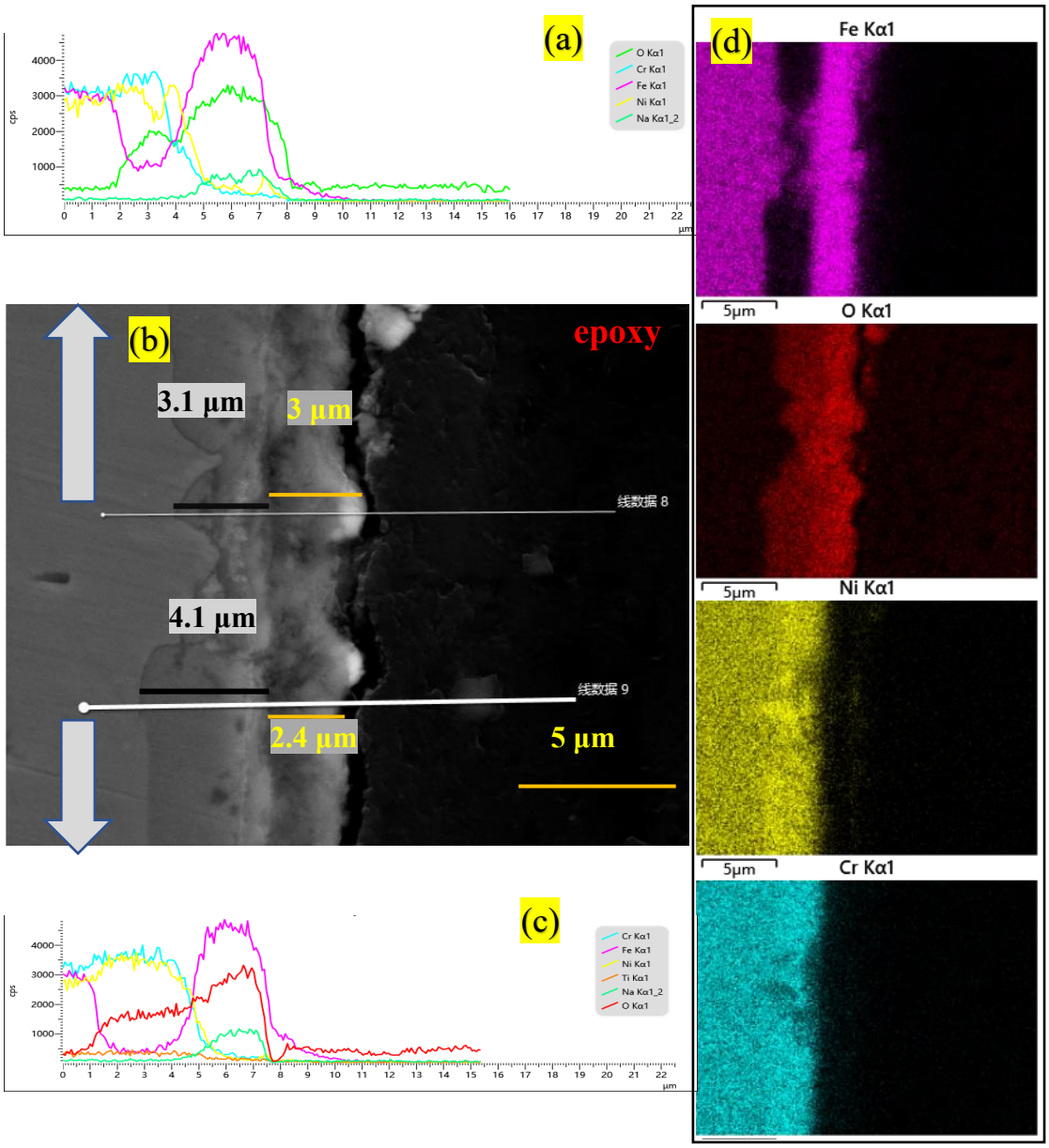

Figure 6-17. SEM-EDS profile of IN 825 after 7-day thermal cycling immersion in Solar salt at 600°C

6.3.5 Discussion

The corrosion rate (CR) obtained from weight loss and depth of corrosion layer was summarised in Table 6-5 (the unit of CR was modified to μm/w). The CR of studied alloys obtained from weight loss and cross-sectional analysis show similar trend with the corrosion of resistance of investigated alloys following this order: IN 625 > IN 825 > AISI 347 > AISI 321. The CR of isothermal immersed samples is 1.5-5 times higher than that under thermal cycling condition. This is different from the conclusion reported in the only literature (Bradshaw and Goods, 2001b) on thermal cycling. However, the thermal cycling experiment protocol published by Sandia Laboratory (Bradshaw and Goods, 2001b) was based on a

7.5 hrs residence time at the maximum temperature of 565 °C and 0.5 hours cooling in ambient air 95°C for 500 cycles. It was reported that thermal cycling increased the corrosion rate of the three stainless steels moderately when compared to isothermal immersion corrosion tests. The difference in the results and conclusions from this study is likely due the longer residence time of 12 hrs between peak and lowest temperatures and corresponding effect of extended duration at lower temperatures in the cycle.

Due to the continuous immersion in molten salt at 600˚C during isothermal tests, the oxide layers on formed have more potential to breakdown and spall off (Encinas-Sánchez et al., 2019). In comparison, the intermittent cooling process or period of immersion at lower temperature during thermal cycling interrupts the continuous thermal effects on the formation and stability of oxide layers, thus reducing the potential for breakdown and spallation of the oxide layers. The spallation behaviour is linked to the instability of oxide layers at high temperatures. The thermal expansion and contraction of corrosion layers is expected to occur during thermal cycling due to the regular change of temperature. Despite the difference in coefficients of thermal expansion and elastic modules of base metal between corrosion layers (Yin et al., 2021), the cooling effect during thermal cycling for 12 hours per 24 hour cycle, induces lower thermal stresses to help to improve the adherence of corrosion multi-layers than in cooling-free isothermal process (Bradshaw and Goods, 2001b). It's worth noting that any residual thermal stress (Yin et al., 2021) caused by cooling process during thermal cycling between multi-layers in this study is likely to be significantly lower than thermal stress levels expected from simulated thermal shock experiments (Bradshaw and Goods, 2001b). The evidence from these studies clearly shows that thermal cycling relieves and delays the thermal effect on the multi-layers, and the tendency for spallation to occur.

Solar salt is known to remain stable at temperatures up to 565 ˚C and will decompose into nitrite salt and oxide ions (Walczak et al., 2018) at higher temperature, thus increasing the corrosivity of the molten salt and the corrosion rate of exposed alloys (Bell et al., 2019). Longer residence at 600 ˚C for isothermal test means that more oxide ions are available within in a progressively increasing corrosive molten salt system than in thermal cycling test (Bonk et al., 2020). The effect of thermal cycling therefore reduces the corrosiveness of the system by slowing down the decomposition process.

Furthermore, referring to the Figure 6-10-Figure 6-17, a double oxide layer was observed at the corrosion interface. An Inner Cr-rich oxides film acts as protective layer against corrosion because of low diffusion rate of oxygen and metal ions through the film (Gui et al., 2017)

and outer Fe-rich layer protect the dissolution of the inner Cr-rich oxide into salt. The diffusion order of metal ions in Cr-oxides is $D_{Fe}>D_{Ni}>D_{Cr}$ (Lobnig et al., 1992b). Atomic diffusion is enhanced by increasing temperature and duration of tests (Bataillou et al., 2018). Longer residence time of immersion at 600˚C for isothermal test is believed to promote the outward diffusion of Fe and Cr from the base material, resulting in forming thicker corrosion layers than in samples from thermal cycling tests. The mechanisms by which thermal cycling is likely to influence the rate of material degradation and corrosion layer behaviours in the long term still needs to be investigated.

Table 6-5. Corrosion rate obtained from weight loss and depth of corrosion (uniform unit: μm/w, ISO and TC indicates isothermal and thermal cycling)

Material/ condition	Inner layer μm	Outer layer μm	Total thickness μm/w	Corrosion rate from WL	
				μm/year	μm/w
AISI 321 ISO	13	12-39	25-52	434	8.32
AISI 321 TC	4.2	5.8	10	114	2.2
AISI 347 ISO	8	8.4	16.4	317	6.08
AISI 347 TC	4.25	5.3	9.56	124	2.38
IN 625 ISO	6.47	3-10	9.5-16.5	128	2.45
IN 625 TC	1.8	2.7	4.5	57.7	1.11
IN 825 ISO	5.9	3.2-7.7	9.1-13.6	109	2.09
IN 825 TC	3.6	2.7	6.3	80.8	1.55

The corrosion layer of Ni-based alloy is thinner than that of stainless steels, indicating that AISI 321 and AISI 347 experienced severer corrosion process than IN 625 and IN 825 from cross-section observation. The double corrosion layer was formed on the surface of stainless steel, and the main corrosion product is outer sodium iron oxide, iron oxide and inner iron chromium oxide. The occurrence of non-uniformity in corrosion thickness for stainless steels is caused by the spallation of the bad adherence corrosion layer, which often occurred in isothermal immersion test. The corrosion products formed on the stainless-steel surface have been previously reported and also are confirmed in this study to be Fe_2O_3 and Fe_3O_4 (Zhang et al., 2020) based on the following Equation 22 to Equation 26 (Hu et al., 2018).

$$NO_3^- + 2e^- \leftrightarrow NO_2^- + O^{2-}$$ Equation 22

$$Fe + O^{2-} \rightarrow FeO + 2e^-$$ Equation 23

$$FeO + O^{2-} \rightarrow Fe_3O_4 + 2e^-$$ Equation 24

$$Fe_3O_4 + O^{2-} \rightarrow Fe_2O_3 + 2e^-$$ Equation 25

$$\frac{1}{2}Fe_2O_3 + \frac{1}{2}O^{2-} + Na^+ \rightarrow NaFeO_2$$ Equation 26

Sodium and potassium nitrate always exhibited weak basic melt below 570°C and iron forms a passive oxide layer to mitigate the diffusion of soluble chromium from the metal substrate (Bell et al., 2019). Above temperature of 570°C and close to 600°C, the basicity increases significantly as the decomposition reaction in Equation 22 from nitrate to nitrite becomes more favourable (Bradshaw and Goods, 2001a, Bell et al., 2019). Meanwhile, according to Equation 26 the iron out layer is converted to sodium ferrite ($NaFeO_2$) which is totally non-protective and consequently results in the corrosion rate increasing (Bradshaw and Goods, 2001a). In this study, the $NaFeO_2$ was identified as the corrosion products on the surface of stainless steels samples from SEM – EDS analysis and XRD patterns in Figure 6-8 and Figure 6-9 respectively. This is also observed in terms of the distribution of elements from cross sectional analysis of alloy – oxide layer interface. The Cr and Ni enriched region was observed in the inner oxide layer line scan due to the selective dissolution and diffusion disparity of alloy elements. Zhang et.al,(Zhang et al., 2020) reported that the corrosion products of $(Fe, Cr, Ni)_3O_4$ mixed oxide spinel are probably present in the inner oxide layer and widely proven to improve the stainless steel corrosion resistance (Soleimani Dorcheh and Galetz, 2016, Liu et al., 2017, Hua et al., 2019) by Equation 27 - Equation 30. In this study, the $FeCr_2O_4$ is the main oxide spinel and well adherent to the bulk material.

$$Ni + O^{2-} \rightarrow NiO + 2e^-$$ Equation 27

$$Cr + 3/2O^{2-} \rightarrow 1/2Cr_2O_3 + 3e^-$$ Equation 28

$$FeO + Cr_2O_3 \rightarrow FeCr_2O_4$$ Equation 29

$$NiO + Cr_2O_3 \rightarrow NiCr_2O_4$$ Equation 30

For nickel-based alloys, they exhibited better corrosion resistance than stainless steels in this study as shown by the result from weight loss measurements and SEM observation. Several researchers have reported that Ni-based alloys' corrosion was insignificant at temperature below 550°C (Kruizenga et al., 2013) with it proving difficult to obtain any

corrosion information through typical SEM/XRD methods (Walczak et al., 2018) at 500°C. According the results above, Ni oxide and iron chromium oxide are the main corrosion product formed on the surface of Ni-based alloys by Equation 27, Equation 28 and Equation 29. IN 625 shows mixed Fe and Ni oxides at the outer layer and Cr oxide at the inner layer, while outer Fe oxide layer and inner (Ni, Cr) oxides forms part of the corrosion product layer of IN 825 in both isothermal and thermal cycling experiments.

In this study, the oxygen consumed for the formation of interfacial oxide layers is linked to the decomposition of nitrate ion to nitrite, especially at temperature of 600°C since test were performed in argon.

6.3.6 Summary

The corrosion behaviour of stainless steels; AISI 321 and AISI 347, and Ni-based alloys; IN 625 and IN 825 in solar salts used in concentrated solar power plants were experimentally investigated under isothermal (at 600°C) and thermal cycling conditions (temperatures between 250-600°C) under argon atmosphere. The results of corrosion performance were comparatively studied to evaluate and understand the corrosion mechanism. The main conclusions are as follows.

1. The interaction of stainless steels and nickel alloys with molten salts led to the formation of multi-layered interfacial oxides in both isothermal and thermal cycling conditions. They consist mainly of an inner layer of $Fe_2O_3/Fe_3O_4/ FeCr_2O_4$ and an outer layer of $NaFeO_2$ on stainless steels: AISI 321 and AISI 347, and an inner layer of NiO and/or $FeCr_2O_4$ on Ni-based alloy: IN 625 and IN 825. Also an outer layer of $NaFeO_2$ was found on the surface of IN 825.
2. The main driving force for material loss is linked to the rate of spallation loosely held, porous, and poorly adherent Sodium–Iron spinel ($NaFeO_2$) layer. This layer easily spalls off to expose the inner and more protective $FeCr_2O_4$ and Fe_3O_4 layer (for stainless steels), and NiO and/or $FeCr_2O_4$ (for Nickel alloys) to further degradation by molten salt species. This process is more dominant under isothermal conditions and mitigated by the thermal cycles used in this study.
3. Rate of material loss was higher in samples from isotheral immersion test at 600 °C than in samples from thermal cycling immersion tests between 250 and 600°C. This was observed for both stainless steel samples and samples from Nickel alloys and believed to be linked to the effect of intermittent night – time cooling over a 12 h residence time at 250°C on the stability and adherence of interfacial oxide layers.

4. The increase in corrosion rate under isothermal conditions is due to increase in the rate of decomposition of nitrate salts to nitrite. This increases the aggressiveness of the corrosion media. This effect is suppressed under thermal cycling conditions.
5. The combined effect of 12 h residence time at 250°C and short experiment duration helped to understand the potential synergy of thermal fatigue effect from thermal cycling and electrochemical activities of molten salt species on the rate of spallation of interfacial oxide layers and overall material loss rate.

6.4 Corrosion evaluation of stainless steels and Ni-based alloys under air condition

This section was originated from conference paper "Corrosion Characteristics of Iron-Nickel-Chromium Alloys in Molten Nitrate Salts Under Isothermal and Thermal Cycling Conditions" in AMPP Annual Conference + Expo.

https://onepetro.org/amppcorr/proceedings/AMPP22/5-AMPP22/D051S049R002/488636

Paper No.
17529

Corrosion Characteristics of Iron-Nickel-Chromium Alloys in Molten Nitrate Salts under Isothermal and Thermal Cycling Conditions

Qingyang Liu
University of Leeds
Woodhouse lane
Leeds, West Yorkshire LS2 9JT
United Kingdom

Richard Barker
University of Leeds
Woodhouse lane
Leeds, West Yorkshire LS2 9JT
United Kingdom

Chun Wang
University of Leeds
Woodhouse lane
Leeds, West Yorkshire LS2 9JT
United Kingdom

Jiong Qian
Zhejiang JIULI Hi-Tech
Huzhi Dadao
Huzhou 313028
China

Anne Neville
University of Leeds
Woodhouse lane
Leeds, West Yorkshire LS2 9JT
United Kingdom

Frederick Pessu
University of Leeds
Woodhouse lane
Leeds, West Yorkshire LS2 9JT
United Kingdom

ABSTRACT

The corrosion degradation of metallic components in Concentrated Solar Power Plants (CSP) with molten salt poses significant threat to the continuous safe operation at high temperature. Updated understanding of the corrosion behavior, mechanisms and the properties of corrosion products formed are needed to explain and optimize the corrosion performance of metals. In this study, the corrosion behavior of 321 SS, 347 SS, Alloy 625 and Alloy 825, are investigated in nitrate salt for 7, 14 and 28 days under isothermal; at 565°C, and thermal cycling conditions (between 565 and 290°C) in air. Several corrosion and advance surface evaluation techniques were implemented to characterize the corrosion process. The results show that the corrosion rate after thermal cycles is lower than in isothermal condition. This was due to increased spallation of corrosion products under isothermal test condition than during thermal cycling tests; particularly in stainless steel samples after 28 days. Multilayer corrosion products were observed on the surface of stainless steels and Ni-based alloys from both isothermal and thermal cycling tests. For stainless steels, an outer layer of sodium iron oxide, intermediate iron oxide and an inner layer of iron chromium spinel were found. NiO and Cr-rich oxides that were detected on the surface of Ni-based alloy, serve as protective layers against further corrosion processes.

Key words: Thermal cycling; Corrosion evaluation; Multi-layer; Spallation

6.4.1 Introduction

Significant research has been carried out to investigate the corrosion performance of these materials in simulated molten salt systems in CSPs. Many of these studies have been focused on the effect of temperature and molten salt chemistry on the corrosion behaviour of selected alloys (Kruizenga et al., 2013, Gomes et al., 2019). However, the effect of thermal cycling on the corrosion behaviour of alloys with molten salt has not received sufficient research attention to date; particularly in the presence of excess amount of oxygen (air). This is critical because oxygen is often considered an impurity in molten salt systems because it increases the risk of corrosion (Bell et al., 2019). As a comparison, the effect of thermal cycling on the corrosion performance of selected material are thoroughly investigated in air.

In this study, the corrosion behaviour of SS 321, SS 347, IN 625 and IN 825, are investigated in nitrate salt for 7, 14 and 28 days under isothermal: at 565°C, and thermal cycling conditions (between 565 and 290°C) in air. Several corrosion and advance surface evaluation techniques were implemented to characterise the corrosion process. The results show that the corrosion rate after several thermal cycles is lower than after exposure to isothermal condition. This was due to increased spallation of corrosion products formed under isothermal condition than those formed under thermal cycling conditions; particularly in stainless steel samples after 28 days. Multilayer corrosion products were observed on the surface of stainless steels and Ni-based alloys from both isothermal and thermal cycling tests. For stainless steels, an outer layer of sodium-iron oxide, intermediate iron oxide and an inner layer of iron-chromium spinel were found. NiO and Cr-rich oxides that were detected on the surface of Ni-based alloy, serve as protective layers against further corrosion processes.

6.4.2 Experiment methodology and test protocol

The material and salt preparation procedure are same with the previous test and detailed procedure are shown in 7.2. In this part, the temperature for isothermal and thermal cycling was adjusted to 565˚C to simulate as close as possible for the real plant operation scenario in a long-run service. The duration for the tests were up to 28 days (cycles) and the samples were taken out after 7 and 14 days to check the evolution of the corrosion process and growth of corrosion products.

6.4.3 Corrosion rate measurement

Figure 6-18 presents the mass loss and corrosion rate data of the studied alloys after isothermal and thermal cycling immersion test in solar salt. In general, the corrosion resistance of four alloys are in this order: 625 > 825 > 347 SS> 321 SS. The mass loss and corrosion rate of samples from isothermal tests are higher than samples from thermal cycling tests, indicating that a more severe corrosion process is occurring under isothermal conditions. This is also consistent with previously published results from similar study under argon atmosphere (Liu et al., 2022a). In both isothermal and thermal cycling tests, the mass loss of stainless steels increased steadily with prolonged immersion time while the mass loss of Ni-based alloys increased only slightly. However, the corrosion rate decreased with increased immersion time over 28 days, which is also consistent with similar studies in the literature (Bell et al., 2019). According to the literature (Bell et al., 2019), the corrosion process can be divided into two regimes; early impurity driven corrosion could lead to an initially high corrosion rate until the impurities are exhausted and corrosion becomes driven by the diffusion of electrochemically active species across the oxide – layer containing interface (Bell et al., 2019). It is known that the formation of a corrosion product layer could provide diffusion barrier to oxygen and metal ions and protect metal against further corrosion(Gui et al., 2017). Under the thermal cycling conditions explored in this study, the results presented in Figure 6-18 shows a lower corrosion rate under thermal cycling conditions than in isothermal tests over 28 days for all alloys investigated. This is an indication that the range of temperature used for the cooling phase and the long residence time during this period helps to slow down the kinetics of corrosion and potentially oxide formation, thereby reducing overall material loss rate, even in unlimited supply of oxygen. The intermittent cooling effect during the thermal cycles is believed to have also provide a break in the aggressive molten salt - metal interaction typically enhanced by high temperature to improve the adherence of initially formed corrosion oxide layers at 565°C (Sutter et al., 2021). Also, the metal ion solubility and diffusion of alloy elements for corrosion

at the interface can be temperature dependent. This implies that thermal cycling process in this study could also affect the corrosion process by altering element distribution of the bulk material towards the molten salt – material interface.

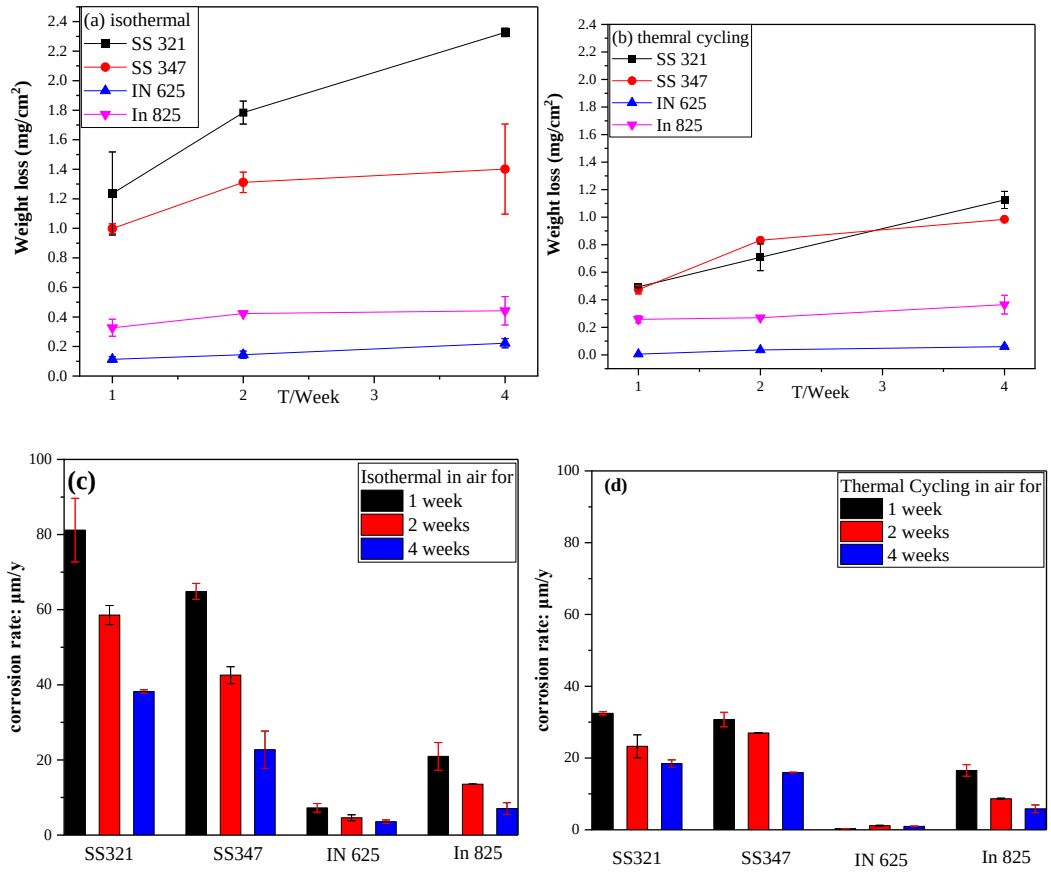

Figure 6-18. Mass loss and corrosion rate of 321 SS 347 SS, 625 and 825 specimens under isothermal and thermal cycling in solar salt for 7 days, 14 days and 28 days.

6.4.4 Identification of corrosion products via XRD and spectra

The XRD patterns confirmed that the oxide layers formed on the surface of 321 SS and 347 SS in solar salt are chromium oxide (Cr_2O_3), iron chromium spinel ($FeCr_2O_4$), iron oxide (Fe_2O_3), and a less dense, and less protective layer of sodium ferrite ($NaFeO_2$). Nickel oxides formed on the corrosion surface of 625, while various forms of iron chromium spinel, chromium oxide and iron oxide were observed on the surface of 825 due to its higher iron content and lower nickel content. Evidence of these corrosion products are presented in Figure 6-19. It is worth noting that the corrosion products formed on isothermal samples after 1-week immersion test, were similar to those formed on the samples from 4-week thermal cycling tests for both stainless steels.

Raman spectroscopy results, shown in Figure 6-20, showed that Fe_2O_3, Cr_2O_3 and $FeCr_2O_4$ spinel were detected on the surface of stainless steels after isothermal and thermal cycling

condition. The corrosion products formed on the surface of 625 were a mixed oxide of Fe and Ni and were identified as $NiFe_2O_4$ ($NiO\text{-}Fe_2O_3$). The main corrosion products formed on the 825 surfaces were identified as Fe_2O_3, Cr_2O_3 and $NiO\text{-}Fe_2O_3$, which shows good agreement with XRD results.

6.4.5 SEM surface observation

To better understand the corrosion process and mechanism, the corrosion layer was examined with SEM. The SEM images and corresponding magnified images are shown in Figure 6-21 - Figure 6-23, as well as EDX data shown in Table 6-6 - Table 6-8.

For 321 SS, as shown in Figure 6-21 (a) – (f) the corrosion surface show evidence of coarse morphology with increase immersion time under isothermal and thermal cycling condition. However, the corrosion surfaces from isothermal tests were coarser than that from thermal cycling tests. From the EDX result, the corrosion products are identified as iron oxide, iron chromium spinel and sodium ferrite. It is worth noting from the results from SEM-EDX and XRD, that $NaFeO_2$ was found on the surface of isothermal samples for all test duration and only found in SS321 after 4-week under thermal cycling condition (identified by XRD). In addition, higher Cr content was observed on the samples after 1-week isothermal and thermal cycling tests, indicating a mild corrosion process under these conditions, as shown in Table 6-6. Thermal cycling suppresses the kinetics of corrosion process through the slower kinetics of formation of corrosion products and its transformation into a porous layer.

A similar trend was observed on the surfaces of 347 SS samples in Figure 6-22 (g) – (l). With increase of isothermal immersion time, the corrosion surfaces became coarser, with evidence of increase coverage by crystalline corrosion oxide layer identified as Fe_2O_3 and $NaFeO_2$ by EDS in Table 6-7. For the samples from thermal cycling test, the concentration of Fe, Cr and Ni decrease from 1-week to 4-week, while the O content continued increasing from 7.7wt % after 1-week to 33.1 wt.% after 4-week, indicating the corrosion/oxidation process are ongoing with increase of immersion time. Na was also observed on samples after all duration isothermal tests and 4-weeks of thermal cycling tests, indicating the formation of $NaFeO_2$. This shows the dynamic growth and evolution of the corrosion products on the surface to form $NaFeO_2$ under thermal cycling conditions take longer time than under isothermal conditions (1 week). This further highlights the effect of thermal cycling on the kinetics of corrosion product evolution in air. The spallation behavior of corrosion products observed in this study for stainless steel samples is consistent with reports by other researchers (Bradshaw and Goods, 2001b, Gomes et al., 2019, Trent et

al., 2016b, Liu et al., 2022a). In this study, the $NaFeO_2$ formed as particles on the surface in Figure 6-22 (h) after 2-week isothermal immersion and spalled off with increase the immersion time to 4 weeks in Figure 6-22 (i).

The corrosion surface of 625 after 4-week isothermal and thermal cycling immersion tests are shown in Figure 6-23 (m) – (r). No obvious corrosion products or corrosion layer was found on the smooth surface. Referring to XRD results, the NiO was the primary oxide layer on the surface of isothermal samples, where the polishing marks are apparent on the surface as shown in Figure 6-23 (m)-(o). In Figure 6-23 (p)-(r), the corrosion surface of sample from thermal cycling test is covered by randomly scattered crystals, which were a mixture of Ni and Fe oxides. According to mass loss and XRD result, the corrosion rate and intensity of oxides are low, indicating a thin and protective layer. This was confirmed by the SEM images. For 825, polishing marks were apparent on the surfaces after 1-week isothermal and thermal cycling immersion tests. With increasing test duration, more crystalline products formed on the samples, which are identified as NiO, Fe_2O_3 and $FeCr_2O_4$ via XRD patterns and Raman spectra.

6.4.6 Cross-sectional observation

Figure 6-24 shows the cross-section images of studied alloys after 4-week corrosion immersion tests in molten salt under isothermal and thermal cycling conditions. A thin layer (~ 3µm) was found on the 321 SS surface, which was identified as Fe_2O_3 via EDX line scan in Figure 6-24 (a) and (b) in both conditions. The corrosion product was scattered on the surface without forming a continuous layer, shows good agreement with the SEM results. A continuous oxide layer; mainly Fe_2O_3 (~3µm) was found on the surface of 347 SS after 4-week isothermal immersion. In comparison with corrosion product on 347 SS sample from thermal cycling tests, Fe_2O_3 crystal was scattered on the surface, as the red arrows shown in Figure 6-24 (d). It can be inferred that the thermal cycling suppresses the kinetics of oxide layer formation due to the intermittent cooling effect, thereby limiting the uniform coverage of the surface by the oxide layers. Thin layer of NiO; not easily visible but identifiable by XRD, were found on the surface of 625 after isothermal or thermal cycling test as shown in Figure 6-24 (e) and (f). 625 exhibited highest corrosion resistance against molten salt in both thermal conditions. In comparison with IN 625 sample, mixed oxides of Fe, Ni and Cr formed on the surface of 825 after 4-week immersion test in molten salt as shown in Figure 6-24 (g) and (h) in both conditions.

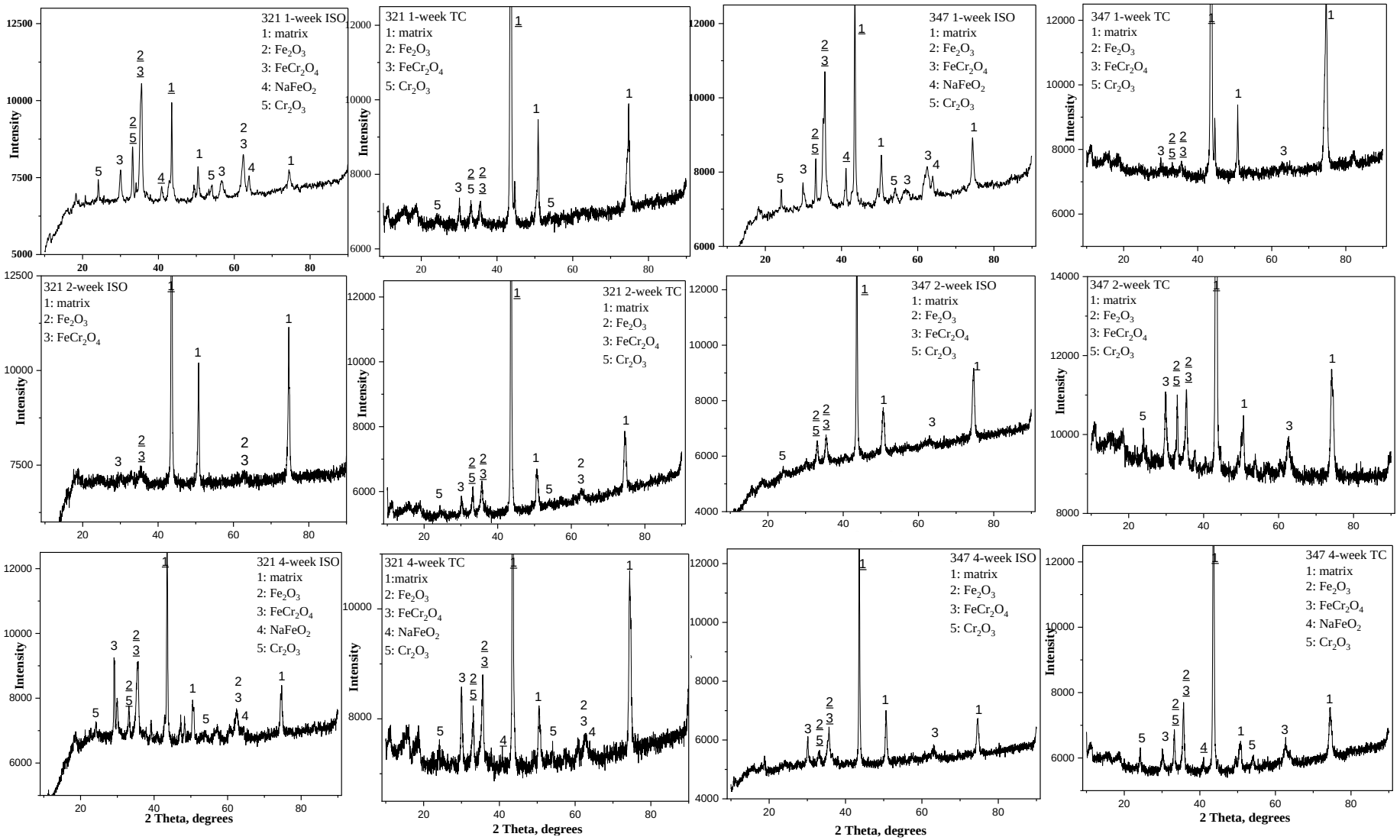
321 1-week ISO
1: matrix
2: Fe2O3
3: FeCr2O4
4: NaFeO2
5: Cr2O3
321 1-week TC
1: matrix
2: Fe2O3
3: FeCr2O4
5: Cr2O3
347 1-week ISO
1: matrix
2: Fe2O3
3: FeCr2O4
4: NaFeO2
5: Cr2O3
347 1-week TC
1: matrix
2: Fe2O3
3: FeCr2O4
5: Cr2O3
321 2-week ISO
1: matrix
2: Fe2O3
3: FeCr2O4
321 2-week TC
1: matrix
2: Fe2O3
3: FeCr2O4
5: Cr2O3
347 2-week ISO
1: matrix
2: Fe2O3
3: FeCr2O4
5: Cr2O3
347 2-week TC
1: matrix
2: Fe2O3
3: FeCr2O4
5: Cr2O3
321 4-week ISO
1: matrix
2: Fe2O3
3: FeCr2O4
4: NaFeO2
5: Cr2O3
321 4-week TC
1:matrix
2: Fe2O3
3: FeCr2O4
4: NaFeO2
5: Cr2O3
347 4-week ISO
1: matrix
2: Fe2O3
3: FeCr2O4
5: Cr2O3
347 4-week TC
1: matrix
2: Fe2O3
3: FeCr2O4
4: NaFeO2
5: Cr2O3
Intensity
2 Theta, degrees

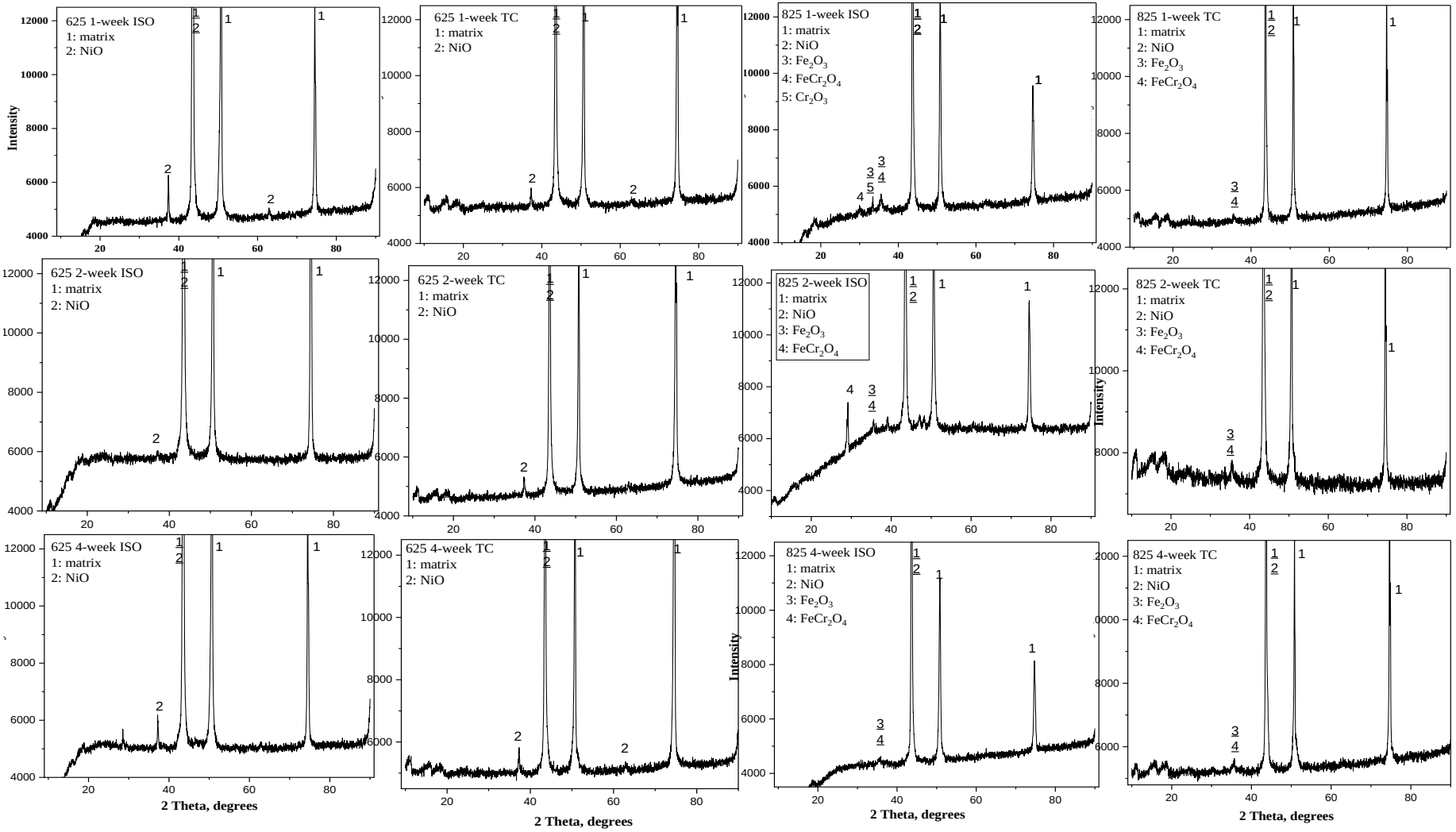

Figure 6-19. XRD patterns of studied alloys under different immersion conditions (phase number with underline meaning the 100% intensity peaks), (a) 321 SS, (b) 347 SS, (c) 625 and (d) 825 after 7-, 14- and 28-day isothermal and thermal cycling test in solar salt.

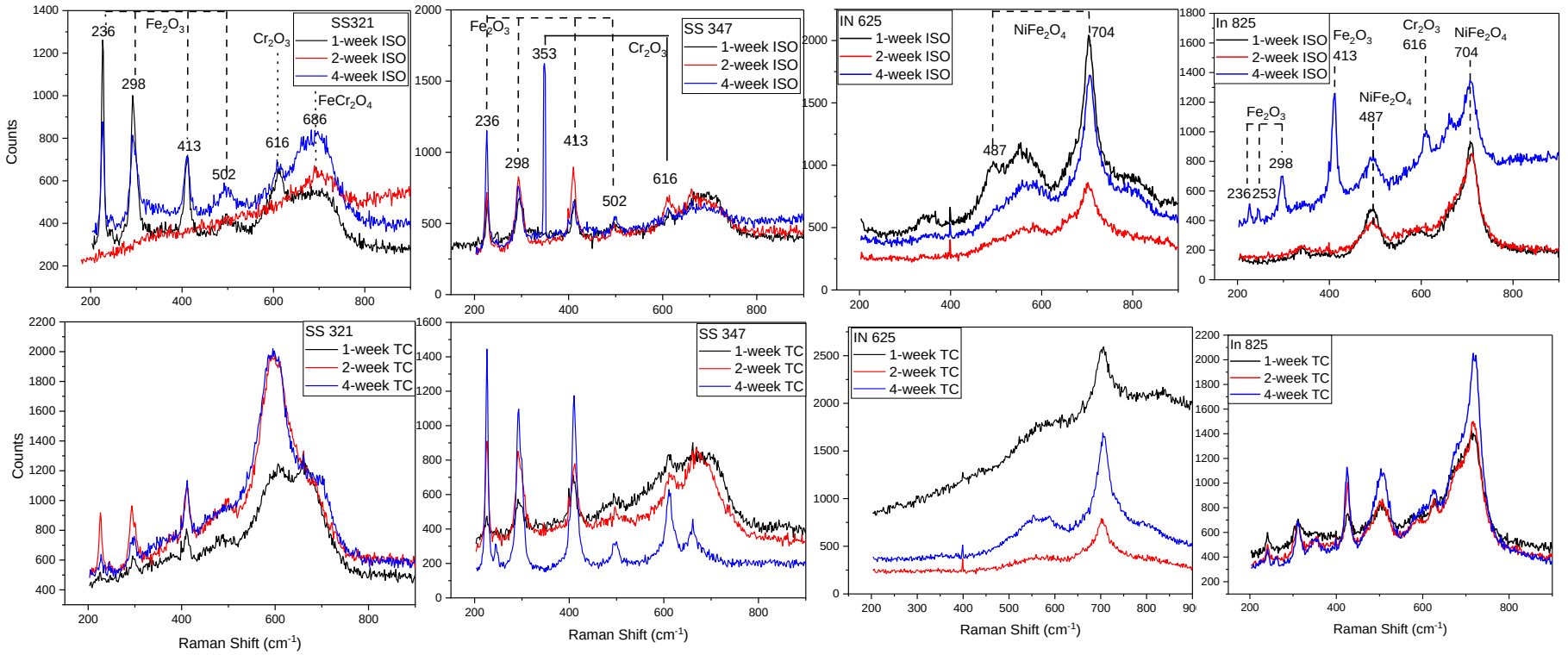

Figure 6-20. Raman spectra of the studied alloys after 1-, 2- and 4-week isothermal and TC tests.

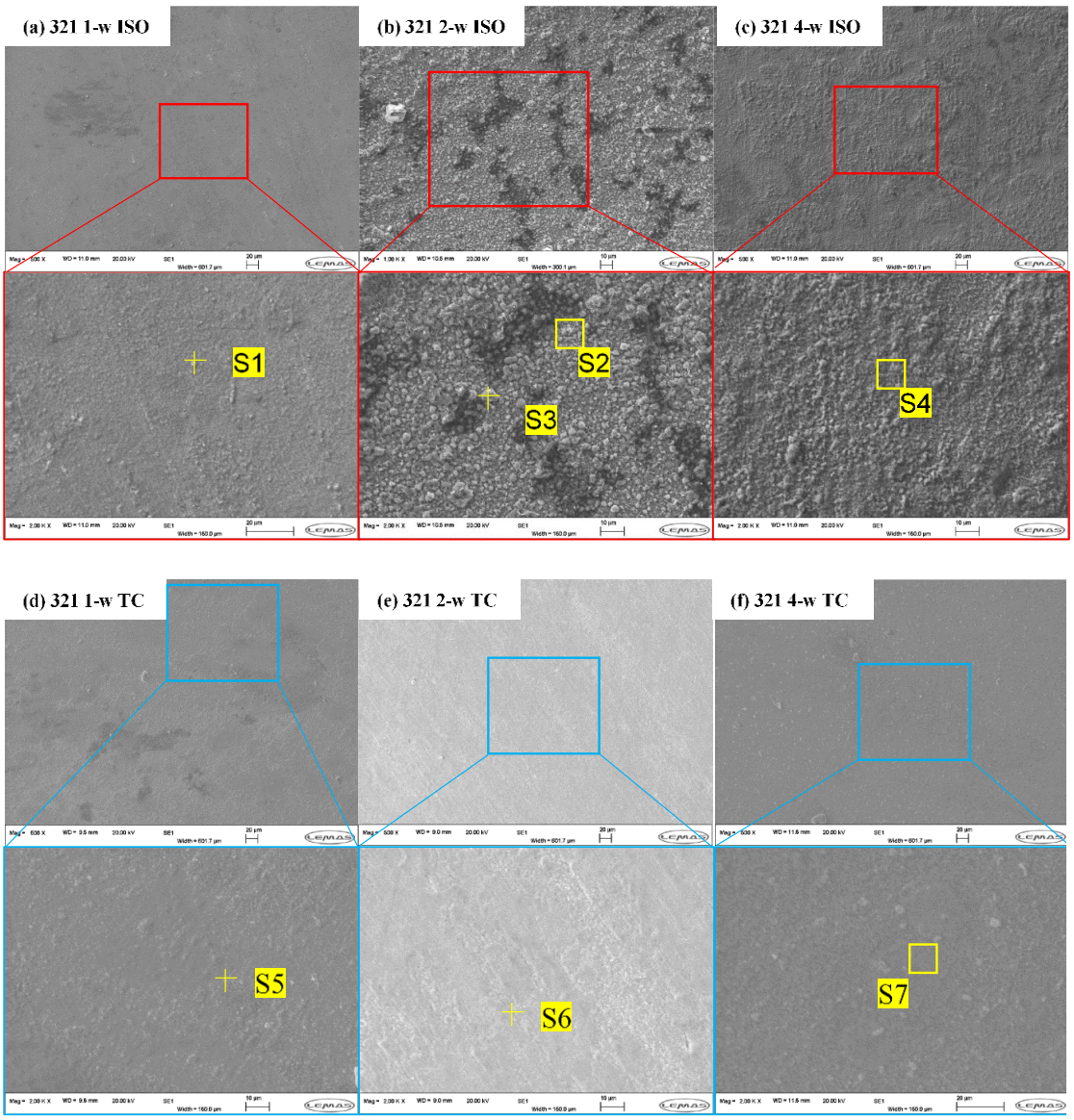

Figure 6-21. SEM surface images and corresponding magnified images of 321 SS

Table 6-6. EDX data for regions in Figure 6-21

Element in wt %	Fe	O	Cr	Na
Spectrum 1	60.1	18.9	12.1	0.1
Spectrum 2	69.30	25.9	1.3	0.5
Spectrum 3	27.6	32.6	1.2	38.6
Spectrum 4	68.8	25.7	1.1	1.0
Spectrum 5	62.3	17.5	10.4	8.3 Ni
Spectrum 6	61	24.6	8.6	5.8 Ni
Spectrum 7	61.1	26.1	6.8	2.7 Ni

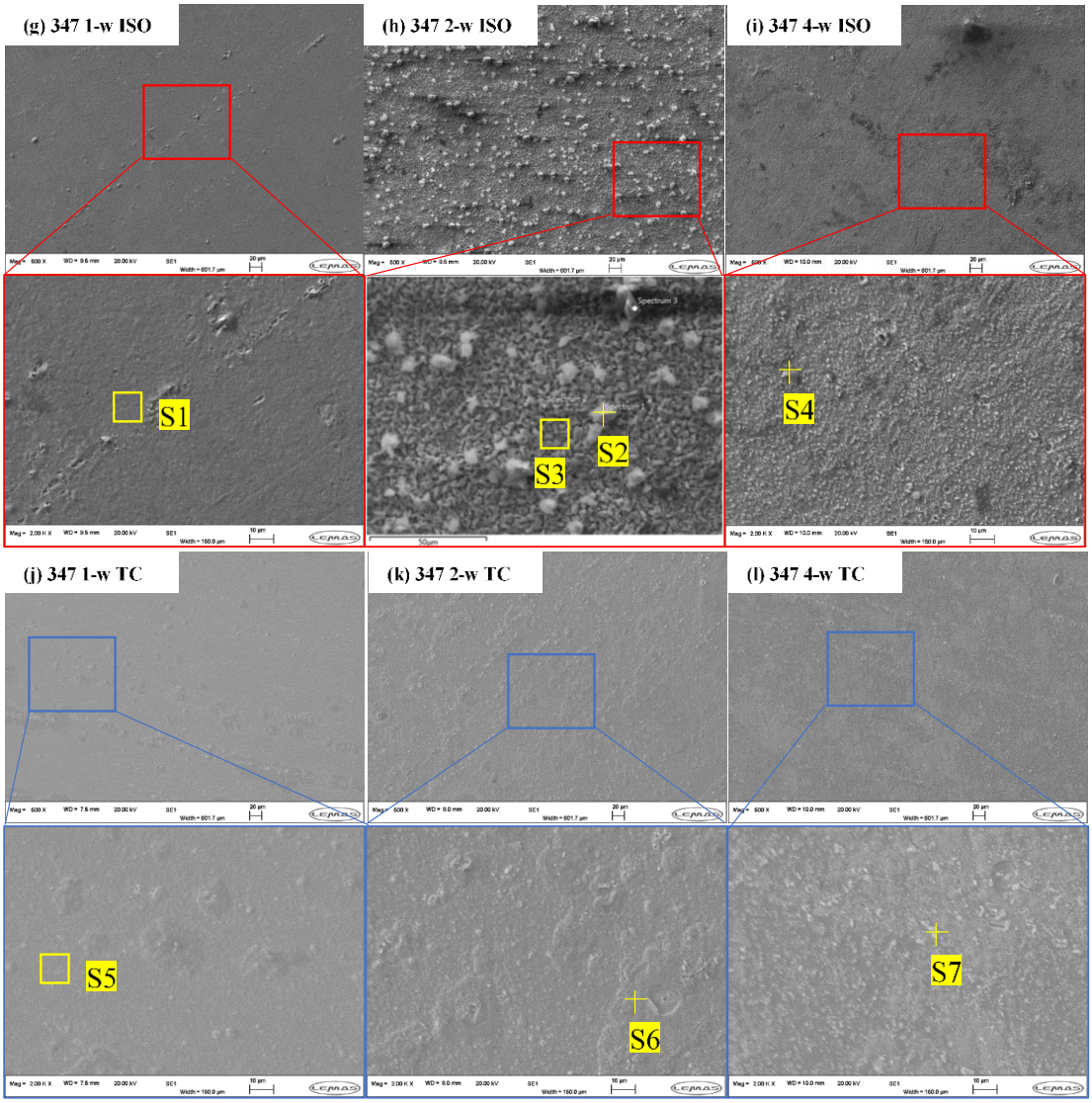

Figure 6-22. SEM surface images and corresponding magnified images of 347 SS

Table 6-7 EDX data for regions in Figure 6-22

Element in wt %	Fe	O	Cr	Na	Ni
Spectrum 1	69.8	17.9	12.1	0.2	12.1
Spectrum 2	18.8	38.7	0.6	30.5	-
Spectrum 3	56.9	28.8	1.2	13.0	-
Spectrum 4	69.1	17.6	2.9	12.5	1.5
Spectrum 5	72.1	7.7	9.3	-	9.9
Spectrum 6	66.1	20.5	8.3	0.2	4.9
Spectrum 7	52.3	33.1	3.0	3.4	1.5

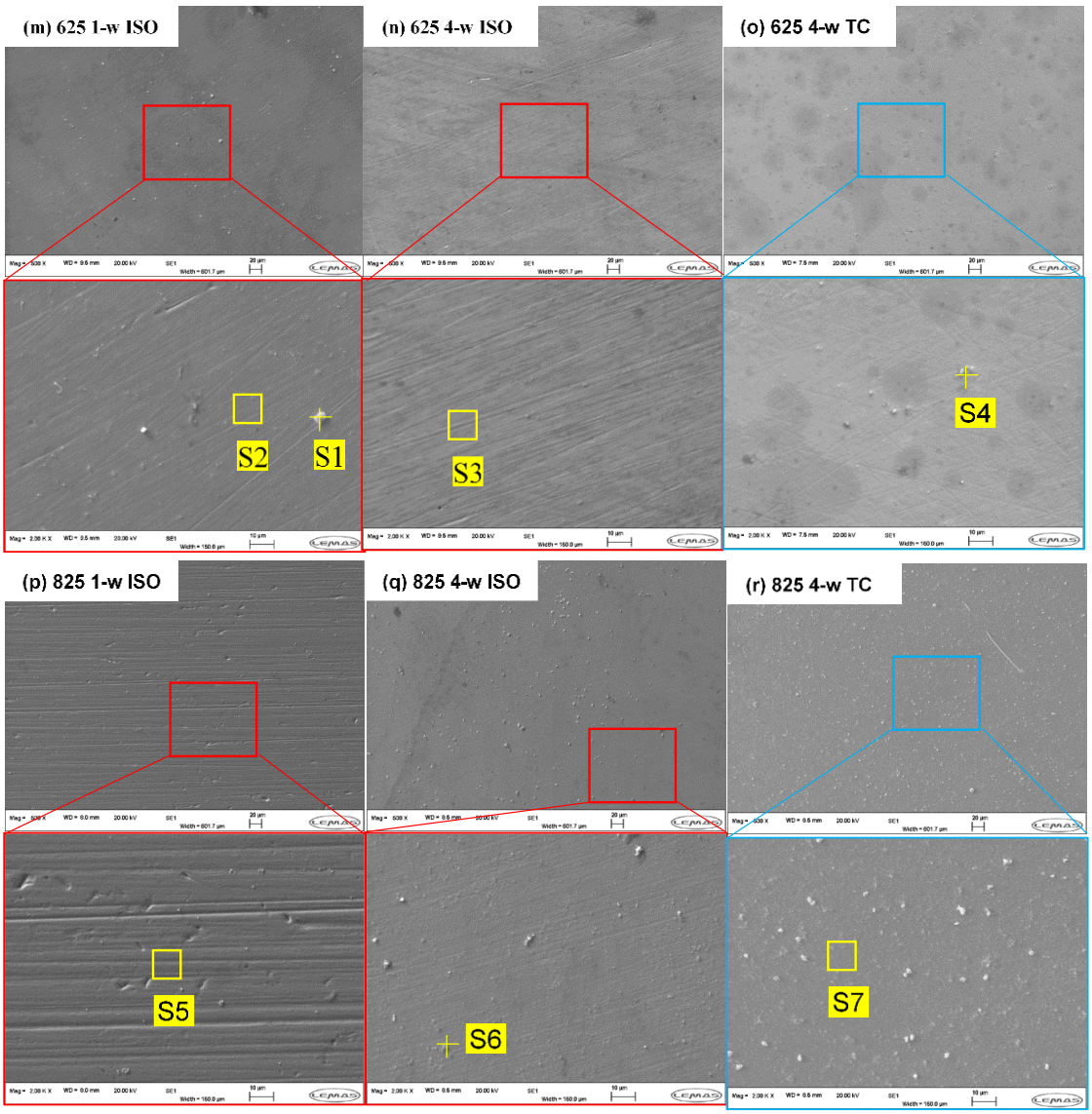

Figure 6-23. SEM surface images and corresponding images of 625 and 825

Table 6-8. EDX data for regions in Figure 6-23

Element in wt %	Ni	Cr	O	Fe	Mo
Spectrum 1	31.1	9.1	24.1	1.5	2.6
Spectrum 2	62.7	17.4	8.7	2.5	5.5
Spectrum 3	57.3	18	11.8	2.7	7.0
Spectrum 4	45.9	12.2	18.6	2.5	2.7
Spectrum 5	38.8	18.6	8.9	28.5	2.1
Spectrum 6	12.8	7.3	25.9	16.5	16.0 Ti
Spectrum 7	36.6	16.9	14.9	28.6	-

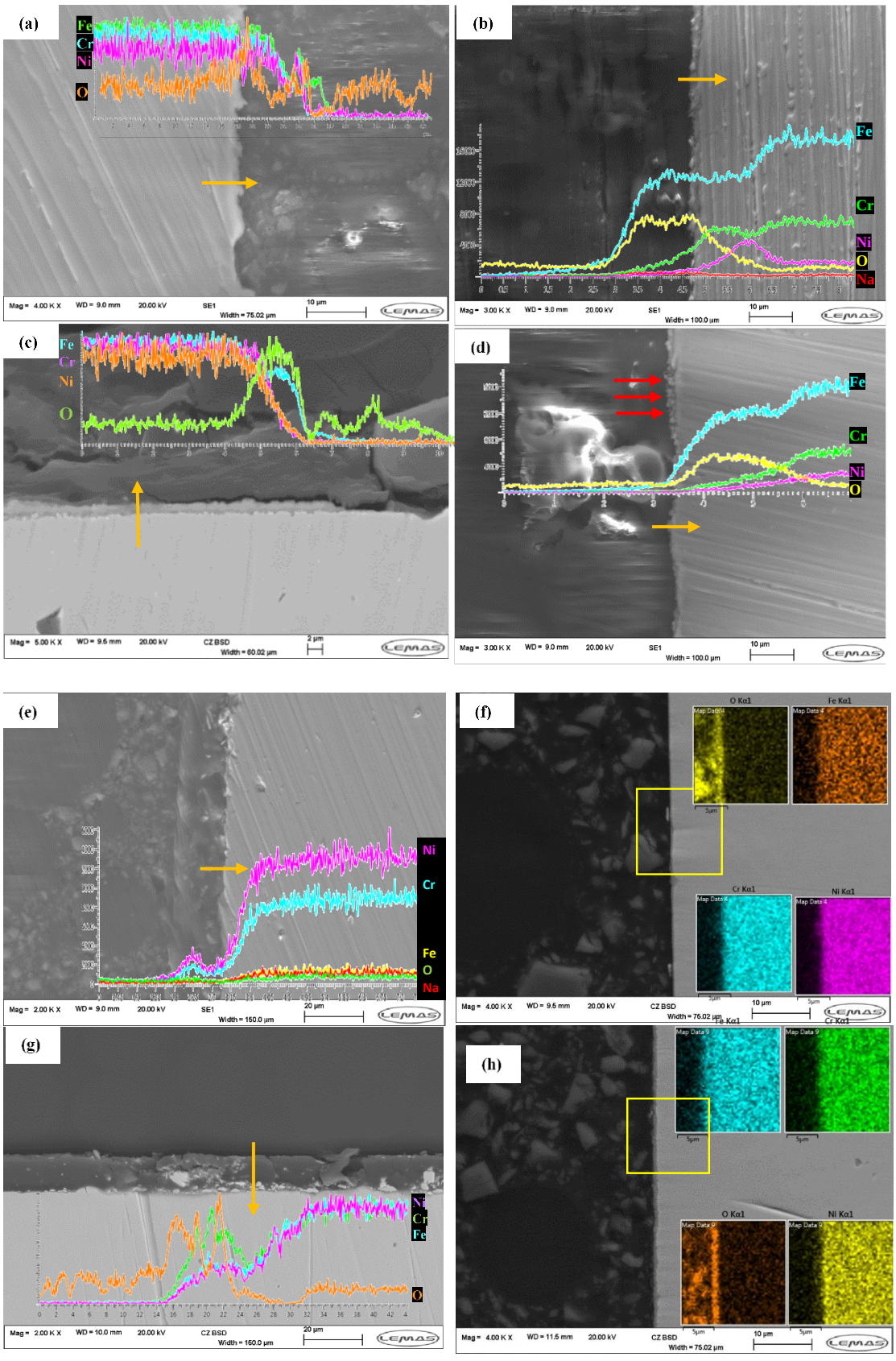

Figure 6-24. Cross-sectional surface observation of studied alloy, (a) (b) 321 SS; (c) (d) 347 SS; (e) (f) 625 and (g) (h) 825 after 4-week isothermal and thermal cycling immersion respectively.

6.4.7 Summary

As previously noted, the higher corrosion rate recorded for isothermal tests than from thermal cycling test in air is mainly linked to the lower time (12 hours per 24 hours experiment time) at maximum temperature of 565°C under thermal cycling condition. A similar trend was also observed in argon atmosphere in a previous publication (Liu et al., 2022a). The cooling effect during thermal cycling, and by extension the lower residence time at peak temperature helps to reduce the kinetics of outward diffusion of key metallic elements within the bulk material, Fe and Cr for oxide formation at the corrosion interface. It is believed that the availability of unlimited supply of oxygen in this work was not able to undermine or suppress the thermal cycling effect. It is therefore likely that the thermal cycling profile adopted in this study helps to improve the resilience, thermal stability and passivity of oxide layers formed. This will be in synergy with the faster kinetics of oxide formation due to the unlimited supply of oxygen. This is likely to reduce metal loss rate and hence lower corrosion rate than in isothermal conditions.

Evidence from SEM images in Figure 6-21 - Figure 6-23; particularly for stainless steel samples shows spallation of formed oxide layers in isothermal tests than under thermal cycling conditions; particularly after 4 weeks. This can also be related to the faster kinetics of $NaFeO_2$ under isothermal conditions (1 week) than under thermal cycling conditions (4 weeks). Total corrosion rate under isothermal conditions is directly influenced by the rate of formation of $NaFeO_2$ and other oxide layers and the rate of its spallation. The former is clearly higher for isothermal tests as shown by the XRD patterns. The latter is due to the stability of $NaFeO_2$ under thermal stresses. $NaFeO_2$ is known to be porous and loosely held to the corroding surface. This is confirmed in Figure 6-21 (b)(c) and Figure 6-22 (h)(i). The intermittent cooling process also helps to prevent the rapid breakdown and spallation of initially formed oxide layers under thermal cycling conditions than under isothermal conditions. This occurs by the tempering effect of extended cooling on the continuous thermal stress build up in isothermal conditions. This helps in maintaining the protective properties of the oxide layers and minimises spallation as shown in Figure 6-21 (d, e, f) and Figure 6-22 (j, k, l). The intermittent cooling effect is also believed to reduce the rate of increase in corrosiveness of molten nitrate salts as result of its response to temperature and linked to the formation of nitrites and oxide ions.

The oxide layer formed on the stainless steels and Ni-based alloys are confirmed as Fe_2O_3, $FeCr_2O_4$, NiO and Cr_2O_3, and follows the equations below.

$$NO_3^- + 2e^- \leftrightarrow NO_2^- + O^{2-}$$ Equation 31

$$Fe + O^{2-} \rightarrow FeO + 2e^-$$ Equation 32

$$FeO + O^{2-} \rightarrow Fe_3O_4 + 2e^-$$ Equation 33

$$Fe_3O_4 + O^{2-} \rightarrow Fe_2O_3 + 2e^-$$ Equation 34

$$\frac{1}{2}Fe_2O_3 + \frac{1}{2}O^{2-} + Na^+ \rightarrow NaFeO_2$$ Equation 35

$$Ni + O^{2-} \rightarrow NiO + 2e^-$$ Equation 36

$$Cr + 3/2O^{2-} \rightarrow 1/2Cr_2O_3 + 3e^-$$ Equation 37

$$FeO + Cr_2O_3 \rightarrow FeCr_2O_4$$ Equation 38

The corrosiveness of nitrate solar salt is linked to its thermal stability and availability of nitrites ions; particularly temperatures ≥ 565°C. Solar salt is known to remain stable at temperatures up to 565˚C, and will decompose into nitrite salt and oxide ions (Walczak et al., 2018) at higher temperature, thus increasing the corrosivity of the salt and the corrosion rate. It is known from classical oxidation theory that the oxidation resistance of these steels depends on the formation and stability of a protective oxide layer, which acts as a diffusion barrier preventing interactions between oxidative or corrosive environments with the underlying metallic substrate (Ramos et al., 2021). In this study, the thin Fe_2O_3 layer was found on the surface of stainless steels as a potential shield to an inner chromium rich oxide layer and Cr depletion.

For nickel-based alloys, they generally exhibited better corrosion resistance than stainless steels in this study as shown by the result from mass loss measurements and SEM observation. Several researchers have reported that Ni-based alloys corrosion is insignificant at temperatures below 550°C (Kruizenga et al., 2013) with evidence of difficulty in obtaining any corrosion information through typical SEM/XRD methods (Walczak et al., 2018). According the results above, Ni oxide and iron chromium oxide are the main corrosion product formed on the surface of IN 825, formed through Equation 36, Equation 37 and Equation 38.

6.4.8 Conclusions

The corrosion behavior of stainless steels; 321 SS and 347 SS, and Ni-based alloys; 625 and 825 in solar salts used in concentrated solar power (CSP) plants were experimentally investigated under isothermal (at 565°C) and thermal cycling conditions (temperatures

between 290-565°C) in air atmosphere for up to 28 days. The results of corrosion behaviour and evolution of interfacial oxide layers were evaluated to improve on current understanding of the underpinning corrosion mechanism. The main conclusions are as follows.

1. From the results, it is clear that even in air with an unlimited supply of oxygen where the kinetics of formation of passive layer can form faster, the overall corrosion rate of samples from isothermal test is still higher than samples from thermal cycling tests. This is more obvious in stainless steels than in nickel alloys.
2. The thermal cycling effect in air is generally linked to intermittent cooling and less residence time at peak temperature over 4 weeks. This also reduces the corrosion rate by suppressing the kinetics of breakdown of nitrate to a more corrosive nitrite.
3. The higher observed corrosion rate in isothermal condition than thermal cycling in air is therefore related to the combination of increased kinetic of oxide formation and breakdown, and rate of spallation of initially formed oxide layer. Interfacial oxide spallation is related to the formation and stability of $NaFeO_2$.
4. $NaFeO_2$ is shown to form faster under isothermal test conditions than thermal cycling test conditions, which is observed and known to be porous and loosely held and likely to spall off easily. The intermittent cooling effect under thermal cycling implies that the kinetics of $NaFeO_2$ formation and spallation is suppressed.

Chapter 7. Comparison of the corrosion behaviour of alloys in air and argon atmosphere

This chapter was originated from paper “Effect of thermal cycling on the corrosion behaviour of stainless steels and Ni-based alloys in molten salts under air and argon” in **Solar Energy**, Volume 238, 15 May 2022, Pages 248-257. https://doi.org/10.1016/j.solener.2022.04.041.

Solar Energy 238 (2022) 248–257

Contents lists available at ScienceDirect

Solar Energy

journal homepage: www.elsevier.com/locate/solener

Effect of thermal cycling on the corrosion behaviour of stainless steels and Ni-based alloys in molten salts under air and argon

Qingyang Liu [a,b,*], Jiong Qian [b,c], Richard Barker [a,b], Chun Wang [a,b], Anne Neville [a,b], Frederick Pessu [a,b]

[a] Institute of Functional Surface, School of Mechanical Engineering, University of Leeds, Leeds LS2 9JT, United Kingdom
[b] Jiuli Corrosion and Integrity Centre Laboratory (University of Leeds), Leeds LS2 9JT, United Kingdom
[c] Engineering Research Centre of High-Performance Nuclear Power Pipe Forming of Zhejiang Province, Huzhou 313028, China

ARTICLE INFO

Keywords:
Thermal cycling
Spallation
Argon
Concentrated solar power
Multi-corrosion layer

ABSTRACT

High temperature corrosion of materials in molten salt is of great interest to renewable energy production industry, especially the wide application of molten salts as thermal energy transfer fluid and storage media in concentrated solar power plants. Molten nitrate salt is used in concentrated solar power plants due to its good balance of thermo-physical properties and cost. Storage tanks and heat transfer pipes are widely made of corrosion resistance alloys such as austenitic stainless steels and nickel-based alloys. The corrosion issues between salt-metal interface poses a critical challenge to safety operation and efficiency. In this study, the corrosion behaviour of stainless steels and Ni-based alloys; AISI 321 and 347, IN 625 and In 825, in Solar (nitrate) salts has been experimentally investigated under isothermal (at 565 °C) and thermal cycling (between 565 °C and 290 °C) conditions, and under air and argon atmosphere. Corrosion assessment of test alloys were achieved using gravimetric measurement in a simulated metal-salt environment in a furnace for 14 days. The micro-morphology and cross-sectional analysis of the corroded surfaces were investigated by a combination of scanning electron microscopy, energy dispersive X-ray diffraction techniques. Compared with isothermal condition in air, thermal cycling in air reduces the corrosion rate of test materials, the severity of corrosion attack and the thickness of corrosion product layers due to the lower exposure time at maximum temperature and cooling effect during thermal cycling, especially in stainless steels. Compared with thermal cycling in air, the obtained corrosion rate was observed to be higher for thermal cycling in argon due to the formation of thick and fragile outer layer of $NaFeO_2$ that easily spalls during the corrosion process. A more resilient and potentially more protective inner layer of Cr_2O_3 and NiO are observed to form in stainless steels and nickel alloys respectively. The formation of intermediate layer of Fe_2O_3 is believed to offer some barrier to potential molten salt induced dissolution of the inner Cr and Ni-rich layer.

7.1 Introduction

Referring to the research related to cover gas atmospheres in CSPs, it is still unclear what the actual concentration of oxygen within CSPs is, particularly as there are no real –time data on this to-date. Although some researchers have concluded that presence of oxygen in molten salt increases corrosion rate, it is believed that there could an optimum oxygen concentration above which oxygen could become a corrosion problem. This scope of research has not been explored. Vignarooban (Vignarooban et al., 2015b) found that

corrosion rate of C-276 in open container at 500˚C is 10 times higher than in sealed container even at 800˚C. Therefore, they concluded that the atmospheric air plays a big role in inducing the corrosion in the molten salt/alloy systems. From a recent research (Bonk et al., 2020), the rate of decomposition of nitrate ions to nitrite ions is shown to be higher at higher temperature in both open and closed test atmosphere, thus resulting in higher oxide ion content. This is shown in the Figure 2-24 (adapted from (Bonk et al., 2020)).

In this chapter, the corrosion behaviour of stainless steels and Ni-based alloys; AISI 321 and 347, IN 625 and IN 825, in Solar (nitrate) salts has been experimentally investigated under isothermal (at 565°C) and thermal cycling (between 565°C and 290°C) conditions, and under air and argon atmosphere. Corrosion assessment of test alloys were achieved using gravimetric measurement in a simulated metal-salt environment in a furnace for 14 days. The micro-morphology and cross-sectional analysis of the corroded surfaces were investigated by a combination of scanning electron microscopy, energy dispersive X-ray diffraction techniques. Compared with isothermal condition in air, thermal cycling in air reduces the corrosion rate of test materials, the severity of corrosion attack and the thickness of corrosion product layers due to the lower exposure time at maximum temperature and cooling effect during thermal cycling, especially in stainless steels. Compared with thermal cycling in air, the obtained corrosion rate was observed to be higher for thermal cycling in argon due to the formation of thick and fragile outer layer of $NaFeO_2$ that easily spalls during the corrosion process. A more resilient and potentially more protective inner layer of Cr_2O_3 and NiO are observed to form in stainless steels and nickel alloys respectively. The formation of intermediate layer of Fe_2O_3 is believed to offer some barrier to potential molten salt induced dissolution of the inner Cr and Ni-rich layer.

7.2 Experimental methodology

As mentioned above, the corrosion assessment of test alloys was achieved using gravimetric measurement in a simulated metal-salt environment in a furnace for 14 days under isothermal and thermal cycling condition in air and argon. After the test, the extracted samples went through the same procedure to remove the corrosion products and same surface characterization procedure as discussed above.

7.3 Results and comparison

7.3.1 Post-experiment salt characterization

Prior to the sample analysis on the corrosion mechanism, the content of salt and aggressiveness of salt system need to be checked before and after different tests to figure out how the salt chemistry change by altering the thermal effect and switch of atmosphere.

Considering the salt chemistry, X-ray Diffraction patterns of salt before and after test has been presented in Figure 6-6. As shown in Figure 6-6 (a), the as-received salt was identified as only mixture of (Na, K)NO_3, and the main patterns of the post-test salts were similar to that of the as-received salt, indicating the conditions of molten salt kept stable. The significant difference between as-received salt and tested salt are that salts after isothermal and thermal cycling test in air and argon exhibited peaks of (Na, K) NO_2 with the varying intensity around 30.001 (100 % intensity) degree and 32.065° (55% intensity, according to Reference code 00–006-0392). This is evidenced that the presence of the nitrite ions from the decomposition from nitrate after 2-week immersion. The main peak of (Na, K) NO_2 at 30.001 degree exhibited highest in Figure 6-6 (d) after 2-week Argon thermal cycling, air-isothermal salt ranked second and air thermal cycled salt showed lowest intensity. It is worth noting that the peak at 32.065° (not main peak for $NaNO_3$ with 14% intensity and main peak for $NaNO_2$ with 55% intensity) in Figure 6-6 (d) for 2-week argon thermal cycling shows a 2500 a.u. intensity higher than that in Figure 6-6 (a), (b) and (c) for as received, 2-week air isothermal and 2-week air thermal cycling test respectively. Many researchers (Han et al., 2021, Bonk et al., 2020) also confirmed that the presence of $NaNO_2$ influenced the thermal physical properties and corrosiveness (Liu et al., 2022a) of molten salt. This clear evidence could confirm that the salt aggressiveness after 2-week thermal cycling in argon is higher than that in air both isothermal and thermal cycling due to increase in nitrite concentration from solar salt decomposition. The detailed comparison of peak intensity of $NaNO_2$ after different test conditions are shown in Table 7-1.

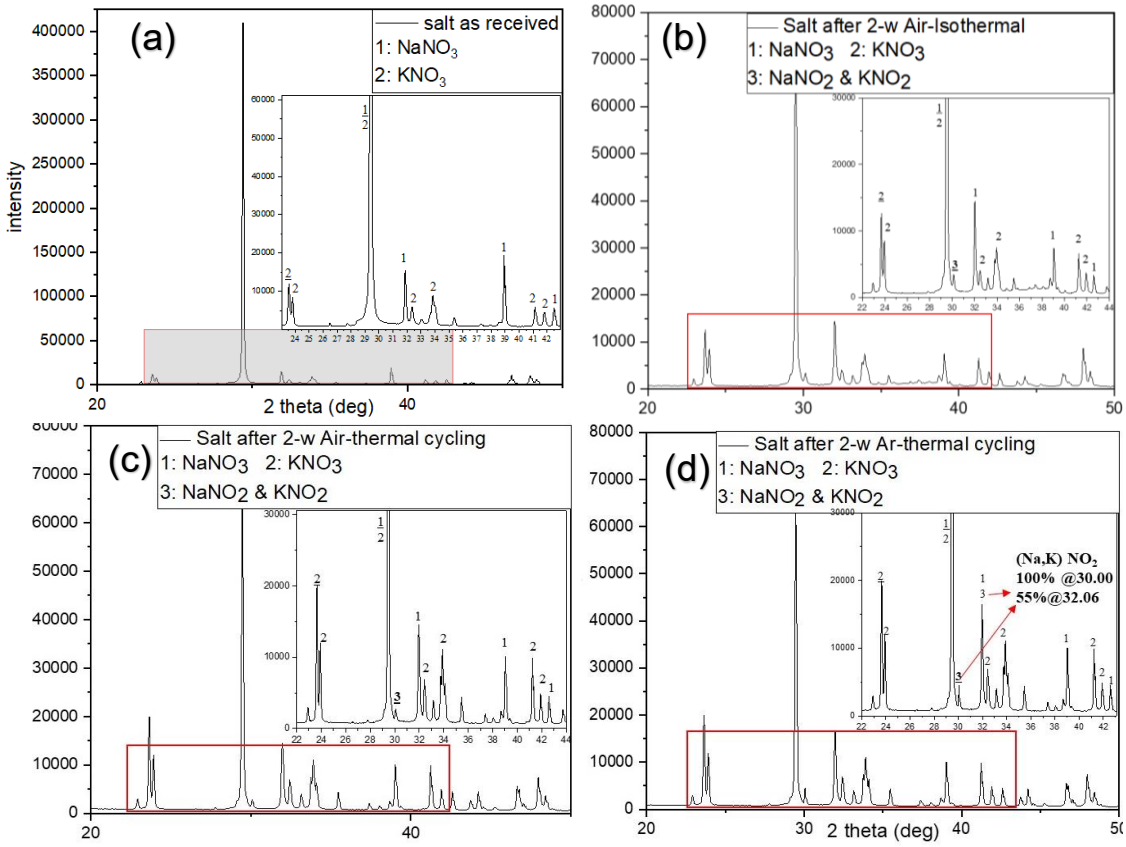

Figure 7-1. XRD results of solar salt before and after immersion test, (a) as received; (b) after 2-week air isothermal; (c) after 2-week air thermal cycling and (d) after 2-week argon thermal cycling (Reference code 00-006-0392, 00-036-1474 and 00-05-0377)

Table 7-1. Main peaks intensity of $NaNO_2$

	$NaNO_2$ intensity at 30 2theta (100% intensity)	$NaNO_2$ intensity at 32 2theta (55% intensity)	$NaNO_3$ intensity at 32 2theta (14% intensity)
As-received salt	0	0	14085
2-week Air isothermal	3366	0	14293
2-week Air thermal cycling	2781	0	14532
2-week Ar thermal cycling	4500	2500	14032

7.3.2 Effect of Thermal Cycling in Air

Figure 7-2 shows the weight loss and corrosion rate of stainless steels and Ni-based alloys after 14-day immersion test under isothermal and thermal cycling under air, and thermal cycling under argon atmosphere (Figure 7-2). Generally, stainless steels exhibited higher weight loss and corrosion rate than that of Ni-based alloys under all conditions.

Referring to Figure 7-2 for samples exposed to air, the corrosion rate from isothermal test was higher than that from thermal cycling tests. The effect of thermal cycling appears to substantially suppress the corrosion process. This is linked to the intermittent cooling at 290°C and the long residence time in the cooling phase (12 hrs) per thermal cycle. The repeated cooling phase is believed to be suppressing the kinetics of corrosion and oxide formation, thereby reducing material loss rate. This intermittent cooling effect could also provide a break in aggressive molten salt - metal interaction enhanced by high temperature to minimise the thermal effects on initially formed corrosion oxide layers at 565°C. This trend was observed for both stainless steel and nickel alloys in this study and shown to restrict the potential transformation from dense oxide layers to loose/porous oxide layers. Detailed evidence and analysis are presented and discussed in the next section on surface characterisation later in this paper.

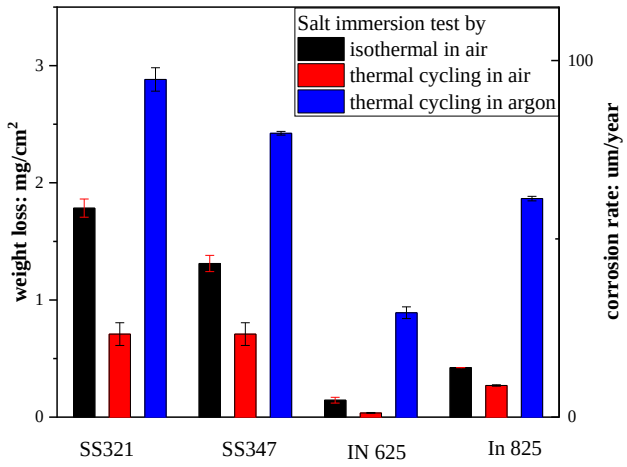

Figure 7-2. Mass loss (and corrosion rate) of AISI 321 AISI 347 IN 625 and IN 825 specimens at different temperature gradient and atmosphere in solar salt for 14 days. (ISO indicates ‘isothermal’ and TC indicates ‘thermal cycling’ in the figure and the same below)

Figure 7-3 and Figure 7-4 shows the XRD patterns and SEM images respectively, of the corroded surface of AISI 321, AISI 347, IN 625 and IN 825 after 14-day immersion in solar salt under isothermal and thermal cycling in air, and thermal cycling in argon. Referring to the XRD patterns in Figure 7-3, it is shown that the oxide layers formed on the surface of

AISI 321 and AISI 347 in solar salt consists of different combination of iron oxide (Fe_2O_3), iron chromium spinel ($FeCr_2O_4$), sodium ferrite ($NaFeO_2$), and chromium oxide (Cr_2O_3). The specific combination of oxide chemistries is dependent on the type of test and cover gas atmosphere. The possible reaction to form the corrosion products are as follows:

$$NO_3^- \rightleftharpoons NO_2^- + \frac{1}{2}O_2(g) \quad \text{Equation 39}$$

$$2NO_2^- \rightleftharpoons NO_2(g) + NO(g) + O^{2-} \quad \text{Equation 40}$$

$$Cr + \frac{3}{4}O_2 \rightarrow \frac{1}{2}Cr_2O_3 \quad \text{Equation 41}$$

$$Ni + \frac{1}{2}O_2 \rightarrow NiO \quad \text{Equation 42}$$

$$3Fe + 2O_2 \rightarrow Fe_3O_4 \quad \text{Equation 43}$$

$$2Fe_3O_4 + \frac{1}{2}O_2 \rightarrow 3Fe_2O_3 \quad \text{Equation 44}$$

$$\frac{1}{2}Fe_2O_3 + \frac{1}{2}O_2 + e^- + Na^+ \rightarrow NaFeO_2 \quad \text{Equation 45}$$

$$Fe + Cr_2O_3 + \frac{1}{2}O_2 \rightarrow FeCr_2O_4 \quad \text{Equation 46}$$

Referring to XRD patterns in Figure 7-3 (a1, a2) and (b1, b2), Cr_2O_3 can be identified on the surface under thermal cycling condition in air, but not under isothermal condition for AISI 321, and for similar test scenarios In AISI 347. While it is expected that Cr_2O_3 forms as a passivating oxide layer in air, the observed trend indicates confirms the formation of Cr_2O_3 in argon atmosphere according to Equation 39 Equation 40 and Equation 41. However, under isothermal condition in air; particularly for AISI 321, the absence of Cr_2O_3 on the XRD pattern is likely due to its dissolution after long residence time of immersion in molten salt (Ahmed, 2013, Bell et al., 2019) . In AISI 347, a similar trend is observed, but observed in terms of lower intensity of the peak Cr_2O_3 under isothermal condition than in thermal cycling in air. These results suggests that under thermal cycling conditions in air, and in comparison with isothermal condition in air, the thermal effect on the resilience of Cr_2O_3 oxide layer is suppressed. This has the potential to reduce the likelihood for Cr_2O_3 oxide layer breakdown/dissolution and overall metal loss rate for test under thermal cycling in air than under isothermal condition in air.

The observed effect of thermal cycling in air is due to the effect of intermittent cooling on the stability of Cr_2O_3 passive layer as already described above. This is evident in the SEM

images in Figure 7-4 (a1) and (a2) and Figure 7-4 (b1) and (b2) for isothermal and thermal cycling test in air of AISI 321 and AISI 347 respectively. The SEM images show the corrosion product layers to be dense and more protective under thermal cycling conditions than in isothermal condition. More coarse grains are found on the rougher isothermal surfaces. The cross-section analysis and EDS line scan is presented in Figure 7-5 (a1) and (a2) for AISI 321, and Figure 7-5 (b1) and (b2) for AISI 347 after isothermal and thermal cycling test in air respectively. The results confirm the corrosion layer to be thinner, dense and more compact with retained integrity under thermal cycling condition (~2.5 µm thickness for AISI 321) than in isothermal condition (~6 µm thickness for AISI 321). These visual evidence correlates with the corrosion rate data in Figure 7-2 and the underpinning mechanism described above. The cross-section analysis and EDS line scans in Figure 7-5 (a1 and a2) and (b1 and b2) for AISI 321 and 347 respectively, also confirms the evidence of an outer layer of Fe_2O_3 and inner Cr_2O_3 and/or $FeCr_2O_4$ layer. This correlates with the XRD patterns in Figure 7-3 (a1 and a2) and (b1 and b2) for AISI 321 and 347 respectively. However, for AISI 321 in air and isothermal condition, Fe_2O_3 dominates the corrosion product layer due to the dissolution of initially formed Cr_2O_3. Observations of dissolution of dense inner chromium oxide layer in nitrate salt and the formation of a Fe_2O_3 layer in molten salt has been reported (Walczak et al., 2018, Bell et al., 2019). Fe_2O_3 is able to provide some barrier to molten nitrate salt but likely not comparable to that offered by the compact Cr_2O_3 layer formed under thermal cycling conditions in air (Goods et al., 1994a, Bradshaw and Goods, 2001a, Bell et al., 2019, Ahmed, 2013).

Similar observation can be deduced from the corrosion rate data, XRD pattern, SEM and EDS line scan of cross sections for nickel alloys in this study, particularly IN 825. For nickel alloys, the chemistry of the corrosion products identified on XRD were similar for both isothermal and thermal cycling tests in air (see Figure 7-3 (c1 and c2) and (d1 and d2) for IN 625 and IN 825 respectively). Nickle oxides (NiO) formed on the corrosion surface of IN 625, while NiO, Fe_2O_3 and $FeCr_2O_4$ was identified on IN 825. The latter is due to the high Fe content in IN 825. In addition to the higher corrosion rate under isothermal condition than thermal cycling, the visual evidence from SEM and EDS line scan from cross section analysis shows that the corrosion product layer are more dense, compact and thinner (~2.1µm thickness for IN 825) under thermal cycling than under isothermal condition (~4.1 µm for IN 825) in air. Referring to Figure 7-3 (c1 and c2) for IN 625, the morphology for NiO formed in air under both isothermal and thermal cycling conditions are similar and exhibiting relative smooth surface even with clear polishing scratch, which correlates with the close

corrosion rates for both systems as shown in Figure 7-2. This reflects the superior corrosion properties over 14 days of IN 625 over the other alloys considered in this study.

7.3.3 Effect of Cover gas on corrosion characteristics during thermal Cycling

Referring to Figure 7-2, corrosion rates recorded after immersion test under thermal cycling in argon is ~5 times higher than that in air across the studied alloys (except for IN 625). This has been linked to a combination of specific reaction pathways that influences the corrosiveness of solar salt, the impact of delayed passivation from Cr_2O_3 and formation of other non-protective oxide layers. It has been reported that the corrosiveness of the solar salt results from the breakdown of nitrate salts, leading to the conversion of nitrate to nitrite, with the release of Na^+ and oxide ions (around 0 % and 0.01 % in open and sealed environment at 550 °C respectively). This reaction pathway is also known to occur in sealed environment with no supply of oxygen (Bonk et al., 2020) according to the reactions in Equation 39 and Equation 40.

In this case, the rate of corrosion will be determined by the ionic strength of molten salts at high temperatures, the rate of availability of oxide and Na^+ ions, and the rate of passive Cr_2O_3 oxide formation and breakdown. The latter will likely be delayed by the rate of availability of oxide ions. A combination of high temperature material dissolution in ionic molten salt and delayed passivation acts to control the rate of passivation of the molten salt – metal interface leading to a higher corrosion rate after 14 days. For the thermal cycling test in air, it is likely that the excess supply of oxygen promotes the quick formation of a thin and dense layer of chromium oxide (Cr_2O_3) to protect the corrosion interface early in the 14 days test. As a result, the corrosion rate over 14 days exposure time is lower for thermal cycling test in air than in argon. It is worth noting that this does not imply that this trend will continue beyond 14 days of exposure.

Referring to results from thermal cycling under argon atmosphere and in comparison, with thermal cycling test in air, $NaFeO_2$ corrosion layer was also identified only on the surface of samples from thermal cycling tests in argon. The formation of $NaFeO_2$ is believed to have followed the reaction of the outer Fe_2O_3 (already described above to offer some shielding to Cr_2O_3) and Na^+ from the molten salt according to the Equation 45 above.

Na^+ in Figure 7-3 (a3, b3) and (d3) is provided from the nitrate salts. $NaFeO_2$ has been observed in this study to be a porous, loosely held and non-protective outer layer as shown in SEM images in Figure 7-4 (a3, b3 and d3) for AISI 321, AISI 347, and IN 825 respectively for thermal cycling test in argon. $NaFeO_2$ is not present on samples after thermal cycling

tests in air as shown by the XRD patterns in Figure 7-3 (a2, b2 and d2) for AISI 321, AISI 347 and IN 825 respectively. The XRD pattern in Figure 7-3 (a3, b3 and d3) in argon also show the presence of Cr_2O_3, $FeCr_2O_4$ and Fe_2O_3. The oxygen consumed to form these oxides is provided by Equation 39 and Equation 40.

Referring to the EDS line scan from cross section analysis, it is evident in Figure 7-5 (a3, b3 and d3) for AISI 321, AISI 347 and IN 825 respectively, that Cr_2O_3/$FeCr_2O_4$ is formed as an inner layer and Fe_2O_3 is formed as an outer layer under argon cover gas. Note that Na is not identified on this line scans to confirm the presence of $NaFeO_2$. However, this has been shown on a complimentary top view EDS map in Figure 7-4 to confirm the presence of the porous and non-protective $NaFeO_2$ as the outmost layer formed under argon cover gas. It is therefore evident that the cross-sectional corrosion product footprint for AISI 321 and AISI 347 consists of a Cr_2O_3 and/or $FeCr_2O_4$ inner layer, Fe_2O_3 middle layer and an outer non-protective $NaFeO_2$ outer layer for test under thermal cycling condition in argon. For IN 825, there is an additional intermediate NiO layer in argon, while the cross-sectional corrosion product footprint for thermal cycling test in air consists of a Cr_2O_3 and/or $FeCr_2O_4$ inner layer and a Fe_2O_3 outer layer.

In terms of the overall corrosion rate for test under thermal cycling in argon, the formation of $NaFeO_2$ via Equation 45 is likely to undermine the integrity of Fe_2O_3 layer to expose the inner layers to aggressive molten salt species (Bradshaw and Goods, 2001a, Goods et al., 1994a, Ahmed, 2013, Bell et al., 2019). As shown by the SEM images in Figure 7-4 (a3, b3 and d3) for AISI 321, AISI 347 and IN 825 respectively, $NaFeO_2$ is susceptible to breakdown by spallation. This is likely to contribute to an increase in corrosion rate. The other mechanism that is likely to contribute to material loss rate is the delay in formation of passive Cr_2O_3 and/or $FeCr_2O_4$ in stainless steels and Nickel alloys.

Delayed passivation will also imply a non-equilibrium of availability of Cr, Fe at the molten salt – alloy interface. The outward diffusion of these atoms (D'Souza et al., 2021) from bulk material to corrosion interface occurs in synergy with the concentration gradient induced by high temperature oxidation, resulting in the migration of atoms to the interface. The absence of a prompt supply of oxygen to promote quick passivation of the interface will lead to the formation of thicker films of a mixture of the oxides these oxide layers; including $NaFeO_2$, as soon as oxygen becomes available via Equation 39 and Equation 40.

To better understand the formation mechanism of these oxides at initial oxidation stage, the possible reactions occurring on the surface of stainless steels were listed in Table 7-2

together with the corresponding standard free energies of formation (ΔG^{θ}) of oxides formation. The change of Gibbs free energy (ΔG) the oxides was calculated by Equation 47 (Tan et al., 2017) (Yin et al., 2021), and listed in Table 7-2 as well.

$$\Delta G = \Delta G^{\theta} + RT\ ln(\frac{(\alpha_O)}{(\alpha_M)(pO_2)^{1/2}}) \qquad \text{Equation 47}$$

The formation of Cr_2O_3 in both AISI 321 and 347 corresponds to lowest ΔG value (~ -1018 kJ/mol) at 565 ˚C, indicating Cr_2O_3 preferentially formed on the surfaces of stainless steels.

As we discussed the solubility of chromium compounds in nitrate salt (Slusser et al., 1985), other oxides started to formed once average Cr concentration was lower than a critical value (N_{Cr}*) (Wagner, 1952). Afterwards, as Fe-based alloys, rapid oxidation triggered the formation of Fe-based oxides at this oxidation stage. It's well known that FeO is preferentially formed at temperature over 600 °C (Birks et al., 2006) and Fe_3O_4 and Fe_2O_3 tend to form at temperatures below 570 °C (Yin et al., 2021). From the ΔG values of oxides and the diffusivity order of metallic ions in chromia ($D_{Fe} > D_{Ni} > D_{Cr}$) (Lobnig et al., 1992a), Fe_3O_4 and Fe_2O_3 starts to form and hence protect further Cr depletion from the base material, which can be well understood in terms of ionic diffusion during the oxidation process. The outward diffusion of Fe in the Cr_2O_3 and high affinity of Fe to oxygen resulted in mixture oxides of Fe and Cr. After dissolution of Cr-oxide, Fe_2O_3 was found on the topmost of the surface of stainless steels after corrosion in molten salt at 565 ˚C, which was also expected to provide a barrier to further limit Cr depletion from the base material afterwards. It is worthwhile that Fe_2O_3 tended to convert to $NaFeO_2$ with increase of exposure time and temperature, thus losing its protection. While in air the passive Cr_2O_3 formed on the early stage and higher diffusion rate of Fe in Cr_2O_3 resulted in formation of Fe_2O_3 to further shield the dissolution of Cr_2O_3 into molten salt.

This is evident from the cross-section analysis in Figure 7-5 (a3, b3 and d3) for AISI 321, AISI 347 and IN 825 respectively. The film thickness is ~11μm, ~12 μm and ~7μm under thermal cycling test in argon, and ~2.5μm, ~2.5 μm and ~2.1μm under thermal cycling test in air for AISI 321, AISI 347 and IN 825 respectively. The thickness of the Cr_2O_3 and/or $FeCr_2O_4$ layers in AISI 321 and 347, and Cr_2O_3 and/or $FeCr_2O_4$, and NiO indicated by the EDS line scans in Figure 7-5 (a3, b3 and d3) for AISI 321, AISI 347 and IN 825 respectively supports the underpinning mechanisms described here. All of these mechanisms are believed to act in synergy to increase corrosion rate under thermal cycling conditions in argon than in air over 14 days.

Table 7-2. Standard free energies of formation of possible oxides (Yin et al., 2021) and change of Gibbs free energy of corresponding reactions in AISI 321 and 347 stainless steels with molten salt at 565˚C.

Alloy	Reaction	∆G°(kJ/mol) 25˚C 1atm	∆G(kJ/mol) 565˚C (838K)	
			AISI 321	AISI 347
Fe_2O_3	$2Fe+1.5O_2= Fe_2O_3$	-742.2	-721.276	-721.24
Fe_3O_4	$3Fe+2O_2=Fe_3O_4$	-1015.5	-1015.5	-986.83
Cr_2O_3	$2Cr+1.5O_2=Cr_2O_3$	-1058	-1018.658	-1018.549
NiO	$Ni+0.5O_2=NiO$	-211.7	-189.520	-189.75

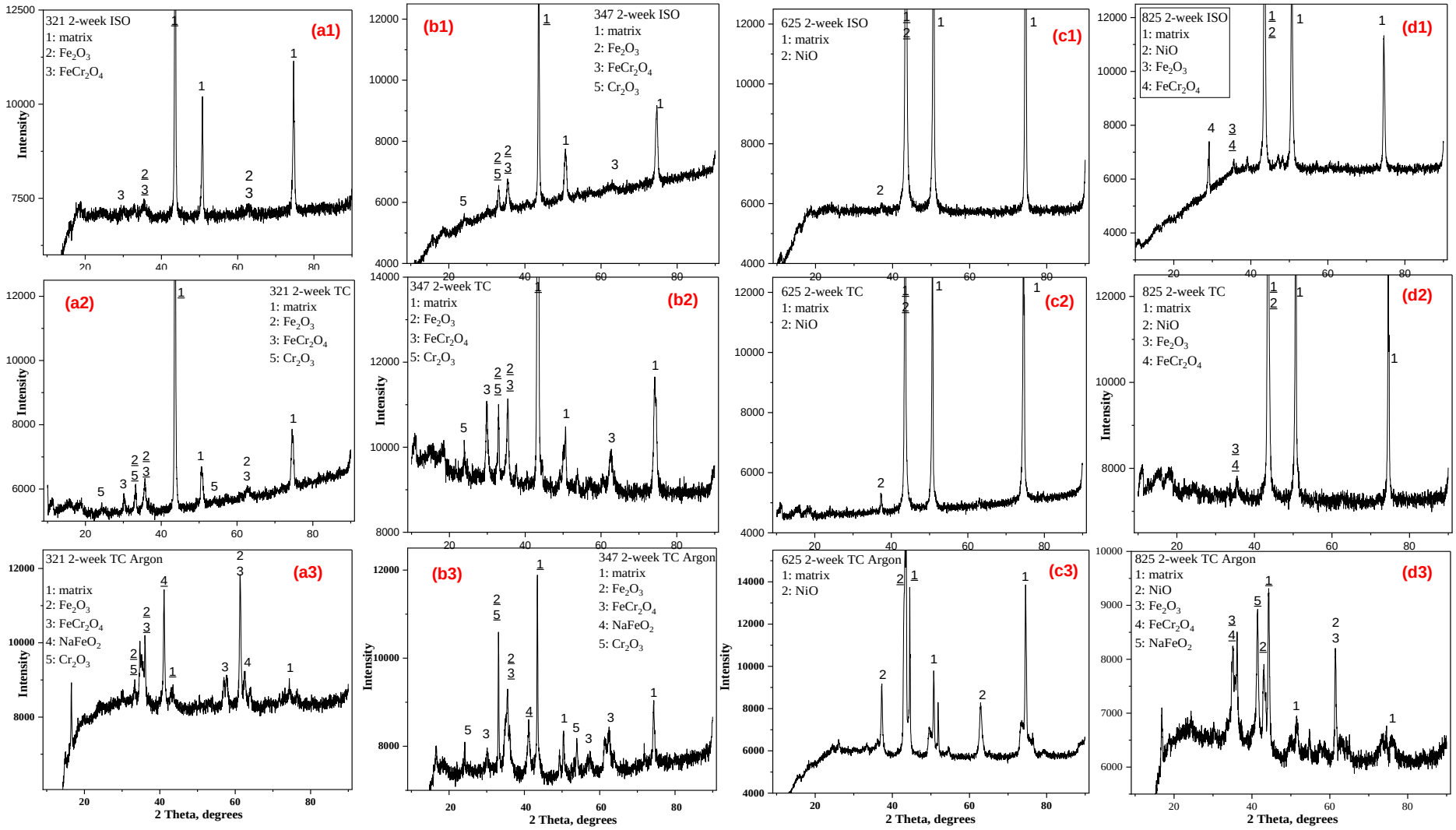

Figure 7-3. XRD patterns of studied alloys under different immersion conditions (phase number with underline meaning the 100% intensity peaks), (a) AISI 321, (b)AISI 347, (c) IN 625 and (d) IN 825 after 14-day immersion test in Solar salt at (1) ISO in air (2)TC in air (3)TC in argon, respectively.

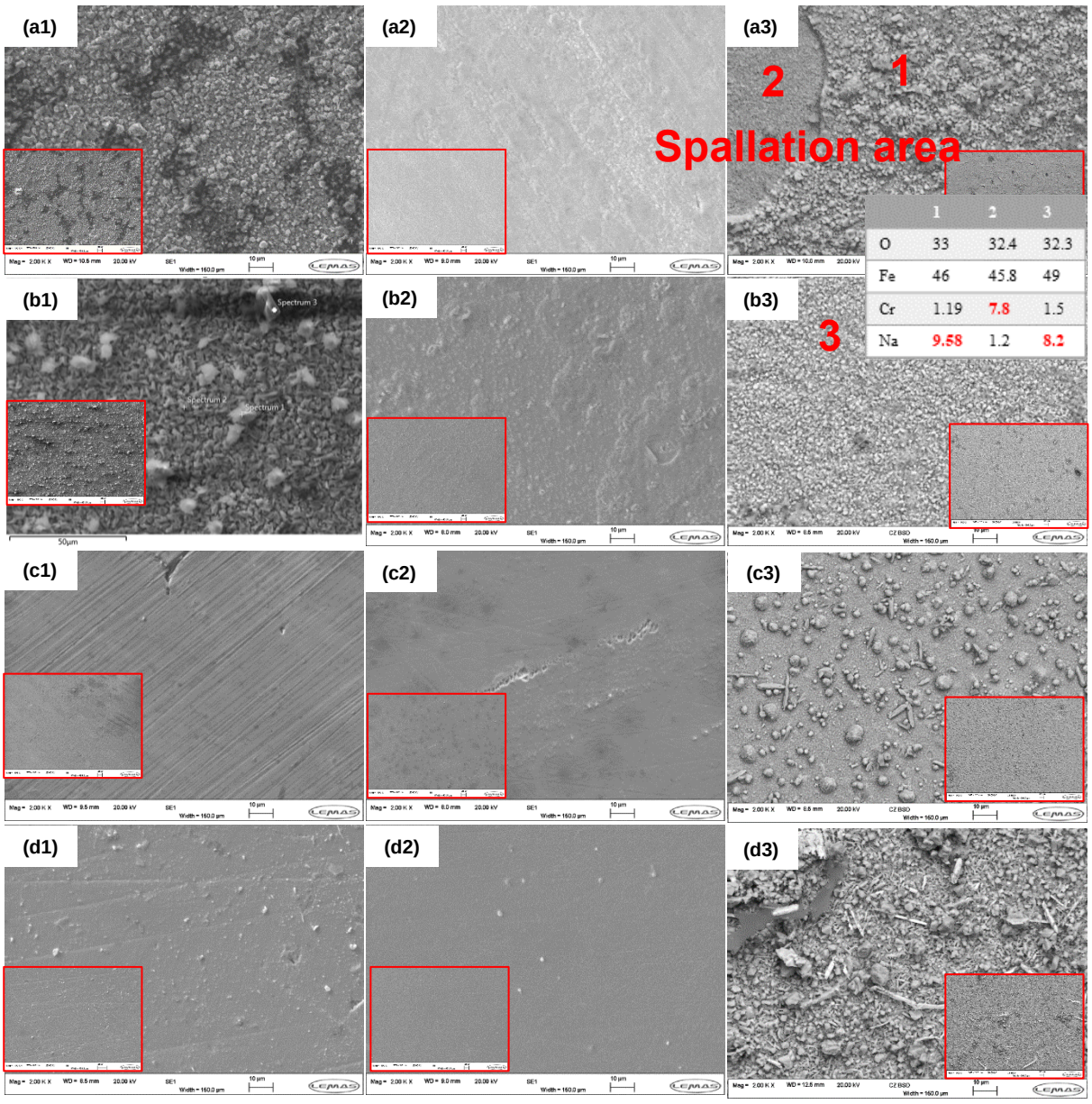

Figure 7-4. SEM top surface of the oxide scales formed on (a) AISI 321, (b)AISI 347, (c) IN 625 and (d) IN 825 after 14-day immersion test in Solar salt at (1) ISO in air (2)TC in air (3)TC in argon, respectively.

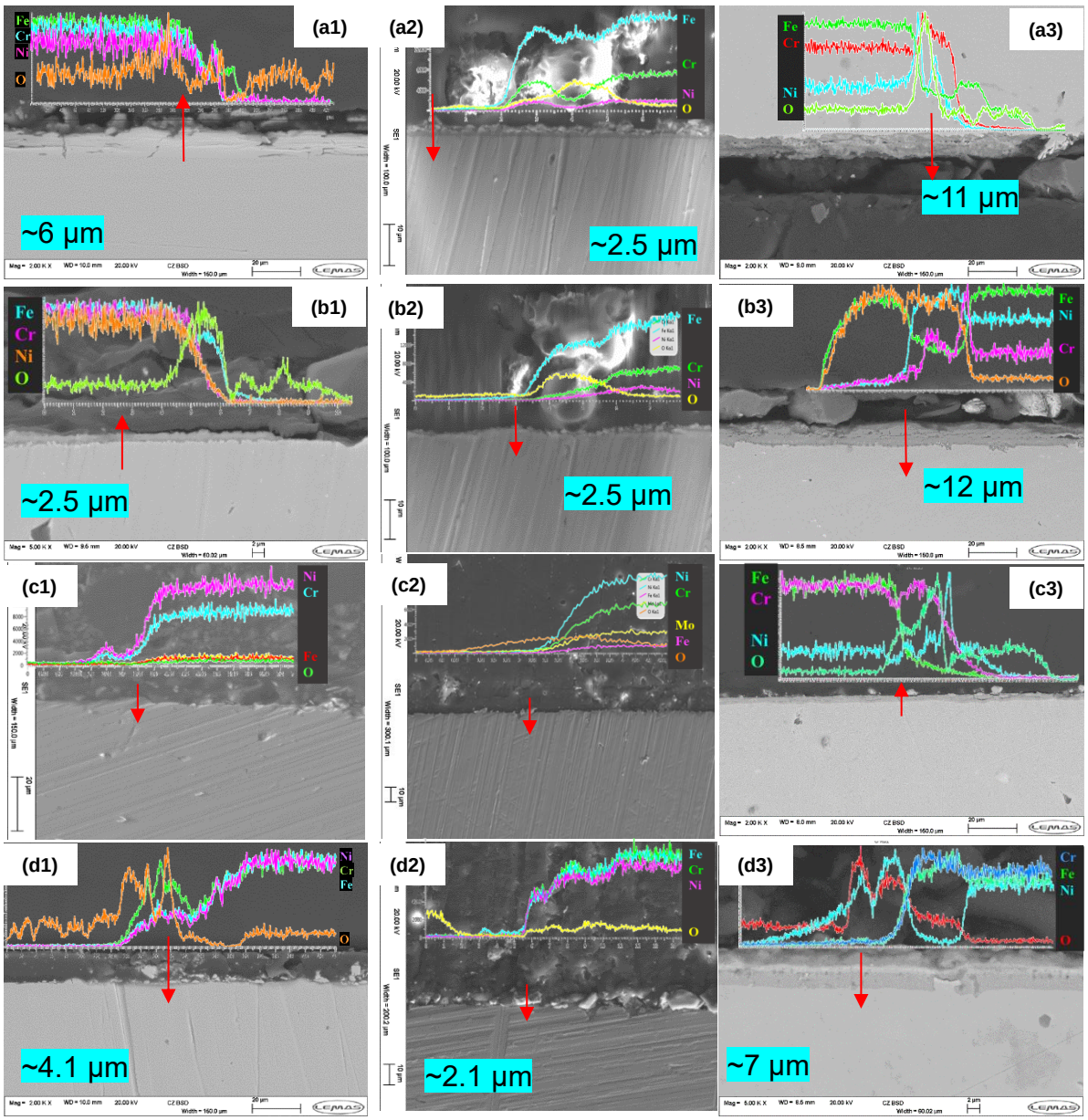

Figure 7-5. SEM-EDS profile of the oxide scales formed on (a) AISI 321, (b)AISI 347, (c) IN 625 and (d) IN 825 after 14-day immersion test in Solar salt at (1) ISO in air (2) TC in air (3)TC in argon, respectively**.**

7.4 Discussions

The corrosion products formed on the stainless-steel surface have been previously reported and are also confirmed in this study to be Fe_2O_3, Cr_2O_3 and $FeCr_2O_4$ (Zhang et al., 2020) based on the above Equations (Hu et al., 2018). Meanwhile, the Fe_2O_3 outer layer is converted to $NaFeO_2$ which is non-protective and consequently results in the corrosion rate increasing (Bradshaw and Goods, 2001a). In this study, the $NaFeO_2$ was identified as the corrosion product on the samples under thermal cycling in argon.

For nickel-based alloys, they exhibited better corrosion resistance than stainless steels in this study as shown by the result from mass loss measurements and SEM observation. The corrosion resistance of these studied alloys obeys IN 625 > IN 825 > AISI 347 > AISI 321. Only NiO was found on the surface of IN625, while NiO and mixed oxide of Fe and Cr are the main corrosion products formed on the surface IN 825.

From the results above, the corrosion rate of isothermal immersed samples is higher than that under thermal cycling condition in air. This is similar to the conclusion reported in the literature (Liu, 2021) where thermal cycling decreased the corrosion rate of the three stainless steels moderately when compared to isothermal immersion corrosion tests in argon at higher temperature. Thermal cycling effects suppresses the corrosion process due to the slowing down the kinetics of corrosion and oxide formation, and the overall thermal effects during the cooling phase. The longer residence time of 12 hrs at maximum temperature promoted the dissolution of initially formed Cr_2O_3 in isothermal condition. Also thinner, dense and more compact corrosion layer was observed to form on TC samples. Iron oxide is able to provide some protection in molten nitrate salt but likely not comparable to the compact Cr_2O_3 layer formed under thermal cycling conditions in air (Goods et al., 1994a, Bradshaw and Goods, 2001a, Bell et al., 2019, Ahmed, 2013).

The corrosion rate, and thickness of corrosion layers and/or corrosion attack depth imply that the corrosion rate is higher when the oven is sealed with argon than open air. The formation and spallation behaviour of $NaFeO_2$ is likely to contribute to an increase in corrosion rate under thermal cycling in argon. The other mechanism that contributes to higher rate loss is the delay in preferential formation of passive Cr_2O_3 due to the availability of oxide ions decomposed from nitrate. The outward diffusion of Fe and Cr from bulk material to corrosion interface is driven by high temperature, resulting increased concentration of atoms at the corrosion interface. The absence of a prompt supply of oxygen to promote quick passivation of the interface will lead to the formation of thicker films of these oxide layers as soon as oxygen becomes available via Equation 39 and Equation 40. While in air the passive Cr_2O_3 formed on the early stage and higher diffusion rate of Fe in Cr_2O_3 resulted in formation of Fe_2O_3 to protect the dissolution of Cr_2O_3 into molten salt (Ahmed, 2013). All of these mechanisms are believed to act in synergy to increase corrosion rate under thermal cycling conditions in argon than in air over 14 days.

As the results shown in this study, the certain combination of temperature and atmosphere could lead to different level of corrosion. And the inert atmospheres (Bell et al., 2021), which

were considered to limit corrosion in other molten salt mixtures, can increase the corrosion rate of alloy. It is not recommended to purge the air with argon in the storage tanks or transfer pipes in the real application where it may cause higher corrosion damage. Also thermal cycling caused by alternation of day and night can mitigate the corrosion to a certain extent by reducing the kinetic of corrosion reaction during cooling period.

7.5 Conclusions

The different corrosion behaviours of stainless steels and Ni-based alloys exposed solar salt under isothermal and thermal cycling in air and argon for 14 days were investigated.

1. Thermal cycling effects suppresses the corrosion process in air by slowing down of the kinetics of corrosion and oxide formation and reducing the thermal effect on oxide layer stability during the cooling phase. This results in thinner, dense and more compact oxide layers forming on the samples.
2. The formation and spallation behaviour of $NaFeO_2$ is likely the main contributor to an increase in corrosion rate under thermal cycling in argon. The delayed preferential formation of passive Cr_2O_3 due to the limitation of availability of oxide ions from decomposed nitrate also result in severer corrosion in argon than in air.
3. The multi-layer was found on surface of stainless steels and IN 825 after immersion test in argon under thermal cycling condition. The composition of double layer was different: outer Fe_2O_3 layer and inner mixed oxides of (Fe, Cr) constituted the corrosion layer of Stainless steels, while outer NiO and inner mixed oxides of (Fe, Cr) constituted the corrosion layer of IN 825.
4. The results presented in this study show that a combination of different alloy, salt and gas atmosphere could lead to different corrosion outcomes. However, thermal cycling has been shown to suppress the corrosion process significantly under any gas atmosphere, including inert argon atmosphere. The application of argon atmosphere to reduce the corrosion in other molten salt has been shown in this study to have the potential to increase the rate of metal loss in molten salt systems.

Chapter 8. Investigation of the Relationship between Thermo-Mechanical Stress and Early-Stage Corrosion Characteristics of Molten Salt – Oxide – Metal Interfaces In Solar Salts

This chapter was originated from paper “Investigation of the Relationship between Thermo-Mechanical Stress and Early-Stage Corrosion Characteristics of Molten Salt – Oxide – Metal Interfaces In Solar Salt” Submitted to Corrosion Science.

8.1 Introduction

Some recent literatures on oxidation of alloys (Yin et al., 2021, Tan et al., 2019) suggested that mechanical properties of the oxide layer are critical in determining its capacity to protect the substrate from further oxidation. This was on the premise that the main factors that influences the oxidation resistance of the alloys is the mechanical integrity of the surface oxide layer (Ramos et al., 2021). This could be linked to internally built - up of stresses (Pu et al., 2014) that arise naturally during the oxidation process (due to the difference in specific volume of oxide and substrate metal) and on thermal stresses that appear during cooling (due to different thermal expansion/contraction coefficients between oxide and substrate (Birks et al., 2006)).

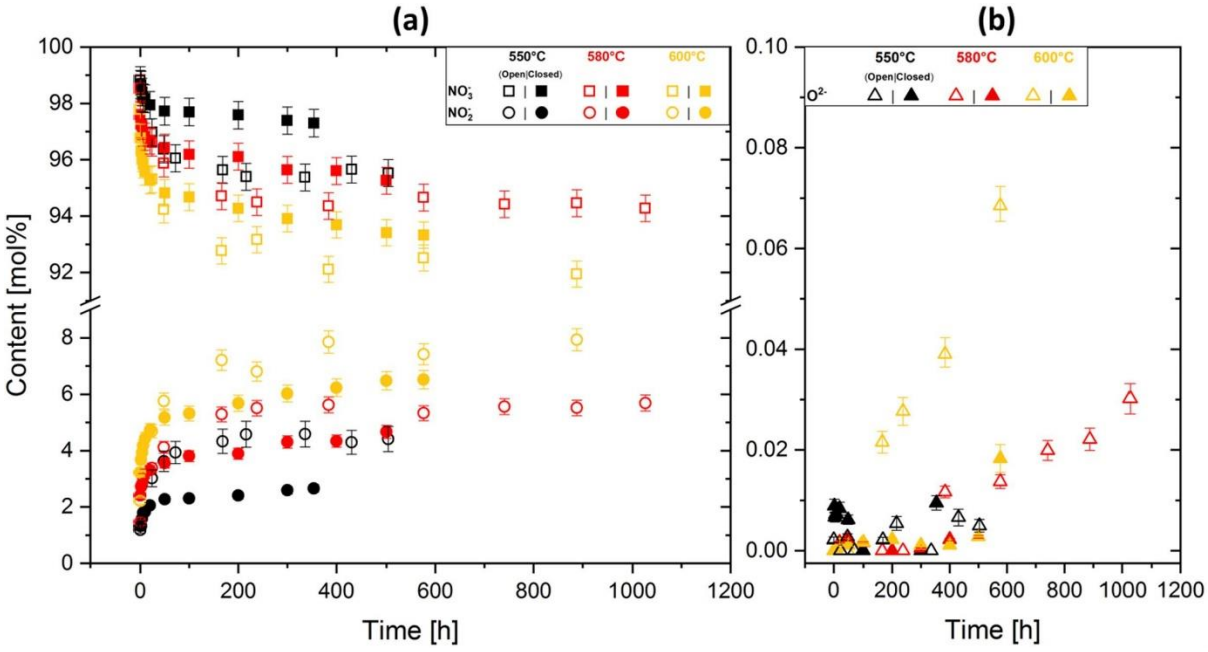

Figure 8-1. Nitrate and nitrite content in Solar Salt stored in open atmosphere (open symbols) and closed atmosphere (closed symbols) at 550 °C, 580 °C and 600 °C. Adapted from Ref (Bonk et al., 2020)

Therefore, in order to fully understand the adherence, protective and interfacial oxide layer spallation behaviours at the molten salt – metal interface, the Nano-mechanical properties of these interfacial oxide layers should be carefully investigated and quantitatively characterised. This study experimentally investigated the corrosion behaviours of two stainless steel and two Ni-based alloys at 565˚C and 600˚C in under air and argon atmospheres using a combination of gravimetric (weight loss) analysis, advanced surface and subsurface characterisation techniques; including Nano-mechanical characterisation using the Nano-indentation technique. This study investigates the formation and protectiveness of corrosion oxide layers in the context of the synergistic effect of temperature and cover atmosphere on the corrosion process. A key part of this study is the investigation of the stress profile across the molten salt – oxide – metal interface using advanced surface/subsurface characterisation techniques. The results from this aspect of the study will help in correlating the thermal stress profile across the interface with the rate and tendency for spallation of these oxides to occur during molten salt induced corrosion processes. Detailed microstructural characterizations and other methods carried out in this study are provided in the subsequent sessions in this paper.

8.2 Experimental methodology

Same stainless steels and Ni-based alloys are employed in this study, and the sample and salt preparation were provided above. The test protocol in this study was immersing the sample in molten salt at constant 565 and 600°C in air and 600°C in argon for 7 days. The post-experimental characterization procedure can be found on the chapter 4.

8.3 Results and discussion

8.3.1 The comparison of corrosion rate measurements

Figure 8-2 shows the weight loss and corrosion rate of stainless steel and Ni-based alloys after 7-day immersion test at 565 and 600˚C in air and argon. Stainless steels always exhibited higher weight loss and corrosion rate than that of Ni-based alloys under any temperature and gas conditions. However, the corrosion rate generally increased with increase in the test temperature from 565 to 600˚C in air.

Highest corrosion rate was recorded after immersion test at 600˚C in argon covering atmosphere for each alloy, approximately 2 times higher than that of air-exposed samples for AISI 321, 347 and IN 825 and around 10 times higher than that of air-exposed samples for IN 625 at 600˚C. Significant increase of corrosion rate of IN 625 was observed from 11.9

μm/y in the air to 128 μm/y for samples exposed to argon. It was reported that IN 625 has overwhelming advantage on corrosion resistance compared to stainless steels (McConohy and Kruizenga, 2014, Kruizenga et al., 2013) in air below 600˚C with corrosion rate of 12.7 μm/y and loses its advantage when temperature exceeding 680˚C in air with corrosion rate of 594 μm/y. The corrosion rate of AISI 321, AISI 347 and IN 825 increases steadily with raising temperature from 565 to 600˚C in air and continued significantly increase after sealing the oven with argon.

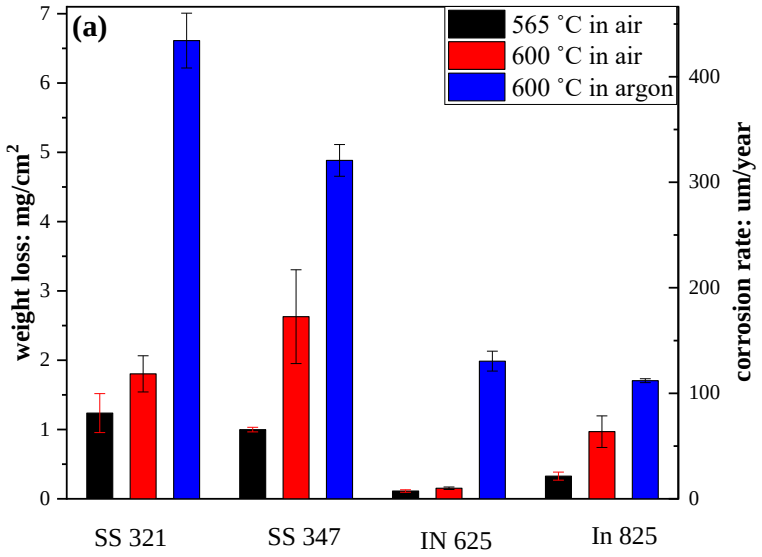

Figure 8-2. Mass loss (and corrosion rate) of AISI 321 AISI 347 IN 625 and IN 825 specimens at different temperature and atmosphere in solar salt for 7 days

8.3.2 Corrosion oxides characterization – XRD analysis

According to the XRD analysis, the chemistry of corrosion oxides formed on the surfaces of both stainless samples; AISI 321 and 347 in air are similar, with the only difference being in terms of the intensity of the identified peaks. Based on the XRD results shown in Figure 8-3 (a1) (a2) (b1) (b2), it can be concluded that the corrosion oxide layer consists of iron oxide (Fe_2O_3), iron chromium spinel ($FeCr_2O_4$), sodium ferrite ($NaFeO_2$), and chromium oxide (Cr_2O_3). XRD patterns show more spikes in oxide chemistry at 600˚C than at 565˚C, indicating the formation of a more complex combination of oxide spinel at 600˚C. In contrast to the corrosion oxides formed under argon (Figure 8-3 (a3), (b3)), the chromium was presented only in form of $FeCr_2O_4$ without forming Cr_2O_3. This is related to the oxide forming corrosion reaction most thermodynamically affected by the availability of oxygen/oxide ions. This will be discussed later in this paper. The corrosion oxides formed on the surface of IN 625 in air is mainly NiO, while Cr_2O_3 and $FeCr_2O_4$ was identified on the surface of argon exposed IN 625 samples. This finding is correlates well with weight loss results in Figure

8-2, where IN 625 samples under argon atmospheres exhibited higher corrosion rate which is directly linked to increased number of corrosion oxides formed on the surface. The main corrosion oxides formed on IN 825 are NiO, Fe_2O_3, $FeCr_2O_4$ and Cr_2O_3. $NaFeO_2$ was found when test was performed at 600˚C at air and argon, indicating the effect of both temperature and gas atmospheres on the formation of $NaFeO_2$.

8.3.3 Corrosion oxide characterization - SEM surface analysis

The oxide layers formed on the surface of samples are believed to protect the base metal from continuous molten salt penetration. Therefore, oxide formation process and mechanisms are important to better understand the overall corrosion mechanism at the molten salt – metal interface. The SEM images of the top surface and possible oxide phases from EDX analysis are shown in Figure 8-4 and Table 8-1. Referring to Figure 8-4 (a1) (b1) (c1) and (d1) after immersion test in air at 565˚C, the corroded surfaces of stainless steels appears to be largely un-corroded with some localised bulge, while the Ni-based alloy surface shows little difference from un-corroded samples with visible evidence of polishing marks. This indicates that the corrosion is mild in air at 565˚C. Referring to Figure 8-4 (a2) (a3) (b2) and (b3) for the stainless-steel samples tested at 600˚C in air and argon, thicker and looser corrosion oxide layers, and evidence of layer spallation behaviors were observed on the surface than that formed at 565˚C. This can be confirmed from results from EDX analysis shown in Table 8-1 (spectrum “S2” and “S3” for AISI 321, and “S6” and “S7” for AISI 347). The morphology of corrosion oxides are different (see Table 8-1; spectrum “S3” and “S4” for AISI 321, and “S6” and “S8” for AISI 347). Significant change in surface morphology of oxide layers was observed on the IN 625 with change of gas atmosphere from air to argon atmosphere at 600˚C, shown in Figure 8-4 (c2) and (c3). In comparison to IN 825 samples exposed to air, clear evidence of a corrosion oxide layer was observed on samples exposed to argon, and particles corrosion oxide layers were dispersed on it. Needle-like corrosion oxides and crystalline oxide grains were randomly dispersed on the surface of IN 825 after test in air, while a porous corrosion oxide layer was observed when sample is exposed to argon, shown in Figure 8-4 (d2) and (d3).

8.3.4 Corrosion oxide characterization: Cross-sectional surface analysis

The cross-sectional analysis using the SEM was conducted to investigate the distribution of corrosion oxides across the depth. This is presented in Figure 8-5.

Referring to Figure 8-5 (a1) (b1) (c1) and (d1), only a few corrosion oxides were formed on samples’ surfaces after immersion test in air at 565˚C; an indication of low corrosion rate

under this condition. The thickness of oxide layers formed on stainless steels increased to ~ 10.5 μm from 3.5 μm at 565°C when the temperature is increased to 600˚C in air. There is also evidence of detachment and/or spallation of interfacial oxides in the form of an inner crack in Figure 8-5 (a2) (b2). When samples are exposed to argon at 600˚C, the image in Figure 8-5 (a3) indicates that the corrosion products formed on AISI 321 have two layers: an outer non-uniform layer (12-35 μm thick) and an inner 13 μm layer. The outer layer was identified as Fe_2O_3 and $NaFeO_2$ (referring to Figure 8-5 (a3) and Table 2, "S4"), while the inner layer was a mixture oxide of (Fe, Cr): $FeCr_2O_4$ spinel. Similar double oxide layers were found on AISI 347 with 8 μm outer Fe_2O_3 and 8-μm inner $FeCr_2O_4$ layer, as shown in Figure 8-5 (b3). For IN 625, no significant differences were observed between test at 565 and 600°C in air, while a 6 μm thick double layer was observed on surface of sample exposed to argon at 600°C. This double oxide layer consists of an outer mixed oxide of Fe and Ni and inner oxide of Cr. For IN 825, a thin oxide layer was formed after immersion test in air at 600˚C, consisting of Fe_2O_3 layer and some copper oxide crystalline (the copper from IN 825 substrate itself in Table 3-1) dispersed on the top layer, as shown in Figure 8-5 (d2). The thickness of corrosion oxide layer formed on the IN 825 samples exposed to argon atmosphere ranges from 9 -13 μm, and consist of an outer Fe_2O_3 layer and an inner mixed oxides of Cr and Ni.

8.3.5 Corrosion oxide characterization - Raman analysis

Raman measurement was used to identify the corrosion oxides and support the results from XRD analysis. The Raman spectra and referred Raman shifts are shown in Figure 8-6 and Table 8-2. Figure 8-6 (a) and (b) indicates that the $NaFeO_2$ and Fe_2O_3 forms as the outmost oxide layers on stainless steels, while the inner layer consists of Cr_2O_3 and $FeCr_2O_4$ spinel. The corrosion oxides formed on the surface of IN 625 are Cr_2O_3 and a mixed oxide of Fe and Ni (identified as $NiFe_2O_4$ ($NiO\text{-}Fe_2O_3$)), shown in Figure 8-6 (c). The main corrosion oxides formed on the IN 825 surface were identified as Fe_2O_3, Cr_2O_3 and $NiO\text{-}Fe_2O_3$ in Figure 8-6 (d). All of the Raman spectra correlates well with the results from XRD analysis.

8.3.6 Residual stresses analysis for interfacial oxide layers

As previously mentioned in this paper, there are internal stresses across the interfacial oxide layers linked to their growth mechanism, and thermal stress related to the conditions at the corroding interface. The internal stress induced by oxide growth is due to the fact that the specific volume of the oxide is rarely the same as that of the metal (Pu et al., 2014), and can be mathematically related to the Pilling-Bedworth ratio (PBR) obtained from Equation 48:

PBR=Vox/Vm Equation 48

Where Vox and Vm represent the Volume of oxide and metal. Generally, the oxide is expected to be in compression if PBR > 1 (the case for most metals), while the tensile stress develops in oxide scale with PBR < 1 (Birks et al., 2006, Yin et al., 2021). Generally metal – oxide interfaces with tensile stresses in the oxide cannot maintain protective films, e.g. K, Mg, Na. The PBR of NiO, Cr_2O_3 and Fe_2O_3 are 1.65, 2.07 and 2.14 respectively (Birks et al., 2006), indicating the protective nature of these oxide layer.

In addition, the thermal stress is generated during changes and fluctuations in the thermal profiles of the corroding interfaces due to the difference in the thermal expansion coefficient of the metal and oxide (Birks et al., 2006).

Note: The authors acknowledge the difficulty in isolating the stress effects due to oxide formation at high temperature and the stress contribution from the cooling of the test specimen at the end of the experiment. It is therefore assumed that both high temperature oxide formation process, and cooling of test specimen contributes to the total thermal stress effects at the molten salt – oxide – metal interface, and hence, the overall spallation behaviours of the interfacial oxide layers. This has now been considered collectively in the terms of Equation 49 (Birks et al., 2006) (the deduction part was shown in supplementary files):

$$\sigma_{Ox} = \frac{-(\alpha_{Ox} - \alpha_M)\Delta T}{\frac{2t_{Ox}(1-\gamma_M)}{t_M E_M} + \frac{(1-\gamma_{Ox})}{E_{Ox}}} \quad \text{Equation 49}$$

Where σ is the stress of the oxide formed for different thermal profiles; α_M and α_{Ox} are the (assumed constant) linear thermal-expansion coefficients for the metal and oxide, respectively; and $\Delta T = T_L - T_H$ is difference between the oxide formation temperature (T_H) and cooling temperature at the end of experiment (T_L), and thus the negative in sign in Equation 49; t_M and t_{Ox} are the thickness of metal and a single-oxide scale; γ_M and γ_{Ox} is the Poisson ratio of the metal and oxide; and E_M and E_{Ox} is the elastic modulus of the metal and oxide respectively. From the Equation 49, the ΔT is assumed negative and α_{Ox} is typically < α_M, and the stress (negative sign) in the oxide is typical compressive.

Table 8-3 lists the coefficients of thermal expansion (CTE) of some common oxides and the studied alloys. However, due to the similarity in the chemistry of the corrosion oxides layers and the variation in their thickness for different temperature and test atmosphere, the samples from test under argon atmosphere at 600˚C were used to for the Nano-indentation

test. This was because this condition provided samples with large enough thickness of the interfacial oxide layers for this analysis. Figure 8-7 (a) shows the load-displacement (P-h) curves obtained on the cross-sections of oxides formed on the alloys in this study. Based on the P-h curves, hardness H and elastic modulus E of the base metal, inner corrosion oxide layer and outer oxide layer were calculated using Oliver-Pharr method (originally developed to measure the hardness and elastic modulus of a single phase elasto-plastic material from the indentation load–depth curve with sharp indenters) (Pharr and Oliver, 1992a) and the results were plotted in Figure 8-7 (b).

The thermal stress values obtained using Equation 49 for the stress between inner layer and bulk material and between inner layer and outer layer were presented in Table 8-4. Referring to Table 8-4 for calculated thermal stress values:

σ_1 represents the stress between the inner oxide layer and bulk substrate for samples under argon atmosphere at 600˚C.

$\boldsymbol{\sigma'_1}$ represents the stress between inner oxide layer and outer oxide layer for samples under argon atmosphere at 600˚C.

σ_2 represents the thermal stress between inner oxide layer and bulk substrate for samples in air at 565˚C.

$\boldsymbol{\sigma'_2}$ represents the thermal stress between inner oxide layer and outer oxide layer for samples in air at 565˚C.

σ_3 represents the stress between the inner oxide layer and bulk substrate for samples in air at 600˚C.

$\boldsymbol{\sigma'_3}$ represents the thermal stress between inner oxide layer and outer oxide layer for samples in air at 600˚C.

Details of calculation is shown in the supplementary files.

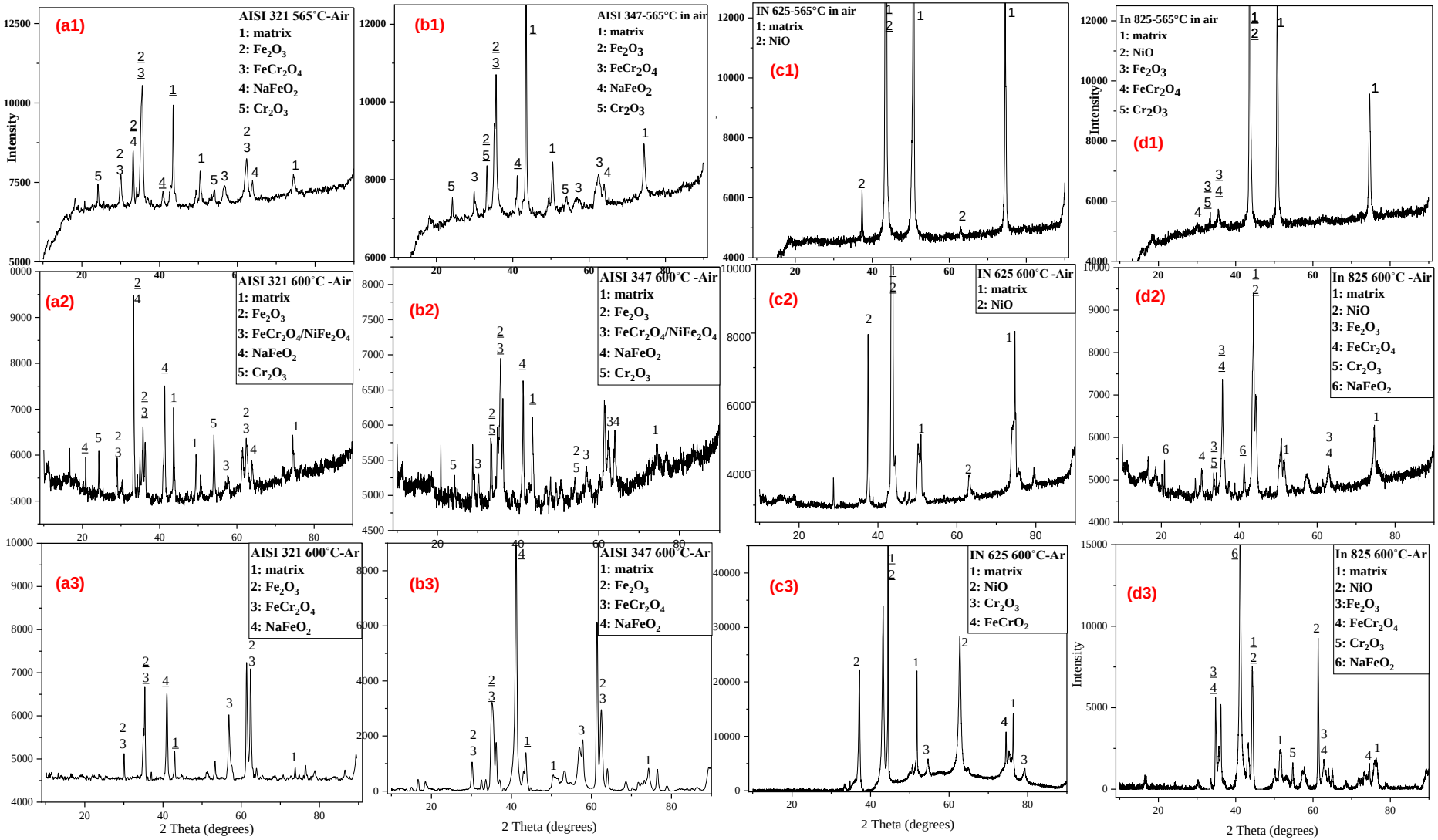

Figure 8-3. XRD patterns of studied alloys under different immersion conditions (phase number with underline meaning the 100% intensity peaks), (a) AISI 321, (b)AISI 347, (c) IN 625 and (d) IN 825 after 7-day immersion test in Solar salt at (1) 565˚C in air (2)600˚C in air (3)600˚C in argon, respectively.

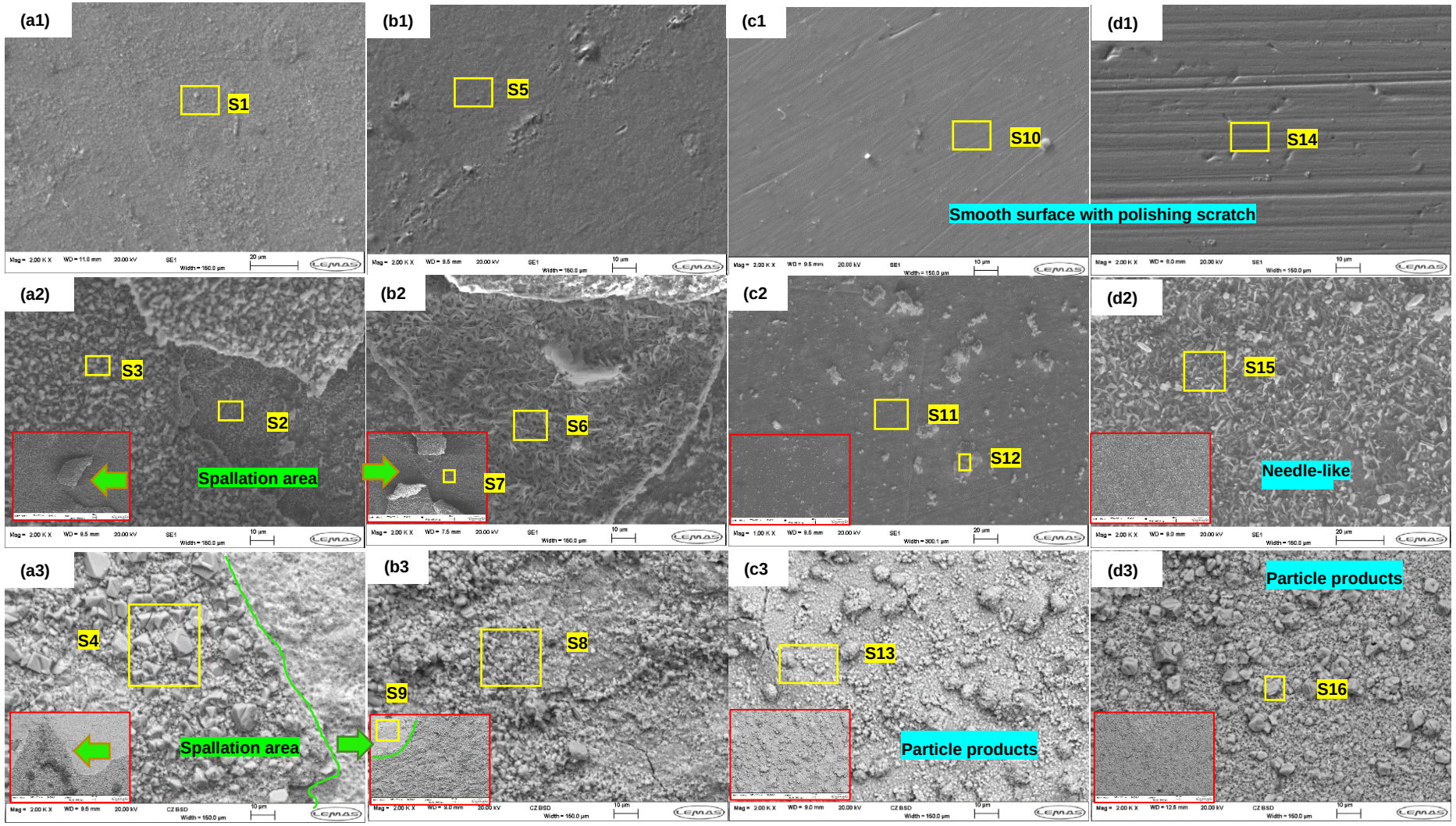

Figure 8-4. SEM top surface of the oxide scales formed on (a) AISI 321, (b)AISI 347, (c) IN 625 and (d) IN 825 after 7-day immersion test in Solar salt at (1) 565˚C in air (2)600˚C in air (3)600˚C in argon

Table 8-1. EDX data for regions and possible phase in Figure 8-4

Element in wt%	Possible phase	Fe	O	Cr	Ni	Na
S1	$FeCr_2O_4$, Fe_2O_3	60.1	18.9	12.1	-	0.1
S2	$FeCr_2O_4$, Fe_2O_3	50.1	22.9	20.6	4.4	0.5
S3	$NaFeO_2$, Fe_2O_3	54.7	20.2	1.4	0.2	22.6
S4	$NaFeO_2$, Fe_2O_3	49.99	32.4	0.62	0.32	6.73
S5	$FeCr_2O_4$, Fe_2O_3	69.8	17.9	12.1	10.1	0.2
S6	$NaFeO_2$, Fe_2O_3	60.7	21.8	1.2	0.6	13.8
S7	$FeCr_2O_4$, Fe_2O_3	66.1	21.1	8.7	2.6	-
S8	$NaFeO_2$, Fe_2O_3	50.64	29.86	0.62	2.99	9.99
S9	$FeCr_2O_4$, Fe_2O_3	51.29	28.78	8.52	4.71	1.43
S10	NiO	2.6	7.1	16.2	54.0	-
S11	NiO	3.0	18.9	4.3	71.8	-
S12	NiO, $(Fe, Cr)_2O_3$	11.6	25.9	2.4	46.4	8.7
S13	NiO, $(Fe, Cr)_2O_3$	7.45	21.53	1.1	60.8	2.08
S14	NiO, $(Fe, Cr)_2O_3$	28.5	8.9	18.6	38.8	-
S15	NiO, Fe_2O_3,$NaFeO_2$	39.1	23.7	8.5	12.8	9.9
S16	NiO, Fe_2O_3,$NaFeO_2$	39.6	34.19	1.04	6.78	9.11

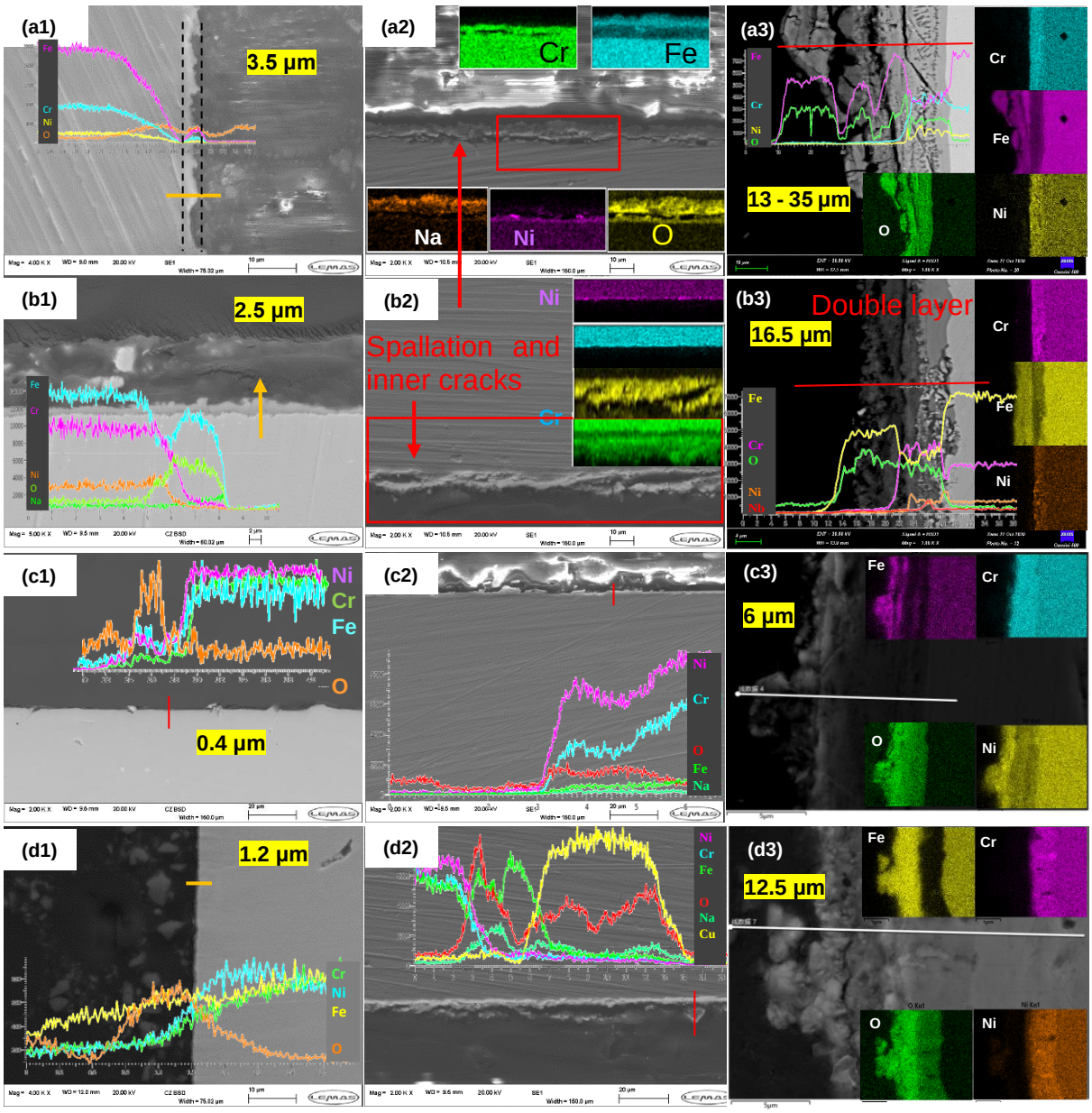

Figure 8-5. SEM-EDX profile of the oxide scales formed on (a) AISI 321, (b)AISI 347, (c) IN 625 and (d) IN 825 after 7-day immersion test in Solar salt at (1) 565˚C in air (2) 600˚C in air (3) 600˚C in argon.

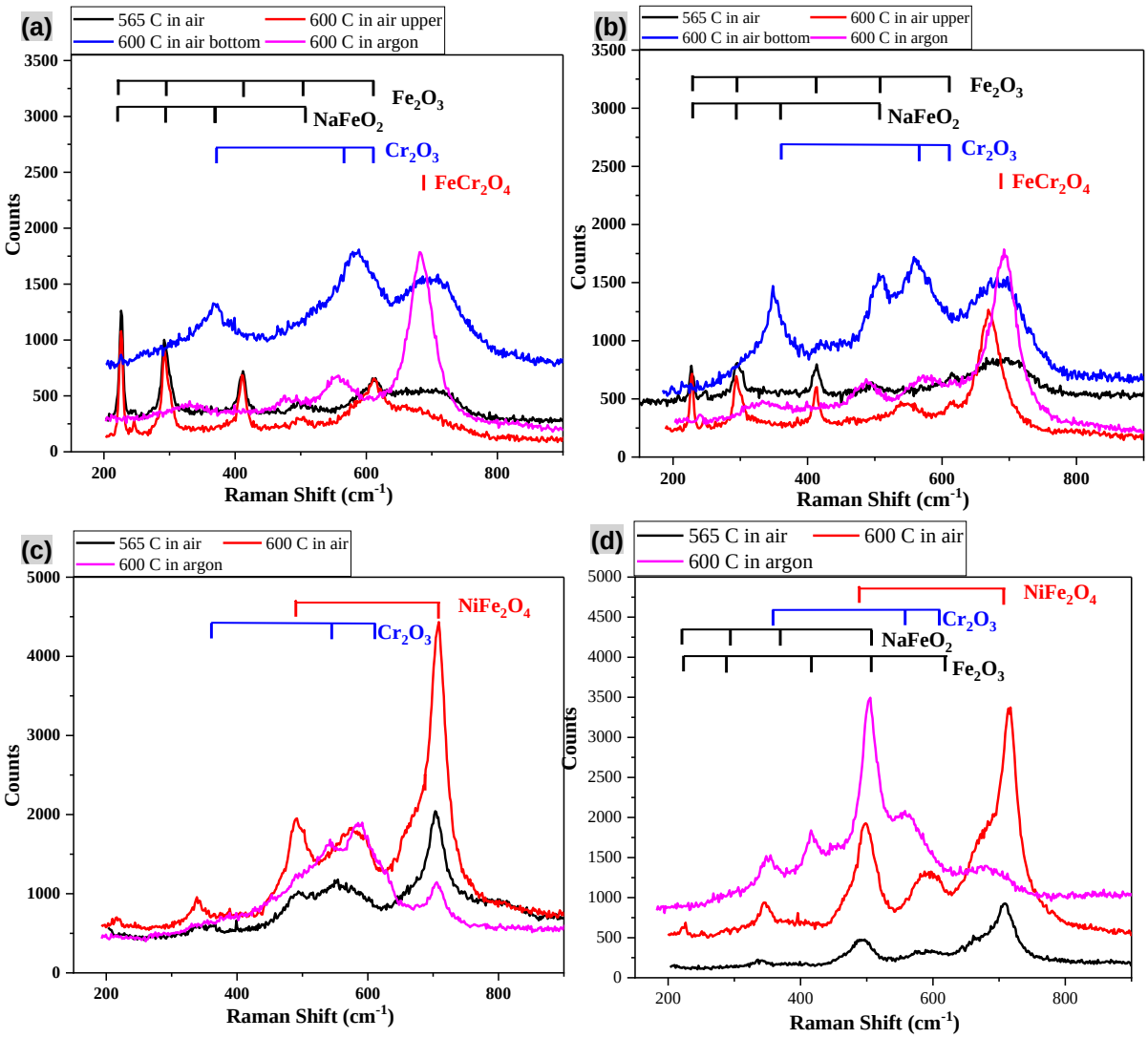

Figure 8-6. The detected Raman spectra for the development of the corrosion product scales on studied alloys (a):AISI 321, (b):AISI 347, (c) IN 625 and (d) IN 825 at various conditions**.**

Table 8-2. Raman frequencies (cm^{-1}) of the oxides studied from literature (Rahmawati et al., 2021, McCarty and Boehme, 1989, Colomban et al., 2008, de Faria et al., 1997)

Oxides	Raman shifts cm^{-1}
Fe_2O_3	225, 290, 411, 501, 610
$NaFeO_2$	220, 290, 350, 507
Cr_2O_3	353, 550, 616
$FeCr_2O_4$	686
$NiFe_2O_4$	487, 704

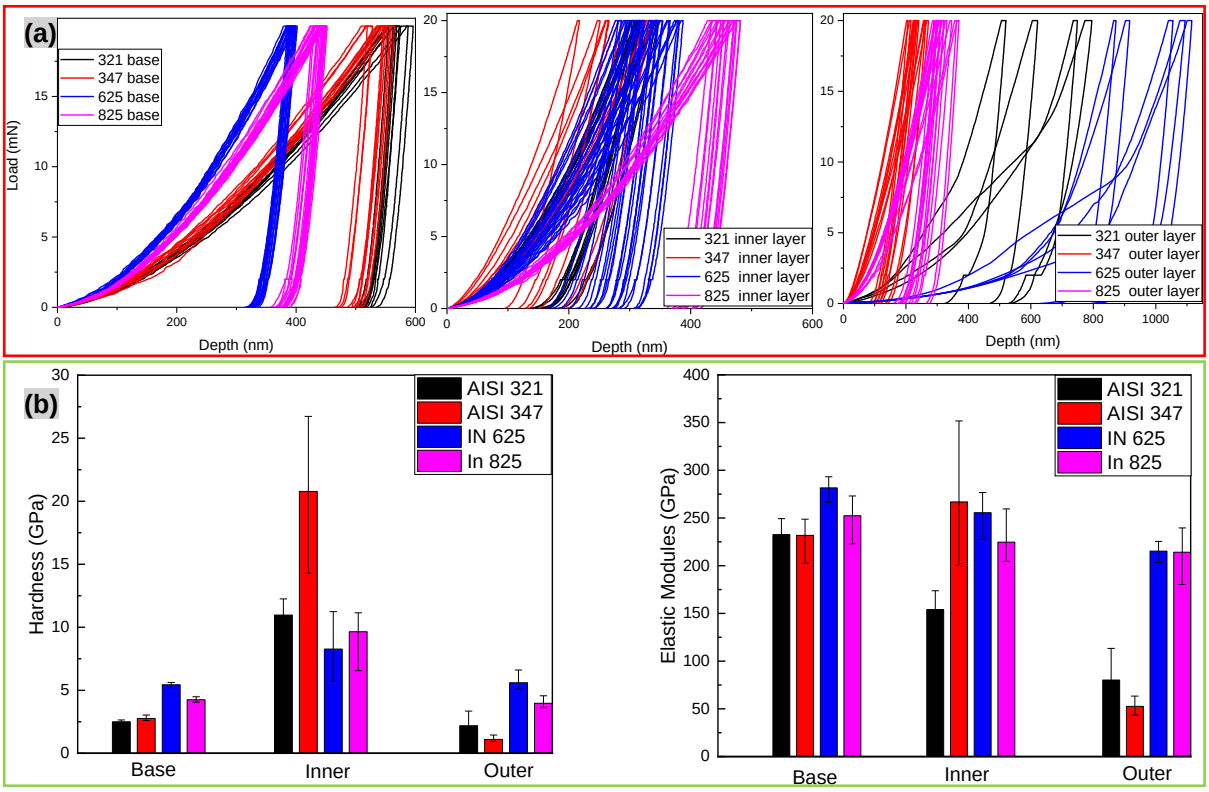

Figure 8-7. (a)Typical P-h curves of base material, inner layer and outer layer of AISI 321, AISI 347, IN 625 and IN 825 and (b) corresponding harness and elastic module (samples after 600˚C isothermal in argon).

Table 8-3. Linear coefficient of thermal expansion of metal and oxide (Hancock and Hurst, 1974) (temperature range 100-800 ˚C)

System	Thermal expansion coefficient (*10^{-6}) of Oxide (Yin et al., 2021)	Thermal expansion coefficient (*10^{-6}) of metal (Yin et al., 2021)	Poisson ratio
Fe-Fe_2O_3 Fe -Fe_3O_4	12 15	15.3	0.25 (Ramos et al., 2021)
Ni-NiO	17.1	17.6	
Cr-Cr_2O_3	7.3	9.5	0.33 (Ramos et al., 2021)
Austenitic SS	-	16.0-19.5 (~17.4)	0.33
Inconel 625	-	13.1-17.8 (~17.8)	0.308

Table 8-4. Calculated thermal stress values from Equation 49 (σ_1 represents the stress between inner layer and bulk and σ_2 represents the stress between inner layer and outer layer of argon isothermal samples, σ_3 and σ_4 represents the thermal stress between oxide layer and bulk material in air isothermal at 565˚C and 600 ˚C respectively).(calculation part was shown in Appendix part)

Material/stress (GPa)	YS/TS (GPa)	Argon 600˚C		Air 565˚C		Air 600˚C	
	At 600˚C	σ_1	σ'_1	σ_2	σ'_2	σ_3	σ'_3
AISI 321	0.13/0.38	-1.335	0.158	-0.348	*	-1.335	0.169
AISI 347	0.16/0.36	-2.31	0.138	-0.229	*	-2.31	0.087
IN 625	0.34/0.80	-2.20	0.491	-0.118	*	-0.125	*
IN 825	0.15/0.48	-1.045	0.013	-0.969	*	-1.032	*

*: Not applicable with unavailable double layer, YS/TS: yield strength and tensile strength

8.4 Discussion

8.4.1 Effect of temperature on the corrosion characteristics and chemical evolution of interfacial oxide layers

Figure 8-2 shows the weight loss and corrosion rate of stainless steels and Ni-based alloys after 7-day immersion test in solar salt, under air and argon atmosphere at 565 and 600˚C.

Referring to Figure 8-2 (a), for all samples exposed to air, the corrosion rate increased with increasing test temperature from 565 to 600˚C, which shows good agreement with the literature (Kruizenga et al., 2013). This is partly due to the effect of temperature in changing the salt chemistry according to Equation 12 and Equation 13. It is reported that the corrosiveness of solar salt result from the decomposition of nitrate salt into nitrite salt and oxide ions, once the salt's stability limit of 565 ˚C is surpassed (Walczak et al., 2018, Fernández and Cabeza, 2019b). The equilibrium constant of Equation 12 at 550 ˚C is reported to decrease with increasing temperatures (Fernández and Cabeza, 2019b), accelerating the formation of NO_2^- and thus increasing the corrosiveness of the salt.

From the results XRD patterns and Raman spectra in Figure 8-3 and Figure 8-6, it is shown that the oxide layers formed on the surface of AISI 321 and AISI 347 in solar salt consists of different combination of iron oxide (Fe_2O_3), iron chromium spinel ($FeCr_2O_4$), sodium ferrite ($NaFeO_2$), and chromium oxide (Cr_2O_3). For IN 625, nickel oxides (NiO) were identified on

the corrosion surface after test in air, and mixture oxide of Ni and Fe was also observed on the Raman spectra. NiO and mixed oxides of (Fe, Cr) are both identified on the samples of IN 825 after test in air at 565 and 600˚C. $NaFeO_2$ was identified on the IN 825 after test at 600˚C in air and under argon atmosphere (see Figure 8-3 (d2)). The specific combination of the oxide chemistries is dependent on the specific combination of test temperature and cover gas atmosphere. The possible reactions to form the corrosion oxides are reported in a previous study (Liu et al., 2022b, Liu et al., 2022a).

For AISI 321, 347 and IN 825 tested in air, $NaFeO_2$ was identified with a higher peak intensity at 600˚C (see Figure 8-3 (a2), (b2) and (d2)), is known to be porous, non-protective, and is likely to spall off as shown by region “S3” and “S6” in Figure 8-4 (a2) and (b2). After spallation of $NaFeO_2$, inner Cr-rich layer was exposed to molten salt as shown by region “S2” and “S7”. This is a recipe for increased corrosion activities at the interface, especially as it has been reported that Cr-containing oxide was likely to dissolve into nitrate salt (Ahmed, 2013), therefore resulting in high corrosion rate in Figure 8-2. The spallation behaviours were also observed on the images from cross-sectional analysis in Figure 8-5 (a2) and (b2). It should mention that a double oxide layer was observed on the surfaces of stainless steels after test at 600˚C in air, consisting of an outer $Fe_2O_3/NaFeO_2$ and inner $FeCr_2O_4/Cr_2O_3$, as shown in Figure 8-5. The initially formed dense and protective Cr_2O_3/ $FeCr_2O_4$ layer prevents or retards the outward diffusion of alloys elements from the metal and inwards diffusion of oxide ions, while the outer Fe_2O_3 can protect the dissolution of Cr-rich later into molten salt. This synergetic protection mechanisms are destroyed once the formation and spallation of $NaFeO_2$ occurred at higher temperature above 600˚C (Bell et al., 2019), therefore resulting in higher corrosion rate and deeper corrosion depth.

The relative smooth surfaces are observed on the surfaces of all samples test at 565°C in air, where the corrosion layer was thin, dense and compact with the bulk metal, as shown in SEM and cross-sectional images in Figure 8-4 and Figure 8-5 (a1) – (d1). Polishing scratches are still visible on the surface of Ni-based alloy as evidence of supressed corrosion activities. Mild corrosion occurred on the samples at 565˚C in air and the corrosion process could be greatly accelerated by elevating temperature to salt unstable temperature.

8.4.2 Effect of test atmosphere on corrosion characteristics and chemical evolution of interfacial oxide layers

As briefly discussed earlier, the corrosion rate of studied alloys increases significantly with change in test atmosphere from air to argon at 600˚C. In argon atmosphere, there is a

general belief that oxidation, and hence corrosion process should have been supressed in the oxygen-free environment. However, in this study, the obtained corrosion rate and the visible corrosion surface indicates that the corrosion process occurring under argon atmosphere is more severe. This has been linked to a combination of specific reaction pathways that influences the corrosiveness of solar salt, the impact of delayed passivation from Cr_2O_3 and preferential formation of other non-protective oxide layers from previous publications (Bell et al., 2022, Liu et al., 2022b) . S. Bell (Bell et al., 2022) was highlighted similar complexity related to corrosion in oxyanionic salt environment, and believed that basicity, and oxygen availability were responsible for the oxidation state of Fe and Cr, thus affecting the corrosion process.

For Stainless steel samples and referring to the XRD patterns in Figure 8-3 (a2), (a3), and (b2), (b3), Cr_2O_3 can be identified on the sample surface in air at 600˚C, not in argon. It is expected that Cr_2O_3 forms as a passive oxide layer to protect the alloy element's outwards diffusion. The absence of Cr_2O_3 on surface of samples under argon atmospheres could be explained by its delayed formation due to the unavailability of oxygen. This has been observed in this study for the early stages in the evolution of the corrosion interface, and corroborates the observations of S. Bell (Bell et al., 2022). Delayed passivation will also imply a non-equilibrium in favour of availability of Cr, Fe at the molten salt – alloy interface. The outward diffusion of these atoms from bulk material to the corrosion interface is driven by high temperature and resulting in concentration of atoms at the interface. The absence of a prompt supply of oxygen to promote quick passivation of the interface will lead to the formation of thicker films of Cr-oxide layers as soon as oxygen becomes available via decomposition of nitrate to nitrite ions. Meanwhile, due to the high affinity of Fe and O, the formation and accumulation of Fe_2O_3 would promote the formation of $NaFeO_2$. This is shown by the higher peak intensity for $NaFeO_2$ in XRD patterns for test under argon atmosphere than in air. Due to the porous and non-protective nature (shown in Figure 8-4), thicker corrosion oxide scales are likely, and with an uneven thickness (shown in Figure 8-5). The $NaFeO_2$ outer layer also have the tendency to spall off.

While the formation and spallation of $NaFeO_2$ is also observed in air, the initially formed inner Cr_2O_3 limits the outward diffusion of Fe and formation of Fe_2O_3, and therefore decrease the amount of $NaFeO_2$. Despite the observation of spallation in Figure 8-4 (a2) (b2), the corrosion oxide layer is thinner with a uniform thickness. The different source and/or availability of oxygen in air and in argon directly affects the kinetics of Cr_2O_3 formation. A recent study also confirmed (Bell et al., 2021) that the corrosion was accelerated when an

inert argon environment was used in chloride/sulphate salt for nickel superalloy based on the basic salt corrosion mechanism and sodium metal oxides are favourable formed. Also our previous study (Liu et al., 2022b) confirmed that the salt aggressiveness after 2-week test in argon was higher than that in air with a higher nitrite concentration due to nitrate decomposition.

8.4.3 Interfacial stress distribution and the corrosion characteristics of interfacial oxides

In this study, the nano-mechanical properties of the corrosion layers are investigated via nano-indentation to explain the spallation due to the different thermal stress between the layers and bulk material. For Stainless steels, the hardness of base metal is higher than that of outer oxide layer and lower than that of inner oxide layer, which indicates that inner oxide layer is denser and more protective whilst outer oxide layer is porous. As shown in Figure 8-5 (a3) (b3), the EDX line and mapping show that inner oxide layer as a Cr-rich layer and the porous outer Fe_2O_3/$NaFeO_2$ layer was attributed to the high-density of defects (e.g. pores and micro-cracks). The high hardness and stiffness associated with the continuous and compact inner oxide layer formed on the Stainless Steels samples (under argon atmosphere at 600°C) indicates that the inner oxide layer is capable of providing an effective barrier to isolate the base metal from the oxidizing molten salt. The high strength inner oxide layer also implies a higher resistance cracking and/or breakdown. For Ni-based alloys, the hardness difference between inner/outer oxide layers with base metal is not as much as that of Stainless Steels. The hardness of base metal is almost same with that of outer oxide layer and slightly lower than that of inner oxide layer. Referring to the cross-sectional images, Cr-rich inner oxide layer was observed on the surfaces of Ni-based alloys, while outer Fe-rich oxide layer was also observed to have more pores and micro-cracks. In comparison with the outer oxide layers formed on all the studied alloys, the hardness of outer oxide layer on Ni-based alloys are almost 2 times higher than that on the stainless-steel samples, indicating the outer oxide layer is more stable on Ni-based alloys.

As earlier discussed, the oxide growth related stress on oxides formed on Stainless steels and Ni-based alloys are protective under compressive stress. Referring to the thermal stress calculated from the Equation 49 (listed in Table 8-4 the negative sign of thermal stress between inner oxide layer and base metal also shows the compressive stress for all the alloys; with values ranging from 1.045 – 2.31 GPa for samples tested in air at 600˚C, and 0.118 - 0.348 GPa for samples test in air at 565˚C. This shows great agreement with the

observed higher strength of compact inner oxide layer and its protectiveness. The tensile stress is found between inner oxide layer and outer oxide layer; with values ranging from 0.013 – 0.491 GPa for samples tested under argon atmosphere, and 0.087 - 0.169 GPa for stainless steels samples tested in air at 600˚C. The tensile stress between inner and outer oxide layers discussed above were calculated for corrosion interface with double oxide layers; This was not applicable for the samples in air at 565˚C or the Ni-based alloys samples at 600˚C in air (see Table 8-4).

This is evident that the compressive stress (negative sign) could help keep the inner oxide layer adhered to base metal and tensile stress (positive sign) could lead to spallation of outer oxide layer. The reasons responsible for the results above are probably attributed to the structure of corrosion oxide layers, where initially formed inner oxide layer was the primary corrosion oxides with higher hardness and strength, and better adherence to the base material. For stainless steel, the outer oxide layer (identified as $NaFeO_2$ by SEM) shows lower hardness than inner oxide layer, and the stress calculation confirmed its poor adherence to inner layer, and thus a recipe potential spallation to occur. The tensile stress or the thermal stress obtained between inner oxide layer and outer oxide layer could be attributed to the thermal expansion coefficient of inner Cr-based oxide layer and outer Fe-based oxide layer, as well as the thickness ratio of the double oxide layer. So the dense protective inner oxide layer is difficult to spall off by thermo-mechanical stress effects. However, this does not completely prevent the electrochemical attack of the inner oxide layer by aggressive molten salt species, particularly after the spallation of the outer oxide layers. As shown in Figure 8-5, the inner oxide layer was associated with less spallation after immersion test in solar salt. It is believed from this study that the tendency for spallation of interfacial oxide layers to occur on the surface of these alloys is closely related to mechanical properties of the interfacial oxide layers.

8.5 Conclusions

This study has successfully investigated the early stages (over 7 days) of corrosion behaviour of various alloys as a function of temperature and test atmosphere with the aim of correlating the overall corrosion characteristics at the molten salt- oxide – metal interface with the stress distribution across the interface. Here are the key conclusions.

- The corrosion rate of stainless steel and Ni-based alloys in molten nitrate salts increases 3-fold with increase in temperature from 565˚C to 600°C in air.

- A synergy of high temperature and argon test atmosphere further increases the corrosion rate at 600°C up to 3 times higher than the test in air at same temperature. This synergy is related to a combination of Arrhenius effect of high temperature on the rate of decomposition of nitrate salts to nitrite and delayed passivation with Cr_2O_3 formation due to supressed availability of oxygen at the corrosion interface.
- The corrosion characteristics at the molten salt – oxide – metal interface was controlled by the overall protective properties of the multiple corrosion oxide layers formed. A more porous and less protective outer oxide layer consisting of a mixture of $NaFeO_2$ and Fe_2O_3 is kinetically favoured to form preferentially at 600°C than at 565°C, and under argon atmosphere than in air.
- The thermo-mechanical stress profile of the interfacial oxides correlates with the tendency for spallation to occur and overall corrosion rate.
- The observed inner Cr-rich oxide layer is more adherent and resilient to degradation than the outer Na/Fe-based oxides. This was observed in this study to be due to the compressive stress between the inner Cr-rich oxide layer and the substrate material, and the destructive tensile stress between inner Cr-rich outer layer and outer Na/Fe-rich oxides layer.
- The spallation of sodium iron oxide ($NaFeO_2$) formed on samples tested in air and under argon atmosphere at 600°C directly correlates to the tensile stress between the Cr-rich inner oxide layer and the $NaFeO_2$ layer.

Chapter 9. Solar thermal irradiation cycles and their influence on the corrosion behaviour of stainless steels with molten salt used in Concentrated Solar Power plants

This chapter was originated from paper “Solar thermal irradiation cycles and their influence on the corrosion behaviour of stainless steels with molten salt used in Concentrated Solar Power plants”. Under review by Solar Energy Material and Solar Cells.

Solar Energy Materials & Solar Cells 251 (2023) 112141

Contents lists available at ScienceDirect

Solar Energy Materials and Solar Cells

journal homepage: www.elsevier.com/locate/solmat

Solar thermal irradiation cycles and their influence on the corrosion behaviour of stainless steels with molten salt used in concentrated solar power plants

Qingyang Liu [a,b,*], Jiong Qian [b,c], Anne Neville [a,b], Frederick Pessu [a,b]

[a] Institute of Functional Surface, School of Mechanical Engineering, University of Leeds, Leeds, LS2 9JT, United Kingdom
[b] Jiuli Corrosion and Integrity Centre Laboratory (University of Leeds), Leeds, LS2 9JT, United Kingdom
[c] Engineering Research Centre of High-Performance Nuclear Power Pipe Forming of Zhejiang Province, Huzhou, 313028, China

ARTICLE INFO

Keywords:
Molten nitrate salt
Isothermal
Thermal cycling
Thermal shock
Interfacial oxides
Spallation

ABSTRACT

In this study, the corrosion behaviour of stainless steels AISI 321 and 347 in molten nitrate salt were investigated for up to 28 days. Three different thermal conditions; isothermal, thermal cycling and thermal shock, were explored to investigate the effect of the likely temperature gradients on the corrosion characteristics of AISI 321 and 347 during the operation of Concentrated solar power plants. Gravimetric corrosion analysis was combined with micro-morphology and cross-sectional analysis of the corrosion interface; using a combination of scanning/transmission electron microscopy, energy dispersive X-ray spectroscopy and X-Ray diffraction techniques, for this study. Results from corrosion rate measurements and surface characterisation show that thermal shock induces higher material degradation rate than the two other temperature profiles. Severe spallation of interfacial corrosion oxide layers was observed under thermal shock conditions other than in isothermal and thermal cycling conditions and correlated to the overall performance after 28 days. The level of spallation of interfacial oxides across the three temperature profiles investigated in this study was linked to the induced stresses from mismatch in the thermal expansion properties between the corrosion oxide layer and the substrates.

9.1 Introduction

The operation of CSPs at the temperature ≥ 600˚C inevitably poses significant corrosion threats to all the metallic components in contact with molten salt. Corrosion threat to metallic components is expected to increase with the recent push towards higher temperature up to 720˚C with more aggressive salt types such as chloride and carbonate salt (Mohan et al., 2019) to reduce the levelised cost of electricity (LCOE) (Bell et al., 2019). In this case, the optimal combination of salt type and metallic materials is of vital importance for safe and stable operation of CSP to avoid any potential failure caused by potential occurrence of corrosion. Many research on the corrosion performance of carbon/low-alloys steel, stainless steels and Ni-based alloys with different salts at different temperatures are summarised by

M. Walczak (Walczak et al., 2018) respectively. Updated corrosion studies (Elbakhshwan et al., 2022, Li et al., 2022, Gao et al., 2022) also conducted isothermal corrosion tests to investigate different alloys resistance in solar salt by immersion and electrochemical tests. Despite different test methods employed, almost all the results are conducted under isothermal condition and provided quick material selection guide for the combination of salt and metals.

However, in the real CSP plants, the operating conditions are more intricate and more complex due to the alternation of day/ night and even unpredictable and sharp weather change within a short period of time. In this study, we will introduce two new methodologies linked to two different temperature profiles encountered during CSP operations. These are 'thermal cycling' and 'thermal shock', which reflects the type of temperature changes that takes place during a typical CSP operation. Thermal cycling was developed to closely simulate real solar irradiation and storage cycles from the industrial scale CSP plant. It accounts for temperature profile during 12-hour peak day-time heating and 12-hour night-time cooling within heat transfer pipes or heat storage tanks (Liu et al., 2022a). In a type CSP with two-tank sensible TES, the tanks and pipes are as much as possible under isothermal conditions. However, pipes from receivers to hot tanks and to turbines / exchangers experience hot isothermal during available solar radiation and 'cold' isothermal at night (just above melting temperature). Hot tanks at daytime would store as much as possible hot salts and then pump them out to turbine to generate electricity at 6-10 pm and 7-9 am (Pelay et al., 2017) (peak-consumption of electricity). Typical CSP-TES systems (Pelay et al., 2017) have maximum 7-hour storage capacity of hot tanks, which would experience 'cold' isothermal (290°C) after running out salt stock or deep cycling (i.e. to 30°C) after drainage of salt. Literatures reporting the effect of thermal cycling on the corrosion performance in CSP plant are limited. Bradshaw (Bradshaw and Goods, 2001b) found that thermal cycles could moderately increase the corrosion rate of stainless steels, while B.Li (Li et al., 2020) investigated how thermal cycling affects the thermal stability and properties of mixed carbonate salts. Previous study (Liu et al., 2022b, Liu et al., 2022a) also reported that the thermal cycling reduces the mass loss and corrosion rate by slowing down the corrosion kinetics of the reactions. The thermal cycling / thermal shock should generally involve chemical degradation / dissolution of molten salt (Bell et al., 2019, Liu et al., 2022a) and mechanical degradation (Mallco et al., 2022, Prieto et al., 2022, Preußner et al., 2016) of material under study, which could further bring more complexity in a CSP fields.

It is well established that, the availability of consistent solar irradiation could significantly affect the electric energy generation capacity and efficiency of CSPs. According to CSP operations and maintenance experience, the receiver pipe panels are expected to experience a rapid temperature drop by a few K per second from working temperature to ambient temperature (25°C) by the weather changes like dark clouds and strong winds. These are common scenarios (described as “thermal shock”) in real tower power plants constructed at northwest of China, where extreme weather attacks frequently. Under this circumstance, the engineers have to cut off the solar irradiation from mirrors (heliostats) in advance to take away the heat on the surface of the receiver pipe panels. The threat posed by irregular thermal shocks on material integrity is significant and always contributes to severe deformation, causing material failure and leading to the shutdown of the CSP system and causing significant economic loss. In other words, the deformation and explosion of receiver pipes induced by thermal stresses and thermal shock are fatal to the whole plant because those expensive parts are highly metallurgical precise and hard to repair. Also researchers affirmed that the spallation behaviours of the oxides layer (Ramos et al., 2021) were attributed to the stresses mismatch (Pu et al., 2014) between the bulk material and oxide layers due to difference in the thermal expansion coefficient and elastic modulus of it (Birks et al., 2006).

There are currently limited studies on effect of thermal shock on the corrosion mechanism and performance of metallic components molten salt. This further introduces more complexities to the corrosion mechanisms in comparison to thermal cycling and isothermal temperature profiles. In this study, the corrosion characteristics and performance of stainless steels, AISI 321 and 347 is investigated under isothermal, thermal cycling and thermal shock condition in molten nitrate salt with air as cover gas for up to 28 days. Thermal shock in this study is simulated between 565 and 30°C, while thermal cycling is simulated between 565 and 290°C. The methodology and results in this study could provide an updated guideline for the characterisation and selection of the materials for use in CSP plants.

9.2 Experimental methodology

Solar salt (60 wt. % $NaNO_3$ and 40 wt. % KNO_3) was selected for this study due to its wide application in CSP plants. The salt was weighed and mixed to achieve the required ratio and placed in a box glove with inert gas for 2 days. Then the salt was moved to the furnace to dry at 120 for 24 hours. Details of salt purity and preparation procedure can be found in previous publication (Liu et al., 2022a).

The materials used in this study were AISI 321 and AISI 347 austenitic stainless steels, and the composition of these alloys is provided in Table 3-1. The as-received pipes were supplied by Zhejiang JIULI Hi-tech Metals Co., Ltd China. Samples with dimension of 23mm*13mm*3mm were wire-cut from the wall of seamless pipes. The test samples were wet grind to 1200 grit with silicon carbide (SiC) paper and followed by polishing with 9 μm, 6μm, 1μm and 0.25 μm diamond paste. Polished samples were then degreased with acetone and deionised water, respectively, following by hot-air drying. The initial dimensions and mass of coupons were recorded using a micrometre and analytical balance (0.01mg, Ohaus Analytical Plus balance, New Jersey, United States).

The test samples were placed in individual crucibles and covered with dried nitrate salt mixture in accordance with the specification of ISO 17245:2015 (2015). The tests commenced after transferring each sample-containing crucible into the muffle furnace. The tests were conducted under isothermal, thermal cycling and thermal shock condition in air for 7 days, 14 days and 28 days respectively, according to the time-temperature profile shown in Figure 9-1 (a) and (b).

The temperature fluctuation between 290 and 565°C every 12 hours in thermal cycling is designed to replicate as closely as possible the real-time cycle between daytime 12-hour peak heating and night-time 12-hour cooling. The heating and cooling rate for thermal cycling is set as 10°C/min. 565°C was set as isothermal temperature and peak temperature for thermal cycling and thermal shock, below which the salt mixtures can remain stable. Most of the pipes and cold tanks are kept above the melting temperature of the salt (220°C) to prevent blockages, so 290°C was chosen for thermal cycling in this study.

For thermal shock, the temperature of the samples drops significantly from 565°C in molten salt to 30°C in air within 10 minutes to simulate the drainage process of molten salt in the receiver pipes during the rapid cooling process that occurs as a result gust of cold wind and cloudiness, that cuts off the supply of solar irradiation. The thermal shock samples were taken out of salt-containing crucibles by tongs and kept in air at room temperature (30 ± 2˚C and relative humidity of 50 ± 5%) for 30 minutes. Afterwards, the samples were re-immersed into liquid salt immediately to exaggerate the effect of thermal shock (Bradshaw and Goods, 2001b). This process was repeated once a day at a fixed time to compare the results with isothermal and thermal cycling test.

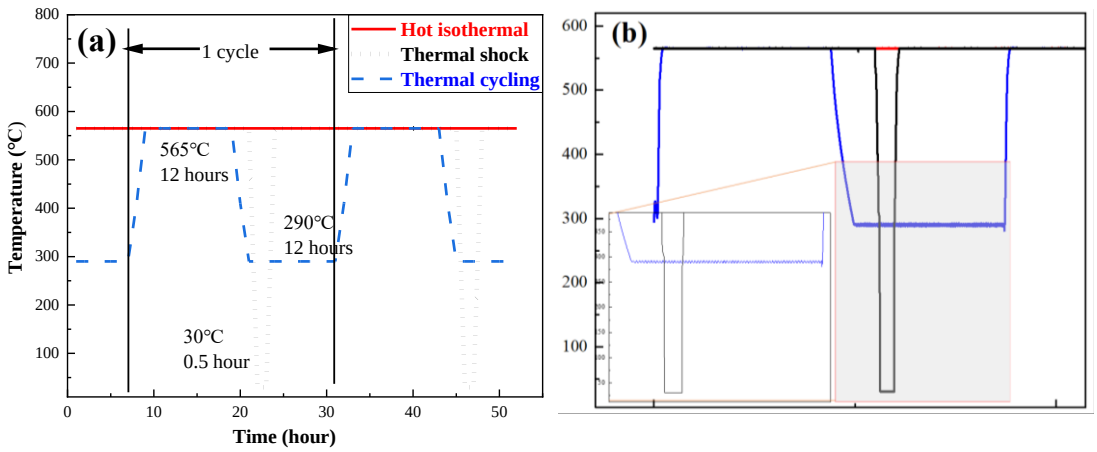

Figure 9-1. (a) the designed and (b) oven recorded time-temperature profile of isothermal immersion, thermal cycling and thermal shock

9.3 Results and discussion

9.3.1 Mass loss and corrosion rate measurements

The time independence of mass loss or corrosion rate can be used to explain the process and mechanism of corrosion reaction. Pieraggi (Pieraggi, 1987) introduced parabolic kinetics to illustrate the corrosion/oxidation performance that mass loss increase linearly with the square root of time and described by the following parabolic law:

$$\Delta m = k_p t^{1/2} + A_p \qquad \text{Equation 50}$$

Where k_p is the parabolic rate constant (mg/(cm^2·h$^{1/2}$)), t is the exposure time (h), A_p is the intercept term (mg/cm^2). Figure 9-2 shows the descaled mass loss with the square root of time for AISI 321 and 347 under different thermal conditions, from where we can observe that the mass loss for all samples increase with increase in exposure time. It is also observed from Figure 9-2 and Figure 9-3 that samples from thermal cycling tests recorded the lowest mass loss and corrosion rate values while samples from thermal shock showed the highest mass loss and corrosion rate values.

In comparison to isothermal corrosion over 28-days, mass loss samples from thermal shock tests were observed to increase by ~35.7% for AISI 321 (from 2.33 mg/cm^2 in isothermal to 3.157 mg/cm^2 in thermal shock after 28 days), and ~285.7% for AISI 347 (from 1.40 mg/cm^2 to 5.40 mg/cm^2 after 28 days). Similarly, mass loss of samples from thermal cycling tests was observed to decrease by 51.7% for AISI 321 (to 1.125 mg/cm^2), and 29.7% for AISI 347 (to 0.9845 mg/cm^2) compared with that from isothermal test after 28 days. It is shown that the AISI 321 and 347 have similar profile of mass loss and corrosion rate changes with time

under isothermal and thermal cycling condition. To have a better comparison between these thermal conditions, the time scale of isothermal, thermal cycling and thermal shock were normalised based on the result of mass loss after 672-hour (4 weeks) immersion test. For AISI 321: 100h ISO ≡ 207.0h TC (total time) ≡ 73.8h TS ≡ 103.5h TC (hot time only), for AISI 347: 100h ISO ≡ 143 h TC (total time) ≡ 25.9h TS ≡ 71.5 h TC (hot time only). It is worth mentioning that the normalised time for thermal cycling was calculated by 'total time' and 'hot time' respectively to give insight into the corrosion kinetics. The samples for AISI 321 would be immersed for 207 hours and 74 hours under thermal cycling and thermal shock condition to obtain the same level corrosion of 100-hour equivalent time for isothermal sample. Meantime, the AISI 347 samples were expecting much less equivalent time for thermal cycling and thermal shock than AISI 321. The detailed normalisation process was shown in the supplementary files.

We concluded that AISI 321 depicts better corrosion resistance to temperature fluctuation, i.e., thermal cycling / shock than AISI 347. The addition of titanium (AISI 321) and niobium (347) to steel composition is efficient to reduce the sensitization (IGC) and lead to different corrosion resistance by precipitating the (Ti, Nb)C (Morshed-Behbahani et al., 2018) rather than Chromium carbide. Titanium is a more efficient stabilizing agent than niobium for the conditions explored in this study (Liu et al., 2021a).

In addition, the mass loss increases linearly with square root of immersion time. This is presented in Figure 9-2. Parabolic terms; k_p and A_p were obtained by fitting of mass loss against square root of time according to Equation 50, listed in Table 9-1. The parabolic rate constants k_p of AISI 321 and 347 increase with change in temperature profile of the immersion tests this order; thermal cycling < isothermal< thermal shock. This observation correlates with the observation mass loss in Figure 9-2 and suggest the influence of the changing temperature profiles on the kinetic of corrosion of AISI 321 and 347 in molten nitrate salts. Also, the values of coefficient of determination (R^2) for the fitted curves are greater than 0.75, indicating the good degree of fitting.

Despite the increase of mass loss over time, the corrosion rate is observed in Figure 9-3 to decrease with time for AISI 321 and 347 under Isothermal and thermal cycling conditions. The corrosion rate of AISI 321 and 347 after 28-day or 28-cycle immersion test were 38.2 and 22.7 µm/yr or 18.5 and 15.9 µm/yr. Referring to the 20 µm/yr of corrosion rate to provide a 30-year lifetime service for CSP plants (Gomez-Vidal, 2017), AISI 321 and 347 can used under thermal cycling condition for 30 years or isothermally employed for 15 years. For thermal shock condition, the mass loss significantly increase between 7 and 14 days of

immersion test, and then decreases again after 28 days. The higher corrosion rate of AISI 347 than 321 shows the unique complexity introduced by the cycles of thermal shock.

As already established in a previous study (Liu et al., 2022b), the range of temperature used for the cooling phase (290°C) during thermal cycling, and the long residence time during this period is believed to help to slow down the kinetics of corrosion, oxide formation, and thereby supress material loss rate. This intermittent cooling effect could also have similar effect on the aggressiveness of the molten salt chemistry (Liu et al., 2022a). Spallation behaviours were more likely to occur on samples from isothermal tests than from thermal cycling. However, the effect of thermal shock is believed to rapidly undermine the integrity and adherence of the corrosion oxide layers to continuously leave the fresh metal exposed to molten salt, and thus leading to an increase of corrosion rate. The detailed evidence and analysis are discussed in the next section.

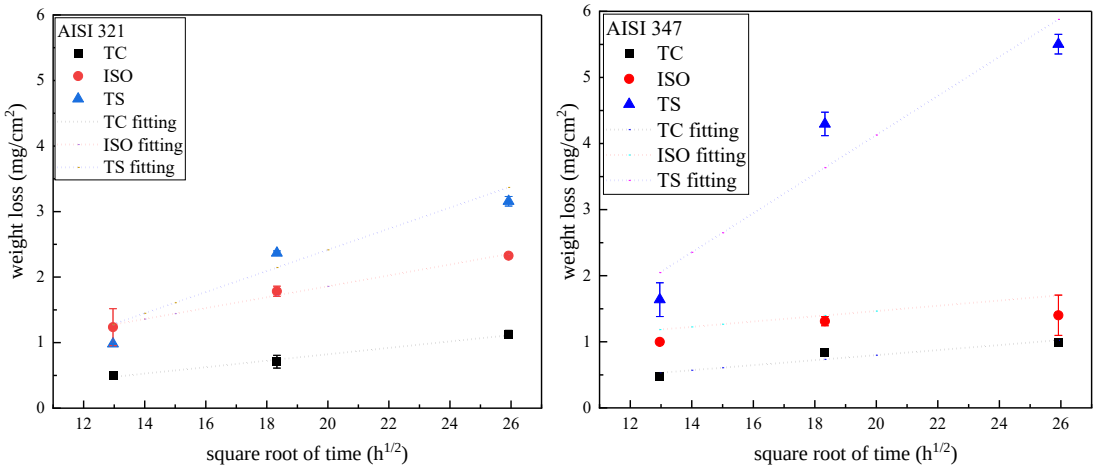

Figure 9-2. Mass loss of AISI 321 and 347 under different thermal conditions. Fitting curves are also presented with dot line in the figure**.**

Table 9-1. Results of linear fitting of weight loss**.**

Alloy	Condition	kp (mg/(cm^2·h$^{1/2}$))	Ap (mg/cm^2)	R^2
321	TC	0.0491	-0.16	0.993
	ISO	0.0833	0.1934	0.990
	TS	0.1612	-0.8082	0.847
347	TC	0.0381	0.0364	0.897
	ISO	0.0398	0.6692	0.843
	TS	0.2957	-1.7854	0.786

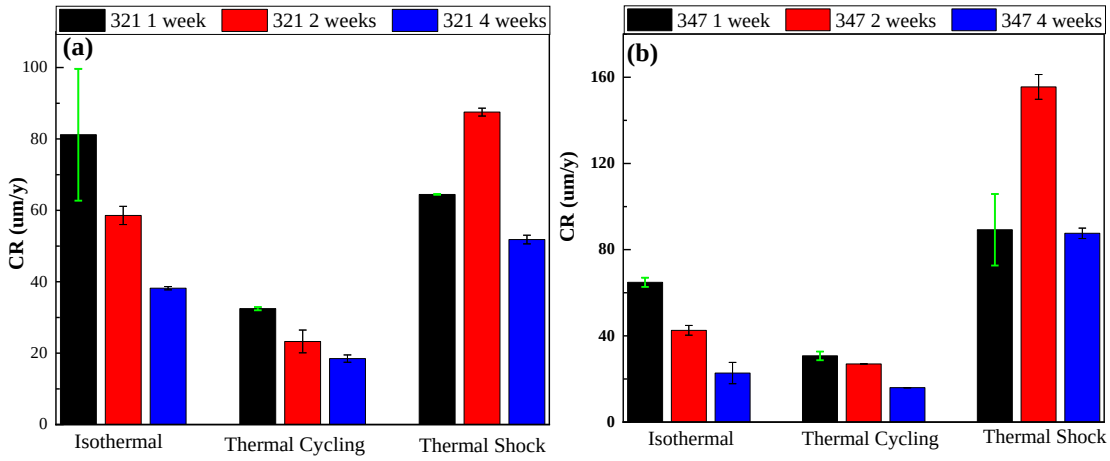

Figure 9-3. Corrosion rate of AISI 321 and 347 under different thermal conditions

9.3.2 XRD analysis

XRD measurements were performed on the corroded surface of samples to characterise the evolution of the chemical footprint of interfacial corrosion oxides at various immersion times for the three temperature profiles. As shown in Figure 9-4 (a, c and e), the main corrosion products formed on the AISI 321 are iron oxide (Fe_2O_3), iron chromium spinel ($FeCr_2O_4$), sodium ferrite ($NaFeO_2$) and chromium oxide (Cr_2O_3), regardless of the thermal profile. Similar corrosion products chemistries were observed on the surface of AISI 347 shown in Figure 9-4 (b, d and f). Cr_2O_3 and $FeCr_2O_4$ are known to be more dense and protective when formed as inner layers, and are capable of providing substantial corrosion barrier to molten salts (Fernández and Cabeza, 2019a). Porous and less protective oxide layers of $NaFeO_2$ and Fe_2O_3 were found as outer layer of the corrosion product. Data on the distribution and relative thickness of the interfacial corrosion oxides are presented and discussed in the next section of this paper.

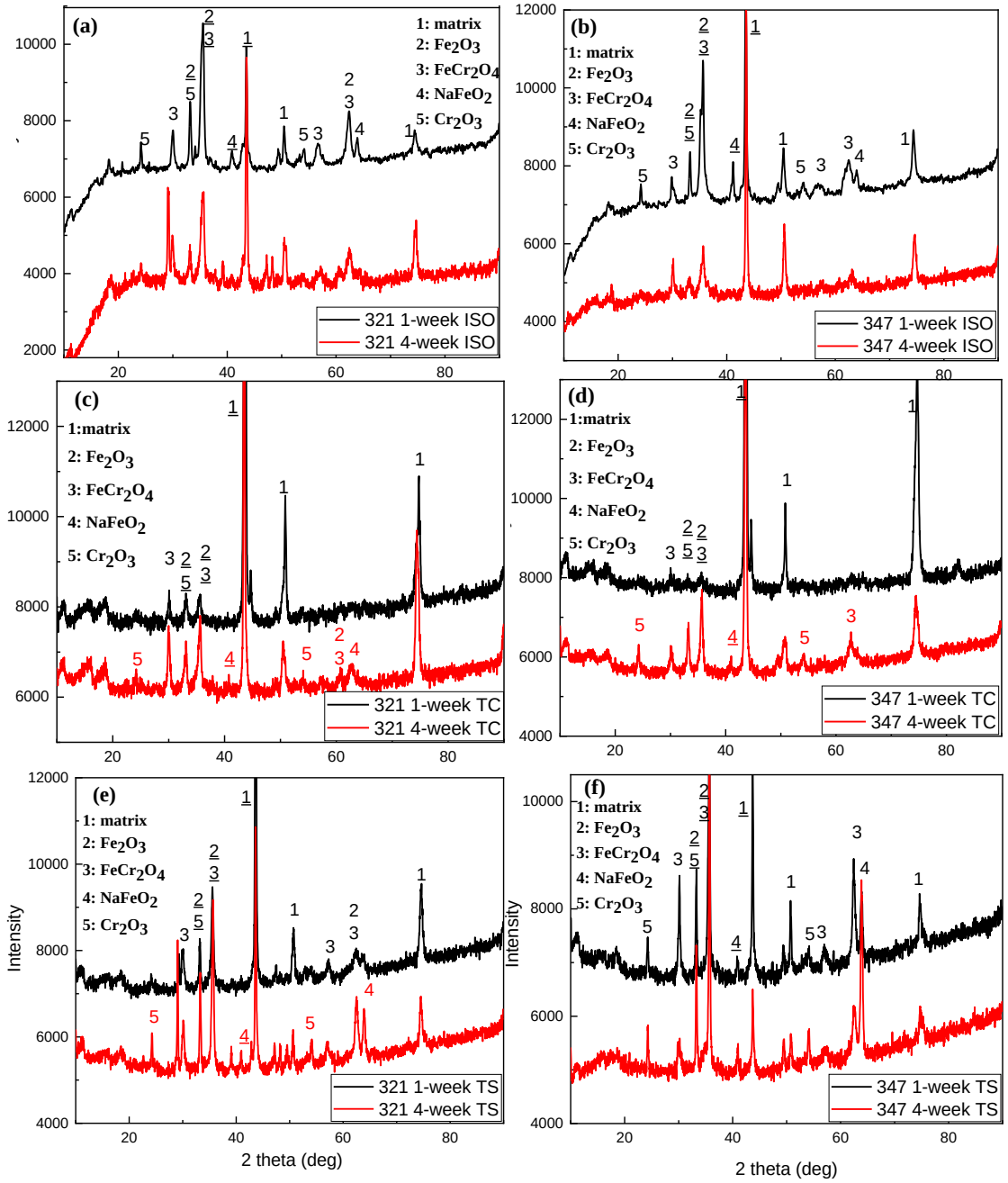

Figure 9-4. XRD patterns of AISI 321 and AISI 347 after 1-week and 4-week under thermal cycling, isothermal and thermal shock condition, respectively (the number with underline represents the 100% intensity of corresponding product).

9.3.3 Characterisation of corrosion oxide layer

After the immersion corrosion test in molten salt, different types of oxide layers were found and were believed to offer variable levels of protection to base metal against further infiltration of molten salt on the surface of samples. The formation process and distribution of corrosion products are important to improve on current understanding of the corrosion

mechanisms. The morphologies and complementary EDX results of AISI 321 and AISI 347 under different thermal conditions are shown in Figure 9-5 and Figure 9-6 respectively.

It is evident that the surfaces became more coarse and were covered by corrosion oxide layers with time for isothermal condition (see Figure 9-5 (a) and (b) for AISI 321, and Figure 9-6(a) and (b) for AISI 347 after 1- and 4-weeks exposure respectively). Iron oxide was the main corrosion products on the surface after the 1-week with 12 wt% Cr contents in Figure 9-5 (a). This indicates the existence of protective Cr_2O_3 and/or $FeCr_2O_4$ oxides with help from XRD result. After 4 weeks, the Fe and Na were found to be higher, while the Cr content reduced significantly in the outer oxide layers as identified from EDX analysis (P4 and P5) in Figure 9-5 (b). This indicates the increase in the formation of porous and non-protective Fe_2O_3 and $NaFeO_2$ outer oxide layers (See Figure 9-5 b). Inner oxides layer, with a higher Cr content, was exposed to molten salt after spallation of outer layer. Similar observation was recorded for AISI 347 in Figure 8 (a) and (b), and EDX analysis in Figure 9-6 (region P3 and P4).

Under thermal cycling conditions, the samples exhibited only a slight difference in terms of the overall surface features on the corroding interface after 1-week and 4-weeks. Referring to Figure 9-5 (c) and (d), and Figure 9-6 (c) and (d) for AISI 321 and AISI 347 respectively, it is evident that the corrosion oxide layers are more resilient and continuous across the entire surface. This is an indication of more stable oxide layers, with little or no spallation. From the result of EDX analysis in Figure 9-5 and Figure 9-6 (c) and (d) and XRD results in Figure 9-4 (c) and (d) , we can confirm that the main corrosion oxides formed on stainless steels under thermal cycling conditions samples are Fe_2O_3 and mixture oxides of Fe and Cr (Cr_2O_3 and $FeCr_2O_4$). The overall effect of lower material loss rate and surface features under thermal cycling conditions than isothermal is related to the effect of long residence time at lower temperature (290°C) in the heating cycle. The duration of the intermittent cooling process in the heating cycles has the direct effect of suppressing the kinetics of corrosion, oxide formation and rate of spallation. All of these three processes collectively influence the overall corrosion behaviour of materials under thermal cycling condition.

Figure 9-5 (e) and (f), and Figure 9-6 (e) and (f), presents the SEM and EDX results for test under thermal shock condition for AISI 321 and 347 sample. Although corrosion oxide layers are observed in localised regions on the surface, there is also evidence of substantial spallation after 1 week (Figure 9-5 (e) for AISI 321 and Figure 9-6 (e) for AISI 347) due to the thermal shock resulting from the temperature profile. The coverage area of corrosion oxide layer reduces after 4 weeks due to severe spallation by extending periods of thermal

shock (See Figure 9-5 (f) and Figure 9-6 (f). After 1-week thermal shock test for AISI 321, the inner surface (region P12 and 13) was observed with higher Cr and Ni content than the exfoliated of outer layer (region P14 and 15) in Figure 9-5 e. This observation is also the same for AISI 347 in Figure 8 (e) and (f). At other regions of the sample, there is evidence of dense, adherent and protective inner layer. This is likely to be a mixture of oxides of Fe and Cr, such as Fe_2O_3, Cr_2O_3 and $FeCr_2O_4$ (region P12 and 13 Figure 9-5 e). Referring to evidence shown in region P14 and 15 from EDX analysis, it is clear that there is an outer Fe and Na rich oxide layer. This is likely to be the porous and poorly adherent layers, identified as Fe_2O_3 and $NaFeO_2$ by XRD spectra in Figure 9-4 (e) and previous publications (Liu et al., 2022a, Liu et al., 2022b). This outer layer is prone to being spalled off; particularly as a result of the substantial thermal amplitude the samples are subjected to under thermal shock conditions. It is also evident from Figure 9-5 (e) and (f), that majority of this outer layer has been lost to the thermal shock effect. After 4-week immersion test under thermal shock condition, severe spallation of corrosion layers was observed. The extend test duration also provided opportunity for reformation of initially spalled off oxide layers. This is shown in Figure 9-5 (f) that pieces of outer layer of $NaFeO_2$ and Fe_2O_3 left after spallation are shown in region P19 for AISI 321. Evidence of Cr and Fe rich inner oxide layer after spallation is shown in region P18. Most of these outer oxide layers are shown in Figure 9-5 (f) to have spalled off due to thermal shock and inner Cr-enriched layer is prone to dissolve into molten salt. After spallation of initially formed layers, new oxide mixtures of Fe, Cr and Na are formed on the site of region P16 and P17 in Figure 9-5 (f). Similar observation to AISI 321 was also recoded for AISI 347 after 4-week test under thermal shock conditions. Evidence of scattered particles identified as $NaFeO_2$ formed on superficial oxide layers can be seen at region P15 and P16 in Figure 9-6 (f).

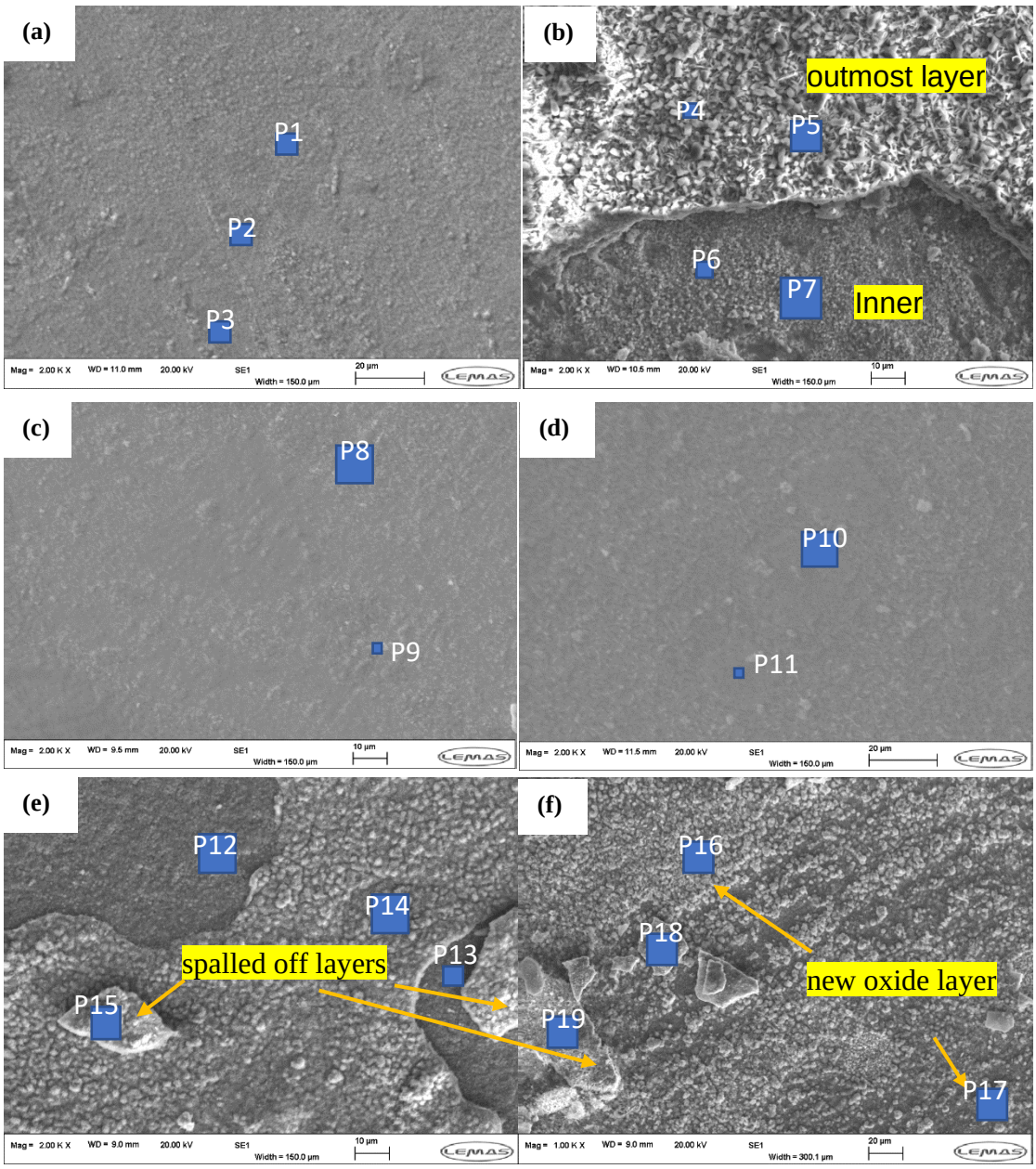

Element in wt %	Fe	O	Cr	Na	Ni
P1 P2 and P3	60.3 ± 0.2	18.3 ± 1.2	12. ± 0.9	0.1	-
P4 and P5	59.4 ± 1.2	30.0 ± 0.6	0.8 ± 0.3	9.4 ± 0.8	-
P6 and P7	68.0 ± 1.4	25.2 ± 0.4	3.7 ± 1.4	0.1	-
P8 and P9	63.3 ± 1.0	16 ± 1.5	10.7 ± 0.2	-	8.7 ± 0.3
P10 and 11	64.2 ± 3.0	24.7 ± 1.3	7.4 ± 0.6	-	2.5 ± 0.2
P12 and 13	65.3 ± 2.5	23.4 ± 2.1	6.5 ± 1.0		2.0
P14 and 15	66.2 ± 4.5	20.3 ± 3.1	1.6 ± 0.2	2.1± 0.2	
P16 and 17	62.1 ± 1.0	23.6± 0.4	2.2 ± 0.5	7.2± 1.2	-
P18 and 19	55.7± 0.2	23.5 ± 3.2	1.1 ± 0.6	5.3 ±1.2	-

Figure 9-5. SEM surface observation of the oxide scales formed on AISI 321 after (a) 1-week Isothermal; (b) 4-week Isothermal; (c) 1-week Thermal cycling; (d) 4-week Thermal cycling; (e) 1-week Thermal shock; (f) 4-week Thermal shock immersion test in molten nitrate salt. Table below shows the EDX data for regions.

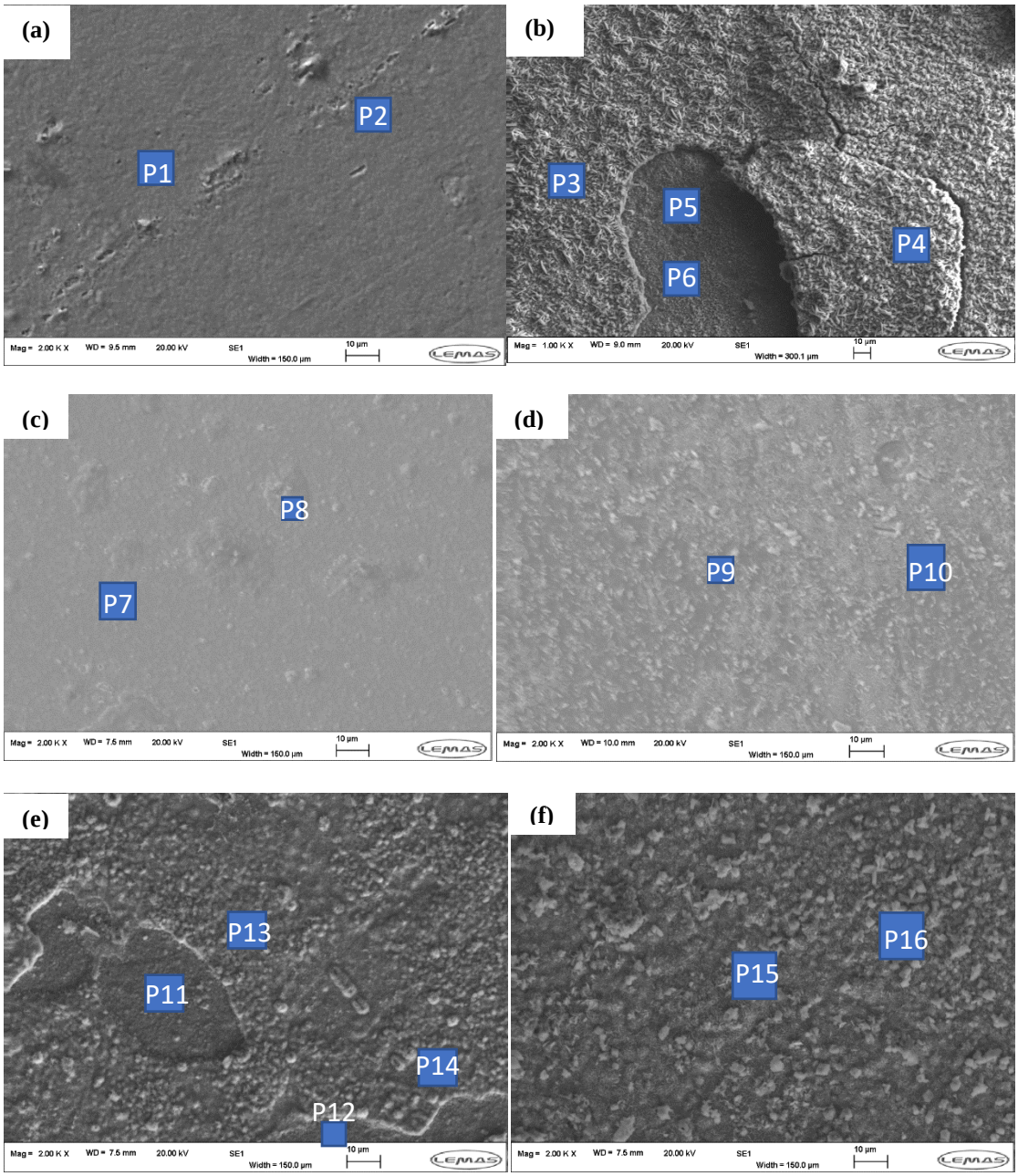

Element in wt %	Fe	O	Cr	Na	Ni
P1 and P2	66.2± 3.2	17.4 ± 0.5	12.6 ± 0.5	0.1	8.5± 0.5
P3 and P4	62.5 ± 0.7	25.7± 0.9	1.1± 0.1	10.8 ± 0.1	0.01
P5 and P6	70.8 ± 0.5	22.8 ± 0.3	3.8 ± 0.4	0.42	1.63
P7 and P8	68.5 ± 3.2	10.4 ± 3.5	8.1± 0.5	0.1	5.5± 0.5
P9 and P10	61.5± 1.7	24.9± 0.6	7.0± 0.6	3.5 ± 0.6	0.9± 0.2
P11 and P12	66.1 ± 1.4	20.6 ± 2	8.0± 0.2	1.35	0.1
P13 and P14	68.5± 2.1	23.7± 2.2	2.1± 0.1	2.7 ± 0.5	0.1
P15 and P16	65.5± 2.4	22.3± 0.9	1.7± 0.1	5.5 ± 1.6	0.1

Figure 9-6. SEM surface observation of the oxide scales formed on AISI 347 after (a) 1-week Isothermal; (b) 4-week Isothermal; (c) 1-week Thermal cycling; (d) 4-week Thermal cycling; (e) 1-week Thermal shock; (f) 4-week Thermal shock immersion test in molten nitrate salt. Table below shows the EDX data for regions.

Cross – Sectional Analysis

Cross-sectional analysis was conducted to examine the corrosion layer formed during the immersion test. As shown in Figure 9-7 for AISI 321, there are no indication of intergranular corrosion. From the SEM analysis above, it is evident that uniform corrosion driven by rate of spallation of interfacial oxide layers is the primary mode of corrosion attack for the conditions and duration explored in this study. Referring to Figure 9-7 and Figure 9-8 for AISI 321 and AISI 347 respectively, oxide layer with a mixture of oxides of Fe and Cr; likely Cr_2O_3 and Fe_2O_3 (confirmed by XRD in Figure 9-4) was found as an interfacial oxide layer under isothermal (after 1 week) and thermal cycling (after 1 and 4 weeks) condition (see Figure 9-5 (a), (c) and (d)). The thickness of the corroded layer are 2 and 4 µm after thermal cycling and 3.5 and 9.3 µm after isothermal test, as annotated in Figure 9-7. For AISI 347, the thickness of the oxide layer formed under isothermal condition was ~2.5 µm, which increases with exposure time; to around 12.5 µm after 4 weeks in a similar trend to AISI 321. A thin corrosion oxide layer formed after thermal cycling immersion test in Figure 9-8 (c) and (d). From the embedded line scan, Fe_2O_3 was the main oxide formed.

Double oxide layers was found on the 4-week isothermal samples in Figure 9-7 (b) for AISI 321. This double oxide layer with an outer $NaFeO_2$ layer was also observed after 4 weeks on AISI 347 (See line scan in Figure 9-8 (b)). This interface consisted of outer (Fe, Na)-rich oxides and inner (Cr, Ni)-rich oxides. This observation corroborates with the XRD pattern in Figure 9-4 and the SEM Images in Figure 9-5 and Figure 9-6.

Fe_2O_3 layer was found on AISI 321 after 1-week thermal shock with uniform thickness of 3 µm (See Figure 9-7 (e). Similar oxide layer with a uniform thickness of 4 µm was observed for AISI 347 as shown in Figure 9-8 (e). After 4 weeks test under thermal shock conditions, a large size detached oxide particle was observed above a continuous corrosion oxide layer. This correlates the spallation process believe to drive the oxide removal mechanism the surface observation in Figure 9-5 (f) and Figure 9-6 (f) for AISI 321 and 347 respectively. Underneath this detached oxide particle of $NaFeO_2$, consist of two thin layers of Fe_2O_3 (intermediate layer) with higher Fe content and inner mixture of oxides of Fe and Cr. The spallation of corrosion oxide layer was also observed on Figure 9-8 (e) for AISI 347 after 1-week thermal shock test. In this case, the detached layer was identified as Fe_2O_3 which has been proven to be protective by other researchers (Ahmed, 2013) under isothermal conditions. It is clear that the protective properties of the Fe_2O_3 has been undermined by the thermal shock heating cycles. Newly formed Fe_2O_3 layer was found beneath the spalled layer to protect the inner mixture oxide of Cr and Fe. After 4-week thermal shock test,

superficial oxide mixtures of Na and Fe; believed to be $NaFeO_2$ and Fe_2O_3 from results of XRD and SEM-EDS. This outer oxide layer is about 3 µm thick and has been shown to be porous and loose in previous study (Zhang et al., 2020, Ma et al., 2022). However inner mixture of $(Fe, Cr)_2O_3$ is 2 µm thick, and is likely to continue to grow due to unhindered molten salt induced corrosion activities at the metal – molten salt interface without the protection from the outer corrosion oxide layers. This is shown in Figure 9-8 (f).

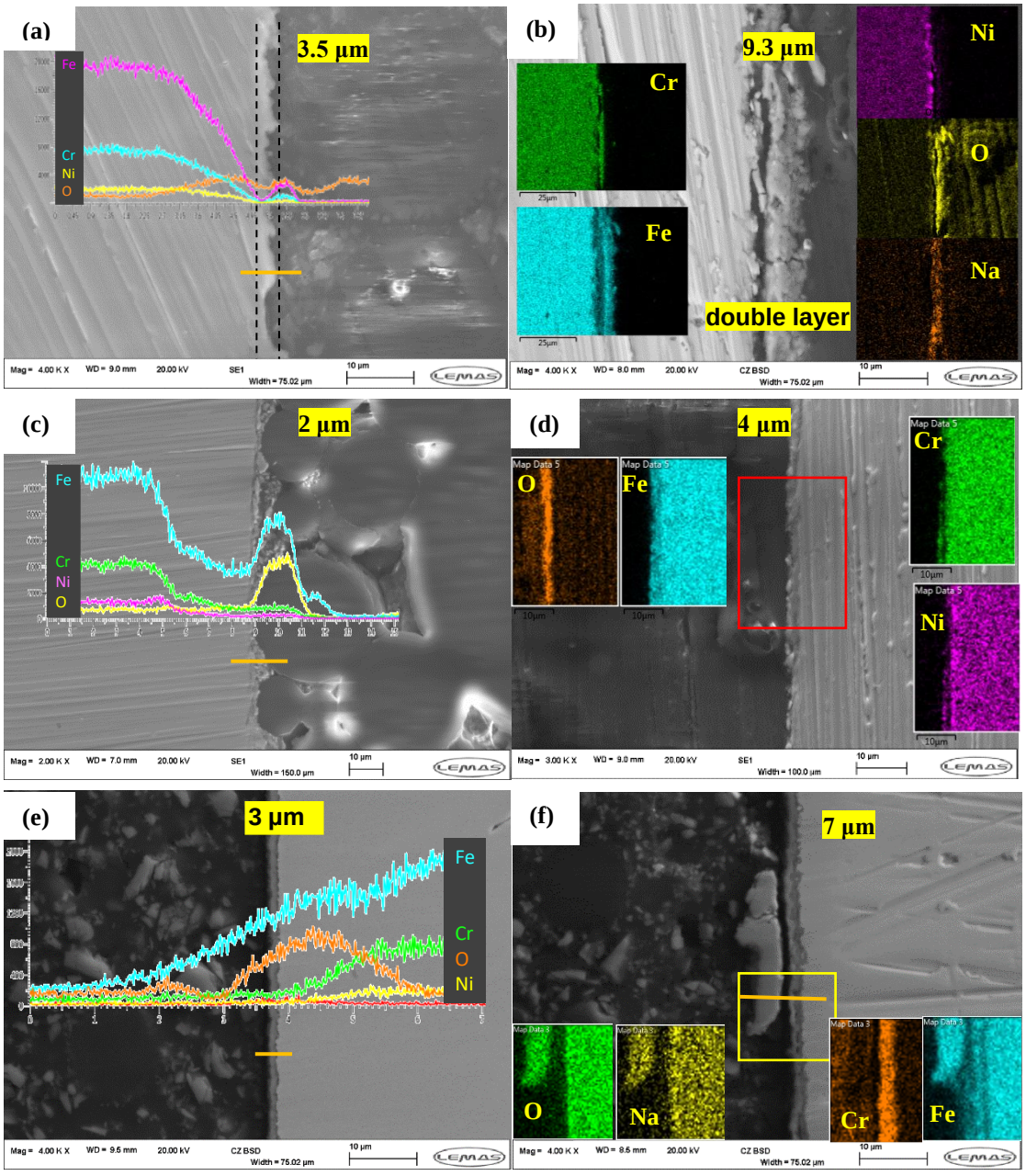

Figure 9-7. cross-sectional images of AISI 321 by SEM-EDX after (a) 1-week Isothermal; (b) 4-week Isothermal; (c) 1-week Thermal cycling; (d) 4-week Thermal cycling; (e) 1-week Thermal shock; (f) 4-week Thermal shock immersion test in molten nitrate salt.

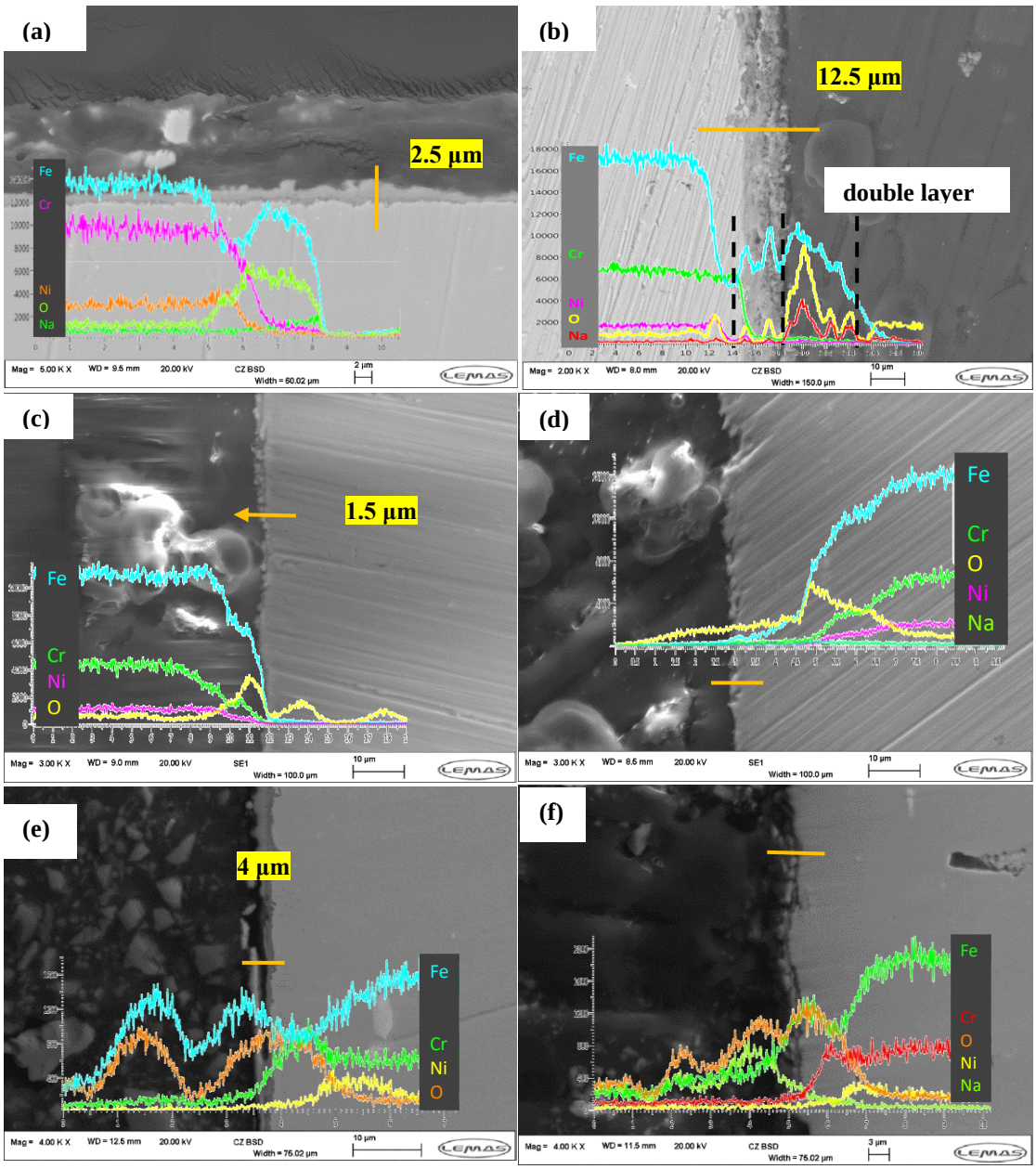

Figure 9-8. SEM-EDX profile of AISI 347 after (a) 1-week Isothermal; (b) 4-week Isothermal; (c) 1-week Thermal cycling; (d) 4-week Thermal cycling; (e) 1-week Thermal shock; (f) 4-week Thermal shock immersion test in molten nitrate salt.

9.3.4 Corrosion behaviour and the Evolution of Interfacial oxide Layers

In order to better understand the evolution and characteristics of the interfacial oxide layers on stainless steel in molten nitrate salt under different thermal conditions, a combination of FIB, SEM and TEM was used to characterise the interfacial oxide layers. This is shown for AISI 321 after 1 week in Figure 9-9 for isothermal, thermal cycling and thermal shock test conditions.

After 1-week test under all thermal conditions, relatively thin oxide layers (below 3 µm) were observed on the AISI 321 surface. Figure 9-9 (a) shows the cross-sectional image, corresponding EDS mapping images, an SEAD patterns for samples after of 1-week test under isothermal condition. A 1.37-µm outer layer was formed on the surface, which was identified as mixture of Fe_2O_3 and $NaFeO_2$ by patterns for annotated area a1 and EDS mapping in Figure 9-9 (a). An intermediate oxide layer of about 0.64 µm thick, was found as Cr-enriched layer in region (a2). The TEM pattern shows the intermediate layer was mainly Cr_2O_3 and $FeCr_2O_4$ spinel, which is known to be protective against further corrosion. A 0.2-µm (Cr, Ni) enriched layer was also found as an inner layer adjacent to the bulk material. This (Cr, Ni) rich inner oxide layer is believed to have been formed at an earlier early stage in the corrosion process.

For samples after thermal cycling tests, the thickness of the oxide layer was about 0.87 µm in Figure 9-9 (b), consisting of a 0.33-µm outer $NaFeO_2$ and Fe_2O_3 layer in region (b1), a 0.16-µm middle mixed (Cr, Fe) oxide layer at region (b2), and a porous mixture of Cr_2O_3, $FeCr_2O_3$ and Fe_2O_3 layer at inner layer in region (b3). The formation of the porous oxide layer is linked to the repressed kinetic of the corrosion reaction and oxide formation by intermittent cooling period at low temperature (290°C) and shorter residence time at peak temperature (565°C) during thermal cycling test when compared to isothermal test condition.

The corrosion layers formed on samples from thermal shock test exhibited multi-layer structure. A 0.38-µm needle like layer; identified as $NaFeO_2$ and Fe_2O_3 was observed as the outmost surface. The middle layer in region (c2) was identified as Fe_2O_3 and inner layer identified as a mixed oxide layer of (Cr, Fe) in form of Cr_2O_3 and $FeCr_2O_4$ spinel. It is worth noting that a 73 % reduction in thickness of outer layer from isothermal to thermal shock was observed, which correlates inversely with significantly higher weight loss results from thermal shock test than isothermal test (Refer to Figure 9-7 (a1) and (c1)). According to the result in SEM surface observation in Figure 9-5 (a) (c) and (e), this is related to the increase in the rate of spallation under thermal shock conditions than under isothermal condition. The thermal stress and the corresponding frequency under thermal shock will cause the interfacial oxide layers to spall off faster leading to higher mass loss and lower thickness of interfacial oxide layers. In general, the multi-layered corrosion products formed on the surface of stainless steels always exhibited an inner Cr-enriched protective layer (Cr_2O_3), which was considered as initially formed layer once the test is exposed to molten salt. Dense inner layer of Cr_2O_3 and $FeCr_2O_4$ as observed in this study are capable of being adherent to substrate, and provide good protection for material against the penetration of molten salt

(Liu et al., 2022a). The dissolution of Cr_2O_3 into solar salt results in Fe_2O_3 were found to be the primary corrosion oxides, and the existence of inner soluble Cr-enriched layers indicates the outer Fe_2O_3 layers are being effective in preventing solar salt penetration (Ahmed, 2013). Fe_2O_3 forms as an outer layer which potentially transforms into $NaFeO_2$ and is spalled off from the surface depending general thermal operating cycles.

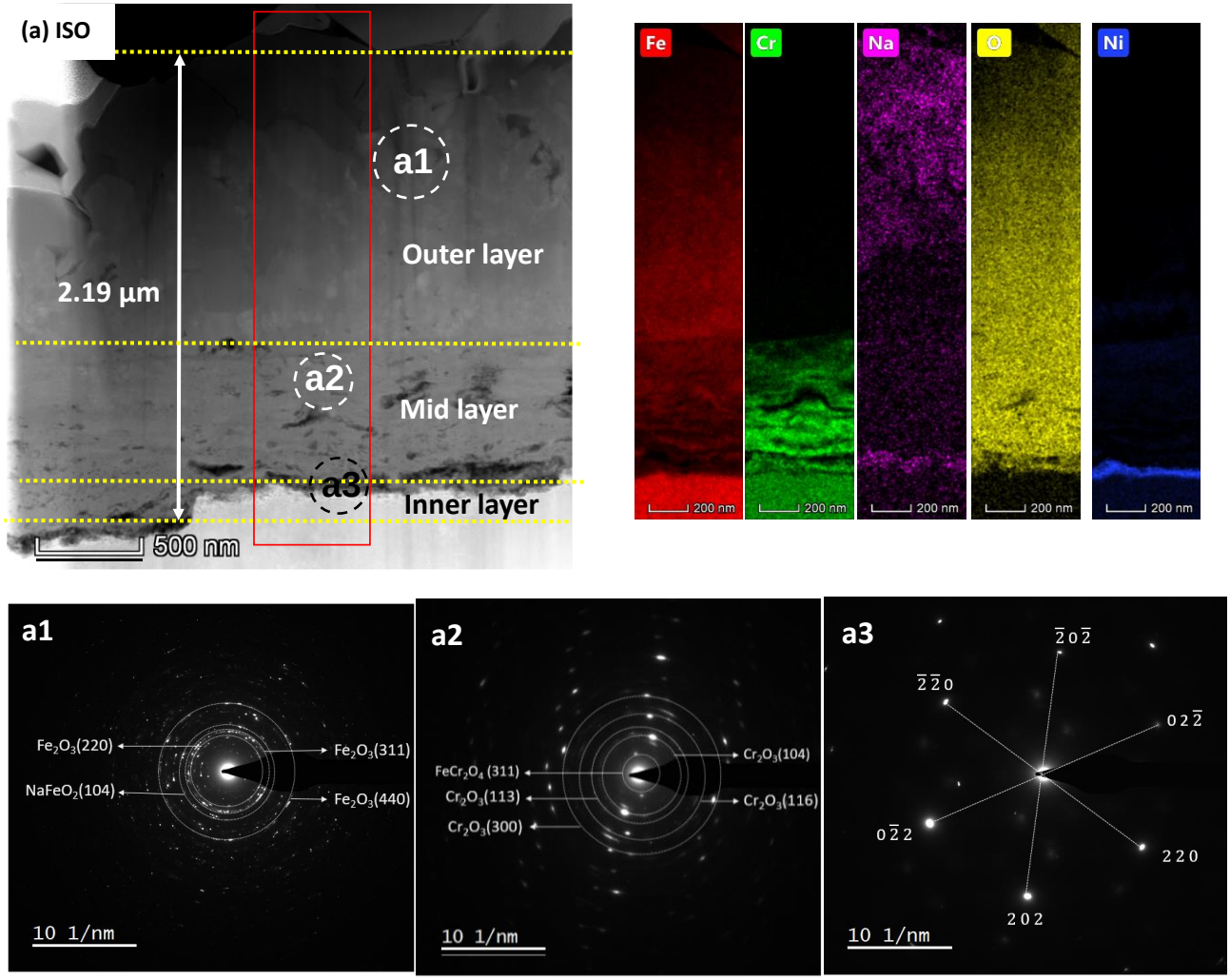

(Figure 9-9 to be continued)

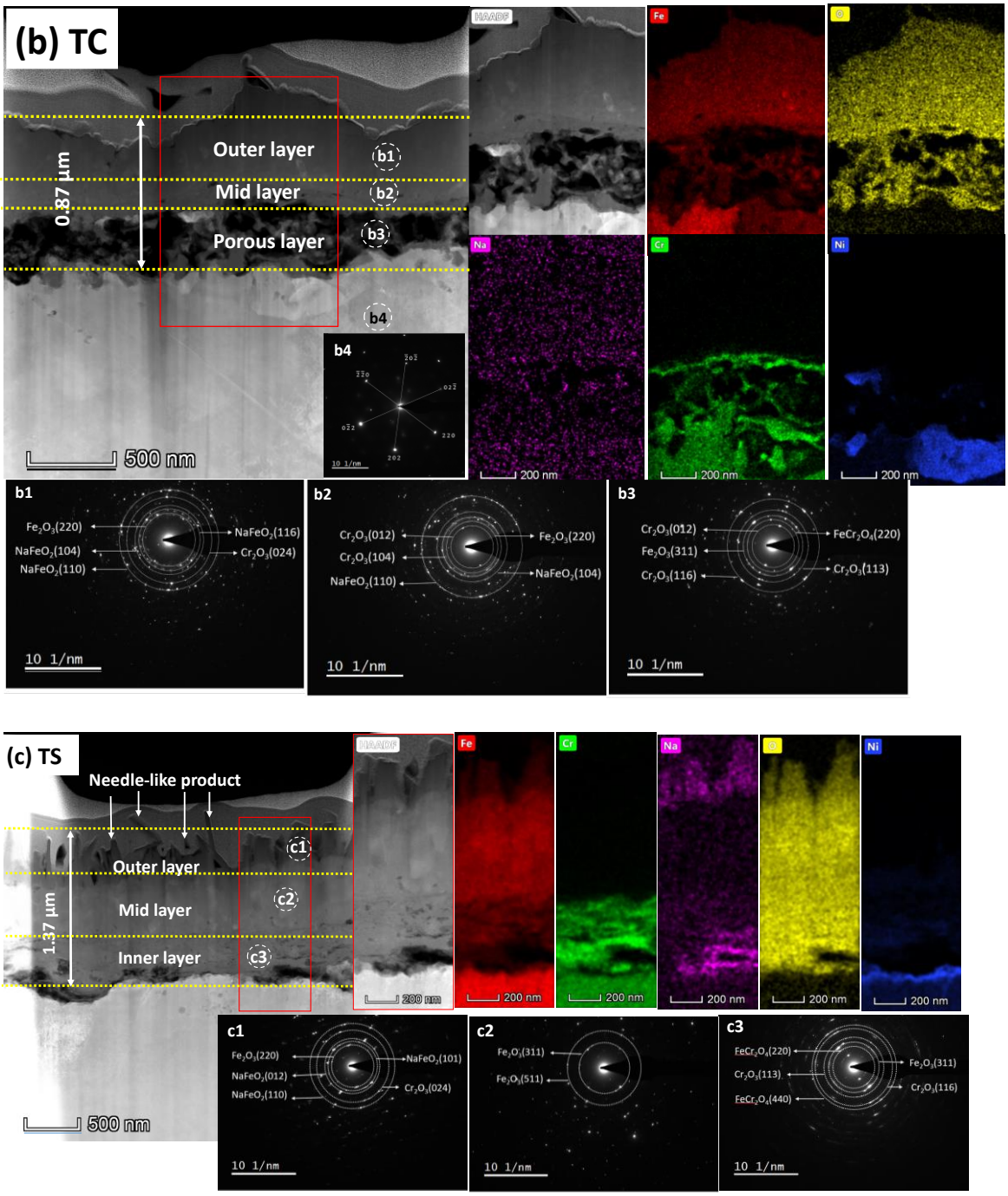

Figure 9-9. HRTEM images of samples after (a) 321 1-week isothermal (b) thermal cycling and (c) thermal shock and its corresponding EDS mapping and SAED patterns

9.3.5 Interfacial Oxide Formation Mechanism, Evolution and Stability in Relation to Oxide spallation and Overall material loss.

While results (Ma et al., 2022, Fernández and Cabeza, 2019b) published recently and from this study have shown a measured rate of material degradation for AISI 321 and 347 in molten nitrate salt, the occurrence of spallation of outer oxide layer due to the thermal stress under thermal shock condition further accelerates corrosion kinetics and increases the rate

of material loss. Therefore, an understanding of the mechanism of formation, evolution and behaviours of interfacial corrosion oxides is critical to better understand the corrosion mechanism of AISI 321 and 347 in molten nitrate salt under different thermal conditions as observed in this study.

Firstly, the passivation and corrosion resistance of stainless steels rely on the formation of thin and dense Cr_2O_3 and $FeCr_2O_4$ directly at the steel surface, protective properties of which can be further improved by alloying with Ni and Mo (Walczak et al., 2018). The formation reactions of Cr_2O_3, Fe_2O_3 and $FeCr_2O_4$ are shown in Equation 51 - Equation 53. However the Cr_2O_3 and Fe_2O_3 have a complete range of solubility across all composition range (Besmann et al., 2012). With the known solubility of Cr compounds in molten nitrate salt, Cr_2O_3 and $FeCr_2O_4$ could be found at the inner region of corrosion layers, identified by XRD spectra in Figure 9-4.

$$2Cr + \frac{3}{2}O_2 \rightarrow Cr_2O_3 \qquad \text{Equation 51}$$

$$FeO + Cr_2O_3 \rightarrow FeCr_2O_4 \qquad \text{Equation 52}$$

$$2\mathrm{Fe} + \frac{3}{2}O_2 \leftrightarrow Fe_2O_3 \qquad \text{Equation 53}$$

The formation of Fe_2O_3 identified in this work occurred due to the oxidizing nature of nitrate salt with oxidizing species like NO_2^- and O_2 from air. Other research (Ahmed, 2013) also found that hematite occupied the middle region of corrosion scales in AISI 304 stainless steel, maintaining its inner protective chromium oxide and limiting chromium depletion from metals (Goods et al., 1994a, Bradshaw and Goods, 2001a).

With increase of immersion time or temperature, the decomposition of nitrate to nitrate becomes more favourable (Bell et al., 2019, Liu et al., 2022a). The relatively more protective Fe_2O_3 outer layer is converted to non-protective $NaFeO_2$ and accelerate the corrosion process. Ahmed (Ahmed, 2013) also found $NaFeO_2$ on stainless steel after exposure to KNO_3 –$NaNO_3$ eutectic and offered the following formation mechanism. Consequently, $NaFeO_2$ formed on the top surface of the corrosion layers.

$$2NaNO_2 \leftrightarrow Na_2O + NO + NO_2 \qquad \text{Equation 54}$$

$$\frac{1}{2}\mathrm{Fe_2}O_3 + \frac{1}{2}Na_2\mathrm{O} \leftrightarrow \mathrm{NaFe}O_2 \qquad \text{Equation 55}$$

Corrosion of AISI 321 and 347 alloy is known to follow a parabolic law at 565˚C in molten salt, indicating the oxidation process was controlled by ion diffusion through the oxide scales

(Kai et al., 2016). Therefore, thermodynamic and kinetic analysis on interfacial oxide scales; typically composed of Fe_2O_3, Cr_2O_3 and/or $FeCr_2O_4$ can help to better understand oxide stability and evolution (Liu et al., 2022b).

The potential oxide forming corrosion reactions and the corresponding Gibbs free energy of formation of oxides on the surface of stainless steels during oxidation process are listed in Table 7-2.

9.4 Summary

In this chapter, the corrosion behaviours of the AISI 321 and 347 were experimentally investigated under isothermal (at 565˚C), thermal cycling (between 290 - 565˚C) and thermal shock (565˚C - 30˚C) at air atmosphere using a combination of gravimetric corrosion method and advanced surface and subsurface characterisation techniques. Here are the key conclusions from this study.

1. Thermal shock causes a higher rate of material loss than isothermal and thermal cycling heating profiles. This is linked to the effect of the synergy of substantial cyclic thermal stress and electrochemical activities on the resilience of the metal – molten salt interface.
2. The higher corrosion rate under thermal shock is also contributed to be the effect of the synergy of substantial cyclic thermal stress and electrochemical activities on the protective properties and/or rate of spallation interfacial oxide layers. The damage and spallation behaviours of the protective oxides layer were attributed to the stresses mismatch between the bulk material and oxide layers due to difference in the thermal expansion coefficient and elastic modulus of it, which needs further consideration by calculating the thermal stresses.
3. The corrosion of AISI 321 and 347 under different thermal cycles follows this order in decreasing corrosion rates; thermal shock > isothermal > thermal cycling. The corrosion rate decreases with increase of immersion time under isothermal and thermal cycling due to the resilience of the interfacial oxide layer relative to test under thermal shock condition.
4. Results from this study suggests that the “thermal cycling” are ideally protective, which has always been considered as a corrosion-accelerate factor. And stainless steel meets the down-selection requirement served as hot tank and pipes for solar thermal energy storage system under isothermal and thermal cycling conditions. And the receiver pipes

should consider using more corrosion-resistant Ni-based alloys, which are likely to suffer from the thermal shock.

5. The evolution in the chemistry of interfacial corrosion oxides was also affected by the different thermal cycles investigated. This is related to the effect of thermal cycles on the diffusion of species across the corrosion interface, kinetics of corrosion and oxide formation.

Chapter 10. Overall Discussions based on the results obtained from the Charter 5 to Chapter 9.

10.1 Introduction

In the chapter 5, 6, 7, 8 and 9, the finding from the experimental study of the material degradation and corrosion behaviours of corrosion resistance alloy (stainless steels and Ni-based alloys) in molten nitrate salt under different thermal irradiation cycles in air and argon have been presented. The emphasis of discussion in this chapter is to highlight the contribution of the thesis has made to the research gap in the literature.

10.2 Material sensitisation in molten salt

In order to quickly characterise and understand the synergic impact of molten salt chemistries and conditions encountered in CSP systems, the occurrence of sensitisations and the propensity for intergranular corrosion of material in molten salt was investigated using the Double loop electrochemical potentiokinetic reactivation (DL-EPR) technique. DL-EPR was combined with electrochemical etching method to quantitatively measure the degree of sensitisation (DOS) in selected alloys by aging in air with and without Solar Salts (60 wt% $NaNO_3$ and 40 wt% KNO_3) at 550–750˚C for 2 h. An important finding from this work relates to how the temperature and molten salt synergistically increase the DOS (degree of sensitisation) of stainless steels and Ni-based alloys, and how the most dominant mechanisms can be determined for each alloy.

10.2.1 The Synergy of high temperature sensitisation and Molten salt induced corrosion

From the results of this study presented and described in Chapter 5, it has been established that the sensitisation behaviour is often due to the depletion of chromium in the form of chromium carbides at grain boundaries /near GBs. In these zones, the minimum chromium content required to provide the passive film is unavailable. The results of studied alloys are shown in Figure 5-5 and Figure 5-6 as function of temperature and the effect of molten salt on the DOS.

In this study, the width of Cr-depleted area was not investigated, however, the results from post experiment analysis shows evidence of the tendency for IGC to occur along the grain boundaries. This has been observed in this study to increase with increasing of temperature and in synergy with molten salt for AISI 321. The effect of temperature on sensitisation

behaviour for stainless steels is linked to the degree of carbide precipitation ($Cr_{23}C_6$, TiC or NbC) at critical temperature. The higher degree of sensitisation in molten salt was due to the corrosion and chemical reaction kinetics that consumes Cr content. Solar salt is known to remain stable at temperatures ≤ 565°C and decomposes at higher temperatures into nitrite and oxygen ions (Bell et al., 2019), which enhanced the corrosivity of salt. This process, in synergy with the high temperatures triggers aggressive reaction with bulk material to form corrosion products, such as mixed oxides of (Cr, Fe and Ni) (Soleimani Dorcheh et al., 2016). Chromium rich corrosion products could result in Cr-depleted zones, where passive film breakdown occurs and are likely to corrode actively. For Ni-based alloys, the reason why molten salt causes the increased degree of sensitisation is similar with that of stainless steels.

The sensitisation mechanism is presented as a schematic illustration in Figure 10-1 to summarise the mechanism of sensitisation behaviour and synergy of temperature and molten salt to influence the tendency for IGC to occur. When “sensitised” samples precipitate Cr-carbide along GBs, inner chromium is hindered more significantly in its ability to diffuse outwards than carbon, thus leading to a Cr-depleted area. More Cr carbides aggregate at the grain boundaries due to the higher diffusion coefficient of Cr with the increase of temperature, thus increasing the width of Cr-depleted area and the tendency for IGC to occur. While in molten salt, according to literature (Sarvghad et al., 2017a, Bell et al., 2019, Walczak et al., 2018), oxidation was the primary attack to the alloys and the formation of Cr and Fe oxides may protect the bulk material against the corrosion. However, the subsequent dissolution of the Cr oxides into molten salt (Bell et al., 2019, Ahmed, 2013) causes the breakdown of this protective film and facilitates the interaction between molten salt and bare metal/alloy to accelerate the consumption of Cr emanating from bulk material as temperature increase. This corrosion/oxidation and dissolution process will remove chromium from the GBs first. Then, due to faster diffusion through GBs at temperatures below about 800°C, it will lead to higher sensitisation near the exposed surface. Therefore, in the presence of molten salt, more chromium is consumed, and Cr-oxides dissolved from the inner grain and along GBs, increasing the width of Cr-depleted area and the tendency for IGC to occur. The dissolution of Cr-oxide into molten salt resulted in higher DOS in molten salt than that in air by consuming chromium adjacent to GBs.

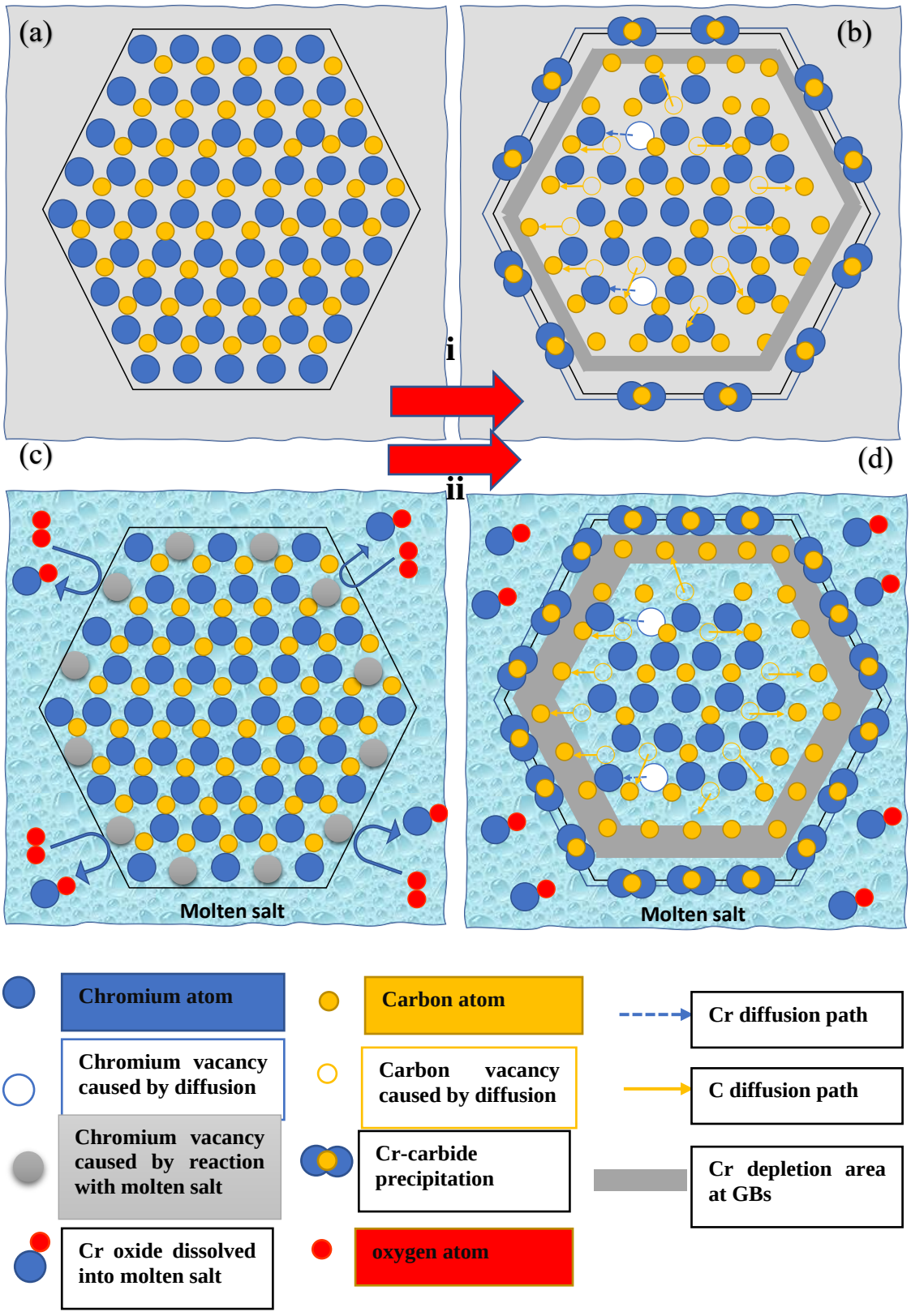

Figure 10-1. Schematic of sensitisation mechanism on the surface of stainless steels/Ni-based alloys (a) and (b) in air, (c) and (d) in molten salts

It is worth mentioning that the anodic and reactivation current of Ni-based alloy is almost four orders of magnitude lower than that of stainless steels, indicating that the passive film

is more stable than that on stainless steels. We can conclude that the passive film on the surface of Ni-based alloys contains mixture of oxides of chromium and nickel due to its higher nickel content, which exhibited a more stable oxide layer at higher temperature; particularly for IN 625, than the chromium oxide film on the surface of stainless steels. Further long-term immersion tests in molten salt are needed to investigate the IGC behaviour to confirm this conclusion.

The results and the findings based on Chapter 5 could provide the guidance for the following 28-day immersion corrosion test in molten salt.

10.3 The evolution of the interfacial corrosion oxides at molten salt – alloy interface

This session discusses the formation and evolution of the corrosion oxides formed on the surface of stainless steels and Ni-based alloys up to 28-day immersion in molten nitrate salt at 565°C (salt stable temperature, for most CSP plant). The results on the corrosion products formation and evolution presented and described in chapter 6 are discussed here.

Iron oxide (Fe_2O_3), chromia (Cr_2O_3) and iron – chromium spinel ($FeCr_2O_4$) were the primary oxide layer on the surface of stainless steels with the capacity to protect against further Cr depletion and increase in corrosion rate. Both NiO and Cr_2O_3 were observed on the surface of Ni-based alloys.

The degree of corrosion/oxidation at 565°C depends on the oxide ions produced from the decomposition of nitrate ions. Solar salt is known to remain stable at temperatures up to 565˚C, and will decompose into nitrite salt and oxide ions at higher temperature (Walczak et al., 2018), thus increasing the corrosivity of the salt and the corrosion rate. There are approximately 0.02 mol% oxide ions at 565 ˚C and 0.07 mol% at 600˚C in open solar salt systems (Bonk et al., 2020). In this study, the corrosion reaction is not expected to be as severe as that at 600˚C, as the corrosion rate and the corrosion depths are lower. It is known from classical oxidation theory that the oxidation resistance of these steels depends on the formation of a protective oxide layer, which acts as a diffusion barrier preventing interactions between oxidative or corrosive environments with the underlying metallic substrate (Ramos et al., 2021). A thin Fe_2O_3 layer was found on the surface of stainless steels to protect inner Cr depletion and alloy elements diffusion. The schematic corrosion mechanism in molten nitrate salt was shown in Figure 10-2.

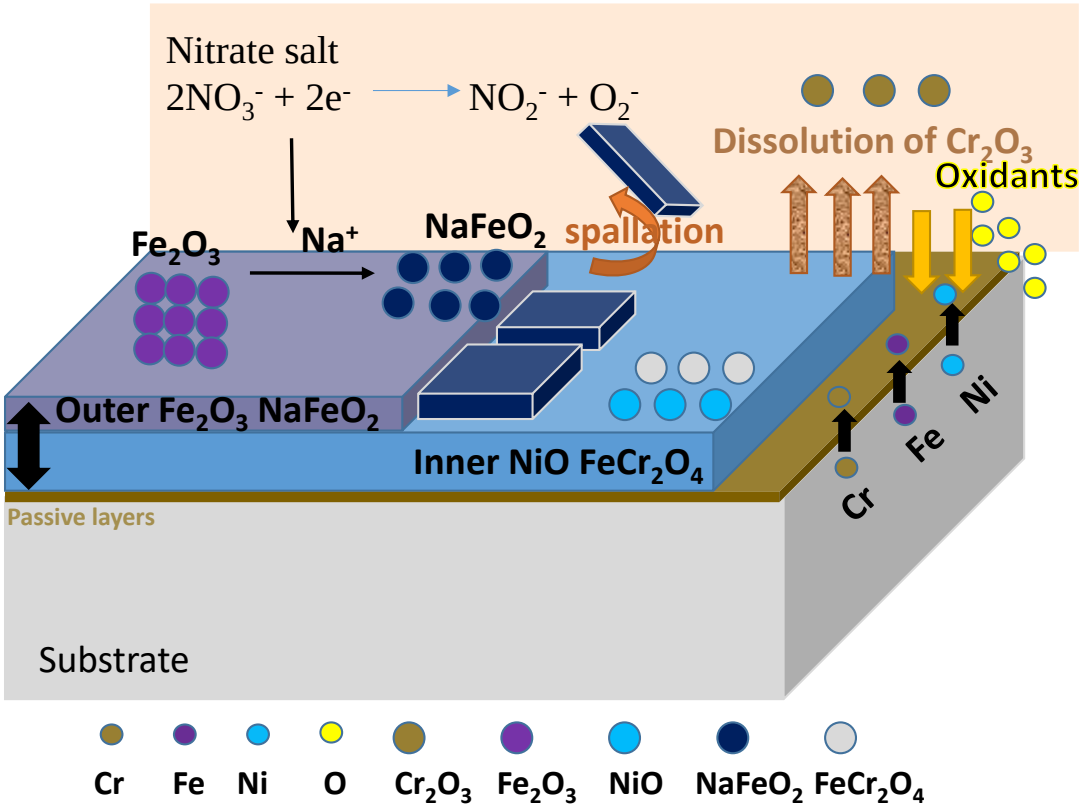

Figure 10-2. Corrosion evolution of the surface oxides exposed to molten nitrate salt.

For nickel-based alloys, they exhibited better corrosion resistance than stainless steels in this study as shown by the result from mass loss measurements and SEM observation. Several researchers have reported that Ni-based alloys corrosion is insignificant at temperatures below 550°C (Kruizenga et al., 2013) with evidence of difficulty in obtaining any corrosion information through typical SEM/XRD methods (Walczak et al., 2018) at 500°C. According to the results above, Ni oxide and iron chromium oxide are the main corrosion product formed on the surface of IN 825.

As the corrosion oxides are identified by many advanced techniques, like XRD, Raman spectroscopy and TEM, robust understanding of the mechanism and order of formation can also benefit from exploration of the underpinning theoretical thermodynamic calculations that supports these interfacial oxide layers. Aspects of the thermodynamic calculations are presented in parts in both in Chapter 7 and Chapter 9.

Corrosion of AISI 321 and 347 alloy is known to follow a parabolic law at 565˚C in molten salt, indicating the oxidation process was controlled by ion diffusion through the oxide scales (Kai et al., 2016). Therefore, thermodynamic and kinetic analysis on interfacial oxide scales; typically composed of Fe_2O_3, Cr_2O_3 and/or $FeCr_2O_4$ can help to better understand oxide stability and evolution (Liu et al., 2022b).

The potential oxide forming corrosion reactions and the corresponding Gibbs free energy of formation of oxides on the surface of stainless steels during oxidation process are listed in Table 7-2. The change of Gibbs free energy of formation of the oxides was obtained by following Equation 56 (Tan et al., 2017).

$$\boldsymbol{\Delta G = \Delta G^{\theta} + RT\ ln(\frac{(\alpha_O)}{(\alpha_M)(pO_2)^{1/2}})} \qquad \text{Equation 56}$$

ΔG^{θ}: standard Gibbs free energy of formation (25˚C, 1 atm); T: temperature in Kelvin; p_{O2}: partial pressure of oxygen in Pa, which was assumed to be 0.21 from other study (Yin et al., 2021); R: gas constant 8.3145 $J{\cdot}K^{-1}{\cdot}mol^{-1}$. α_O and α_M represent the activity of the oxide and the metal. α_O is 1; α_M can be approximately obtained by atomic concentrations.

Cr_2O_3 is believed to be preferentially formed due to the lowest ΔG value (~ -1018 kJ/mol) at 565˚C for stainless steels. Considering the solubility of chromium compounds in nitrate salt (Slusser et al., 1985), other oxides starts to formed once average Cr concentration was lower than a critical value (N_{Cr}*) (Wagner, 1952). Afterwards, the Fe-based oxides starts forming at this stage. FeO is known to form at temperature over 1000°C (Birks et al., 2006) and Fe_xO_y tend to form at temperatures below 570°C (Yin et al., 2021). According to ΔG values of Fe_xO_y in Table 7-2 and the diffusivity order of metallic ions in chromia ($D_{Fe} > D_{Ni} > D_{Cr}$) (Lobnig et al., 1992a), Fe_3O_4 and Fe_2O_3 starts to form to provide a level of protection against further Cr dissolution from the substrate. This oxidation process is controlled by ionic diffusion. The outward diffusion of Fe in the Cr_2O_3 and high affinity of Fe to oxygen resulted in formation of (Fe, Cr) oxides mixture (Liu et al., 2022b). As shown in this study, Fe_2O_3 preferentially forms as the most outer layer of the interfacial oxide layers shield inner Cr-oxide layer from aggressive molten salts. Meanwhile, it is worth noting that Fe_2O_3 tended to convert to $NaFeO_2$ with increase of exposure time and temperature, thus causing the corrosion interface to lose its outermost shielding layer increase overall material loss.

10.4 Effects of temperature and thermal irradiation cycles on the corrosion of stainless steels and Ni-based alloys in nitrate salts

In the real CSP plants, the operating conditions are more intricate and more complex due to the alternation of day/night and even unpredictable amid sharp weather changes within a short period of time. In this study, two new methodologies linked to two different temperature profiles encountered during CSP operations were introduced. These are ‘thermal cycling’ and ‘thermal shock’, which reflects the type of temperature changes that takes place during a typical CSP operation. Thermal cycling was developed to closely simulate real solar

irradiation and storage cycles from the industrial scale CSP plant. It accounts for temperature profile during 12-hour peak day-time heating and 12-hour night-time cooling within heat transfer pipes or heat storage tanks (Liu et al., 2022a).

It is well established that, the availability of consistent solar irradiation could significantly affect the electric energy generation capacity and efficiency of CSPs. According to CSP operations and maintenance experience, a sudden change of weather (appearance of clouds) and/or gust of cold wind can cut off the solar irradiation from mirrors (heliostats) or take away the heat on the surface of pipe panels. This can also affect the receiver panels. As a result, the temperature could suddenly drop by a few Kelvin per second. This scenario can be described as “thermal shock”. The threat posed by irregular thermal shocks on material integrity is significant and always contributes to severe deformation and/or expansion of the materials used as receiver pipes, causing material failure, and leading to the shutdown of the CSP system and causing significant economic loss. In Chapter 9, we systematically introduce and compare the effect of different thermal irradiation cycles on the corrosion behaviours of stainless steels.

The timescale of thermal cycling and thermal shock was normalized based on the weight loss results of isothermal samples, as shown in Figure 10-3. For all durations, the equivalent time of thermal cycling was also twice of the isothermal, indicating that the cooling effect during thermal cycling reduced the corrosion rate by suppressing the kinetic of the corrosion reactions.

After 1-week immersion test for both materials, the equivalent duration of thermal shock was relatively close to 168 hours, when the impurities in the salt play a more dominated role affecting the initial corrosion than thermal shock. With increasing of immersion time, the breakdown of protective layer on the samples due to the thermal shock results in a lower equivalent time for thermal shock than isothermal condition in Figure 10-3. Evidence from SEM and cross-sectional observation confirmed that the corrosion rate has been accelerated after spallation of the outer layer, especially for AISI 347 after 4-week test.

(a) (b)

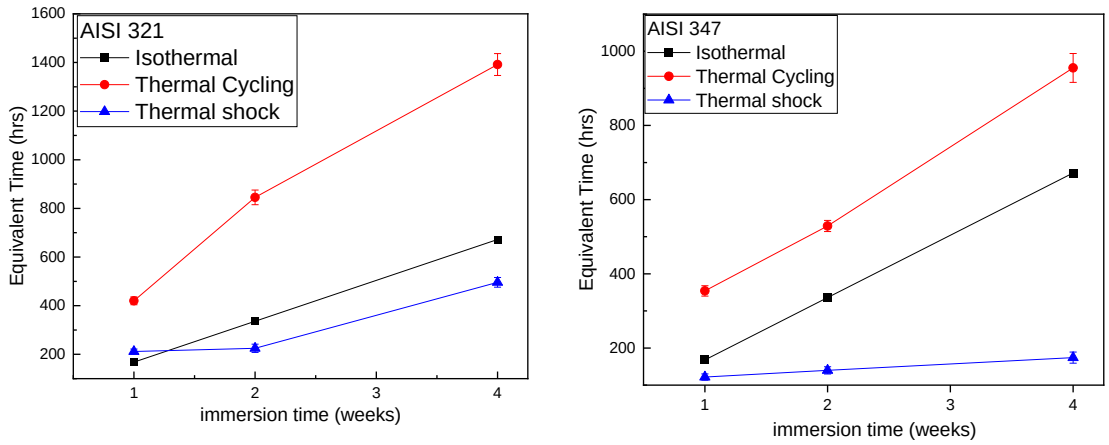

Figure 10-3. The equivalent time for the stainless steels under thermal cycling and thermal shock conditions normalised in reference to target weight loss measurement from test in molten salt under isothermal conditions over 4 weeks (a): AISI 321, (b) AISI347

After 1-week test under isothermal condition, relatively thin oxide layers (below 3 µm) were observed on the AISI 321 surface. Figure 9-9 (a) shows the cross-sectional image, corresponding EDS mapping images, and SEAD patterns for samples after of 1-week test under isothermal condition. A 1.37-µm outer layer was formed on the surface, which was identified as mixture of Fe_2O_3 and $NaFeO_2$ by patterns for annotated area a1 and EDS mapping in Figure 9-9 (a). An intermediate oxide layer of about 0.64 µm thick, was found as Cr-enriched layer in region (a2). The TEM pattern shows the intermediate layer was mainly Cr_2O_3 and $FeCr_2O_4$ spinel, which is known to be protective against further corrosion. A 0.2-µm (Cr, Ni) enriched layer was also found as an inner layer adjacent to the bulk material. This (Cr, Ni) rich inner oxide layer is believed to have been formed at an earlier early stage in the corrosion process.

For samples after thermal cycling tests, the thickness of the oxide layer was about 0.87 µm in Figure 9-9 (b), consisting of a 0.33-µm outer $NaFeO_2$ and Fe_2O_3 layer in region (b1), a 0.16-µm middle mixed (Cr, Fe) oxide layer at region (b2), and a porous mixture of Cr_2O_3, $FeCr_2O_3$ and Fe_2O_3 layer at inner layer in region (b3). The formation of the porous oxide layer is linked to the repressed kinetic of the corrosion reaction and oxide formation by intermittent cooling period at low temperature (290°C) and shorter residence time at peak temperature (565°C) during thermal cycling test when compared to isothermal test condition.

The corrosion layers formed on samples from thermal shock test exhibited multi-layer structure. A 0.38-µm needle like layer; identified as $NaFeO_2$ and Fe_2O_3 was observed as the outmost surface. The middle layer in region (c2) was identified as Fe_2O_3 and inner layer

identified as a mixed oxide layer of (Cr, Fe) in form of Cr_2O_3 and $FeCr_2O_4$ spinel. It is worth noting that a 73% reduction in thickness of outer layer from isothermal to thermal shock was observed, which correlates inversely with significantly higher weight loss results from thermal shock test than isothermal test. According to the result in SEM surface observation, this is related to the increase in the rate of spallation under thermal shock conditions than under isothermal condition. The thermal stress and the corresponding frequency under thermal shock will cause the interfacial oxide layers to spall off faster leading to higher mass loss and lower thickness of interfacial oxide layers. In general, the multi-layered corrosion products formed on the surface of stainless steels always exhibited an inner Cr-enriched protective layer (Cr_2O_3), which was considered as initially formed layer once the test is exposed to molten salt. Dense inner layer of Cr_2O_3 and $FeCr_2O_4$ as observed in this study are capable of being adherent to substrate, and provide good protection for material against the penetration of molten salt (Liu et al., 2022a). Fe_2O_3 forms as an outer layer which potentially transforms into $NaFeO_2$ and is spalled off from the surface depending general thermal operating cycles.

10.5 Effect of cover gas on the degradation of corrosion resistance alloys in molten salt

In chapter 6 and chapter 7, we introduce argon as test atmosphere to investigate the effect of thermal cycling on the corrosion behaviour and compare the results with the test in air.

In chapter 6, we found that the CR from isothermal tests is 1.5-5 times higher than that under thermal cycling condition in argon. This is different from the conclusion reported in the literature (Bradshaw and Goods, 2001b) on thermal cycling. However, the thermal cycling experiment protocol published by Sandia Laboratory was based on a 7.5 h residence time at the maximum temperature of 565°C and 0.5 hours cooling in ambient air at 95°C for 500 cycles. They (Bradshaw and Goods, 2001b) reported that thermal cycling increased the corrosion rate of the three stainless steels moderately when compared to isothermal immersion corrosion tests. The difference in the results obtained and conclusions from this study is likely due the longer residence time for the cooling process; 12 hrs between peak and lowest temperatures per cycle, and corresponding effect of extended duration at lower temperatures in the cycle.

Due to the continuous immersion in molten salt at 600˚C during isothermal tests, the oxide layers formed have more potential to breakdown and spall off (Encinas-Sánchez et al., 2019). In comparison, the intermittent cooling process or period of immersion at lower

temperature during thermal cycling interrupts the continuous thermal effects on the formation and stability of oxide layers, thus reducing the potential for breakdown and spallation of the oxide layers. The spallation behaviour is linked to the instability of oxide layers at high temperatures. The thermal expansion and contraction of corrosion layers is expected to occur during thermal cycling due to the regular change of temperature. Despite the difference in coefficients of thermal expansion and elastic modules of base metal between corrosion layers (Yin et al., 2021), the cooling effect during thermal cycling for 12 hours per 24 hour cycle, induces lower thermal stresses to help to improve the adherence of corrosion multi-layers than in cooling-free isothermal process (Bradshaw and Goods, 2001b). It's worth noting that any residual thermal stress (Yin et al., 2021) caused by cooling process during thermal cycling between multi-layers in this study is likely to be significantly lower than thermal stress levels expected from simulated thermal shock experiments (Bradshaw and Goods, 2001b). The evidence from this study clearly shows that thermal cycling relieves and delays the thermal effect on the multi-layers, and the tendency for spallation to occur. Solar salt is known to remain stable at temperatures up to 565 ˚C and will decompose into nitrite salt and oxide ions (Walczak et al., 2018) at higher temperature, thus increasing the corrosivity of the molten salt and the corrosion rate of exposed alloys (Bell et al., 2019). Longer residence at 600 ˚C for isothermal test means that more oxide ions are available within in a progressively increasing corrosive molten salt system than in thermal cycling test (Bonk et al., 2020). The effect of thermal cycling therefore reduces the corrosiveness of the system by slowing down the decomposition process.

Furthermore, a double oxide layer was observed at the corrosion interface. An Inner Cr-rich oxides film acts as protective layer against corrosion because of low diffusion rate of oxygen and metal ions through the film (Gui et al., 2017) and outer Fe-rich layer protect the dissolution of the inner Cr-rich oxide into salt. The diffusion order of metal ions in Cr-oxides is $D_{Fe}>D_{Ni}>D_{Cr}$ (Lobnig et al., 1992b). Atomic diffusion is enhanced by increasing temperature and duration of tests (Bataillou et al., 2018). Longer residence time of immersion at 600˚C for isothermal test is believed to promote the outward diffusion of Fe and Cr from the base material, resulting in forming thicker corrosion layers than in samples from thermal cycling tests.

The double corrosion layer was formed on the surface of stainless steel, and the main corrosion product is an outer sodium iron oxide/iron oxide and inner iron chromium oxide. The occurrence of non-uniformity in corrosion thickness for stainless steels is caused by the spallation of the poorly adhered corrosion layer, which often occurs in isothermal immersion

tests. The corrosion products formed on the stainless-steel surface have been previously reported and are also confirmed in this study to be Fe_2O_3 and Fe_3O_4 (Zhang et al., 2020). Sodium and potassium nitrate always exhibited weak basic melt below 570°C and iron forms a passive oxide layer to mitigate the diffusion of soluble chromium from the metal substrate (Bell et al., 2019). Above the temperature of 570°C and close to 600°C, the basicity increases significantly as the decomposition reaction from nitrate to nitrite becomes more favourable (Bradshaw and Goods, 2001a, Bell et al., 2019). Meanwhile, the iron outer layer is converted to sodium ferrite ($NaFeO_2$) which is non-protective and consequently results in the corrosion rate increasing (Bradshaw and Goods, 2001a). In this study, the $NaFeO_2$ was identified as the corrosion product on the surface of stainless steels samples from SEM–EDX analysis and XRD patterns. This is also observed in terms of the distribution of elements from cross-sectional analysis of the alloy–oxide layer interface. The Cr and Ni enriched region was observed in the inner oxide layer line scan due to the selective dissolution and diffusion disparity of alloy elements. Zhang et.al. (Zhang et al., 2020) reported that the corrosion products of $(Fe, Cr, Ni)_3O_4$ mixed oxide spinel are probably present in the inner oxide layer and widely proven to improve the stainless steel corrosion resistance (Soleimani Dorcheh and Galetz, 2016, Liu et al., 2017, Hua et al., 2019). In this study, $FeCr_2O_4$ is the main oxide spinel and well adhered to the bulk material.

From the results in chapter 7, the corrosion rate of isothermal immersed samples is higher than that under thermal cycling condition in air. This is similar to the conclusion reported in the literature (Liu, 2021) where thermal cycling decreased the corrosion rate of the three stainless steels moderately when compared to isothermal immersion corrosion tests in argon at higher temperature. Thermal cycling effects suppresses the corrosion process due to the slowing down the kinetics of corrosion and oxide formation, and the overall thermal effects during the cooling phase. The longer residence time of 12 hrs at maximum temperature promoted the dissolution of initially formed Cr_2O_3 in isothermal condition. Also thinner, dense and more compact corrosion layer was observed to form on TC samples. Iron oxide is able to provide some protection in molten nitrate salt but likely not comparable to the compact Cr_2O_3 layer formed under thermal cycling conditions in air (Goods et al., 1994a, Bradshaw and Goods, 2001a, Bell et al., 2019, Ahmed, 2013).

The corrosion rate, thickness of corrosion layers and/or corrosion attack depth imply that the corrosion rate is higher when the oven is sealed with argon than open air. The formation and spallation behaviour of $NaFeO_2$ is likely to contribute to an increase in corrosion rate under thermal cycling in argon. The other mechanism that contribute to higher rate loss is

the delay in preferential formation of passive Cr_2O_3 due to the availability of oxide ions decomposed from nitrate. The outward diffusion of Fe and Cr from bulk material to corrosion interface is driven by high temperature, resulting increased concentration of atoms at the corrosion interface. The absence of a prompt supply of oxygen to promote quick passivation of the interface will lead to the formation of thicker films of these oxide layers as soon as oxygen becomes available via decomposition of the nitrate into nitrite. While in air the passive Cr_2O_3 formed on the early stage and higher diffusion rate of Fe in Cr_2O_3 resulted in formation of Fe_2O_3 to protect the dissolution of Cr_2O_3 into molten salt (Ahmed, 2013). All of these mechanisms are believed to act in synergy to increase corrosion rate under thermal cycling conditions in argon than in air over 14 days.

As the results shown in this study, the certain combination of temperature and atmosphere could lead to different level of corrosion. And the inert atmospheres (Bell et al., 2021), which were considered to limit corrosion in other molten salt mixtures, can increase the corrosion rate of alloy. It is not recommended to purge the air with argon in the storage tanks or transfer pipes in the real application where it may cause higher corrosion damage. Also thermal cycling caused by alternation of day and night can mitigate the corrosion to a certain extent by reducing the kinetic of corrosion reaction during cooling period.

Above all, the spallation of the outer layer and the protectiveness of inner layer need more characterisation to justify the above statement. So the following test characterizing the thermal stress between multilayers were employed.

10.6 Evaluation of the relationship between the corrosion characteristics and thermal stress developed within interfacial oxides

As for the effect of temperature, the stainless steel and Ni-based alloys experienced mild corrosion when exposed molten nitrate salts at 565˚C in air. The corrosion was accelerated with increased temperature and was further increased when an inert argon environment was employed – resulting in up to 3 times higher corrosion rate of samples in 7-day immersion.

In chapter 8, the nano-mechanical properties of the corrosion layers are investigated via nano-indentation to explain the spallation due to the different thermal stress between the layers and bulk material. For Stainless steels, the hardness of base metal is higher than that of outer oxide layer and lower than that of inner oxide layer, which indicates that inner oxide layer is denser and more protective whilst outer oxide layer is porous. From the EDX line and mapping results, the inner oxide layer as a Cr-rich layer and the porous outer

$Fe_2O_3/NaFeO_2$ layer was attributed to the high-density of defects (e.g. pores and micro-cracks). The high hardness and stiffness associated with the continuous and compact inner oxide layer formed on the Stainless Steels samples (under argon atmosphere at 600°C) indicates that the inner oxide layer is capable of providing an effective barrier to isolate the base metal from the oxidizing molten salt. The high strength inner oxide layer also implies a higher resistance cracking and/or breakdown. For Ni-based alloys, the hardness difference between inner/outer oxide layers with base metal is not as much as that of Stainless Steels. The hardness of base metal is almost same with that of outer oxide layer and slightly lower than that of inner oxide layer. Referring to the cross-sectional images, Cr-rich inner oxide layer was observed on the surfaces of Ni-based alloys, while outer Fe-rich oxide layer was also observed to have more pores and micro-cracks. In comparison with the outer oxide layers formed on all the studied alloys, the hardness of outer oxide layer on Ni-based alloys are almost 2 times higher than that on the stainless-steel samples, indicating the outer oxide layer is more stable on Ni-based alloys.

As earlier discussed, the oxide growth related stress on oxides formed on Stainless steels and Ni-based alloys are protective under compressive stress. Referring to the thermal stress, the negative sign of thermal stress between inner oxide layer and base metal also shows the compressive stress for all the alloys; with values ranging from 1.045 – 2.31 GPa for samples tested in air at 600˚C, and 0.118 - 0.348 GPa for samples test in air at 565˚C. This shows great agreement with the observed higher strength of compact inner oxide layer and its protectiveness. The tensile stress is found between inner oxide layer and outer oxide layer; with values ranging from 0.013 – 0.491 GPa for samples tested under argon atmosphere, and 0.087 - 0.169 GPa for stainless steels samples tested in air at 600˚C. The tensile stress between inner and outer oxide layers discussed above were calculated for corrosion interface with double oxide layers; This was not applicable for the samples in air at 565˚C or the Ni-based alloys samples at 600˚C in air.

This is evident that the compressive stress (negative sign) could help keep the inner oxide layer adhered to base metal and tensile stress (positive sign) could lead to spallation of outer oxide layer. The reasons responsible for the results above are probably attributed to the structure of corrosion oxide layers, where initially formed inner oxide layer was the primary corrosion oxides with higher hardness and strength, and better adherence to the base material. For stainless steel, the outer oxide layer (identified as $NaFeO_2$ by SEM) shows lower hardness than inner oxide layer, and the stress calculation confirmed its poor adherence to inner layer, and thus a recipe potential spallation to occur. The tensile stress

or the thermal stress obtained between inner oxide layer and outer oxide layer could be attributed to the thermal expansion coefficient of inner Cr-based oxide layer and outer Fe-based oxide layer, as well as the thickness ratio of the double oxide layer. So the dense protective inner oxide layer is difficult to spall off by thermo-mechanical stress effects. However, this does not completely prevent the electrochemical attack of the inner oxide layer by aggressive molten salt species, particularly after the spallation of the outer oxide layers. The inner oxide layer was associated with less spallation after immersion test in solar salt. It is believed from this study that the tendency for spallation of interfacial oxide layers to occur on the surface of these alloys is closely related to mechanical properties of the interfacial oxide layers.

Chapter 11. Conclusion from corrosion analysis and degradation of stainless steels and Ni-based alloys and future work

11.1 Conclusions

Corrosion evaluation of the stainless steels and Ni-based alloys has been completed in different thermal irradiation to replicate as closely as possible the real conditions encountered in CSP plants. The contribution of temperature induced corrosion, covering gas and thermal gradient interactions to final corrosion failure were quantified using post-experiment surface analysis techniques. The key findings from this study are summarised in the following sections.

11.1.1 Corrosion evolution of stainless steels and Ni-based alloy in Solar salt in air

The corrosion behaviour of stainless steels; 321 SS and 347 SS, and Ni-based alloys; 625 and 825 in solar salts used in concentrated solar power (CSP) plants were experimentally investigated under isothermal (at 565°C) and thermal cycling conditions (temperatures between 290-565°C) under air atmosphere for up to 28 days.

- Mass loss of samples from isothermal test were higher at 565°C than those from thermal cycling tests between 290 and 565°C. This was believed to be linked to the effect of intermittent night – time cooling over a 12 h residence time at 250°C on the stability and adherence of interfacial oxide layers.
- Iron oxide, Chromia and iron – chromium spinel were the primary oxide layer on the surface of stainless steels with the capacity to protect against further Cr depletion and increase corrosion rate. The decomposition and oxide formation process are more dominant under isothermal conditions and mitigated by the thermal cycles used in this study.

11.1.2 The corrosion behaviours of stainless steels induced by different solar irradiation cycles

- The nature of the intermittent availability of solar energy will bring the instability of the whole CSP plant caused by different solar irradiation, including isothermal (at 565˚C), thermal cycling (between 290 - 565˚C) and thermal shock (565˚C - 30˚C) at air atmosphere. Thermal shock causes a higher rate of material loss than isothermal and thermal cycling heating profiles. This is linked to the effect of the synergy of

substantial cyclic thermal stress and electrochemical activities on the resilience of the metal – molten salt interface.

- The higher corrosion rate under thermal shock is also contributed by the effect of the synergy of substantial cyclic thermal stress and electrochemical activities on the protective properties and/or rate of spallation interfacial oxide layers.
- The corrosion of AISI 321 and 347 under different thermal cycles follows this order in decreasing corrosion rates; thermal shock > isothermal > thermal cycling. The corrosion rate decreases with increase of immersion time under isothermal and thermal cycling due to the formation of protective layer. This is not suitable for thermal shock condition with complicated spallation of corrosion layer with prolonging exposure time.
- The evolution in the chemistry of interfacial corrosion oxides was also affected by the different thermal cycles investigated. This is related to the effect of thermal cycles on the chemical stability of molten salt chemistries, diffusion of species across the corrosion interface, kinetics of corrosion and oxide formation.

11.1.3 Corrosion behaviour of test alloys under isothermal and thermal cycling in argon

- The interaction of stainless steels and nickel alloys with molten salts led to the formation of multi-layered interfacial oxides in both isothermal and thermal cycling conditions. They consist mainly of an inner layer of Fe_2O_3/Fe_3O_4/ $FeCr_2O_4$ and an outer layer of $NaFeO_2$ on stainless steels: AISI 321 and AISI 347, and an inner layer of NiO and/or $FeCr_2O_4$ on Ni-based alloy: IN 625 and IN 825. Also an outer layer of $NaFeO_2$ was found on the surface of IN 825.

- The main driving force for material loss is linked to the rate of spallation loosely held, porous, and poorly adherent Sodium–Iron spinel ($NaFeO_2$) layer. This layer easily spalls off to expose the inner and more protective $FeCr_2O_4$ and Fe_3O_4 layer (for stainless steels), and NiO and/or $FeCr_2O_4$ (for Nickel alloys) to further degradation by molten salt species. This process is more dominant under isothermal conditions and mitigated by the thermal cycles used in this study.

- Rate of material loss was higher in samples from isotheral immersion test at 600°C than in samples from thermal cycling immersion tests between 250 and 600°C. This was observed for both stainless steel samples and samples from Nickel alloys, and

believed to be linked to the effect of intermittent night – time cooling over a 12 h residence time at 250°C on the stability and adherence of interfacial oxide layers.

- The increase in corrosion rate under isothermal conditions is due to increase in the rate of decomposition of nitrate salts to nitrite. This increases the aggressiveness of the corrosion media. This effect is suppressed under thermal cycling conditions.
- The combined effect of 12 h residence time at 250°C and short experiment duration helped to understand the potential synergy of thermal fatigue effect from thermal cycling and electrochemical activities of molten salt species on the rate of spallation of interfacial oxide layers and overall material loss rate.

11.1.4 Comparison of Corrosion behaviours of test alloys in air and argon

The different corrosion behaviours of stainless steels and Ni-based alloys exposed solar salt under isothermal and thermal cycling in air and argon for 14 days were investigated.

- Thermal cycling effects suppresses the corrosion process in air by slowing down of the kinetics of corrosion and oxide formation and reducing the thermal effect on oxide layer stability during the cooling phase. This results in thinner, dense and more compact oxide layers forming on the samples.
- The formation and spallation behaviour of $NaFeO_2$ is likely the main contributor to an increase in corrosion rate under thermal cycling in argon. The delayed preferential formation of passive Cr_2O_3 due to the limitation of availability of oxide ions from decomposed nitrate also result in severer corrosion in argon than in air.
- The multi-layer was found on surface of stainless steels and IN 825 after immersion test in argon under thermal cycling condition. The composition of double layer were different: outer Fe_2O_3 layer and inner mixed oxides of (Fe, Cr) constituted the corrosion layer of Stainless steels, while outer NiO and inner mixed oxides of (Fe, Cr) constituted the corrosion layer of IN 825.
- The results presented in this study show that a combination of different alloy, salt and gas atmosphere could lead to different corrosion outcomes. However, thermal cycling has been shown to suppress the corrosion process significantly under any gas atmosphere; including inert argon atmosphere. The application of argon atmosphere to reduce the corrosion in other molten salt has been shown in this study to have the potential to increase the rate of metal loss in molten salt systems.

11.1.5 Evaluation of the relationship between the corrosion characteristics and thermal stress developed within interfacial oxides

This study has successfully investigated the early stages (over 7 days) of corrosion behaviour of various alloys as a function of temperature and test atmosphere with the aim of correlating the overall corrosion characteristics at the molten salt- oxide – metal interface with the stress distribution across the interface. Here are the key conclusions.

- The corrosion rate of stainless steel and Ni-based alloys in molten nitrate salts increases 3-fold with increase in temperature from 565˚C to 600°C in air.
- A synergy of high temperature and argon test atmosphere further increases the corrosion rate at 600°C up to 3 times higher than the test in air at same temperature. This synergy is related to a combination of Arrhenius effect of high temperature on the rate of decomposition of nitrate salts to nitrite and delayed passivation with Cr_2O_3 formation due to supressed availability of oxygen at the corrosion interface.
- The corrosion characteristics at the molten salt – oxide – metal interface was controlled by the overall protective properties of the multiple corrosion oxide layers formed. A more porous and less protective outer oxide layer consisting of a mixture of $NaFeO_2$ and Fe_2O_3 is kinetically favoured to form preferentially at 600°C than at 565°C, and under argon atmosphere than in air.
- The thermo-mechanical stress profile of the interfacial oxides correlates with the tendency for spallation to occur and overall corrosion rate.
- The observed inner Cr-rich oxide layer is more adherent and resilient to degradation than the outer Na/Fe-based oxides. This was observed in this study to be due to the compressive stress between the inner Cr-rich oxide layer and the substrate material, and the destructive tensile stress between inner Cr-rich outer layer and outer Na/Fe-rich oxides layer.
- The spallation of sodium iron oxide ($NaFeO_2$) formed on samples tested in air and under argon atmosphere at 600°C directly correlates to the tensile stress between the Cr-rich inner oxide layer and the $NaFeO_2$ layer.

11.2 Industrial Relevance and Novelty of Work Completed

- In the real CSP plants, the operating conditions are more intricate and more complex due to the alternation of day/ night and even unpredictable and sharp weather change within a short period of time. It is well established that the availability of consistent solar irradiation could significantly affect the electric energy generation capacity and efficiency of CSPs. The relevant automatic control systems need more action for monitoring the weather changes in terms of thermal shock.
- It is evident from these empirical studies that the oxygen availability is a critical factor in the corrosion of stainless steels and nickel alloys in Solar Salt. Both dissolution and oxidation processes are affected by oxygen content in the atmosphere available to the salt, which is related to the acidity/ basicity of the salt (Bell et al., 2022). Results from literature (Bell et al., 2021) also show that certain combinations of alloys and molten salts can result in extensive corrosion, and inert atmospheres - which are often used to limit corrosion in other types of molten salt - can increase the rate at which metal is consumed. Corrosion in molten salt environments, particularly oxyanionic salts where the anion can dissociate, is complex. It is proposed that understanding and regulating the basicity of the salt, by controlling parameters such as salt type, CO_2 and O_2 partial pressure, and electrical bias is important for preventing excessive corrosion in molten salt/metal systems.
- Stresses present a real and valid risk of stress corrosion cracking in the material in combination with a molten salt corrosive environment. There are many potential sources of thermal stress in a CSP plants, like thermal energy storage system (Bell et al., 2019). The weight of the storage media in large tanks, induced stresses from thermal cycling and expansion of the storage media, and residual stresses from manufacturing techniques such as welding are all potential sources of mechanical stress. The calculation of thermal stress in this study could briefly direct the research methodology in many area relevant to spallation resistance of the double-layers formed on the surfaces.

11.3 Possible future work based on main findings from this work

Corrosion and corrosion mechanism in molten salts is complex and dependent upon many variables. The salt anion and cation species, temperature, temperature gradient and thermal cycling rate, impurity concentration, atmosphere gas and pressure, alloying elements, composition and microstructure all greatly influence corrosion mechanism and rates. Still

lots of research have been investigated to address the concerns above, there still many future works need attention.

- Further studies to develop in-situ electrochemical study is required to monitor the corrosion process and understand the evolution of the corrosion oxides and its properties. Electrochemical study on the formation and corrosion mechanism of the alloys with molten salt includes open circuit potential, cyclic potentiodynamic polarisation and electrochemical impedance spectrometry.
- Research into stress corrosion cracking (SCC) in molten salts is extremely sparse and represents a large gap in knowledge in this area. One reason is that the standard testing method uses metal tokens submerged in a molten salt which are not under load. Also, applying mechanical load to produce a stress, particularly a known stress, is tricky and no standard testing method has been developed. It is somewhat telling that the main places where SCC has been reported in molten salts, is in operational systems where components are under load. Intergranular corrosion, particularly when coupled with mechanical stress, could cause stress corrosion cracking, which needs to be well understood for long term systems reliability. This is another problem which needs to be fully understood under TES system conditions and throughout the full system life of the system. For this to occur, an easy to implement standard testing method needs to be developed, and testing conducted on proposed alloys.
- Considering the flowing behaviour and static storage behaviour of molten salt in the flow lines and storage tanks, it is easy to imagine that the metallic parts are either immersed in the salt or above the liquid line of the molten salt, whereas the air or salt vapour. The material exposed to mixed environment with molten salt vapour and oxygen would suffer a higher degree of corrosion. Because of the relative low vapour pressure of the nitrate salt, there was few open literatures reported the salt vapour of nitrate salt. The corrosion performance of metallic material in nitrate salt vapour should be investigated before the large-scale use of newly type salts to figure out corrosion or protection dominates the corrosion behaviour in this condition.
- Considering molten salt flowing in the heat transfer pipes, the fluid velocity of molten salt plays a significant role in corrosion behaviour. Lots of studies are in static corrosion condition and the effects of dynamic corrosion on different steels are researched in other corrosive conditions. Investigation into the corrosion behaviour at dynamic condition with different velocity of molten salt are increasingly becoming

more relevant recently. This will help understand and evaluate the potential corrosion mechanism.

- There is also a need to investigate the corrosion mechanism of other forms of salts with different chemical species, including oxyanionic salts (Carbonates, Nitrates, and Sulphates) and halide salts (fluoride and chloride salt).
- In general, nitrate salts are relatively benign and have acceptable corrosion rates at temperatures below 600°C for stainless steels. To prevent substantial dealloying and corrosion in chloride and fluorides, the salts must be very pure, free from moisture, and an inert atmosphere must be maintained. Pre-forming thick oxide layers may help. Carbonate salts will also require purification and atmosphere control, and dealloying is also a concern. Using sulphate salts may induce additional corrosion mechanism via sulphidation. High nickel alloys and coatings are likely to be the most resistant to attack, and chromium will leech into the salt, unless it's solubility can be reduced, or it is diffusion limited in some way – via microstructural modification, alloying, surface coatings or the use of low chromium alloys.

Chapter 12. Appendix file

12.1 Equation derivation

Calculation of corrosion rate from I_{CORR}, for Equation 4 and Equation 14 in thesis,

Q=nFm/A=iT,

Q is coulombs, n = number of electrons, F the Faraday (96,487 coulombs/equivalent), m = mass (g), A = atomic weight, i = current (A), T = time (s).

Since Equivalent Weight (EW) = A/n, so m = iT(EW)/F

Then Corrosion Rate (g/s) = m/T = i(EW)/F

From the engineering standpoint, it is convenient to express Corrosion Rate in mm/yr, Divide both sides of the equation:

Corrosion Rate (g/s) = m/t = i(EW)/F by electrode area and density,

Corrosion Rate (cm/s) = i(EW)/FρA, i/A = current density (I).

Corrosion rate (mm/yr) = 0.00327 Icorr(EW) / ρ

$$\mathbf{CR}=\frac{\boldsymbol{Icorr}\cdot\boldsymbol{K}}{\boldsymbol{A}\,\boldsymbol{\rho}\,\sum(\frac{\boldsymbol{fi}\cdot\boldsymbol{ni}}{\boldsymbol{MWi}})}=\boldsymbol{K}\frac{\boldsymbol{icorr}}{\boldsymbol{\rho}}\boldsymbol{EW}$$

ρ is alloy density, the alloy density of SS321, SS347, IN625 and IN 825 is 7.94, 8.03, 8.14 and 8.14 g/cm^3, respectively. K is constant 3.27*10-3, mm g/μA cm yr. I_{corr} is corrosion current (μA/cm^2), f_i is weight fraction of elezment i, n_i is number of electrons being transferred in i, i is 2, 3 and 2 for Fe, Cr and Ni respectively in this study. MW_i is atomic weight of i. The alloy equivalent weight, EW = atomic weight / number of electrons, is considered dimensionless in these calculations The EW of SS 321, SS347, IN 625 and IN 825 is 25.13, 25.29, 25.89 and 25.52 respectively.

12.2 Thermal stress calculation

Even when no stress exists at the oxidation temperature, stresses will be generated during cooling process because of different in thermal expansion coefficient of the metal and oxide (Birks et al., 2006). The following derivation is for the specific case of an oxide on both top and bottom of the metal, and thus no bending of the oxide-metal system. As shown in Figure 12-1, at the oxidation higher temperature (T_H) both metal and oxide have length l_1 and, after cooling to a lower temperature (T_L), they have length l. If they were not bonded, on cooling

to T_L, the metal and oxide would experience free thermal strains as shown in below Equation 57 and Equation 58.

$$\varepsilon_{thermal}^{metal} = \alpha_M \Delta T \qquad \text{Equation 57}$$

$$\varepsilon_{thermal}^{oxide} = \alpha_{Ox} \Delta T \qquad \text{Equation 58}$$

Where α_M and α_{Ox} are the (assumed constant) linear thermal-expansion coefficients for the metal and oxide, respectively, and $\Delta T = T_L - T_H$ and is thus negative in sign. Because they are bonded, the oxide and metal also experience mechanical strain due to residual stress, see Equation 59 and Equation 60.

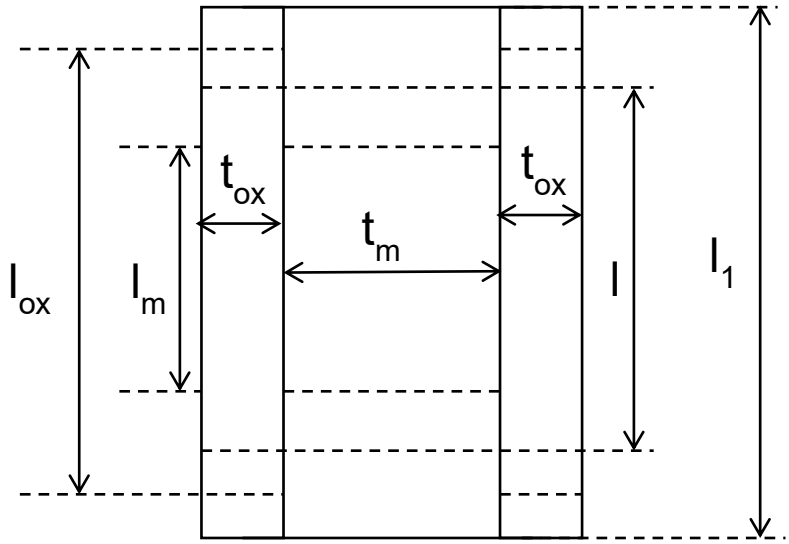

Figure 12-1. schematic section through an oxidized sheet of metal showing the dimensions needed to calculate the thermal stress in the oxide.

$$\varepsilon_{mechanical}^{metal} = \frac{\sigma_M (1 - \gamma_M)}{E_M} \qquad \text{Equation 59}$$

$$\varepsilon_{mechanical}^{oxide} = \frac{\sigma_{Ox} (1 - \gamma_{Ox})}{E_{Ox}} \qquad \text{Equation 60}$$

Where Hooke's law for an equal biaxial state of stress has been used. Because the oxide and metal are bonded, their total axial strains must be the same, so the Equation 61 was obtained. Afterwards, performing a force balance on the specimen, where t_M and t_{Ox} are the thickness of metal and a single-oxide scale, yields Equation 62;

$$\varepsilon_{thermal}^{metal} + \varepsilon_{mechanical}^{metal} = \varepsilon_{thermal}^{oxide} + \varepsilon_{mechanical}^{oxide} \qquad \text{Equation 61}$$

$$\sigma_M t_M + 2\sigma_{Ox} t_{Ox} = 0 \qquad \text{Equation 62}$$

Combining these equations yields Equation 63 and Equation 64; Considering if no Poisson ratio mismatch between the metal and oxide, the formula simplifies to Equation 49.

$$\alpha_M \Delta T - \frac{2\sigma_{Ox} t_{Ox}(1-\gamma_M)}{t_M E_M} = \alpha_{Ox}\Delta T + \frac{\sigma_{Ox}(1-\gamma_{Ox})}{E_{Ox}} \quad \text{Equation 63}$$

$$\sigma_{Ox} = \frac{-(\alpha_{Ox} - \alpha_M)\Delta T}{\frac{2t_{Ox}(1-\gamma_M)}{t_M E_M} + \frac{(1-\gamma_{Ox})}{E_{Ox}}} \quad \text{Equation 64}$$

$$\sigma_{Ox} = \frac{-E_{Ox}(\alpha_{Ox} - \alpha_M)\Delta T}{(1-\gamma)(1+2\frac{t_{Ox}E_{Ox}}{t_M E_M})} \quad \text{Equation 65}$$

Because ΔT is assumed negative and α_{Ox} is typically less than that α_M, the stress in the oxide is typical negative. For the case of a thin oxide on only one side of a thick metal substrate, it may still be reasonable to assume no bending deformation of the oxide-metal laminate. In such cases, the Equation 49 can be used if the factor 2 in the last term if the denominator is removed. In cases where the oxide is very thin relative to the thickness of the metal, the last term in the denominator of Equation 49 can be neglected, yielding Equation 66.

$$\sigma_{Ox} = \frac{-E_{Ox}(\alpha_{Ox} - \alpha_M)\Delta T}{(1-\gamma)} \quad \text{Equation 66}$$

Which corresponds the typical case of residual stresses in the oxide inducing essentially no deformation in the metal. Equation 49 and Equation 66 have been widely used for calculating thermal stresses in oxides (Tien et al., 1975).

The presence of thermal stresses often results in spalling of protective oxides. This generally makes exposures in which the temperature is cycled more severe than isothermal exposures. As mentioned, the thermal expansion coefficient for the oxide will generally be less than that for the metal, as seen in Table 8-3, so that compressive stresses will develop in the oxide during cooling. The magnitude of the stresses will be proportional to $\Delta\alpha = \alpha_M - \alpha_{Ox}$. This is consistent with the observation that scales formed on Ni and Co tend to remain adherent after cooling whereas those on Cu and Cr do not.

Table 12-1. Linear coefficient of thermal expansion of metal and oxide (Hancock and Hurst, 1974) (temperature range 100-800 ˚C)

System	Oxide coefficient $*10^{-6}$	Metal coefficient$*10^{-6}$	Thermal expansion of some oxides and alloys (Yin et al., 2021) $*10^{-6}$	Young's Module and Poisson ratio
Fe-FeO	12.2	15.3	12-17	
Fe-Fe_2O_3-Fe_3O_4	14.9	15.3	9-12 Fe_2O_3 9-15 Fe_3O_4	280 GPa and 0.25 for Fe_2O_3 (Ramos et al., 2021)
Ni-NiO	17.1	17.6		
Co-CoO	15	14		
Cr-Cr_2O_3	7.3	9.5	7.3-8.5	290 GPa and 0.33 (Ramos et al., 2021)
Cu-Cu_2O	4.3	18.6		
Cu-CuO	9.3	18.6		
Austenitic SS	-	-	16.0-19.5 (~17.4)	0.33
Inconel 625	-	-	13.1-17.8 (~17.8)	0.308

12.2.1 Growth stress

However, in the oxide scale systematically accompanied the development of growth stresses during isothermal oxidation and of thermal stresses during cooling (Pu et al., 2014). The growth stress is due to the fact that the specific volume of the oxide is rarely the same as that of the metal which is consumed in its formation. The sign of the stress in the oxide may be related to the Pill-Bedworth ratio (PBR):

$$PBR=Vox/Vm \qquad \text{Equation 67}$$

The typical PBRs for a number of system is listed in Table 12-2 (Birks et al., 2006). The oxide is expected to be in compression if the PBR is greater than unity (the case for most metals) and in tension if the PBR is less than unity. Generally those systems which develop

tensile stresses in the oxide, e.g. K, Mg, Na, cannot maintain protective films. The oxides on most metal and allots form in compression as expected from the PBR. However, the development of compressive stress would only seem to be feasible if the oxide were growing at the scale-metal interface by inward migration of oxide ions, in fact the development of compressive stress during the growth of an oxide depends upon the experimental conditions. If the oxide is growing at the scale-metal interface by the inward migration of oxide ions, compressive stress should develop providing the oxide scale cannot move outward away from the metal, as in the case of small coupon specimens. Scales forming at the oxide-gas interface on a planar specimen should not develop stresses because the volume difference between metal and an oxide is simply reflected in the scale thickness. Also, the magnitudes of the stresses are not always in the order expected from the PBR. Clearly, while the volume ratio is a cause of growth stresses in some cases, other mechanisms must also be operative in many systems.

Table 12-2. Oxide-metal-volume ratios of some typical metals

Oxide	Oxide-metal-volume ratio
K_2O	0.45
MgO	0.81
Na_2O	0.97
Al_2O_3	1.28
Cu2O	1.64
NiO	1.65
FeO (on α-Fe)	1.68
TiO_2	1.70-1.78
Cr_2O_3	2.07
Fe_3O_4 (on α-Fe)	2.10
Fe_2O_3 (on α-Fe)	2.14
Nb_2O_5	2.68
V_2O_5	3.19

12.2.2 Calculation and analysis

In this study, the nano-indentation test was performed on the corrosion layer formed on the surface of argon-exposed samples.

The typical p-h curve was shown in Figure 12-2.

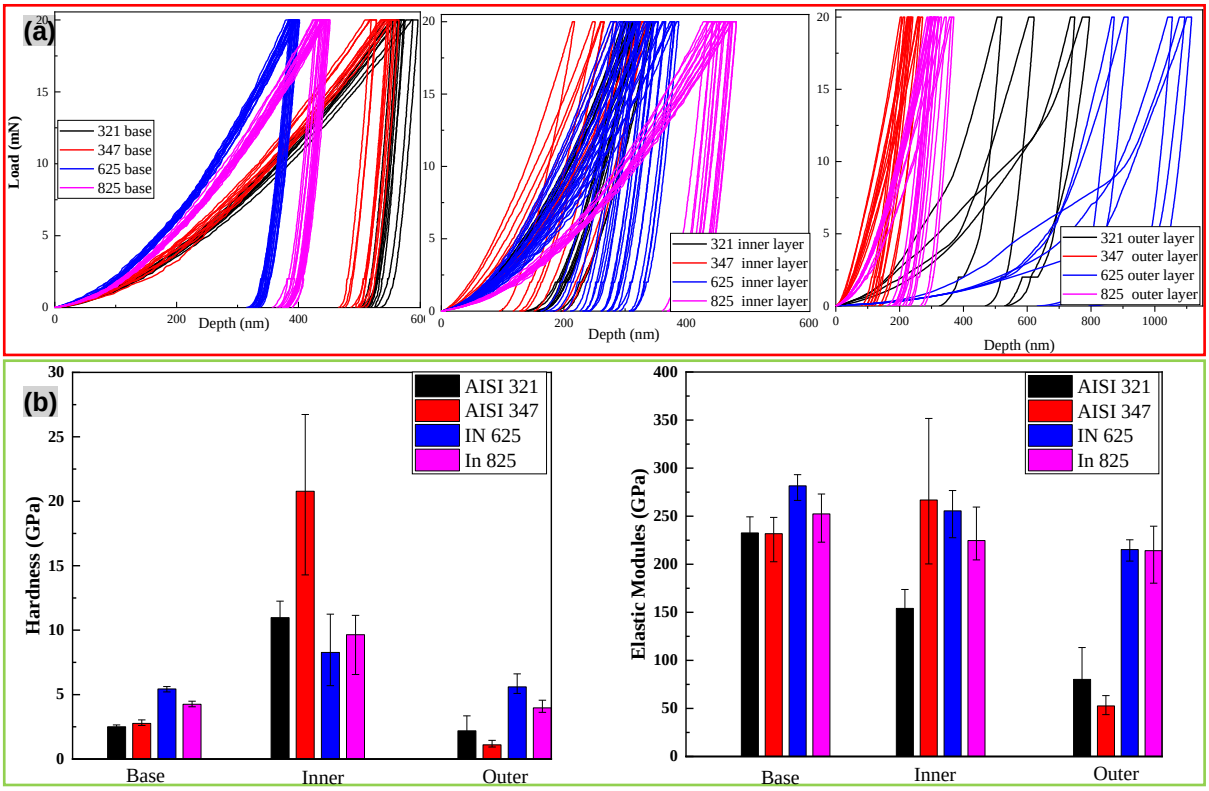

Figure 12-2. (a)Typical P-h curves of base material, inner layer and outer layer of AISI 321, AISI 347, IN 625 and IN 825 and (b) corresponding harness and elastic modulus (samples after 600˚C isothermal in argon).

The calculation of the thermal stress between the corrosion layer and bulk metal can be used to explain the spallation behaviour of the oxide layer.

For Isothermal samples, the temperature difference come from the cooling process when finishing the test.

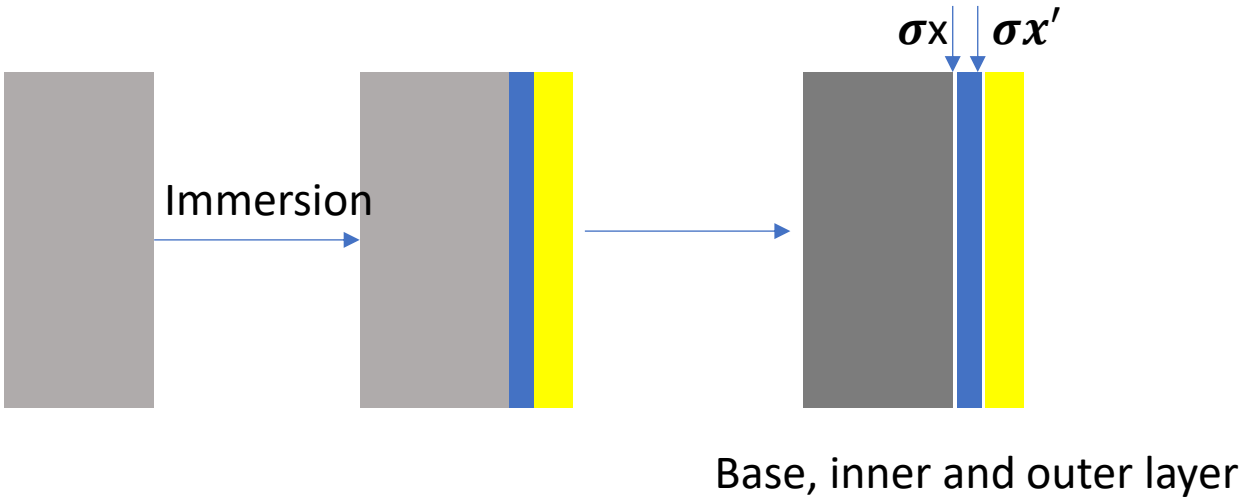

In argon 600C

For SS 321 isothermal, stress between inner layer (Ox, Cr_2O_3) and bulk material (seen as M), the thickness can be neglected;

$$\sigma_{Ox} = \frac{-E_{Ox}(\alpha_{Ox}-\alpha_M)\Delta T}{(1-\gamma)(1+2\frac{t_{Ox}E_{Ox}}{t_M E_M})} = \frac{-154GPa*(7.3*10^{-6}-17.4*10^{-6})K^{-1}(-575K)}{1-0.33}$$ = -1.335 GPa

For SS 321 <u>isothermal</u>, stress between outer oxide layer (Ox, Fe_2O_3) and inner layer (seen as M, Cr_2O_3), the thickness of layer should

$$\sigma'_{Ox} = \frac{-(\alpha_{Ox}-\alpha_M)\Delta T}{\frac{2t_{Ox}(1-\gamma_M)}{t_M E_M}+\frac{(1-\gamma_{Ox})}{E_{Ox}}} = \frac{-(12*10^{-6}-7.3*10^{-6})K^{-1}*(-575K)}{\frac{2*12*(1-0.33)}{13*154GPa}+\frac{1-0.25}{80\ GPa}}$$= 0.158 GPa

The stress between bulk metal and inner layer was obtained, -1.335 GPa, the negative means that the stress is compressive stress, increasing the adherence of the inner layer to bulk metal. The stress between inner layer and outer layer was found to be 0.158GPa, and the stress is tensile stress, resulting in spallation.

For SS 347 isothermal, stress between inner layer (Ox, Cr_2O_3) and bulk material (seen as M), the thickness can be neglected;

$$\sigma_{Ox} = \frac{-E_{Ox}(\alpha_{Ox}-\alpha_M)\Delta T}{(1-\gamma)(1+2\frac{t_{Ox}E_{Ox}}{t_M E_M})} = \frac{-267GPa*(7.3*10^{-6}-17.4*10^{-6})K^{-1}(-575K)}{1-0.33}$$= -2.31 GPa

For SS 347 isothermal, stress between outer oxide layer (Ox, Fe_2O_3) and inner layer (seen as M, Cr_2O_3), the thickness of layer should

$$\sigma'_{Ox} = \frac{-(\alpha_{Ox}-\alpha_M)\Delta T}{\frac{2t_{Ox}(1-\gamma_M)}{t_M E_M}+\frac{(1-\gamma_{Ox})}{E_{Ox}}} = \frac{-(12*10^{-6}-7.3*10^{-6})K^{-1}*(-575K)}{\frac{2*8.4*(1-0.33)}{8*267GPa}+\frac{1-0.25}{52.6\ GPa}}$$= 0.138 GPa

For IN 625 isothermal, stress between inner layer (Ox, Cr_2O_3, 7.3) and bulk material (seen as M), the thickness can be neglected;

$$\sigma_{Ox} = \frac{-E_{Ox}(\alpha_{Ox}-\alpha_M)\Delta T}{(1-\gamma)(1+2\frac{t_{Ox}E_{Ox}}{t_M E_M})} = \frac{-255.6GPa*(7.3*10^{-6}-17.8*10^{-6})K^{-1}(-575K)}{1-0.308}$$= -2.20 GPa

For IN625 isothermal stress between outer oxide layer (Ox, Fe_2O_3&NiO (12&17.1-14.55)) and inner layer (seen as M, Cr_2O_3), the thickness of layer should

$$\sigma'_{Ox} = \frac{-(\alpha_{Ox}-\alpha_M)\Delta T}{\frac{2t_{Ox}(1-\gamma_M)}{t_M E_M}+\frac{(1-\gamma_{Ox})}{E_{Ox}}} = \frac{-(14.55*10^{-6}-7.3*10^{-6})K^{-1}*(-575K)}{\frac{2*6*(1-0.308)}{6.5*255.6GPa}+\frac{1-0.25}{215.3GPa}}$$=0.491 GPa

For IN 825 isothermal, stress between inner layer (Ox, NiO&Cr_2O_3, 12.2) and bulk material (seen as M), the thickness can be neglected;

$$\sigma_{Ox} = \frac{-E_{Ox}(\alpha_{Ox}-\alpha_M)\Delta T}{(1-\gamma)(1+2\frac{t_{Ox}E_{Ox}}{t_M E_M})} = \frac{-224.6GPa*(12.2*10^{-6}-17.8*10^{-6})K^{-1}(-575K)}{1-0.308}$$= -1.045 GPa

For IN 825 isothermal stress between outer oxide layer (Ox, Fe_2O_3, 12) and inner layer (seen as M, NiO&Cr_2O_3, 12.2), the thickness of layer should

$$\sigma'_{Ox} = \frac{-(\alpha_{Ox}-\alpha_M)\Delta T}{\frac{2t_{Ox}(1-\gamma_M)}{t_M E_M}+\frac{(1-\gamma_{Ox})}{E_{Ox}}} = \frac{-(12*10^{-6}-12.2*10^{-6})K^{-1}*(-575K)}{\frac{2*5.4*(1-0.308)}{5.9*224.6GPa}+\frac{1-0.25}{214.2GPa}}$$= 0.013GPa

In air 565 and 600C

AISI 321 565 ˚C isothermal in air

$$\sigma_2 = \frac{-E_{Ox}(\alpha_{Ox}-\alpha_M)\Delta T}{(1-\gamma)(1+2\frac{t_{Ox}E_{Ox}}{t_M E_M})} = \frac{-80GPa*(12*10^{-6}-17.4*10^{-6})K^{-1}(-540K)}{1-0.33}$$= -0.348 GPa **inner with bulk**

σ'_2=0 (outer layer is unavailable for 565 samples)

*** no outer layer*

AISI 321 600 ˚C isothermal in air

$$\sigma_3 = \frac{-E_{Ox}(\alpha_{Ox}-\alpha_M)\Delta T}{(1-\gamma)(1+2\frac{t_{Ox}E_{Ox}}{t_M E_M})} = \frac{-154GPa*(7.3*10^{-6}-17.4*10^{-6})K^{-1}(-575K)}{1-0.33}$$ = -1.335GPa*inner with bulk**

$$\sigma'_3 = \frac{-(\alpha_{Ox}-\alpha_M)\Delta T}{\frac{2t_{Ox}(1-\gamma_M)}{t_M E_M}+\frac{(1-\gamma_{Ox})}{E_{Ox}}} = \frac{-(12*10^{-6}-7.3*10^{-6})K^{-1}*(-575K)}{\frac{2*6*(1-0.33)}{8*154GPa}+\frac{1-0.25}{80\ GPa}}$$= 0.169 GPa ***outer with inner**

AISI 347 565 ˚C isothermal in air

$$\sigma_2 = \frac{-E_{Ox}(\alpha_{Ox}-\alpha_M)\Delta T}{(1-\gamma)(1+2\frac{t_{Ox}E_{Ox}}{t_M E_M})} = \frac{-52.6\ GPa*(12*10^{-6}-17.4*10^{-6})K^{-1}(-540K)}{1-0.33}$$= -0.229 GPa ***inner with bulk**

σ'_2=0

AISI 347 600 ˚C isothermal in air

$$\sigma_3 = \frac{-E_{Ox}(\alpha_{Ox}-\alpha_M)\Delta T}{(1-\gamma)(1+2\frac{t_{Ox}E_{Ox}}{t_M E_M})} = \frac{-267GPa*(7.3*10^{-6}-17.4*10^{-6})K^{-1}(-575K)}{1-0.33}$$= -2.31 GPa

***inner with bulk**

$$\sigma'_3 = \frac{-(\alpha_{Ox}-\alpha_M)\Delta T}{\frac{2t_{Ox}(1-\gamma_M)}{t_M E_M}+\frac{(1-\gamma_{Ox})}{E_{Ox}}} = \frac{-(12*10^{-6}-7.3*10^{-6})K^{-1}*(-575K)}{\frac{2*10*(1-0.33)}{3*267GPa}+\frac{1-0.25}{52.6\ GPa}}$$= 0.087 GPa

outer with inner

IN 625 565˚C isothermal in air

$$\sigma_2 = \frac{-E_{Ox}(\alpha_{Ox}-\alpha_M)\Delta T}{(1-\gamma)(1+2\frac{t_{Ox}E_{Ox}}{t_M E_M})} = \frac{-215.3\ GPa*(17.1*10^{-6}-17.8*10^{-6})K^{-1}(-540K)}{1-0.308}$$ = -0.118 GPa

σ'_2=0 (double layer unavailable for Ni-based alloy)

IN 625 600 ˚C isothermal in air

$$\sigma_3 = \frac{-E_{Ox}(\alpha_{Ox}-\alpha_M)\Delta T}{(1-\gamma)(1+2\frac{t_{Ox}E_{Ox}}{t_M E_M})} = \frac{-215.3\ GPa*(17.1*10^{-6}-17.8*10^{-6})K^{-1}(-575K)}{1-0.308}$$ = -0.125GPa

σ'_3=0

IN 825 565˚C isothermal in air

$$\sigma_2 = \frac{-E_{Ox}(\alpha_{Ox}-\alpha_M)\Delta T}{(1-\gamma)(1+2\frac{t_{Ox}E_{Ox}}{t_M E_M})} = \frac{-214.2\ GPa*(12*10^{-6}-17.8*10^{-6})K^{-1}(-540K)}{1-0.308}$$ = -0.969 GPa

σ'_2=0

IN 825 600˚C isothermal in air

$$\sigma_3 = \frac{-E_{Ox}(\alpha_{Ox}-\alpha_M)\Delta T}{(1-\gamma)(1+2\frac{t_{Ox}E_{Ox}}{t_M E_M})} = \frac{-214.2\ GPa*(12*10^{-6}-17.8*10^{-6})K^{-1}(-575K)}{1-0.308}$$ = -1.032 GPa

σ'_3=0

Table 12-3. Calculated thermal stress values from Equation 49 (σ_1 represents the stress between inner layer and bulk and $\boldsymbol{\sigma'_1}$ represents the stress between inner layer and outer layer of argon isothermal samples at 600˚C, σ_2 and $\boldsymbol{\sigma'_2}$ represents the thermal stress between inner layer and bulk and between inner layer and outer for air samples at 565˚C, σ_3 and $\boldsymbol{\sigma'_3}$ for air samples at 600˚C respectively).*: Not applicable with unavailable double layer

Material/stress (GPa)	**Argon 600˚C**		**Air 565˚C**		**Air 600˚C**	
	σ_1	σ'_1	σ_2	σ'_2	σ_3	σ'_3
AISI 321	-1.335	0.158	-0.348	*	-1.335	0.169
AISI 347	-2.31	0.138	-0.229	*	-2.31	0.087
IN 625	-2.20	0.491	-0.118	*	-0.125	*
IN 825	-1.045	0.013	-0.969	*	-1.032	*

12.3 Time-scale normalization process:

AISI 321 for instance:

Isothermal: Corrosion rate: $\frac{\Delta \boldsymbol{m1}}{\boldsymbol{T0}} = \frac{2.33\ mg/cm2}{672\ hours} = 0.00346\ mg/(cm2 \cdot h)$

100-hour equivalent mass loss: $\frac{\Delta \boldsymbol{m1}}{\boldsymbol{T0}} * T = 0.00346\ mg/(cm2 \cdot h)$ * 100 h =0.346 mg/cm2

Thermal cycling: Corrosion rate: $\frac{\Delta \boldsymbol{m2}}{\boldsymbol{T0}} = \frac{1.125\ mg/cm2}{672\ hours} = 0.001125\ mg/(cm2 \cdot h)$

equivalent time: $\frac{\frac{\Delta \boldsymbol{m1}}{\boldsymbol{T0}} * T}{\frac{\Delta \boldsymbol{m2}}{\boldsymbol{T0}}} = \frac{\Delta \boldsymbol{m1}}{\Delta \boldsymbol{m2}} * \boldsymbol{T} = \frac{0.346 mg/cm2}{0.001125\ mg/(cm2 \cdot h)} = 207\ hours$

AISI 321	Isothermal	Thermal cycling	Thermal shock	Thermal cycling hot
mass loss (4-week)	2.33	1.125	3.157	1.125
Equivalent time (h)	100	$\frac{2.33}{1.125} * 100 = 207$	$\frac{2.33}{3.157} * 100 = 73.8$	$\frac{207}{2} = 103.5$
AISI 347 mass loss	Isothermal	Thermal cycling	Thermal shock	Thermal cycling hot
mass loss (4-week)	1.4	0.9845	5.4	0.9845
Equivalent time (h)	100	143	25.9	71.5

References

2015. *BSI Standards Publication Corrosion of metals and alloys — Test method for high temperature corrosion testing of metallic materials by immersing in molten salt or other liquids under static conditions* [Online]. Available: https://www.iso.org/standard/59473.html [Accessed].

2017. *Solargis. Download free solar resource maps.* [Online]. Available: https://solargis.com/maps-and-gis-data/download/world [Accessed].

AHMED, O. 2013. Corrosion behaviour of AISI 304 stainless steel in contact with eutectic salt for concentrated solar power plant applications.

AI, H., YE, X.-X., JIANG, L., LENG, B., SHEN, M., LI, Z., JIA, Y., WANG, J.-Q., ZHOU, X., XIE, Y. & XIE, L. 2019. On the possibility of severe corrosion of a Ni-W-Cr alloy in fluoride molten salts at high temperature. *Corrosion Science,* 149**,** 218-225.

ALVA, G., LIN, Y. & FANG, G. 2018. An overview of thermal energy storage systems. *Energy,* 144**,** 341-378.

AYDOĞDU, G. H. & AYDINOL, M. K. 2006. Determination of susceptibility to intergranular corrosion and electrochemical reactivation behaviour of AISI 316L type stainless steel. *Corrosion Science,* 48**,** 3565-3583.

BARAKA, A., ABDEL-ROHMAN, A. I. & HOSARY, A. A. E. 1976. Corrosion of Mild Steel in Molten Sodium Nitrate–Potassium Nitrate Eutectic. *British Corrosion Journal,* 11**,** 44-46.

BARKER, R. J. 2012. *Erosion-corrosion of carbon steel pipework on an offshore oil and gas facility*, University of Leeds.

BARLEV, D., VIDU, R. & STROEVE, P. 2011. Innovation in concentrated solar power. *Solar Energy Materials and Solar Cells,* 95**,** 2703-2725.

BATAILLOU, L., DESGRANGES, C., MARTINELLI, L. & MONCEAU, D. 2018. Modelling of the effect of grain boundary diffusion on the oxidation of Ni-Cr alloys at high temperature. *Corrosion Science,* 136**,** 148-160.

BELL, S., JONES, M. W. M., GRAHAM, E., PETERSON, D. J., VAN RIESSEN, G. A., HINSLEY, G., STEINBERG, T. & WILL, G. 2022. Corrosion mechanism of SS316L exposed to NaCl/Na2CO3 molten salt in air and argon environments. *Corrosion Science,* 195**,** 109966.

BELL, S., RHAMDHANI, M. A., STEINBERG, T. & WILL, G. 2021. Aggressive corrosion of C-276 nickel superalloy in chloride/sulphate eutectic salt. *Solar Energy,* 227**,** 557-567.

BELL, S., STEINBERG, T. & WILL, G. 2019. Corrosion mechanisms in molten salt thermal energy storage for concentrating solar power. *Renewable and Sustainable Energy Reviews,* 114.

BELLEZZE, T., GIULIANI, G. & ROVENTI, G. 2018. Study of stainless steels corrosion in a strong acid mixture. Part 1: cyclic potentiodynamic polarization curves examined by means of an analytical method. *Corrosion Science,* 130**,** 113-125.

BESMANN, T. M., KULKARNI, N., SPEAR, K. & VIENNA, J. Predicting Phase Equilibria of Spinel-Forming Constituents in Waste Glass Systems. Environmental Issues and Waste Management Technologies in the Ceramic and Nuclear Industries X: Proceedings of the 106th Annual Meeting of The American Ceramic Society, Indianapolis, Indiana, USA 2004, 2012. John Wiley & Sons, 121.

BIRKS, N., MEIER, G. H. & PETTIT, F. S. 2006. *Introduction to the high temperature oxidation of metals*, Cambridge university press.

BONK, A., BRAUN, M., SÖTZ, V. A. & BAUER, T. 2020. Solar Salt – Pushing an old material for energy storage to a new limit. *Applied Energy,* 262**,** 114535.

BRADSHAW, R. & CLIFT, W. 2010. Effect of chloride content of molten nitrate salt on corrosion of A516 carbon steel.

BRADSHAW, R. W. & GOODS, S. H. 2001a. Corrosion of alloys and metals by molten nitrates. Sandia National Lab.(SNL-CA), Livermore, CA (United States).

BRADSHAW, R. W. & GOODS, S. H. 2001b. Corrosion resistance of stainless steels during thermal cycling in alkali nitrate molten salts. Sandia National Laboratories.

BRADSHAW, R. W. & MEEKER, D. E. 1990. High-temperature stability of ternary nitrate molten salts for solar thermal energy systems. *Solar Energy Materials,* 21**,** 51-60.

CHENG, Y. F., WILMOTT, M. & LUO, J. L. 1999. The role of chloride ions in pitting of carbon steel studied by the statistical analysis of electrochemical noise. *Applied Surface Science,* 152**,** 161-168.

CHO, H.-S., VAN ZEE, J. W., SHIMPALEE, S., TAVAKOLI, B. A., WEIDNER, J. W., GARCIA-DIAZ, B. L., MARTINEZ-RODRIGUEZ, M. J., OLSON, L. & GRAY, J. 2015. Dimensionless Analysis for Predicting Fe-Ni-Cr Alloy Corrosion in Molten Salt Systems for Concentrated Solar Power Systems. *CORROSION,* 72**,** 742-760.

ČíHAL, V. R. & ŠTEFEC, R. 2001. On the development of the electrochemical potentiokinetic method. *Electrochimica Acta,* 46**,** 3867-3877.

COLOMBAN, P., CHERIFI, S. & DESPERT, G. 2008. Raman identification of corrosion products on automotive galvanized steel sheets. 39**,** 881-886.

D'SOUZA, B., ZHUO, W., YANG, Q., LEONG, A. & ZHANG, J. 2021. Impurity driven corrosion behavior of HAYNES® 230® alloy in molten chloride Salt. *Corrosion Science,* 187**,** 109483.

DAHASH, A., OCHS, F., JANETTI, M. B. & STREICHER, W. 2019. Advances in seasonal thermal energy storage for solar district heating applications: A critical review on large-scale hot-water tank and pit thermal energy storage systems. *Applied Energy,* 239**,** 296-315.

DE FARIA, D. L. A., VENÂNCIO SILVA, S. & DE OLIVEIRA, M. T. 1997. Raman microspectroscopy of some iron oxides and oxyhydroxides. 28**,** 873-878.

DE LA ROCHE, J., GÓMEZ, P. A., ALVARADO-OROZCO, J. M. & TORO, A. 2020. Hot corrosion and thermal shock resistance of Dense-CYSZ/YSZ bilayer thermal barrier coatings systems applied onto Ni-base superalloy. *Journal of the European Ceramic Society,* 40**,** 5692-5703.

DESIDERI, U. & CAMPANA, P. E. 2014. Analysis and comparison between a concentrating solar and a photovoltaic power plant. *Applied Energy,* 113**,** 422-433.

DING, W., BONK, A. & BAUER, T. 2018. Corrosion behavior of metallic alloys in molten chloride salts for thermal energy storage in concentrated solar power plants: A review. *Frontiers of Chemical Science and Engineering,* 12**,** 564-576.

ELBAKHSHWAN, M., LEE, D. H. & ANDERSON, M. 2022. Corrosion resistance of high nickel alloys in solar salt at 600 °C for up to 4000 h. *Solar Energy Materials and Solar Cells,* 245**,** 111837.

ENCINAS-SÁNCHEZ, V., DE MIGUEL, M. T., LASANTA, M. I., GARCÍA-MARTÍN, G. & PÉREZ, F. J. 2019. Electrochemical impedance spectroscopy (EIS): An efficient technique for monitoring corrosion processes in molten salt environments in CSP applications. *Solar Energy Materials and Solar Cells,* 191**,** 157-163.

FABRE, S., CABET, C., CASSAYRE, L., CHAMELOT, P., DELEPECH, S., FINNE, J., MASSOT, L. & NOEL, D. 2013. Use of electrochemical techniques to study the corrosion of metals in model fluoride melts. *Journal of Nuclear Materials,* 441**,** 583-591.

FEDERSEL, K., WORTMANN, J. & LADENBERGER, M. 2015. High-temperature and Corrosion Behavior of Nitrate Nitrite Molten Salt Mixtures Regarding their Application in Concentrating Solar Power Plants. *Energy Procedia,* 69**,** 618-625.

FERNÁNDEZ, A. G. & CABEZA, L. F. 2019a. Corrosion monitoring and mitigation techniques on advanced thermal energy storage materials for CSP plants. *Solar Energy Materials and Solar Cells,* 192**,** 179-187.

FERNÁNDEZ, Á. G. & CABEZA, L. F. 2019b. Molten salt corrosion mechanisms of nitrate based thermal energy storage materials for concentrated solar power plants: A review. *Solar Energy Materials and Solar Cells,* 194**,** 160-165.

FERNÁNDEZ, A. G., CORTES, M., FUENTEALBA, E. & PÉREZ, F. J. 2015a. Corrosion properties of a ternary nitrate/nitrite molten salt in concentrated solar technology. *Renewable Energy,* 80**,** 177-183.

FERNÁNDEZ, A. G., GALLEGUILLOS, H., FUENTEALBA, E. & PÉREZ, F. J. 2015b. Corrosion of stainless steels and low-Cr steel in molten Ca(NO3)2–NaNO3–KNO3 eutectic salt for direct energy storage in CSP plants. *Solar Energy Materials and Solar Cells,* 141**,** 7-13.

FERNÁNDEZ, A. G., LASANTA, M. I. & PÉREZ, F. J. 2012. Molten Salt Corrosion of Stainless Steels and Low-Cr Steel in CSP Plants. *Oxidation of Metals,* 78**,** 329-348.

G1-03, A. 2017. *Standard Practice for Preparing, Cleaning, and Evaluating Corrosion Test Specimens* [Online]. West Conshohocken , PA: ASTM International. Available: www.astm.org [Accessed].

GAO, Q., LU, Y., YU, Q., WU, Y., ZHANG, C. & ZHI, R. 2022. High-temperature corrosion behavior of austenitic stainless steel in quaternary nitrate molten salt nanofluids for concentrated solar power. *Solar Energy Materials and Solar Cells,* 245**,** 111851.

GELLINGS, P. & DE JONGH, M. J. C. S. 1967. Grain boundary oxidation and the chromium-depletion theory of intercrystalline corrosion of austenitic stainless steels. 7**,** 413-421.
GOMES, A., NAVAS, M., URANGA, N., PAIVA, T., FIGUEIRA, I. & DIAMANTINO, T. C. 2019. High-temperature corrosion performance of austenitic stainless steels type AISI 316L and AISI 321H, in molten Solar Salt. *Solar Energy,* 177**,** 408-419.
GOMEZ-VIDAL, J. C. 2017. Corrosion resistance of MCrAlX coatings in a molten chloride for thermal storage in concentrating solar power applications. *npj Materials Degradation,* 1.
GOMEZ-VIDAL, J. C., NOEL, J. & WEBER, J. 2016. Corrosion evaluation of alloys and MCrAlX coatings in molten carbonates for thermal solar applications. *Solar Energy Materials and Solar Cells,* 157**,** 517-525.
GOMEZ-VIDAL, J. C. & TIRAWAT, R. 2016. Corrosion of alloys in a chloride molten salt (NaCl-LiCl) for solar thermal technologies. *Solar Energy Materials and Solar Cells,* 157**,** 234-244.
GONZALEZ-RODRIGUEZ, J. G., MEJIA, E., LUCIO-GARCIA, M. A., SALINAS-BRAVO, V. M., PORCAYO-CALDERON, J. & MARTINEZ-VILLAFAÑE, A. 2009. An electrochemical study of the effect of Li on the corrosion behavior of Ni3Al intermetallic alloy in molten (Li+K) carbonate. *Corrosion Science,* 51**,** 1619-1627.
GOODS, S., BRADSHAW, R., PRAIRIE, M. & CHAVEZ, J. 1994a. Corrosion of stainless and carbon steels in molten mixtures of industrial nitrates. Sandia National Lab.(SNL-CA), Livermore, CA (United States).
GOODS, S., BRADSHAW, R. W. J. J. O. M. E. & PERFORMANCE 2004. Corrosion of stainless steels and carbon steel by molten mixtures of commercial nitrate salts. 13**,** 78-87.
GOODS, S. H., BRADSHAW, R. W., PRAIRIE, M. R. & CHAVEZ, J. M. 1994b. Corrosion of stainless and carbon steels in molten mixtures of industrial nitrates. Office of Scientific and Technical Information (OSTI).
GRÉGOIRE, B., OSKAY, C., MEIßNER, T. M. & GALETZ, M. C. 2020. Corrosion mechanisms of ferritic-martensitic P91 steel and Inconel 600 nickel-based alloy in molten chlorides. Part I: NaCl–KCl binary system. *Solar Energy Materials and Solar Cells,* 215**,** 110659.
GROSU, Y., NITHIYANANTHAM, U., ZAKI, A. & FAIK, A. 2018. A simple method for the inhibition of the corrosion of carbon steel by molten nitrate salt for thermal storage in concentrating solar power applications. *npj Materials Degradation,* 2.
GROT, A. S. & SPRUIELL, J. E. 1975. Microstructural stability of titanium-modified type 316 and type 321 stainless steel. *Metallurgical transactions A,* 6**,** 2023-2030.
GUI, Y., MENG, X. B., ZHENG, Z. J. & GAO, Y. 2017. Critical temperature determination of detectable Cr diffusion enhancement by nanostructure through structural evolution analysis of the oxide films at 25–450°C on 304 stainless steel. *Applied Surface Science,* 419**,** 512-521.
GUNEN, A. & KANCA, E. J. M. 2017. Microstructure and Mechanical Properties of Borided Inconel 625 Superalloy. 22.
HAMDY, E., OLOVSJÖ, J. N. & GEERS, C. 2021. Perspectives on selected alloys in contact with eutectic melts for thermal storage: Nitrates, carbonates and chlorides. *Solar Energy,* 224**,** 1210-1221.
HAN, Y., ZHANG, C., WU, Y. & LU, Y. 2021. Investigation on thermal performance of quaternary nitrate-nitrite mixed salt and solar salt under thermal shock condition. *Renewable Energy,* 175**,** 1041-1051.
HANCOCK, P. & HURST, R. 1974. The mechanical properties and breakdown of surface oxide films at elevated temperatures. *Advances in corrosion science and technology.* Springer.
HE, R., GAHLAWAT, S., GUO, C., CHEN, S., DAHAL, T., ZHANG, H., LIU, W., ZHANG, Q., CHERE, E., WHITE, K. & REN, Z. 2015. Studies on mechanical properties of thermoelectric materials by nanoindentation. *physica status solidi (a),* 212**,** 2191-2195.
HERRMANN, U., KELLY, B. & PRICE, H. 2004. Two-tank molten salt storage for parabolic trough solar power plants. *Energy,* 29**,** 883-893.
HOFMEISTER, M., KLEIN, L., MIRAN, H., RETTIG, R., VIRTANEN, S. & SINGER, R. F. 2015a. Corrosion behaviour of stainless steels and a single crystal superalloy in a ternary LiCl–KCl–CsCl molten salt. *Corrosion Science,* 90**,** 46-53.
HOFMEISTER, M., KLEIN, L., MIRAN, H., RETTIG, R., VIRTANEN, S. & SINGER, R. J. C. S. 2015b. Corrosion behaviour of stainless steels and a single crystal superalloy in a ternary LiCl–KCl–CsCl molten salt. 90**,** 46-53.

HU, Y., HAN, Y., QIN, Y. & ZHOU, H. 2018. Corrosion Behavior of 45 Steel in Molten Nitrate Salts with 3wt% Impurities at 773.15K. *IOP Conference Series: Materials Science and Engineering,* 394**,** 032117.
HUA, Y. 2015. *An Experimental Study of Corrosion for Long Distance Carbon Transportation Pipelines.* University of Leeds.
HUA, Y., XU, S., WANG, Y., TALEB, W., SUN, J., ZHANG, L., BARKER, R. & NEVILLE, A. 2019. The formation of FeCO3 and Fe3O4 on carbon steel and their protective capabilities against CO2 corrosion at elevated temperature and pressure. *Corrosion Science,* 157**,** 392-405.
INSTITUTION, B. S. 2009. *ISO 8047: Corrosion of metals and alloys - Removal of corrosion products from corrosion test specimens* [Online]. Available: https://www.iso.org/standard/42634.html [Accessed].
INTERNATIONAL, A. 2015a. ASTM A262-15, Standard Practices for Detecting Susceptibility to Intergranular Attack in Austenitic Stainless Steels. West Conshohocken: PA.
INTERNATIONAL, A. 2015b. *Standard Practice for Microetching Metals and Alloys* [Online]. West Conshohocken, PA. Available: www.astm.org [Accessed].
KAI, W., LI, C. C., CHENG, F. P., CHU, K. P., HUANG, R. T., TSAY, L. W. & KAI, J. J. 2016. The oxidation behavior of an equimolar FeCoNiCrMn high-entropy alloy at 950°C in various oxygen-containing atmospheres. *Corrosion Science,* 108**,** 209-214.
KEKKONEN, T., AALTONEN, P. & HANNINEN, H. 1985. Intergranular corrosion testing of nickel-base alloys. *Scand. J. Metall.,* 14**,** 243-251.
KENISARIN, M. M. 2010. High-temperature phase change materials for thermal energy storage. *Renewable and Sustainable Energy Reviews,* 14**,** 955-970.
KIM, H.-J., JEON, S.-H., KIM, S.-T., LEE, I.-S., PARK, Y.-S., KIM, K.-T. & KIM, Y.-S. 2014. Investigation of the sensitization and intergranular corrosion of tube-to-tubesheet welds of hyper duplex stainless steel using an electrochemical reactivation method. *Corrosion Science,* 87**,** 60-70.
KOKAWA, H., SHIMADA, M. & SATO, Y. S. 2000. Grain-boundary structure and precipitation in sensitized austenitic stainless steel. *JOM,* 52**,** 34-37.
KOLLI, S., JAVAHERI, V., OHLIGSCHLÄGER, T., KÖMI, J. & PORTER, D. 2020. The importance of steel chemistry and thermal history on the sensitization behavior in austenitic stainless steels: Experimental and modeling assessment. *Materials Today Communications,* 24**,** 101088.
KONDO, M., NAGASAKA, T., SAGARA, A., NODA, N., MUROGA, T., XU, Q., NAGURA, M., SUZUKI, A. & TERAI, T. 2009. Metallurgical study on corrosion of austenitic steels in molten salt LiF–BeF2 (Flibe). *Journal of Nuclear Materials,* 386-388**,** 685-688.
KRUIZENGA, A. & GILL, D. 2014. Corrosion of Iron Stainless Steels in Molten Nitrate Salt. *Energy Procedia,* 49**,** 878-887.
KRUIZENGA, A. M., GILL, D. D., LAFORD, M. & MCCONOHY, G. J. A. S. N. L. S.-. 2013. Corrosion of High Temperature Alloys in Solar Salt at 400, 500, and 680 C.
KRUIZENGA, A. M. J. S. N. L., LIVERMORE, CA REPORT NO. SAND- 2012. Corrosion mechanisms in chloride and carbonate salts.
KUTZ, M. 2018. *Handbook of environmental degradation of materials*, William Andrew.
LEJČEK, P. 2010. Models of equilibrium grain boundary segregation. *Grain Boundary Segregation in Metals.* Springer.
LI, B.-R., TAN, H., LIU, Y., LIU, Q., ZHANG, G.-Q., DENG, Z.-F., XU, G.-Z., GUO, Y.-Q. & DU, X.-Z. 2020. Experimental investigations on the thermal stability of Na2CO3–K2CO3 eutectic salt/ceramic composites for high temperature energy storage. *Renewable Energy,* 146**,** 2556-2565.
LI, D., GUO, Q., GUO, S., PENG, H. & WU, Z. 2011. The microstructure evolution and nucleation mechanisms of dynamic recrystallization in hot-deformed Inconel 625 superalloy. *Materials & Design,* 32**,** 696-705.
LI, H., FENG, X., WANG, X., YANG, X., TANG, J. & GONG, J. 2022. Impact of temperature on corrosion behavior of austenitic stainless steels in solar salt for CSP application: An electrochemical study. *Solar Energy Materials and Solar Cells,* 239**,** 111661.
LI, S.-X., HE, Y.-N., YU, S.-R. & ZHANG, P.-Y. 2013. Evaluation of the effect of grain size on chromium carbide precipitation and intergranular corrosion of 316L stainless steel. *Corrosion Science,* 66**,** 211-216.

LIMA, A. S., NASCIMENTO, A. M., ABREU, H. F. G. & DE LIMA-NETO, P. 2005. Sensitization evaluation of the austenitic stainless steel AISI 304L, 316L, 321 and 347. *Journal of Materials Science,* 40**,** 139-144.

LIU, B., WEI, X., WANG, W., LU, J. & DING, J. 2017. Corrosion behavior of Ni-based alloys in molten NaCl-CaCl 2 -MgCl 2 eutectic salt for concentrating solar power. *Solar Energy Materials and Solar Cells,* 170**,** 77-86.

LIU, L., LI, Y., ZENG, C. & WANG, F. 2006. Electrochemical impedance spectroscopy (EIS) studies of the corrosion of pure Fe and Cr at 600°C under solid NaCl deposit in water vapor. 51**,** 4736-4743.

LIU, M., STEVEN TAY, N. H., BELL, S., BELUSKO, M., JACOB, R., WILL, G., SAMAN, W. & BRUNO, F. 2016. Review on concentrating solar power plants and new developments in high temperature thermal energy storage technologies. *Renewable and Sustainable Energy Reviews,* 53**,** 1411-1432.

LIU, Q. 2021. The corrosion behaviour of stainless steels and Ni-based alloys in nitrate salts under thermal cycling conditions in Concentrated Solar Power plants. *Solar Energy,* .Under review.

LIU, Q., BARKER, R., WANG, C., QIAN, J., NEVILLE, A. & PESSU, F. 2022a. The corrosion behaviour of stainless steels and Ni-based alloys in nitrate salts under thermal cycling conditions in concentrated solar power plants. *Solar Energy,* 232**,** 169-185.

LIU, Q., QIAN, J., BARKER, R., WANG, C., NEVILLE, A. & PESSU, F. 2021a. Application of double loop electrochemical potentio-kinetic reactivation for characterizing the intergranular corrosion susceptibility of stainless steels and Ni-based alloys in solar nitrate salts used in CSP systems. *Engineering Failure Analysis,* 129**,** 105717.

LIU, Q., QIAN, J., BARKER, R., WANG, C., NEVILLE, A. & PESSU, F. 2022b. Effect of thermal cycling on the corrosion behaviour of stainless steels and Ni-based alloys in molten salts under air and argon. *Solar Energy,* 238**,** 248-257.

LIU, Q., WANG, Z., LIU, W., YIN, H., TANG, Z. & QIAN, Y. 2021b. Ni-Mo-Cr alloy corrosion in molten NaCl-KCl-MgCl2 salt and vapour. *Corrosion Science,* 180**,** 109183.

LIU, Q., XU, H., YIN, H., LI, N., WANG, W., LI, L., TANG, Z. & QIAN, Y. 2022c. Corrosion behaviour of 316 stainless steel in NaCl-KCl-MgCl2 salt vapour at 700°C. *Corrosion Science,* 194**,** 109921.

LOBNIG, R., SCHMIDT, H., HENNESEN, K. & GRABKE, H. 1992a. Diffusion of cations in chromia layers grown on iron-base alloys. *Oxidation of Metals,* 37**,** 81-93.

LOBNIG, R., SCHMIDT, H., HENNESEN, K. & GRABKE, H. J. O. O. M. 1992b. Diffusion of cations in chromia layers grown on iron-base alloys. 37**,** 81-93.

MA, L., ZHANG, C., WU, Y. & LU, Y. 2022. Comparative review of different influence factors on molten salt corrosion characteristics for thermal energy storage. *Solar Energy Materials and Solar Cells,* 235**,** 111485.

MAHMOUDI, A., ESMAILIAN, M. & AGHAMIRI, S. 2012. Effect of Stabilizing Heat Treatment on Intergranular Corrosion Resistance of Welded Stainless Steel AISI 321. *Advanced Materials Research,* 535-537**,** 692-696.

MALLCO, A., PINEDA, F., MENDOZA, M., HENRIQUEZ, M., CARRASCO, C., VERGARA, V., FUENTEALBA, E. & FERNANDEZ, A. G. 2022. Evaluation of flow accelerated corrosion and mechanical performance of martensitic steel T91 for a ternary mixture of molten salts for CSP plants. *Solar Energy Materials and Solar Cells,* 238**,** 111623.

MCCARTY, K. F. & BOEHME, D. R. 1989. A Raman study of the systems Fe3−xCrxO4 and Fe2−xCrxO3. *Journal of Solid State Chemistry,* 79**,** 19-27.

MCCONOHY, G. & KRUIZENGA, A. 2014. Molten nitrate salts at 600 and 680°C: Thermophysical property changes and corrosion of high-temperature nickel alloys. *Solar Energy,* 103**,** 242-252.

MEHOS, M., TURCHI, C., VIDAL, J., WAGNER, M., MA, Z., HO, C., KOLB, W., ANDRAKA, C. & KRUIZENGA, A. 2017. Concentrating solar power Gen3 demonstration roadmap. National Renewable Energy Lab.(NREL), Golden, CO (United States).

MEVREL, R. J. M. S. & TECHNOLOGY 1987. Cyclic oxidation of high-temperature alloys. 3**,** 531-535.

MOAYED, M. H. & NEWMAN, R. C. 2006. Evolution of current transients and morphology of metastable and stable pitting on stainless steel near the critical pitting temperature. *Corrosion Science,* 48**,** 1004-1018.

MOHAN, G., VENKATARAMAN, M. B. & COVENTRY, J. 2019. Sensible energy storage options for concentrating solar power plants operating above 600 °C. *Renewable and Sustainable Energy Reviews,* 107**,** 319-337.
MORSHED-BEHBAHANI, K., NAJAFISAYAR, P., PAKSHIR, M. & SHAHSAVARI, M. 2018. An electrochemical study on the effect of stabilization and sensitization heat treatments on the intergranular corrosion behaviour of AISI 321H austenitic stainless steel. *Corrosion Science,* 138**,** 28-41.
NISHIKATA, A., NUMATA, H., TSURU, T. J. M. S. & A, E. 1991. Electrochemistry of molten salt corrosion. 146**,** 15-31.
OLIVARES, R. I. & EDWARDS, W. 2013. LiNO3–NaNO3–KNO3 salt for thermal energy storage: Thermal stability evaluation in different atmospheres. *Thermochimica Acta,* 560**,** 34-42.
OLSON, L., SRIDHARAN, K., ANDERSON, M. & ALLEN, T. 2010. Intergranular corrosion of high temperature alloys in molten fluoride salts. *Materials at High Temperatures,* 27**,** 145-149.
OUYANG, F.-Y., CHANG, C.-H., YOU, B.-C., YEH, T.-K. & KAI, J.-J. 2013. Effect of moisture on corrosion of Ni-based alloys in molten alkali fluoride FLiNaK salt environments. *Journal of Nuclear Materials,* 437**,** 201-207.
PADILHA, A. F., PLAUT, R. L. & RIOS, P. R. 2003. Annealing of Cold-worked Austenitic Stainless Steels. *ISIJ International,* 43**,** 135-143.
PAPAELIAS, M., CHENG, L., KOGIA, M., MOHIMI, A., KAPPATOS, V., SELCUK, C., CONSTANTINOU, L., MUÑOZ, C. Q. G., MARQUEZ, F. P. G. & GAN, T.-H. 2016. Inspection and Structural Health Monitoring techniques for Concentrated Solar Power plants. *Renewable Energy,* 85**,** 1178-1191.
PARDO, A., MERINO, M. C., COY, A. E., VIEJO, F., CARBONERAS, M. & ARRABAL, R. 2007. Influence of Ti, C and N concentration on the intergranular corrosion behaviour of AISI 316Ti and 321 stainless steels. *Acta Materialia,* 55**,** 2239-2251.
PELAY, U., LUO, L., FAN, Y., STITOU, D. & ROOD, M. 2017. Thermal energy storage systems for concentrated solar power plants. *Renewable and Sustainable Energy Reviews,* 79**,** 82-100.
PENG, Q., DING, J., WEI, X., YANG, J. & YANG, X. 2010. The preparation and properties of multi-component molten salts. *Applied Energy,* 87**,** 2812-2817.
PERRARD, F., DESCHAMPS, A., BLEY, F., DONNADIEU, P. & MAUGIS, P. 2006. A small-angle neutron scattering study of fine-scale NbC precipitation kinetics in the [alpha]-Fe-Nb-C system. *Journal of Applied Crystallography,* 39**,** 473-482.
PERRARD, F., DESCHAMPS, A. & MAUGIS, P. 2007. Modelling the precipitation of NbC on dislocations in α-Fe. *Acta Materialia,* 55**,** 1255-1266.
PESSU, F. O. 2015a. *Investigation of pitting corrosion of carbon steel in sweet and sour oilfield corrosion conditions: a parametric study.* University of Leeds.
PESSU, F. O. 2015b. *Investigation of Pitting Corrosion of Carbon Steel in Sweet and Sour Oilfield Corrosion Conditions: A Parametric Study*, University of Leeds (Institute of Functional Surfaces, School of Mechanical Engineering).
PHARR, G. & OLIVER, W. J. M. B. 1992a. Measurement of thin film mechanical properties using nanoindentation. 17**,** 28-33.
PHARR, G. M. & OLIVER, W. C. 1992b. Measurement of Thin Film Mechanical Properties Using Nanoindentation. *MRS Bulletin,* 17**,** 28-33.
PIERAGGI, B. 1987. Calculations of parabolic reaction rate constants. *Oxidation of Metals,* 27**,** 177-185.
PREUßNER, J., PFEIFFER, W., PIEDRA, E., OESER, S., TANDLER, M., VON HARTROTT, P. & MAIER, C. Long-term material tests in liquid molten salts. Advances in Materials Technology for Fossil Power Plants - Proceedings from the 8th International Conference, 2016. 1126-1137.
PRIETO, C., RUIZ-CABAÑAS, J., MADINA, V., FERNÁNDEZ, A. I. & CABEZA, L. F. 2022. Lessons learned from corrosion of materials with molten salts during molten salt tank preheating. *Solar Energy Materials and Solar Cells,* 247**,** 111943.
PU, E., ZHENG, W., XIANG, J., SONG, Z. & LI, J. 2014. Hot deformation characteristic and processing map of superaustenitic stainless steel S32654. *Materials Science and Engineering: A,* 598**,** 174-182.

QIAN, J., CHEN, C., YU, H., LIU, F., YANG, H. & ZHANG, Z. 2016. The influence and the mechanism of the precipitate/austenite interfacial C-enrichment on the intergranular corrosion sensitivity in 310S stainless steel. *Corrosion Science,* 111**,** 352-361.

R.A. RAPP, Y. S. Z. 1994. *Hot corrosion of materials: Fundamental studies* [Online]. [Accessed].

RAHMAWATI, F., KUSUMANINGTYAS, A. A., SARASWATI, T. E., PRASETYO, A. & SUENDO, V. 2021. Mn-doped NaFeO2 from a low purity-Fe precursor and its performance as cathode for Sodium-Ion Battery. *Inorganic and Nano-Metal Chemistry,* 51**,** 383-390.

RAMOS, P., COELHO, R. S., SOLDERA, F., PINTO, H. C., MÜCKLICH, F. & BRITO, P. 2021. Residual stress analysis in thermally grown oxide scales developed on Nb-alloyed refractory austenitic stainless steels. *Corrosion Science,* 178**,** 109066.

SAHLAOUI, H., SIDHOM, H. & PHILIBERT, J. 2002. Prediction of chromium depleted-zone evolution during aging of Ni–Cr–Fe alloys. *Acta Materialia,* 50**,** 1383-1392.

SARVGHAD, M., STEINBERG, T. A. & WILL, G. 2017a. Corrosion of steel alloys in eutectic NaCl+Na2CO3 at 700°C and Li2CO3 + K2CO3 + Na2CO3 at 450°C for thermal energy storage. *Solar Energy Materials and Solar Cells,* 170**,** 48-59.

SARVGHAD, M., STEINBERG, T. A. & WILL, G. 2017b. Corrosion of steel alloys in eutectic NaCl+Na 2 CO 3 at 700 °C and Li 2 CO 3 + K 2 CO 3 + Na 2 CO 3 at 450 °C for thermal energy storage. *Solar Energy Materials and Solar Cells,* 170**,** 48-59.

SARVGHAD, M., WILL, G. & STEINBERG, T. A. 2017c. Corrosion of Inconel 601 in molten salts for thermal energy storage. *Solar Energy Materials and Solar Cells,* 172**,** 220-229.

SHANKAR, A., MATHIYA, S., THYAGARAJAN, K. & MUDALI, K. 2010. Corrosion and Microstructure Correlation in Molten LiCl-KCl Medium. *Metallurgical and Materials Transactions A,* 41**,** 1815-1825.

SHANKAR, A. R., KANAGASUNDAR, A. & MUDALI, U. K. J. C. 2012. Corrosion of nickel-containing alloys in molten LiCl-KCl medium. 69**,** 48-57.

SHANKAR, V., BHANU SANKARA RAO, K. & MANNAN, S. L. 2001. Microstructure and mechanical properties of Inconel 625 superalloy. *Journal of Nuclear Materials,* 288**,** 222-232.

SIEGEL, N. P., BRADSHAW, R. W., CORDARO, J. B. & KRUIZENGA, A. M. Thermophysical property measurement of nitrate salt heat transfer fluids. Energy Sustainability, 2011. 439-446.

SLUSSER, J., TITCOMB, J., HEFFELFINGER, M. & DUNBOBBIN, B. J. J. 1985. Corrosion in molten nitrate-nitrite salts. 37**,** 24-27.

SOLEIMANI DORCHEH, A., DURHAM, R. N. & GALETZ, M. C. 2016. Corrosion behavior of stainless and low-chromium steels and IN625 in molten nitrate salts at 600 °C. *Solar Energy Materials and Solar Cells,* 144**,** 109-116.

SOLEIMANI DORCHEH, A. & GALETZ, M. C. 2016. Slurry aluminizing: A solution for molten nitrate salt corrosion in concentrated solar power plants. *Solar Energy Materials and Solar Cells,* 146**,** 8-15.

SOURMAIL, T. 2001. Precipitation in creep resistant austenitic stainless steels. *Materials science and technology,* 17**,** 1-14.

SRIDHARAN, K. & ALLEN, T. 2013a. Corrosion in Molten Salts. *Molten Salts Chemistry***,** 241-267.

SRIDHARAN, K. & ALLEN, T. R. 2013b. 12 - Corrosion in Molten Salts. *In:* LANTELME, F. & GROULT, H. (eds.) *Molten Salts Chemistry.* Oxford: Elsevier.

STOPHER, M. A., LANG, P., KOZESCHNIK, E. & RIVERA-DIAZ-DEL-CASTILLO, P. E. J. 2016. Modelling hydrogen migration and trapping in steels. *Materials & Design,* 106**,** 205-215.

STOTT, F. & WEI, F. 1989. High temperature oxidation of commercial austenitic stainless steels. *Materials science and technology,* 5**,** 1140-1147.

SUKUMARAN, A., GUPTA, R. K. & ANIL KUMAR, V. 2017. Effect of Heat Treatment Parameters on the Microstructure and Properties of Inconel-625 Superalloy. *Journal of Materials Engineering and Performance,* 26**,** 3048-3057.

SUN, H., ZHANG, P. & WANG, J. 2018. Effects of alloying elements on the corrosion behavior of Ni-based alloys in molten NaCl-KCl-MgCl2 salt at different temperatures. *Corrosion Science,* 143**,** 187-199.

SUTTER, F., OSKAY, C., GALETZ, M. C., DIAMANTINO, T., PEDROSA, F., FIGUEIRA, I., GLUMM, S., BONK, A., AGÜERO, A., RODRÍGUEZ, S., RECHE-NAVARRO, T. J. & CARON, S. 2021. Dynamic corrosion testing of metals in solar salt for concentrated solar power. *Solar Energy Materials and Solar Cells,* 232**,** 111331.

TAN, Q., MO, N., JIANG, B., PAN, F., ATRENS, A. & ZHANG, M.-X. 2017. Combined influence of Be and Ca on improving the high-temperature oxidation resistance of the magnesium alloy Mg-9Al-1Zn. *Corrosion Science,* 122**,** 1-11.

TAN, Q., MO, N., LIN, C.-L., ZHAO, Y., YIN, Y., JIANG, B., PAN, F., ATRENS, A., HUANG, H. & ZHANG, M.-X. 2019. Generalisation of the oxide reinforcement model for the high oxidation resistance of some Mg alloys micro-alloyed with Be. *Corrosion Science,* 147**,** 357-371.

TANG, Y., ZUO, Y., WANG, J., ZHAO, X., NIU, B. & LIN, B. 2014. The metastable pitting potential and its relation to the pitting potential for four materials in chloride solutions. *Corrosion Science,* 80**,** 111-119.

THORVALDSSON, T. & DUNLOP, G. L. 1980. Precipitation reactions in Ti-stabilized austenitic stainless steel. *Metal Science,* 14**,** 513-518.

THORVALDSSON, T. & DUNLOP, G. L. 1982. Effect of stabilizing additions on precipitation reactions in austenitic stainless steel. *Metal Science,* 16**,** 184-190.

THORWALDSSON, T. & DUNLOP, G. 1979. The influence of composition on precipitation in stabilized austenitic stainless steels. *Strength of Metals and Alloys,* 1**,** 755-760.

TIAN, Y. & ZHAO, C. Y. 2013. A review of solar collectors and thermal energy storage in solar thermal applications. *Applied Energy,* 104**,** 538-553.

TIEN, J., DAVIDSON, J. J. S. E. & METALS, T. O. O. 1975. Oxide spallation mechanisms(protective scale destruction during thermal cycling). 200-219.

TRENT, M., GOODS, S. & BRADSHAW, R. Comparison of corrosion performance of grade 316 and grade 347H stainless steels in molten nitrate salt. AIP Conference Proceedings, 2016a. AIP Publishing LLC, 160017.

TRENT, M. C., GOODS, S. H. & BRADSHAW, R. W. 2016b. Comparison of corrosion performance of grade 316 and grade 347H stainless steels in molten nitrate salt. 1734**,** 160017.

TRILLO, E. A. & MURR, L. E. 1998. Effects of carbon content, deformation, and interfacial energetics on carbide precipitation and corrosion sensitization in 304 stainless steel. *Acta Materialia,* 47**,** 235-245.

VIGNAROOBAN, K., XU, X., ARVAY, A., HSU, K. & KANNAN, A. M. 2015a. Heat transfer fluids for concentrating solar power systems – A review. *Applied Energy,* 146**,** 383-396.

VIGNAROOBAN, K., XU, X., WANG, K., MOLINA, E. E., LI, P., GERVASIO, D. & KANNAN, A. M. 2015b. Vapor pressure and corrosivity of ternary metal-chloride molten-salt based heat transfer fluids for use in concentrating solar power systems. *Applied Energy,* 159**,** 206-213.

VILLADA, C., BONK, A., BAUER, T. & BOLÍVAR, F. 2018. High-temperature stability of nitrate/nitrite molten salt mixtures under different atmospheres. *Applied Energy,* 226**,** 107-115.

WAGNER, C. 1952. Theoretical analysis of the diffusion processes determining the oxidation rate of alloys. *Journal of the electrochemical Society,* 99**,** 369.

WALCZAK, M., PINEDA, F., FERNÁNDEZ, Á. G., MATA-TORRES, C. & ESCOBAR, R. A. 2018. Materials corrosion for thermal energy storage systems in concentrated solar power plants. *Renewable and Sustainable Energy Reviews,* 86**,** 22-44.

WALTER, M., SCH**?**TZE, M. & RAHMEL, A. 1993. Behavior of oxide scales on 12Cr-1Mo steel during thermal cycling. *Oxidation of Metals,* 39**,** 389-410.

WAS, G. S., TISCHNER, H. H. & LATANISION, R. M. 1981. INFLUENCE OF THERMAL TREATMENT ON THE CHEMISTRY AND STRUCTURE OF GRAIN BOUNDARIES IN INCONEL 600. *Metallurgical transactions. A, Physical metallurgy and materials science,* 12 A**,** 1397-1408.

WEI, X., YIN, Y., QIN, B., WANG, W., DING, J. & LU, J. 2020. Preparation and enhanced thermal conductivity of molten salt nanofluids with nearly unaltered viscosity. *Renewable Energy,* 145**,** 2435-2444.

WEST, D., HULANCE, J., HIGGINSON, R. L. & WILCOX, G. D. 2013. σ-phase precipitation in 347HFG stainless steel. *Materials Science and Technology,* 29**,** 835-842.

WILSON, F. G. 1971. Mechanism of Intergranular Corrosion of Austenitic Stainless Steels—Literature Review. *British Corrosion Journal,* 6**,** 100-108.

WU, T.-F. & TSAI, W.-T. 2003. Effect of KSCN and its concentration on the reactivation behavior of sensitized alloy 600 in sulfuric acid solution. *Corrosion Science,* 45**,** 267-280.

XU, B., LI, P. & CHAN, C. 2015. Application of phase change materials for thermal energy storage in concentrated solar thermal power plants: A review to recent developments. *Applied Energy,* 160**,** 286-307.

YI, Y., CHO, P., AL ZAABI, A., ADDAD, Y. & JANG, C. 2013. Potentiodynamic polarization behaviour of AISI type 316 stainless steel in NaCl solution. *Corrosion Science,* 74**,** 92-97.
YIN, Y., FAULKNER, R. G., MORETON, P., ARMSON, I. & COYLE, P. 2010. Grain boundary chromium depletion in austenitic alloys. *Journal of Materials Science,* 45**,** 5872-5882.
YIN, Y., TAN, Q., ZHAO, Y., SUN, Q., SHI, Z., BERMINGHAM, M., ZHUANG, W., HUANG, H. & ZHANG, M.-X. 2021. A cost-effective Fe-rich compositionally complicated alloy with superior high-temperature oxidation resistance. *Corrosion Science,* 180**,** 109190.
ZENG, C. L., WANG, W. & WU, W. T. 2001. Electrochemical impedance models for molten salt corrosion. 43**,** 787-801.
ZHANG, H. L., BAEYENS, J., DEGRÈVE, J. & CACÈRES, G. 2013. Concentrated solar power plants: Review and design methodology. *Renewable and Sustainable Energy Reviews,* 22**,** 466-481.
ZHANG, X., TANG, J., LIU, H. & GONG, J. 2019. Effects of pre-strain on sensitization and interganular corrosion for 304 stainless steel. *Engineering Failure Analysis,* 106**,** 104179.
ZHANG, X., TIAN, J., XU, K. & GAO, Y. 2003. Thermodynamic evaluation of phase equilibria in NaNO3-KNO3 system. *Journal of Phase Equilibria,* 24**,** 441-446.
ZHANG, X., ZHANG, C., WU, Y. & LU, Y. 2020. Experimental research of high temperature dynamic corrosion characteristic of stainless steels in nitrate eutectic molten salt. *Solar Energy,* 209**,** 618-627.
ZHANG, Y. J., XIAO, L. L., LIU, J. H., LIU, M. L. & FU, M. H. Corrosion behavior of Incoloy 800 in molten nitrate salt. Advanced Materials Research, 2014. Trans Tech Publ, 357-361.
ZHU, M., ZENG, S., ZHANG, H., LI, J. & CAO, B. 2018. Electrochemical study on the corrosion behaviors of 316 SS in HITEC molten salt at different temperatures. *Solar Energy Materials and Solar Cells,* 186**,** 200-207.